A Bifacial Photovoltaic Energy Yield Model with 3D Shading: Development, validation, and applications in tracked and mid-to-high latitude systems

Annie Russell

Thesis submitted to the University of Ottawa
in partial Fulfillment of the requirements for the
Doctorate in Philosophy in Electrical and Computer Engineering

©Annie Russell, Ottawa, Canada, 2024

Abstract

As of 2030, bifacial photovoltaic (PV) modules – which collect light on both the front and rear sides – are predicted to make up 60% of annual global PV expansion, exceeding 375 GW of installed capacity per year. Therefore, accurate and accessible bifacial PV performance models are crucial in enabling rapid global PV expansion. This thesis proposes a highly-parameterized, physics-based bifacial PV performance model that: (a) reduces uncertainty with respect to two-dimensional (2D) view factor models by eliminating key user-defined loss parameters, and (b) achieves greater computational efficiency than a ray tracing approach. The model computes shade-inclusive 2D front and rear irradiance profiles which interface with a cell-to-array level electrical model, producing per-timestamp current-voltage curves. A validation against measured power in fixed-tilt and single-axis tracked systems demonstrates a mean absolute error in modelled hourly power of 14.2 mW and 17.3 mW per watt of installed capacity, for each system respectively.

Due to its flexible parameterization, the model can be used to both predict and better understand PV system performance. To exemplify such use cases, this thesis includes a chapter on the energy yield impact of three physical effects in tracked bifacial PV, namely: (1) brightening at the edges of a row of PV modules, (2) angle of incidence losses in light reflected off of supportive racking, and (3) the addition of a secondary tracking axis in double-axis tracked bifacial modules. A subsequent chapter discusses the model's applicability in emerging PV markets at mid-to-high latitude locations, presenting another three studies on the energy yield impact of: (1) time-varying air mass, (2) latitude-dependent row spacing, and (3) ground accumulated snow. Such studies contribute to the global effort to reduce bifacial PV energy yield modelling uncertainty in both established and emerging markets and to de-risk bifacial PV investment around the world.

Acknowledgements

This work would not have been possible without the support and kindness of so many. First, thank you to my co-supervisors Prof. Karin Hinzer and Dr. Joan Haysom: to Karin for your deft guidance, incredible generosity with knowledge, and immense care for your students; to Joan for convincing me to take a stab at this model and for our conversations, full of perspective and possibility, ever since. • To my fellow SUNLAB members past and present: thank you for sharing your perseverance, passion, curiosity, homesickness, and humour. Thanks to our research associates and professors for your keen eyes, good questions, and kind encouragement. In particular, I am eternally grateful to Dr. Chris Valdivia for the years of support and guidance, patience and perspective. To my collaborators Erin, Cédric, Mandy, and Trevor - what a joy to wonder with you and make things that weren't there before. Thanks to Chu Tu (Robert) Li for the kind introduction to the wonderful world of bifacial PV. To Christine Couture and Dr. John Cook for your tireless work to keep our work working. • Thank you also to Jill Tymchak for the generous conversations and collaboration; Dr. Nicholas Riedel-Lynksgaer for correspondence on the stellar open-access dataset featured throughout this work; David Chuet and Dr. Maxime Darnon for efficient data and analysis support; Prof. Michael Ross and Simon Geoffroy-Gagnon for generous sharing on Northern energy issues; Dr. Silvana Ovaitt and Dr. Josh Stein for the IEA Bifacial Modelling Round Robin. • Outside the world of PV, my heart is bursting with gratitude to my family for their endless support, boundless encouragement, and many cross-country visits. To my mom and dad for the late night talks, Rolly runs, penguin breaks, and reminders to follow my joy. To my sister for the laughter, snuggles, and your deep love for this world. • I am also ever grateful to the friends who made these years more full: to Ben for the immense support, steadying conversations, and countless episodes of Bake-Off; Luise & Reed and family for your unending kindness; Magdalena and Andhra for sharing space and time and life; Emma, Calen, K, D, & J for reminding me to skate, play, read, and wonder between all the work; Myriam & Julien for your welcoming company; the UltimateBikers1000++ for all the wonderful adventures; S for enjoying the joy; and E for everything. • Much of this work was completed during the COVID 19 pandemic. I am grateful to the front-line workers and artists who kept us going. • I acknowledge the financial support of the Natural Sciences and Engineering Research Council of Canada.

I conducted this work from the unceded, occupied land of the Anishinaabe Algonquin Nation; the Musqueam, Squamish, and Tsleil-Waututh Nations; and the Katzie Nation. Indigenous communities, governments, and youth have continuously advanced the forefront of the transition/return to sustainable and resilient energy systems on these lands; I hold this decisive work as a foundation for current research in applied photovoltaics.

Statement of originality

Unless otherwise noted, all contributions described in this thesis are the author's own original work.

As first author of the reproduced texts in Chapters 3.1 and 5.3, **ANNIE C. J. RUSSELL** performed modifications to the model code; prepared and ran the described simulations; analyzed, visualized, and synthesized results; and wrote and edited the texts. As the primary developer of the model, Annie selected, or designed, and coded the algorithms described in this text, unless otherwise stated below.

The following sections, organized by topic or chapter, detail contributions that others have made to this work. As the primary developer of the model, Annie contributed to two of the studies discussed in Chapters 4 & 5 as second author and to one as third author; a full list of the co-authors' contributions to those manuscripts can be found in the cited texts.

Supervision & model development

As director of the University of Ottawa's SUNLAB research group, **PROF. KARIN HINZER** supervised Annie's research and led the development of the model described in this thesis. She provided guidance on software development priorities, methodology design, and results analysis and synthesis. She edited and revised the texts reproduced in this thesis as well as the co-authored publications cited. Karin was also principal investigator on the SUNLAB's research on mid-to-high latitude bifacial solar.

As an associate professor at the University of Ottawa and Innovative Energy Market Chief at J. L. Richards and Associates Ltd., **DR. JOAN. E. HAYSOM** provided supervision and industry context to help prioritize parameters of interest in Annie's research. For the texts reproduced in this thesis, Joan gave feedback on data analysis and synthesis and provided editing support.

As a senior research scientist at the University of Ottawa's SUNLAB research group, **DR. CHRISTOPHER E. VALDIVIA** assisted in guiding the development of the model and all related research. He provided feedback on algorithm design and implementation, software documentation and testing, study methodology design, and analysis of measured and modelled results. Chris' specific contributions to the the model code were: initial structuring of main Python classes, selection and initial implementation of just-in-time compiling, selection and initial implementation of two

ray-primitive intersections, and development of a script to extract cell-level single-diode model inputs from module-level current-voltage curves. Chris also edited and revised the texts reproduced in this thesis as well as the co-authored publications cited.

Chapter 3.1

The sky and ground meshing, as well as the finite element coupling and compensation algorithms, were demonstrated in Chu Tu Li's 2016 thesis [1].

As an undergraduate student assisting with the validation of the model, **CÉDRIC BOHÉMIER** performed data cleaning on the field data used in this chapter and helped generate the input files for the simulation of the two systems at the Technical University of Denmark test site.

Chapter 3.5.1

Figure 3.19 was modified from an International Energy Agency Photovoltaic Power Systems Programme (IEA PVPS) Task 13 report section written by Silvana Ayala Pelaez and Joshua S. Stein [2].

Chapter 3.5.2

Formerly at the J.L. Richards Innovative Energy Group, **JILL TYMCHAK** performed the PVsyst simulations for S1 and S4 scenarios in the IEA PVPS Task 13 Bifacial Modelling Comparison in this section and contributed to discussions on PVsyst parameters.

Chapter 4.2

As third author of the study referenced in this chapter and available in [3], Russell's contributions to this work included: study conceptualization and methodology design; design of the incidence angle modifier algorithm for torque-tube-reflected irradiance and 2-in-portrait system implementation; assistance with data interpretation; and editing the proceeding. **TREVOR J. COATHUP** and **MANDY R. LEWIS** modified the bifacial_radiance code, performed bifacial_radiance and DUET simulations, and analyzed results. A full list of their - and all our co-authors' - contributions can be found in [3].

Chapter 4.3

For the validation of the double-axis tracking model, **DAVID CHUET** provided several iterations of measured data from the Université de Sherbrooke test site and contributed to discussion on measured data and feedback on double-axis tracking validation analysis. **PROF. MAXIME DARNON**, formerly at the Université de Sherbrooke, contributed to discussion on measured data and feedback on validation analysis.

Chapter 5.1

As second author of the text referenced in this chapter and available in [4], Russell developed an approach to account for an air mass modifier in the model's electrical simulations, performed preliminary system-level simulations, wrote the first draft of Section III of the text, and assisted in revision. **MANDY R. LEWIS** generated the air mass modifier lookup table, performed further system-level simulations, analysed the data, and wrote the text. A full list of her - and all our co-authors' - contributions can be found in [4].

Chapter 5.2

As second author of the the study discussed in this chapter and available in [5], Annie co-designed the study methodology, provided guidance on data analysis and investigation, and reviewed and edited the text. **ERIN M. TONITA** co-designed the methodology, ran the simulations, analyzed and visualized the results (including Fig. 5.1 in this thesis), and wrote the text. A full list of her - and all our co-authors' - contributions can be found in [5].

List of publications

The author contributed to a number of publications and conference proceedings throughout the duration of her thesis work, listed below. The **bold** text denotes first author or co-authored publications presented in this thesis.

Journal articles

1. E. M. Tonita, C. E. Valdivia, A. C. J. Russell, M. Martinez-Szewczyk, M. I. Bertoni, and K. Hinzer, "Quantifying spectral albedo effects on bifacial photovoltaic module measurements and system model predictions," in Progress in Photovoltaics, vol. 32, no. 4, pp. 468-480, 2024, doi:10.1002/pip.3789

2. M. R. Lewis, T. J. Coathup, A. C. J. Russell, C. E. Valdivia, and K. Hinzer, "Quantifying Structural Shading & Reflection Effects on Single Axis Tracked Bifacial Photovoltaic System Performance," Advanced Energy and Sustainability Research, 2400007, 2024, doi: https://doi.org/10.1002/aesr.202400007.

3. **E. M. Tonita, A. C. J. Russell, C. E. Valdivia, and K. Hinzer, "Optimal ground coverage ratios for tracked, fixed-tilt, and vertical photovoltaic systems for latitudes up to 75°N," Solar Energy, vol. 258, pp. 8–15, 2023, doi: 10.1364/OE.481301.**

4. **T. J. Coathup, M. R. Lewis, A. C. J. Russell, J. E. Haysom, C. E. Valdivia, and K. Hinzer, "Impact of torque tube reflection on bifacial photovoltaic single axis tracked system performance," Opt. Express, vol. 31, no. 4, pp. 6143–6155, 2023, doi: 10.1016/j.solener.2023.04.038.**

5. E. M. Tonita, C. E. Valdivia, A. C. J. Russell, M. Martinez-Szewczyk, M. I. Bertoni, and K. Hinzer, "A general illumination method to predict bifacial photovoltaic system performance," Joule, vol. 7, pp. 5–12, 2023, doi: 10.1016/j.joule.2022.12.005.

6. **A. C. J. Russell, C. E. Valdivia, C. Bohémier, J. E. Haysom and K. Hinzer, "DUET: A Novel Energy Yield Model With 3-D Shading for Bifacial Photovoltaic Systems,"**

in IEEE Journal of Photovoltaics, vol. 12, no. 6, pp. 1576-1585, Nov. 2022, doi: 10.1109/JPHOTOV.2022.3185546.

Conference proceedings

1. E. M. Tonita, C. E. Valdivia, A. C. J. Russell, K. Hinzer, "Impact of spectral versus broadband albedo on bifacial silicon heterojunction photovoltaic devices across North America," Proc. SPIE PC12416, Physics, Simulation, and Photonic Engineering of Photovoltaic Devices XII, PC124160G (10 March 2023), doi: 10.1117/12.2650155.

2. **A. C. J. Russell, C. E. Valdivia, J. E. Haysom and K. Hinzer, "Impact of Snow Depth on Single-Axis Tracked Bifacial Photovoltaic System Performance," 2022 IEEE 49th Photovoltaics Specialists Conference (PVSC), Philadelphia, PA, USA, 2022, pp. 1-4, doi: 10.1109/PVSC48317.2022.9938750.**

3. M. R. Lewis, T. J. Coathup, A. C. J. Russell, J. Guerrero-Perez, C. E. Valdivia and K. Hinzer, "Racking Reflection and Shading Effects on Single Axis Tracked Bifacial Photovoltaic Modules," 2022 IEEE 49th Photovoltaics Specialists Conference (PVSC), Philadelphia, PA, USA, 2022, pp. 406-406, doi: 10.1109/PVSC48317.2022.9938693.

4. T. J. Coathup, M. R. Lewis, A. C. J. Russell, A. Conesa, J. Guerrero-Perez, C. E. Validivia, K. Hinzer, "Impact of reflective torque tube on rear side irradiance in bifacial photovoltaic modules," Proc. SPIE 11996, Physics, Simulation, and Photonic Engineering of Photovoltaic Devices XI, 119960A (4 March 2022), doi: 10.1117/12.2615658.

5. M. R. Lewis, A. C. J. Russell, C. E. Valdivia, J. E. Haysom, M. I. Bertoni, K. Hinzer, "Impact of Spectral Correction on Bifacial Silicon Heterojunction Module Energy Yield in High Latitude Locations," Proc. SPIE 11681, Physics, Simulation, and Photonic Engineering of Photovoltaic Devices X, 116810R (5 March 2021), doi: 10.1117/12.2578783.

6. **M. R. Lewis, A. C. J. Russell, C. E. Valdivia, J. E. Haysom, M. I. Bertoni and K. Hinzer, "Impact of Air Mass on Energy Yield Calculation for Bifacial Silicon Heterojunction Photovoltaic Modules in High-Latitude Conditions," 2020 47th IEEE Photovoltaic Spe-**

cialists Conference (PVSC), Calgary, AB, Canada, 2020, pp. 0371-0375, doi: 10.1109/PVSC45281.2020.9300441.

7. M. R. Lewis, A. C. J. Russell, E. M. Tonita, C. E. Valdivia, J. E. Haysom, M. I. Bertoni, K. Hinzer, "Impact of bifacial photovoltaic cell characteristics on module energy yield in high-latitude locations," Proc. SPIE 11275, Physics, Simulation, and Photonic Engineering of Photovoltaic Devices IX, 112750W (10 March 2020), doi: 10.1117/12.2546583.

8. A. C. J. Russell, C. E. Valdivia, M. R. Lewis, J. E. Haysom and K. Hinzer, "Modelling Bifacial Solar Energy Yield for Single-Axis Tracked Systems with Racking," 2019 International Conference on Numerical Simulation of Optoelectronic Devices (NUSOD), Ottawa, ON, Canada, 2019, pp. 61-62, doi: 10.1109/NUSOD.2019.8807097.

9. A. C. J. Russell, C. E. Valdivia, M. R. Lewis, J. E. Haysom and K. Hinzer, "Modelling Energy Yield Including Rack Shading for Single-Axis Tracked Bifacial Solar Panels," 2019 Photonics North (PN), Quebec City, QC, Canada, 2019, pp. 1-1, doi: 10.1109/PN.2019.8819539.

Industry report

1. **J. Stein, C. Reise, J. Castro, G. Friesen, G. Mauger, E. Urrejola, S. Ranta, M. Alam, M. Anoma, S. Pelaez, D. Berrian, E. Bertrand, M. Chiodetti, D. Chudinzow, H. Colin, I. Devoto, R. French, E. Fuentealba, F. Haffner, A. Halm, J. Haysom, K. Hinzer, I. Horvath, H. Huerta, M. Khan, M. Klenk, R. Kopecek, J. Libal, M. Lindh, B. Marion, M. Mikofski, R. Molinero, M. Monarch, A. Neubert, M. Patel, A. Petersson, G. Poulin, S. Ramesh, O. Rhazi, N. Riedel-Lyngskær, D. Riley, A. Russell, A. Schneider, C. Stark, T. Timofte, D. Tune, J. Tymchak, C. Valdivia, F. Valencia, and M. Wang, "Bifacial Photovoltaic Modules and Systems: Experience and Results from International Research and Pilot Applications: Report IEA-PVPS T13-14:2021," International Energy Agency, Tech. Rep., 2021.**

Contents

Abstract **ii**

Acknowledgements **iii**

Statement of originality **v**

List of publications **viii**

List of figures **xiii**

List of tables **xviii**

List of acronyms **xix**

1 Introduction **1**

2 Bifacial photovoltaic (PV) performance modelling **5**

2.1 Bifacial PV cells, modules, and systems 5

2.2 Optical models for bifacial PV 24

2.3 Field measurements for PV model validation 41

2.4 Software concepts 44

3 Model development and validation **52**

3.1 Novel energy yield model with 3-D shading for bifacial photovoltaic systems . . . 52

3.2 Details on simulated environment 65

3.3 Details on optical model 68

3.4 Details on electrical model 79

3.5 Cross-software comparisons 88

3.6 Computational efficiency 97

4 Use-cases in tracking PV **102**

4.1 Inter-module edge brightening and current mismatch loss 102

4.2 Supportive structure shading and reflection 112
4.3 Double-axis tracking at 45°N 116

5 Use-cases in mid-to-high latitude PV 130
5.1 Air mass impact on short circuit current 130
5.2 Latitude impact on optimal row spacing 132
5.3 Snow-dependent ground clearance 134

6 Summary and outlook 140

7 Appendices 149

References 149

Appendix A 171

Appendix B 183

Appendix C 184

List of Figures

2.1 Silicon doping and behaviour of p-n junction under bias and illumination. 7
2.2 (a) Cell current-voltage (IV) curve. (b) Single diode model and parameters [6]. . . 10
2.3 (A) Full and half-cut cells with busbars for rectangular and pseudo-square wafer shape. (B) Full and half-cut cell modules with cell electrical interconnection and bypass diodes shown in black. 13
2.4 Electrical specifications - Trina Solar Module Datasheet 16
2.5 (A) Fixed-tilt array layout (top) and collector position with fixed-tilt β. (B) North-south horizontal single-axis tracking array layout (top) and collector axis of tilt rotation (bottom). (C) Double axis tracking array layout (top) and collector axes of tilt and azimuth rotation. 18
2.6 (A) Module orientation naming convention - P = portrait, L = landscape. (B) Multi-row array layout with row and table gaps. (C) Common supportive racking structures for single-axis tracking systems. 19
2.7 Backtracking adjusts single-axis tracking tilt angle, β, to a shallower angle, β', to avoid direct beam shading. 21
2.8 (A) Bifacial PV irradiance sources. (B) Sun elevation, zenith, and azimuth. (C) Ground reflection with Lambertian and specular components. 25
2.9 Modelled clear sky spectral irradiance [7] incident on a horizontal plane at noon at Ottawa summer solstice AM1.1, Whitehorse summer solstice AM1.3, and Ottawa winter solstice AM2.7, compared to extraterrestrial AM0 spectrum. Mono-c Si EQE overlaid in dotted grey. 26
2.10 (A.i) Three dimensional view factor (3D VF). (A.ii) Example of 3D VF at two points on two rectangular polygons with a shared edge. (B) 2-dimensional VF collapses the scenario in A.ii into a cross-section. (C) Reverse ray tracing probes the path of rays exiting the module sample point for intersection with surfaces. . . 33
2.11 Finite element approach to solving view factor between two arbitrary surfaces S_1 and S_2 as the summation of coupling between i'th and j'th elements of finite area A_i, Aj. 36

2.12 Irradiance measurement devices for DHI and GHI (A, pyranometer), DNI (B, Pyrheliometer) and albedo (C, albedometer) 41
2.13 Example of the rotation of a volume from initial position to final position. 45
2.14 Tait-Bryan rotations. 46
2.15 Example of a bounding volume hierarchy and primitive check list. 48
3.1 Diffuse sky dome and ground mesh element definitions. 66
3.2 3D shading primitives with labeled parameters. 67
3.3 Sky-to-ground compensation factor vs. sky element resolution 70
3.4 Front and rear ground-to-module compensation factor vs. tilt angle for varied azimuth mesh densities. 71
3.5 Front and rear ground-to-module compensation factor vs. tilt angle for varied radial mesh densities. 72
3.6 Front and rear ground-to-module compensation factor vs. tilt angle for varied ground mesh densities. 72
3.7 Front and rear ground-to-module compensation factor vs. tilt angle for varied ground surface extents. 73
3.8 Front and rear sky-to-module compensation factor vs. tilt angle. 75
3.9 (A) DUET v.uO-2024 bounding volume hierarchy. (B) DUET v.uO-2024 bounding volume hierarchy decision tree. 78
3.10 Module non-uniform irradiance scenarios A-E for IV curve demonstration. 80
3.11 Current-voltage curve for module shading scenario A: 90% shaded single cell . . . 81
3.12 Current-voltage curve for module shading scenario B: 50% shaded single cell . . . 82
3.13 Current-voltage curve for module shading scenario E: Gradual shading within a single submodule. 83
3.14 Current-voltage curve for module shading scenario C: 90% shading across bottom row of full cells 84
3.15 Current-voltage curve for module shading scenario C: 90% shading across bottom row of full cells with -0.7 V cell breakdown voltage. Inset: power gain vs. breakdown voltage. 85

3.16 Current-voltage curve for module shading scenario D: 90% shading across bottom two rows of half-cut cells. 86
3.17 Current-voltage curve for module edge brightening scenario F: brightening across right-most column of full cells. 87
3.18 Current-voltage curve for module edge brightening scenario G: brightening across right-most submodule of full cells. 88
3.19 Selected IEA PVPS Task 13 Bifacial Modelling Comparison results with DUET results de-anonymized. 91
3.20 PVsyst simulation parameters for IEA Bifacial Modelling Comparison scenario S4 in Groningen 93
3.21 Description of IEA PVPS Task 13 Bifacial Modelling Comparison fixed-tilt Scenario 1 for DUET v.uO-2020 and PVsyst v6.86. 93
3.22 Comparison between DUET v.uO-2020 and PVsyst v6.86 front irradiance for IEA Bifacial Modelling Comparison single-axis tracked scenario S4 [2] in three locations. 95
3.23 Comparison between DUET v.uO-2020 and PVsyst v6.86 rear irradiance for IEA Bifacial Modelling Comparison single-axis tracked scenario S4 [2] in three locations. 96
3.24 Single-day normalized computation time vs. mesh density for a 2P per-module single-axis tracked system. 101
3.25 Single-day normalized energy yield vs. mesh density for a 2P per-module single-axis tracked system. 101
4.1 Birdseye view of a 2P row in the fixed-tilt and single-axis tracked (SAT) systems at the Technical University of Denmark (reproduction of Section 3.1 Fig.6b). . . . 105
4.2 Average hourly modelled irradiance on front and rear of fixed-tilt and single-axis tracking rows. 107
4.3 Average modelled irradiance non-uniformity on front and rear of fixed-tilt row and a single-axis tracking rows. 107
4.4 Annual energy yield gain with respect to center module in each table for each module of the fixed-tilt and single-axis tracked rows. 109

4.5 Mean bias error and mean absolute error between DUET v.uO-2022 modelled and measured data for the single-axis tracking row at the Technical University of Denmark, including *full row with mismatch loss* results. 111
4.6 Birdseye view and cross-section of 2P torque tube reflection coupling. 114
4.7 A schematic of front/rear tracker head classification for a double-axis tracker under investigation. 119
4.8 Double-axis backtracking schematics based on [8]. 120
4.9 Layout of the Université de Sherbrooke double-axis tracking site. 121
4.10 Schematic of a 7L, 6-column double axis tracker head at the Université de Sherbrooke site. 122
4.11 Modelled vs. measured power for single module within the green tracker head in Fig. 4.9 for August 2022. 123
4.12 Modelled and measured power timeseries for the six yellow modules in Fig. 4.10 for bifacial and monofacial trackerheads on a clear August 20, 2022. 124
4.13 Summer and winter average the Hourly Ontario Electricity Price and energy yield profiles for bifacial and monofacial double-axis tracked PV, and single-axis tracked and fixed-tilt monofacial PV. 127
4.14 Double- and single-axis tracking gains in revenue based on the Hourly Ontario Electricity Price 2016-2022. 128
4.15 Bifacial gain in revenue based on the Hourly Ontario Electricity Price 2016-2022. . 129
5.1 Trends in optimal ground coverage ratio (GCR) for fixed-tilt, horizontal SAT (HSAT) and vertical E-W systems for (A) 5%, (B) 10%, and (C) 15% inter-row loss cases. Figure reproduced from Tonita et al. [5]. 134
7.1 Ray-polygon intersection test schematic. 172
7.2 Flowchart for ray-polygon intersection [9] 173
7.3 Ray-cylinder intersection test schematic. 174
7.4 Flowchart for ray-cylinder intersection (Part 1) [10] 176
7.5 Flowchart for ray-cylinder intersection (Part 2) [10] 177
7.6 Flowchart for ray-cylinder intersection (Part 3) [10] 178
7.7 Ray-prism (axis-aligned rectangular) intersection check. 179

7.8 Flowchart for ray-prism intersection : axis-aligned rectangular prisms [11] 180
7.9 Ray-prism (arbitrarily oriented rectangular) intersection check. 181
7.10 Flowchart for ray-prism intersection : arbitrarily-oriented rectangular prisms [12] . 182
7.11 Modelled increase in (Δ) cell temperature due to rear irradiance for three cell temperature models in 2P SAT east-west modules and fixed-tilt north-south modules. . 187

List of Tables

1 Comparison of transposition model types. 32
2 The three locations in the IEA PVPS Task 13 Bifacial Modelling Comparison (based on Table 16 in [2]). UAE: United Arab Emirates, CL: Chile, NL: The Netherlands, DNI: Direct normal insolation (annual), DHI: Diffuse horizontal insolation (annual), $\bar{T}_{\text{a}}$: Average ambient temperature. 89
3 Energy yield comparison for the three row modelling methods described in 4.1.1. . 110
4 Annual and seasonal energy yield impacts of novel modelling approaches demonstrated in this thesis. 141
5 *Estimated* absolute difference in bifacial vs. monofacial average coefficients of variation in power ($\Delta\bar{\text{CV}}$ in P), across three temperature models. $\bar{\Delta}T_c$: average difference in bifacial vs. monofacial cell temperature; $\bar{\text{CV}}$ in ΔT_c: average CV in difference between bifacial and monofacial cell temperature; μ_P: temperature coefficient of power. 188
6 *Calculated* absolute difference in bifacial vs. monofacial average coefficients of variation in power ($\Delta\bar{\text{CV}}$ in P), across three temperature models. $\bar{\text{CV}}$ in P_{bi}: average CV in bifacial power; $\bar{\text{CV}}$ in P_{mono}: average CV in monofacial power. 188
7 Calculated absolute difference in coefficients of variation (ΔCV) in bifacial vs. monofacial *annual energy yield* (EY_{bi}, EY_{mono}) across three temperature models. . 188

List of Acronyms

1D / 2D	one / two dimensional
XL	X-in-landscape
XP	X-in-portrait
AC	alternating current
AM	air mass
AOI	angle of incidence
ARC	anti-reflective coating
ASHRAE	American Society of Heating, Refrigerating and Air-Conditioning Engineers
BRDF	bi-directional reflectance distribution function model function
BVH	bounding volume hierarchy
CL	Chile
CPU	central processing unit
CV	coefficient of variation
DAT	double-axis tracker
DC	direct current
DHI	diffuse horizontal irradiance
DNI	direct normal irradiance
DTU	Technical University of Denmark
E	east
EQE	external quantum efficiency
EVA	ethyl-vinyl-acetate
FT	fixed-tilt
STC	standard test conditions
GCR	ground coverage ratio
GHI	global horizontal irradiance
HOEP	Ontario hourly wholesale energy price
HPC	high performance computing
HSAT	horizontal single-axis tracker
IAM	incidence angle modifier
IBC	interdigitated back contact
IEA	International Energy Agency
IEEE	Institute of Electrical and Electronics Engineers
IV	current-voltage
JIT	just-in-time (compiling)
MAE	mean absolute error/deviation
MBE	mean bias error/deviation
mono-c	mono-crystalline
N	north
NL	The Netherlands
NOCT	nominal operating cell temperature
NREL	National Renewable Energy Laboratory (United States)
PID	potential induced degradation
POA	plane-of-array
PV	photovoltaic
PVPMC	PV Performance Modeling Collaborative Collaborative
PVPS	PV Power Systems Programme
PVSC	Photovoltaic Specialists Conference
S	south
SAM	System Advisory Model (NREL)
SAT	single-axis tracker
Si	silicon
TMY	typical meteorological year
U.S.	United States
UAE	United Arab Emerates
VF	view factor
W	west
Wp	watt-peak (installed capacity)

List of Symbols

α	transparency of primitive
$\angle_{\text{lat}}$	latitude
β, β_{m}	plane-of-array tilt angle
β'	backtracking tilt angle
β_{p}	tilt (or pitch) about the Y' axis of primitive p
β_{B}	sun elevation angle
β_s	sky dome element elevation angle in the Perez all-sky luminance model [13]
γ	angle between the sun and sky element s
γ_{m}	plane-of-array roll
γ_{p}	roll angle about the X' axis of primitive p
ΔT	change in temperature, or Sandia temperature model module-to-cell temperature differential [14]
Δ	'change in', or sky brightness in the Perez all-sky luminance model [13]
ΔCV	absolute difference between two coefficients of variation
$\Delta\bar{\text{C}}\text{V}$	absolute difference between bifacial vs. monofacial average coefficients of variation
ΔT_c	per-timestamp absolute difference between bifacial vs. monofacial cell temperature
$\bar{\Delta} T_c$	average difference between bifacial vs. monofacial cell temperature
δ'	updated shading coefficient to be multiplied into any stored coefficient δ for previous shading checks on the same ray
δ_{S}	approximate solar declination
$\delta_{\text{B},g}$	shading coefficient between the direct beam and ground element g
$\delta_{\text{B},m}$	shading coefficient between the direct beam and module element m
$\delta_{e,i}$	shading factor between emitting element e and irradiated element i
$\delta_{g,m}$	shading coefficient between ground element g and module element m
$\delta_{s,g}$	shading coefficient between sky element s and ground element g
$\delta_{s,m}$	shading coefficient between sky element s and module element m
ϵ	sky clearness in the Perez all-sky luminance model [13]
η	day angle
$\theta_{e,i}$	angle of incidence between emitting element e and irradiated element i
θ_1 / θ_2	angles of incidence between $R_{1,2}$ and the normals of S_1 and S_2 for each set of points (x_1, y_1) and (x_2, y_2)
θ_i, θ_j	angle of incidence of ray between i and j
λ	wavelength of incident irradiance in nm
μ	average
μ_{I}	temperature coefficient of current
μ_P	temperature coefficient of power
ρ	albedo
σ	standard deviation
τ	distance along the sun unit vector $\vec{s}$ that results in an intersection at point d in the plane of tracker head j
ϕ	module bifaciality factor
φ	azimuth angle

φ_{m}	plane-of-array azimuth (or yaw) angle
φ_{p}	azimuth (or yaw) angle about the Z' axis of primitive p
$\chi_{\mathrm{G},m}$	compensation factor between the reflecting ground surface and the the m'th module element
$\bar{\chi}_{\mathrm{G},m}$	the average $\chi_{\mathrm{G},m}$ across all N_{M} module elements
$\chi_{\mathrm{S},g}$	compensation factor between the diffuse sky dome and the the g'th ground element
$\chi_{\mathrm{S},m}$	compensation factor the diffuse sky dome and the m'th module element
$\chi_{S_1,j}$	compensation between emitting surface S_1 and j'th mesh element on the irradiated surface S_2
$\Omega_{i,j_{\mathrm{proj}}}$	projected solid angle between finite elements represented by central points i and j
$\Omega_{e,i}$	solid angle between emitting element e and irradiated element i
$\Omega_{i,j}$	solid angle between finite elements represented by central points i and j
a	Sandia temperature model coefficient [14] or Perez all-sky luminance model coefficient [13]
A_1 / A_2	total areas of the surfaces S_1 and S_2
A_c	area of the cell c in m^2
A_g	ground element area
A_i, A_j	area of the finite elements represented by central points i and j
A_m	area of module element m
A_{p}	area of the polygon
A_s	sky element area
A_{x}	sum of the areas of N triangles formed between p_{x} and $N-1$ pairs of polygon corners
$a-e$	Perez all-sky luminance model coefficients [13]
b	Sandia temperature model coefficient [14] or Perez all-sky luminance model coefficient [13]
$b_{0,x-z}$	minimum bounds of axis-aligned bounding box bounds in coordinate system X, Y, and Z, based on an origin at $(0,0)$
$b_{1,x-z}$	maximum bounds of axis-aligned bounding box bounds in coordinate system X, Y, and Z, based on an origin at $(0,0)$
$B_{i,x/y}$	x and y coordinates of point B_i at the farthest edge of a tracker such that point p_i and B_i form a line parallel to the ground
b_c	central point of a rectangular prism
b_c	rectangular prism central coordinate
b_h	half-lengths along the direction of unit vectors b_u in three axes of the oriented prism that point away from a central origin point, b_c
b_u	rectangular prism unit vectors in three axes of the oriented prism that point away from a central origin point, b_c
BG_{PVsyst}	a form of bifacial irradiance gain required for PVsyst mismatch loss calculation
c	cell number, or the speed of light in $\mathrm{nm/s}$
$\vec{c}$	line segment delineating cylinder central axis
c_0 / c_1	cylinder start and end coordinates
$C_{g,m}$	coupling coefficient between the g'th ground element and the m'th module element
$C_{i,j}$	coupling coefficient representing the radiation transfer between a set of coupled finite elements with center points i and j
C_{f}	fixed ground clearance

$C_{s,g}$	coupling coefficient between the s'th sky element and the g'th ground element
$C_{s,m}$	coupling coefficient between the s'th sky element and the m'th module element
$C_{\mathrm{s}}(t)$	snow-dependent ground clearance at time t
$c - e$	Perez all-sky luminance model coefficient [13]
$\bar{\mathrm{CV}}$	average coefficient of variation
d	row spacing, or Perez all-sky luminance model coefficient [13]
d_j	vector between p_j and intersection point d between the plane of tracker head j and sun vector $\vec{s}$
$\vec{d}$	ray direction vector
d_0	ray origin
$d_{j,x}$	component of vector d_j along the tier-wise direction of tracker head
$d_{j,y}$	component of vector d_j along the column-wise direction of tracker head
dA_1 / dA_2	variables of integration denoting integration across all continuous points on S_1 and S_2
e	emitting source, or Perez all-sky luminance model coefficient [13]
$E_{\mathrm{g,STC}}$	bandgap energy of silicon at T_{STC}, and
EQE_c	external quantum efficiency (EQE) of cell c
EY_{X}	energy yield per installed capacity [$\mathrm{Wh/Wp}$] for a given system or module type described in subscript
$F_{\mathrm{G},m}$	view factor between an infinite ground plane and module element m
$F_{\mathrm{S},g}$	view factor between the total diffuse sky dome and ground element g
$F_{\mathrm{S},m}$	view factor between the diffuse sky dome and the module element m
$F_{1,2}$	view factor representing the fraction of energy emitted from surface S_1 that is incident on surface S_2
g	ground element number
G_0	extraterrestrial irradiance
$\bar{G}_0$	average annual extraterrestrial irradiance
G_2	irradiance incident on S_2 emitted by S_1
G_{B}	direct normal (beam) irradiance
G_{c}	total average irradiance on front and rear of the cell
$G_c(\lambda)$	spectral irradiance incident on the cell c in $\mathrm{W/m^2/nm}$
$G_{c,\mathrm{f}}$	average irradiance on front of cell c neglecting reflection losses
$G_{c,\mathrm{r}}$	average irradiance on rear of cell c neglecting reflection losses
G_{D}	diffuse horizontal irradiance
$\bar{G}_{(\mathrm{f/r})}$	per-timestamp average front/rear irradiance
G_g	irradiance incident on ground element g
G_{H}	global horizontal irradiance
G_i	radiance emitted from each finite element of surface S_1 with area A_i
G_m	average irradiance incident on the module
G_m^{B}	direct beam effective irradiance on module element m, including reflection losses
G_m^{D}	diffuse effective irradiance on module element m, including reflection losses
G_m^{R}	ground-reflected effective irradiance on module element m, including reflection losses
$G_{m,\mathrm{r}}$	effective irradiance on rear of module element m
G_s	irradiance at the sky element s
G_{STC}	irradiance under standard test conditions

G_{Z}	irradiance at the sky dome zenith
h	Plank's constant in $\mathrm{J} \cdot \mathrm{s}$, or fractional hour of the day in solar time
H	hour angle
$h_{u,v,w}$	half length along each rectangular prism unit vector, dictating prism dimensions
i	irradiated element, or central point of coupled finite element on surface S_1
I	current
I_0	(dark) saturation current
I_c	current of cell c
I_L	light-generated current
I_{mp}	current at maximum power point
$I_{\mathrm{sc,c}}$	short circuit current of cell c
I_{sc}	short circuit current
$I_{\mathrm{sc},c}$	short circuit current of cell c
j	central point of coupled finite element on surface S_1 and S_2
k	Boltzmann's constant
l	magnitude of the vector $d\vec{P}$ representing the shortest distance between the ray and the cylinder line segment
L	collector width (i.e., tier-wise height of row or tracker head)
L_{X}	installed capacity per land area $[\mathrm{Wp}/\mathrm{m}^2]$ for a given system type
L_s	radiance of sky element s
m	air mass, or module element
M	current or electrical mismatch loss
M_{PVsyst}	PVsyst bifacial mismatch loss factor
n	cell ideality factor
$\vec{n}$	normal vector to a surface
N_1 / N_2	total number of mesh elements on each surface S_1 and S_2
$N_{\beta_{\mathrm{s}}}$	number of sky azimuth divisions
$N_{\varphi_{\mathrm{G}}}$	number of ground azimuth divisions
n_{d}	fractional day of the year
n_i	intrinsic (undoped) carrier concentration of silicon
N_{M}	number of module elements
N_{S}	number of sky elements
$n_{i,\mathrm{STC}}$	intrinsic carrier concentration of Si at T_{STC},
N_{TT}	number of torque tube mesh elements
$d\vec{P}$	vector representing the shortest distance between the ray and the cylinder line segment
$P_{0-(N-1)}$	N-vertex polygons corner coordinates
P_1	total power emitted from S_1
P_2	power incident on S_2 as fraction of P_1
P, P_{X}	power, of array or module if described in subscript
P_{bi}	bifacial power
P_c	power of cell c
$P_{c,\mathrm{f}}$	optical power on front of cell c
$P_{c,\mathrm{r}}$	optical power on rear of cell c
$p_{i,x/y}$	x and y coordinates of the rotation point on tracker head i under investigation

$p_{j,x/y}$	x and y coordinates of the rotation point on tracker head j analogous to $p_{i,x/y}$ on tracker head i
P_{mono}	monofacial power
P_{mp}	maximum power point
p_{x}	intersection point between an infinite line extending along ray direction $\vec{d}$ and a polygon plane
q	elementary electric charge in C
$\Re$	cell responsivity at standard test condition in $\mathrm{A/W}$
$\Re_c(\lambda)$	spectral responsivity of cell c in $\mathrm{A/W}$
R	rotation matrix
$R_{1,2}$	length of a ray between a set of points (x_1, y_1) and (x_2, y_2) on the surfaces S_1 and S_2
r_c	cylinder radius
$r_{g,\text{O}}$ / $r_{g,\text{I}}$	outer and inner radii of the ground element
R_{s}	cell series resistance
R_{sh}	cell shunt resistance
$R_{\text{sh,STC}}$	shunt resistance under STC
$R_{i,j}$	length of ray connecting finite element centers i and j
R_x	rotation matrix for rotation around body-fixed axis, X'
R_y	rotation matrix for rotation around body-fixed axis, Y'
R_z	rotation matrix for rotation around body-fixed axis, Z'
s	sky element number
s / t	distances along ray direction $\vec{d}$ and cylinder axis $\vec{c}$, respectively, that result in the shortest distance between the ray and the cylinder line segment
$\vec{s}$	sun vector
S_1 / S_2	example surfaces
$S(t)$	snow depth at time t
T	temperature
t_1 / t_2	points at which a ray with origin d_0 and direction $\vec{d}$ crosses closest and farthest bounds of an arbitrarily-oriented bounding box face such that $t_1 < t_2$.
T_{a}	ambient temperature
T_c	temperature of cell c
$t_{\text{max},x-z}$	distance along ray direction $\vec{d}$ from ray origin d_0 at which a given ray crosses the farthest bound of an axis-aligned bounding box from d_0 for a given axis X,Y or Z.
$t_{\text{min},x-z}$	distance along ray direction $\vec{d}$ from ray origin d_0 at which a given ray crosses the closest bound of an axis-aligned bounding box to d_0 for a given axis X,Y or Z.
T_m	average temperature incident on the module
T_{NOCT}	nominal operating cell temperature
T_{STC}	standard test conditions temperature (25°C)
uvw	initial primitive unit vectors aligned with global coordinate frame
$\vec{u}'$ / $\vec{v}'$ / $\vec{w}'$	unit vectors normal to three defining faces of a rectangular prism, post-rotation
U_0	constant Faiman model heat transfer coefficient [15]
U_1	convective Faiman model heat transfer coefficient [15]
V	voltage or bias applied to the terminals of a device
V_{b}	cell breakdown voltage
V_{bi}	cell built-in voltage

V_c	voltage of cell c
V_{mp}	voltage at maximum power point
V_{oc}	open circuit voltage
$\vec{w_0}$	vector between the origins of a ray and a cylinder line segment
w_M	weighting coefficient of M'th module *IV*
w_S	weighting coefficient of S'th module string *IV*
X, Y, Z	axes of the right-handed global coordinate frame
X',Y',Z'	body-fixed axes rotating with primitive, initially aligned with the global coordinate frame prior to rotation
(x_1, y_1), (x_2, y_2)	sets of points on surfaces S_1 and S_2
Z	sun zenith angle, or Z-axis of right-handed global coordinate frame
$Z_{s,\text{U}}$ / $Z_{s,\text{L}}$	upper and lower zenith angles bounding sky element s

1 Introduction

1.1 Motivation

To power an electrified world with zero-emissions energy by 2050, jurisdictions around the globe will collectively need to install more than 630 GW of solar photovoltaic (PV) capacity *every year* as of 2030. This annual expansion exceeds the PV capacity installed globally in 2020 by 4.7 fold [16]. To enable this expansion, tools like PV *performance models* - which predict the annual or instantaneous energy yield of a PV system - will be crucial. Engineers and PV plant owners will rely on PV performance models to provide accurate energy yield estimates to optimize plant designs and de-risk financial investments. Plant operators will compare actual plant performance against these same models to detect and diagnose issues. Grid system operators will use the output of these models as inputs to short- and long-term forecasts to balance electricity supply and demand. We must therefore ensure that our PV performance models are both accurate and computationally efficient - a task akin to sharpening the tools in our energy transition toolkit and keeping them accessible.

In particular, we will need to ensure access to accurate *bifacial* PV system performance models. Bifacial modules - which collect light on both the front and rear faces - are predicted to make up 60% of annual added PV capacity by 2030, overtaking their one-sided *monofacial* counterparts [17]. (See **Chapter 2** for an introduction to bifacial PV cells, modules, and systems). As the price margin between bifacial and monofacial modules has thinned over the last decade, the industry has rapidly adopted bifacial PV, shedding previous doubt as to whether the energy yield gain due to rear side light could offset additional module costs. With this transition, the purpose of bifacial energy yield models has shifted away from assessing the viability of a novel technology; these models are now essential to reducing risk in PV plant financing and monitoring.

Improving bifacial PV model accuracy will be a key step to further reducing this financial and operational risk across the globe. As PV plant designs evolve to fit increasingly complex parcels of land, this decade's most accurate bifacial PV models will excel at capturing the optical and electrical impacts of complex physical environments under dynamic operating conditions. Validating both optical and electrical models at short and long timescales will reduce uncertainty within an

inherently intermittent energy supply, improving economic appetite for PV capacity expansion and increasing grid resiliency.

1.2 Research gap

To predict bifacial PV energy yield, a model must quantify the light that is incident on the front and rear of the modules within a complex scene: supportive structures block or reflect incident light; ground cover has temporally or spatially-varying reflectivity; and the amount of diffuse, ground-reflected and direct light contributing to module energy yield varies depending on the tilt angle of the PV modules and the time of day and year. Currently, most bifacial PV performance models either: (a) simplify this complexity, relying on annualized, user-defined loss factors to account for physical phenomena, or (b) require significant computational resources to perform a physically-realistic calculation of radiation transfer within the scene.

The first, simplified approach is found in *two-dimensional view factor* (2D VF) models; this approach introduces user error due to a lack of sector-wide agreement on user-defined loss factors [18] and lagging research on geographic and temporal trends in these factors. Conversely, the physically-realistic *ray tracing* approach can capture geographically- and temporally-specific light patterns on the modules including shading and reflection; however, the associated computational intensity is prohibitive for any users looking to optimize a PV system design without access to high performance computing. (See Section 2.2 and Section 3.1 for a more in-depth review of existing bifacial PV modelling approaches).

With improved access to cloud computing, ray tracing models are increasingly used in a post-optimization step to determine user-defined parameters for the 2D VF models that have historically been considered bankable in financing. Despite reduced uncertainty in annual energy predictions, this cumbersome workflow still results in a lower instantaneous agreement between modelled and measured results on a per-timestamp basis. Thus, the existing modelling landscape has suffered from an accessibility-accuracy gap that suggests a need for alternative modelling approaches.

1.3 Thesis objectives and scope

To fill the accessibility-accuracy gap seen in bifacial PV modelling, this thesis aims to:

1. demonstrate and describe an integrated optical and DC-side electrical bifacial PV performance model that achieves greater computational efficiency than ray tracing while quantifying 3D shading;
2. validate these optical and electrical models against measured field data to quantify accuracy;
3. investigate the energy yield impacts of complex system features and dynamic operating conditions in existing and emerging markets using the proposed model.

The following topics in energy yield modelling are beyond the scope of this work: soiling, DC and AC wiring losses, DC-AC conversion, optical modelling for non-flat terrain, non-silicon devices, and meteorological forecasting.

1.4 Research contributions

This thesis introduces a highly-parameterized, physics-based optical and electrical PV performance model that computes two dimensional shade-inclusive front and rear irradiance profiles and cell-to-array level current-voltage curves; this model captures shading and electrical mismatch losses without the need for user-defined factors seen in 2D VF models and with lower computational intensity than ray tracing models. **Chapter 3** of this thesis explains the optical and electrical sub-models and provides a validation comparing modelled and measured irradiance and power data for fixed-tilt and single-axis tracked systems.

The author's notable contributions to model development include: developing the 3D coordinate mapping for a flexible, user-defined PV array for fixed-tilt, single-axis tracking and double-axis tracking systems with backtracking; designing the shading algorithm to account for common supportive racking types, including a novel approach to module frame shading and PV-specific bounding volume hierarchy; and implementing an electrical model with cell-to-array level current-voltage curves. Her contributions to this electrical model include implementing: half-cut or shingled cells in portrait or landscape module orientation; three common temperature models; defined cell behaviour at reverse bias breakdown voltage; user-defined wiring architecture including bypass diodes and series/parallel interconnections from cell-to-array level; and electrical current-mismatch loss calculations within and between modules.

Beyond module development, this thesis subsequently demonstrates how the described model can be applied to a variety of use-cases in existing and emerging markets. For example, 94% of new utility-scale PV in the U.S. in 2022 was installed on single-axis trackers [19] which rotate modules from east to west throughout the day to capture more direct sunlight than fixed-tilt systems. Therefore, **Chapter 4** focuses on quantifying the energy impacts of three concepts relevant to bifacial PV on tracked systems: (1) irradiance non-uniformity across a row of trackers, (2) reflections off of the *torque tube* - an integral component of the supportive racking structure, and (3) the addition of a second axis of rotation in *double-axis tracking*. These studies help prioritize the physical effects that should be considered in bifacial PV energy yield modelling for tracked systems.

Another use-case for PV performance models emerges as we begin to understand the sources of uncertainty that hinder PV investment in emerging markets today. As mid-to-high latitude jurisdictions look to PV to offset carbon-intensive energy sources and to meet increasingly electrified energy demand, accurate PV performance modelling will require an improved understanding of geographically-specific effects such as snow, air mass, and row-to-row shading. **Chapter 5** demonstrates how we can apply a highly-parameterized, spatially-resolved, and geographically-specific model such as the one described in this thesis to quantify the impact of the physical effects that are currently driving PV investment uncertainty in these emerging PV markets.

2 Bifacial photovoltaic (PV) performance modelling

To contextualize the original contributions described in this thesis, this chapter begins with an introduction to bifacial photovoltaic (PV) cells, modules, and systems. Section 2.2 then contrasts existing approaches to bifacial PV optical modelling, complementing the review of existing models provided in the introduction of the manuscript reproduced in Section 3.1. Section 2.3.1 introduces the field data required to validate bifacial PV models for optical, thermal, and electrical accuracy, and the chapter concludes with a brief primer to key software concepts referenced in subsequent discussions on algorithm design.

2.1 Bifacial PV cells, modules, and systems

2.1.1 Cells

In a solar photovoltaic (PV) system, electric current is generated within the PV *cells* that make up the solar panels or *modules*. This thesis focuses primarily on PV systems built from *bifacial* cells. Unlike one-sided or *monofacial* cells, bifacial cells convert the light incident on both sides of the cell into electricity, allowing collection of diffuse and ground-reflected light in ground-mount systems. In 1960, Mori [20] proposed the first bifacial cell with discretized rear electrical contacts, rather than the planar contact that covered the full rear face of conventional monofacial cells; by 1994, Moehlecke et al. demonstrated the first bifacial device with a viable 18% efficiency [21]. While bifacial PV manufacturing and installation were originally plagued with higher costs and additional energy yield modelling uncertainty, the International Technology Roadmap for Photovoltaics (ITRPV) [17] estimates that these cells now make up more than 45% of the global market. The following section provides a high-level summary of the principles governing current generation in bifacial cells including materials, semiconductor junctions, equivalent circuit models, and current-voltage behaviour under varied operating conditions. This summary is based primarily on the detailed descriptions in Wenham [22], Masters [6], and Nelson [23].

Materials According to the ITRPV [17], more than 90% of all cells manufactured globally in 2022 were composed of mono-crystalline silicon (mono-c Si) - a semiconductor material in which

covalent bonds bind Si atoms in a repeating crystal lattice. As a semiconductor, mono-c Si undergoes the *photovoltaic effect* when illuminated. Photons with energy greater or equal to the bandgap of the semiconductor (i.e., with energy greater or equal to the energy difference between the conduction and valence bands) are *absorbed* by the lattice. This energy transfer *excites* electrons from the valence band to the conduction band allowing the excited electron to move freely in the material and leaving behind a positively charged *hole* in the lattice. In the presence of an electric field, these free electrons can be extracted from the material to perform work in a circuit.

To provide a built-in electric field in the device, a Si solar cell requires at least one junction between two regions with different concentrations of free electrons or holes. These regions are created by *doping* pure silicon with intentional impurities or *dopants* - a process which also increases the conductivity of both materials allowing charge collection at the device terminals. In *n-doped* Si, small concentrations of group V atoms like phosphorous are covalently bonded to silicon atoms throughout the crystal lattice (Fig. 2.1, left in blue). This process results in additional free electrons since each phosphorous atom has five valence electrons - one more than can be bond with the four adjacent Si atoms. These electrons are known as the *majority carriers* in n-doped Si, whereas holes are the *minority carriers*.

Conversely, in *p-doped* Si (Fig. 2.1, left in pink), group III atoms like boron are introduced into the silicon lattice. Since each boron atom has only three valence electrons, this process leaves an unpaired Si valence electron for every boron atom. These positively-charged *holes*, where electrons would be in a neutral pure Si lattice, form the majority carriers in p-doped Si where free electrons are the minority carriers. When we conceptualize holes moving through the material, we are really referring to the movement of excited electrons leaving a hole behind and moving in the direction opposite to the conceptual hole movement.

P-N junctions When the n-doped and p-doped materials are brought together together in an n-p or *p-n junction*, the majority carriers near the junction diffuse away from their respective materials, leaving behind minority carriers in a *depletion or state-charge region* around the junction (pale pink and blue in Fig. 2.1). This region of opposing charges generates an electric field with a *built-in voltage*. This field begins to offset the continual *diffusion current* of majority carriers across the junction by sweeping minority carriers near the depletion region across the junction in a

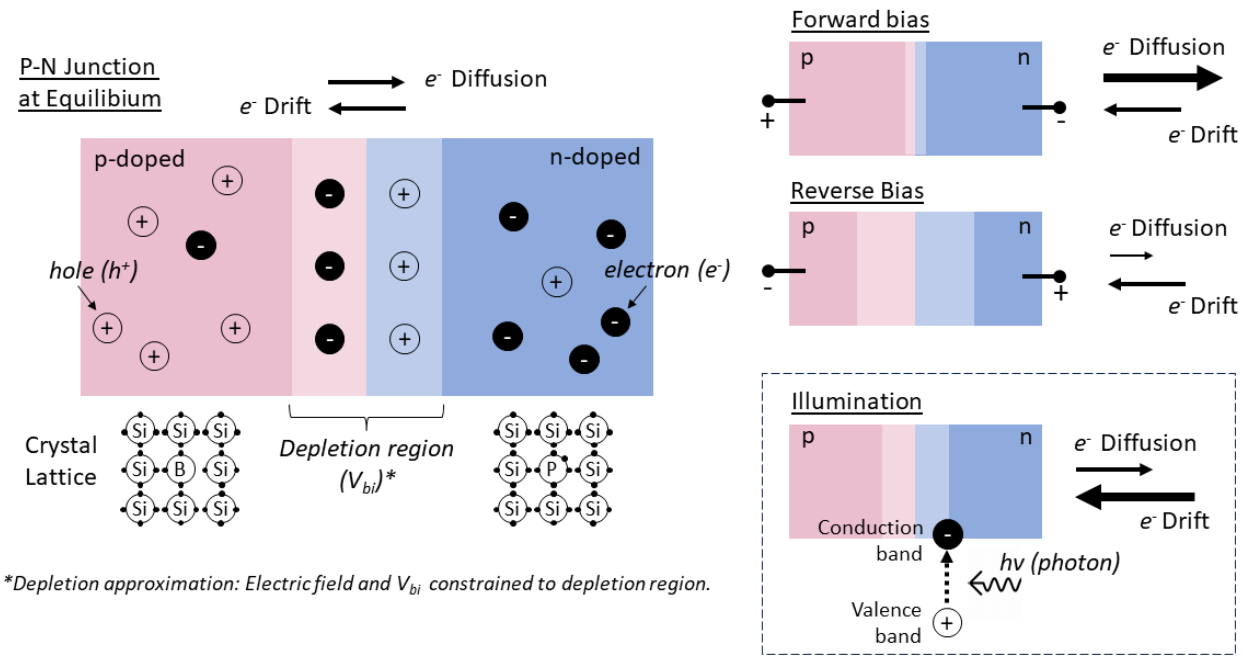


Figure 2.1: Left: p-n junction between p-doped (boron) and n-doped (phosphorous) silicon regions at equilibrium. Right top: p-n junction under forward bias with thin depletion region and dominant electron (e^-) diffusion current. Right middle: p-n junction under reverse bias with widening depletion region and dominant e^- drift current. Right bottom: p-n junction under illumination by photon with energy hv where h is Planks constant and v is frequency and with dominant drift current due to excited minority carriers in and near the depletion region. Figure adapted from [24–26].

drift current. These two opposing currents eventually settle to be equal and opposite in a state of equilibrium. Hu [24] provides a useful description of p-n junction formation and behaviour under bias. Nelson [23] provides a derivation of the diode current equations.

Applying a forward bias to the p-n junction (Fig. 2.1, top right), in the opposite direction to the built-in field, reduces the voltage differential between the p and n regions allowing more majority carriers to overcome the potential barrier to diffusion and increasing diffusion current exponentially. This diffusion current dominates current flow under significant forward bias since the applied voltage has little effect on the the drift current. Drift current is still limited by the near-equilibrium minority carrier concentration close to the junction and the minority carrier concentration is primarily affected by light and temperature - both absent in this dark forward bias scenario.

Applying a moderate reverse bias (Fig. 2.1, middle right), in the same direction as the built-in-voltage, increases both the width of the depletion layer and the built-in voltage. Fewer majority carriers can overcome the potential barrier to diffusion which drastically reduces the diffusion cur-

rent. Drift current, still limited by the concentrations of minority carriers near the depletion region, remains approximately the same as at equilibrium. The small net current under reverse bias conditions is called the *dark saturation current*, I_0, and is dominated by this drift current. I_0 is dependent on temperature and Si quality.

The net current generation under bias, I_d, can be described by the *ideal diode equation* [26,27]:

$$I_\mathrm{d} = I_0(e^{\frac{q(V-V_b)}{kT}} - 1) \tag{1}$$

where V is the applied bias, V_b is the built-in voltage, I_0 is the dark saturation current, known as the saturation current, k is Boltzmann's constant, q is the absolute value of electron charge, and T is the temperature. This equation holds under dark conditions for an ideal diode.

In an ideal diode, it is assumed that electrons and holes do not *recombine* while in the depletion region. Since the location and dominant type of recombination differs from this assumption in real cells, an ideality factor, n, between 1 and 2 is added to the ideal diode equation [26, 27]:

$$I_\mathrm{d} = I_0(e^{\frac{q(V-V_b)}{nkT}} - 1) \tag{2}$$

While the above section describes a p-n junction, junctions with other doping characteristics (e.g., p-p+) exist to control the movement of carriers within a cell. Libal, Kopecek et al. [28] has a detailed description of various bifacial cell designs including the material and order of junctions.

Light-generated current While a solar cell behaves like a diode in the dark, it must be illuminated to generate a significant current. *N-type* monofacial solar cells are illuminated on the p-doped region known as the *emitter* with a thicker n-doped region beneath known as the *bulk*. Conversely, *p-type* monofacial cells are illuminated on the n-doped emitter with a p-doped base. Bifacial cells are illuminated on both sides, with rear light entering through the equivalent of the monofacial base.

When light is applied to the p-n junction (Fig. 2.1, bottom right), the minority electrons that are excited within a *diffusion length* from the depletion region - i.e., are close enough to the depletion region to diffuse to the field without recombining [29, 30] - will be accelerated toward the n-doped region. Analogously, minority holes generated within a diffusion length of the depletion region are

swept to the p-doped region. In the absence of a forward bias, the resulting drift current dominates. The superposition principle allows the net current generated under illumination, temperature, and bias to be a direct combination of this light-generated current, I_L, and the ideal diode equation [27, 31]:

$$I = I_L - I_0(e^{\frac{q(V-Vb)}{nkT}} - 1). \tag{3}$$

Current-voltage curves Under illumination and bias, there are three points on the *current-voltage (IV) curve* described by Eq. (4) and shown in Fig. 2.2.A that are of particular importance to solar cell and module characterization and operation [6, 31]:

- If the terminals of the device are connected directly as a short circuit, no external bias voltage is applied. The net current is primarily due to light- and thermally-generated minority carriers swept across the depletion region by the built-in electric field. This *short circuit current*, I_{sc}, is the maximum current that can be produced by the cell under the given illumination conditions and is proportional to the number of incident photons. For bifacial cells, the ratio of rear-illuminated I_{sc} to front-illuminated I_{sc} is a measure of rear-side collection efficiency called the *bifaciality factor*, ϕ, [28], ranging from 0.7-0.9 depending on cell design [17] with highly symmetrical *silicon heterojunction* cells resulting in the highest ratio.

- Alternatively, if a forward bias is applied that is equal and opposite to the built-in voltage, the net current will be zero. This *open circuit voltage*, V_{oc}, is the maximum operating voltage of the solar cell.

- At a forward bias slightly smaller than the open circuit voltage, the current and voltage are co-maximized. This is the *maximum power point*, P_{mp}, and occurs at the largest applied forward bias in which the light-generated drift current exceeds the opposing diffusion current.

Under extreme reverse bias, a final condition arises known as *breakdown* (Fig. 2.2.A, grey region). Si cells experience *avalanche breakdown* when the strong electric field formed by the widening depletion region eventually accelerates carriers with enough energy to knock additional electrons free of the lattice [24]. This avalanche of free, rapidly accelerated electrons causes an exponential increase in drift current. This phenomenon occurs at reverse bias voltages of $\sim$-10 V

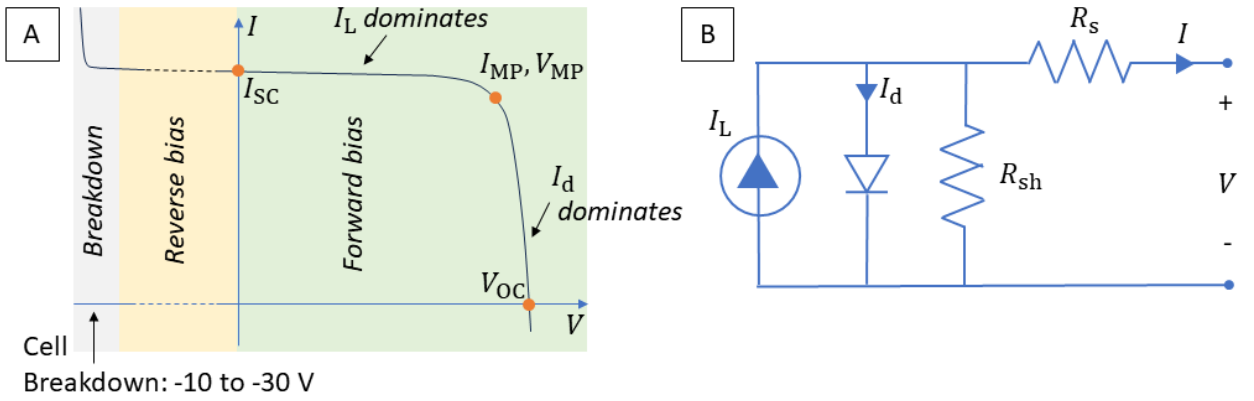


Figure 2.2: (a) Cell current-voltage (IV) curve. (b) Single diode model and parameters [6].

to -30 V [32] in silicon cells, known as the *breakdown voltage*, and necessitates the use of bypass diodes in PV modules (see Section 3.4.1).

Single diode model The single diode model [6, 31] further describes the current-voltage behaviour of a non-ideal solar cell through the equivalent circuit in Fig. 2.2. The light-generated current source, I_{L}, is connected in parallel to a non-ideal diode with dark saturation current, I_0, and ideality factor, n, such that the net current is dominated by light generated current at low forward bias and by diode diffusion current and recombination at high forward bias.

The model also displays two parasitic resistances that reduce output power at the cell terminals. The *shunt resistance*, R_{sh}, is in parallel with the current source and diode and represents alternate current pathways through the cell that bypass the built-in voltage, often caused by micro-cracks or impurities in the lattice. The *series resistance*, R_{s}, represents resistance to diffusion in the semiconductor bulk and resistance in, and at the junction with, front and rear metal contacts. Ideally, the shunt resistance is infinitely high and the series resistance is zero. The resulting net current is [6, 31]:

$$I = I_{\mathrm{L}} - I_0[\exp\left(\frac{q(V + IR_{\mathrm{s}})}{nkT}\right) - 1] - \frac{V + IR_{\mathrm{s}}}{R_{\mathrm{sh}}} \tag{4}$$

A second parallel diode can be added to this model to describe the recombination rate of electron-hole pairs in the depletion region, replacing the single ideality factor [33]. However, in

materials such as Si where the minority carrier diffusion lengths are much longer than the p- or n-doped depletion region widths, recombination in the depletion region is insignificant [34]. Thus, the single diode model best describes Si IV characteristics.

Temperature and irradiance effects Several parameters in the single diode model depend on temperature or irradiance; therefore, a temperature- and irradiance-dependent single-diode model can be used to find IV curves and maximum power points that represent non-standard test conditions. Calculation of cell temperature itself is discussed in Section 2.1.4. Rucschel et al. [35] discuss secondary order temperature and irradiance effects and alternate approaches to those discussed below.

A solar cell's temperature dependence lies primarily within the dark saturation current, I_0, which is proportional to the square of the *intrinsic* (undoped) carrier concentration of silicon, n_i^2, which in turn depends on the cube of cell temperature. Thus increasing cell temperature increases I_0 with the following relationship [36]:

$$\frac{I_0(T_c)}{I_{0,\text{STC}}} = (\frac{T_c}{T_{\text{STC}}})^3 \exp{[\frac{1}{k}(\frac{E_{\text{g,STC}}}{T_{\text{STC}}} - \frac{E_{\text{g}}(T_c)}{T_c})]} \propto \frac{n_i^2(T_c)}{n_{i,\text{STC}}^2} \tag{5}$$

where T_c is the cell temperature, T_{STC} is the STC temperature of 25°C, $n_{i,\text{STC}}$ is the intrinsic carrier concentration of Si at T_{STC}, $E_{\text{g,STC}}$ is the bandgap energy of Si at T_{STC}, and k is the Boltzmann constant. Here, the temperature dependence of the bandgap is described as in De Soto et al. [36] with $E_{g,\text{STC}} \simeq$1.12eV for silicon.

$$\frac{E_{\text{g}}(T_c)}{E_{g,\text{STC}}} = 1 - 2.677 * 10^{-4}(T_c - T_{\text{STC}}) \tag{6}$$

Since the bandgap decreases with increasing temperature, I_{L} (and thus I_{sc}) increases slightly as more minority carriers overcome the bandgap energy to contribute to the drift current. However, V_{oc} decreases significantly with increasing temperature due to its strong dependence on I_0. As a result of V_{oc} decreasing more rapidly with temperature than I_{sc} increases, maximum power (P_{mp}) will decrease as the cell heats up. I_{sc}, V_{oc}, and P_{mp} temperature coefficients are reported on module datasheets as percent losses or gains per °C with approximate values of +0.06%/°C, -0.3%/°C, and -(0.4-0.5)%/°C, respectively [31]. These temperature coefficients can be applied to adjust the I or

V of the single-diode model.

Finally, De Soto et al. [36] outlines that effective modelled shunt resistance should increase with decreasing incident irradiance and current-generation. R_{sh} scales inversely with irradiance, normalized to G_{STC} such that:

$$\frac{R_{\text{sh}}}{R_{\text{sh,STC}}} = \frac{G_{\text{STC}}}{G_{\text{c}}} \tag{7}$$

where G_{c} is the total average irradiance on front and rear of the cell, and $R_{\text{sh,STC}}$ is the shunt resistance and irradiance under STC conditions.

Spectral effects Each solar cell has a unique current generation response to a given radiation spectrum based on its materials, material quality, and design. This response is known as the cell's *external quantum efficiency* (EQE), or the number of electrons collected at the device terminals for each incident photon at each wavelength [31, 37]. Fig. 2.9 in Section 2.2.1 shows a typical EQE for an encapsulated mono-c Si cell overlaid on multiple solar spectra.

The cell's short circuit current can be found as in [37]:

$$I_{\text{sc}} = A_c * \int G_c(\lambda)\Re_c(\lambda)d\lambda \tag{8}$$

$$\Re_c(\lambda) = \frac{q}{hc}\int \lambda EQE_c(\lambda)d\lambda \tag{9}$$

where A_c is the area of the cell in m^2, λ is the wavelength of incident irradiance in nm, $G_c(\lambda)$ is the spectral irradiance incident on the cell in $\mathrm{W/m^2/nm}$, and $\Re_c(\lambda)$ is the cell's spectral responsivity in $\mathrm{A/W}$. This spectral responsivity depends on the elementary electric charge q in C, Plank's constant h in $\mathrm{J \cdot s}$, the speed of light c in $\mathrm{nm/s}$, λ in nm, and the cell EQE, EQE_c. Cells with different EQEs will generate different currents under the same spectrum, and a single cell will generate different currents under different spectra, even if the integrated irradiance of the light is the same.

While an EQE is typically measured based on front-side illumination, the rear-side EQE of an asymmetric bifacial cell will differ from front-side EQE [38]. On average, rear-incident light excites electrons farther from the depletion region than front-incident light, increasing the likelihood of recombination and contributing to reduced rear current generation at most wavelengths. The bifaciality factor, ϕ, captures this effect in a rear-to-front current or power ratio less than 1. Addi-

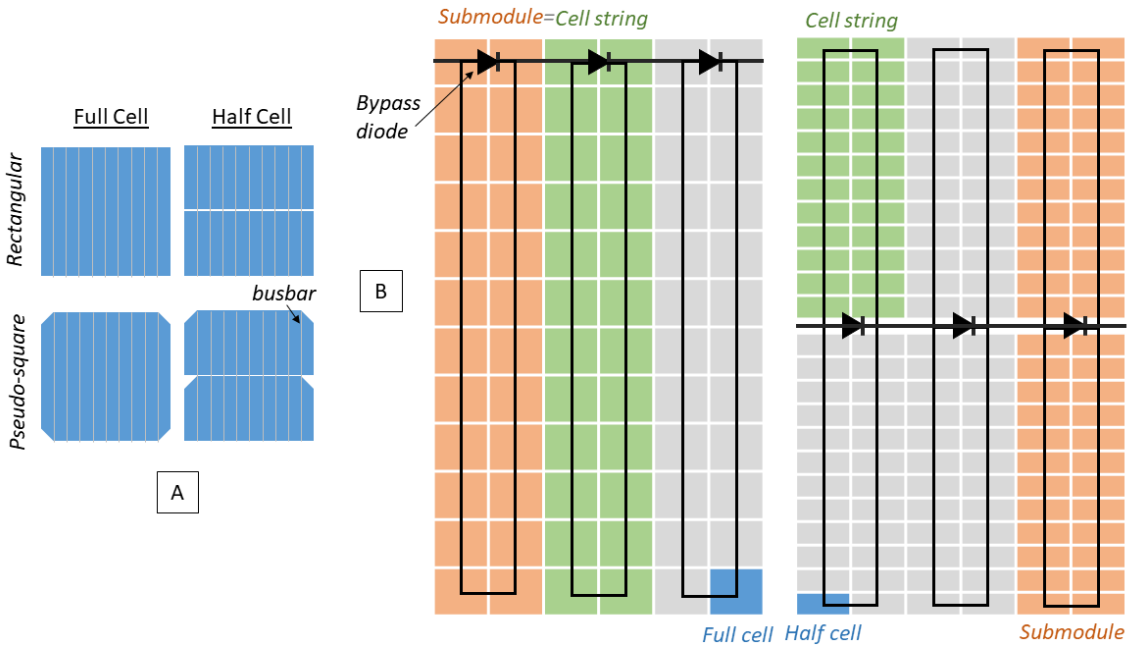


Figure 2.3: (A) Full and half-cut cells with 9 busbars shown in silver for rectangular and pseudo-square wafer shape. (B) Full and half-cut cell modules with cell electrical interconnection and bypass diodes shown in black, submodules hightlighted in orange, cell-strings in green (equivalent to submodule in full cell case), and cells in blue.

tionally, higher rear recombination and lower EQE is expected for high energy, short wavelength photons since they are absorbed closest to the rear surface and farthest from the depletion region.

2.1.2 Modules

Cell interconnection Carriers are extracted from the emitter and bulk of the solar cells via contacts called *fingers* which lead to *busbars* shown in silver in Fig. 2.3.A. These busbars connect the cells in series to form *cell strings*. One cell string, or multiple cell strings in parallel - as in the right of Fig. 2.3.B, form a *submodule*. Generally, submodules are connected in series in groups of three to form the PV *module*. The layers of a bifacial module typically consist of an anti-reflective coating (ARC) followed by glass, encapsulant - often ethyl-vinyl-acetate (EVA), silicon cell, encapsulant, glass or transparent backsheet, and rear ARC. In 90% of modules, these layers are supported by a metal frame around the perimeter of the module [17]. Commercial modules are approximately 1-1.3 m x 2-2.4 m, with recent trends toward larger modules with 182mm or 210mm cells [17].

Recently, modules made of *full cells* with a 1:1 aspect ratio have been superseded by modules with **half-cut** cells, which now make up >85% of modules made with 182 mm wafer sizes [17]

(Fig. 2.3 left and right, respectively.). These half-cut cells are full cells that have been split along the horizontal center resulting a 1:2 aspect ratio, and these modules typically feature 6 columns of 22-26 half-cells as compared to 12x6 full cells, as shown in the right of Fig. 2.3.B. The half-cut light generated current is thus half of the full-cell current, reducing power lost to series resistance [39]. Additionally, the three (11-13)x2 cell strings on the top half of the module are each strung in parallel with the three vertically symmetrical cell strings on the bottom; thus, any shading on one half of the module does not limit current in the other half.

Bypass diodes When a single cell in a cell string is shaded, its photogenerated current is lower than the photogenerated current of the neighbouring, unshaded cells. Thus, the majority carriers in the neighbouring cells cannot pass through the shaded cell; instead, they begin to build up on either side of the cell, generating a field and effectively forward biasing the unshaded cells. Assuming the voltage setpoint of the module does not change, the shaded cell is forced into a reverse bias to absorb the effect of this generated field; under these conditions, current generated in the unshaded cell that exceeds the shaded cell current may pass through parallel pathways in the cell, generating heat. In the single diode model, this power loss is represented by current passing through the shunt resistance under negative bias.

In the absence of any protection mechanism, the reverse bias across a single shaded cell in a primarily unshaded string of 12+ full cells or 22-26+ half-cells could surpass the cell breakdown voltage, resulting in irreparable damage. To protect cells from entering breakdown and generating *hotspots*, each submodule is connected in parallel with a *bypass diode* in reverse polarity [6]. This diode allows current to bypass the submodule when irradiance non-uniformity results in a forward bias across the bypass diode that is greater than its forward voltage. In this case, power from the bypassed submodule is lost, but does not impact the power output of the two other submodules.

Module IV curves Some PV performance models, such as PVsyst [40], apply a responsivity to average plane-of-array irradiance to generate module current for use in a single diode model which determines maximum power. This approach neglects power losses or gains due to irradiance non-uniformity, including bypass diode and half-cut cell power savings, and requires user-defined loss factors to account for these effects.

The module IV curve can instead be constructed from cell IV curves via: (1) the *series summa-*

tion of cell IV curves, (2) the *parallel summation* of IV curves for any parallel strings and bypass diodes within each submodule, and (3) the series summation of each submodule IV curve [6]. The *pvmismatch* package in the *pvlib* python library [41] provides an open-source implementation of such an approach. Here, series summation refers to the sum of device voltages at each current step within a range, and parallel summation refers to the sum of device currents at each voltage step within a range. The maximum power at the inflection point of the resulting *power vs. voltage* curve provides the maximum power point of the module. The *module efficiency* under the modelled conditions is then the ratio of the maximum power to the total power of the radiation incident on the module.

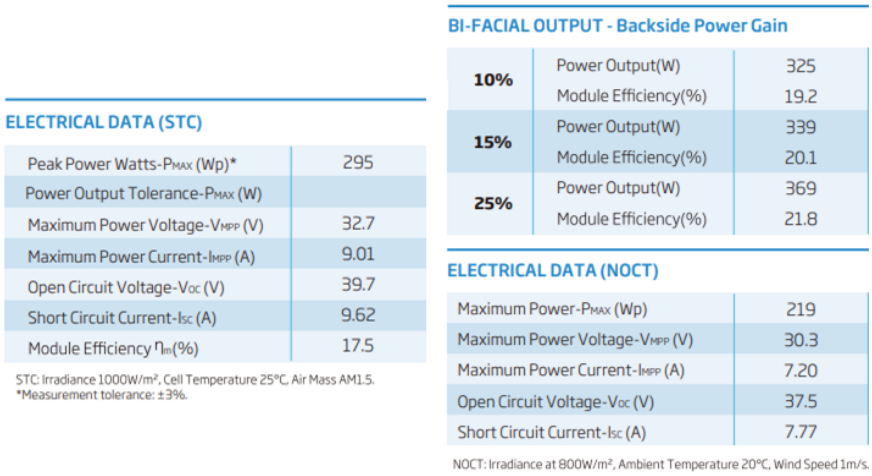
While bypass diodes limit power loss due to harsh partial shading, milder irradiance non-uniformity still causes power loss within the module since lower irradiance cells will operate under mild reverse bias, reducing the voltage of the maximum power point. The net power loss due to irradiance non-uniformity in a module is called the *current* or *electrical mismatch loss*, M, and has been modelled within a module or system for a given timestamp as [42]:

$$M[\%] = 1 - \frac{P_{\mathrm{X}}}{\sum P_c} \tag{10}$$

where P_{X} is power of the array or module and $\sum P_c$ is the sum of the power of all cells. For an annual mismatch loss, we can replace power with energy yield in this formula.

In contrast, locally brighter cells or submodules cause power gains with respect to uniform illumination. The lowest irradiance cells in the module still limit the module current; however, the higher irradiance cells operating at this limited current are at a higher forward bias. Thus, the brighter cells contribute higher voltages to a current-wise summation of IV curves, moving the maximum power point to both higher V_{mp}. Therefore, brightening on the edge of a module or row of modules will increase the maximum power of the module or row. (See Section 3.4.1 and 4.1 for further discussion).

Most often, modules in utility-scale systems will be combined in series to form *module strings*; in this case, a *maximum power point tracker* will continually monitor the string IV characteristics, setting the string voltage to maximize power. Alternatively, each module can be equipped with a power optimizer or micro-inverter in which bias is applied to each module individually to maintain



ELECTRICAL DATA (STC)

Peak Power Watts-P_{MAX} (Wp)*	295
Power Output Tolerance-P_{MAX} (W)	
Maximum Power Voltage-V_{MPP} (V)	32.7
Maximum Power Current-I_{MPP} (A)	9.01
Open Circuit Voltage-V_{OC} (V)	39.7
Short Circuit Current-I_{SC} (A)	9.62
Module Efficiency η_m(%)	17.5

STC: Irradiance 1000W/m², Cell Temperature 25°C, Air Mass AM1.5.
*Measurement tolerance: ±3%.

BI-FACIAL OUTPUT - Backside Power Gain

10%	Power Output(W)	325
	Module Efficiency(%)	19.2
15%	Power Output(W)	339
	Module Efficiency(%)	20.1
25%	Power Output(W)	369
	Module Efficiency(%)	21.8

ELECTRICAL DATA (NOCT)

Maximum Power-P_{MAX} (Wp)	219
Maximum Power Voltage-V_{MPP} (V)	30.3
Maximum Power Current-I_{MPP} (A)	7.20
Open Circuit Voltage-V_{OC} (V)	37.5
Short Circuit Current-I_{SC} (A)	7.77

NOCT: Irradiance at 800W/m², Ambient Temperature 20°C, Wind Speed 1m/s.

Figure 2.4: Electrical specifications provided in the datasheet for Trina Solar Module TSM-DE G5C.20(II) (295W) [45].

maximum power from all modules [43].

Datasheet A module datasheet, published by the manufacturer, provides the module performance metrics under standard test conditions (STC) at 25°C (T_{STC}) and 1000 $\mathrm{W/m^2}$ irradiance (G_{STC}) along with a Nominal Operating Cell temperature (NOCT, see Section 2.1.4). These metrics are shown for the module datasheet in Fig. 2.4. Bifacial module manufacturers must provide these values for an effective front irradiance representing 10% and 20% rear irradiance gains and provide the module's bifaciality factor as the minimum of the rear-to-front I_{sc} and P_{mp} ratios under STC conditions [44].

Based on these datasheet values, the responsivity of the cell in $\mathrm{A/W}$ can be found by the following formula:

$$R = \frac{I_{\text{sc,c}}}{G_{\text{STC}} * A_{\text{c}}} \tag{11}$$

where A_{c} is the area of the cell, $I_{\text{sc,c}}$ is the cell short circuit current equal to that of the module for full-cells or half that of the module for half-cut cells.

The California Energy Commission PV Module List [46] provides single diode model parameters for many modules available on the market. Single diode parameters for a module can also be found from the regression of flashtest or datasheet IV curves; single diode model parameters for the cell can be found by scaling the module IV curve prior to regression [47, 48].

2.1.3 System configuration

Tracking type This thesis focuses primarily on ground-mount systems in which PV modules are installed at a fixed tilt angle on static racking structures or on a dynamic *tracker* at variable tilt angle, β, and/or azimuth angle, φ, which orients the modules to minimize the angle of incidence between the sun beam and the plane-of-array [49].

Fixed-tilt systems are typically equator-facing with a tilt angle, β, optimized for the given location (Fig. 2.5.A). This optimal tilt angle is generally considered to be within 15°of the latitude with shallower angles in cloudier locations [50, 51]. Alternative fixed-tilt systems also exist including vertical bifacial PV with either side of the modules facing directly east and west which shown promise in agrivoltaics (i.e., in co-located agricultural and photovoltaic land use) to allow grazing, alleviate ground shading, and allow machine passage [52].

A *single-axis tracker* (SAT) orients the modules at a variable tilt *or* azimuth throughout the day. A horizontal SAT (HSAT) allows variable tilt, often within a range of ± 60, around an axis of rotation parallel to the ground which most commonly runs north-south (Fig. 2.5.B); this approach rotates modules from east-facing (+60°) to west-facing (-60°) throughout the day, with a horizontal orientation at solar noon. While the axis of a SAT can be slanted at an angle approaching the latitude of the site to limit cosine losses due to low sun elevation in winter months, horizontal SAT systems allow longer rows and require less costly racking, thereby reducing the cost of electricity for any given plant.

A *double-axis tracker* (DAT) alleviates winter angle of incidence losses by pointing modules directly perpendicular to the beam throughout the day. This requires both tilt and azimuthal axes of rotation (Fig. 2.5.C). While concentrating solar has been the primary market for DATs historically, reduction in Si PV prices has renewed interest in methods to quantify bifacial flat panel performance on DATs - particularly in mid-to-high latitude locations with a low average annual solar zenith and a significant summer solar resource at a wide range of azimuth angles.

To determine whether additional energy production can offset additional cost associated with tracking for a given location, *tracking gain* can be computed as the relative increase in annual energy yield between a module on a given tracked system vs. a module on a fixed-tilt system. Once calculated, this economically-agnostic metric can be applied to updated economic estimates at any

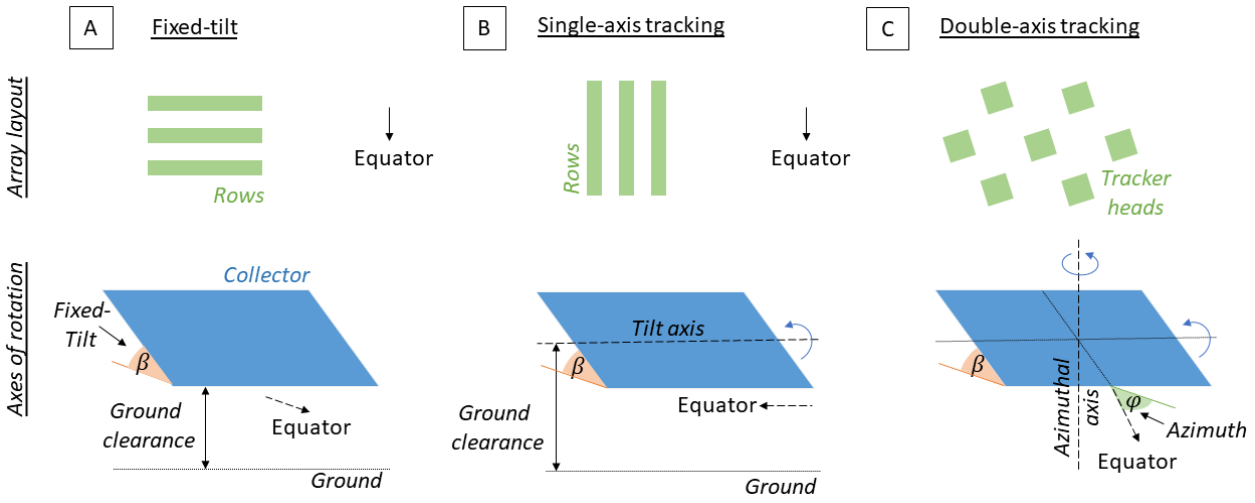


Figure 2.5: (A) Fixed-tilt array layout (top) and collector position with fixed-tilt β and ground clearance to leading edge (bottom). (B) North-south horizontal single-axis tracking array layout (top) and collector axes of rotation with variable tilt (bottom). (C) Double axis tracking array layout with individual tracker heads in checkerboard pattern (top) and collector axes of rotation with variable tilt and azimuth, φ (bottom).

point in the future - with adjustments for any change in meteorological trends at the given location.

Module orientation Each row of a fixed-tilt system or tracker consists of *columns* of modules. A column can be a single module or multiple modules laid out in *tiers* along the *collector width* (i.e., the dimension perpendicular to the row length). These modules may be oriented with the short side parallel to the row length, known as *portrait* orientation, or with the long side parallel to the row length, known as *landscape* orientation. Systems are labelled based on the 'XP/L' convention where X is the number of tiers and P or L refers to the first letter of the orientation (Fig. 2.6.A). For example, a system with 1 tier in portrait would be referred to as 1P and a system with 4 tiers in landscape would be referred to as 4L. With this convention in mind, we can note that two columns of 1P modules have the same aspect ratio in the plane-of-array as one column of 2L modules; the same is true for 2P and 4L.

Gaps in the row Columns of modules are often separated into groups called *tables* with *table gaps* between them as seen in Fig. 2.6.B. In HSAT systems, small table gaps accommodate pilings or slewing drive motors; these motors either rotate the two tables on either side as a single tracker or drive a shaft that rotates tables in multiple rows. Gaps between individually driven trackers are also

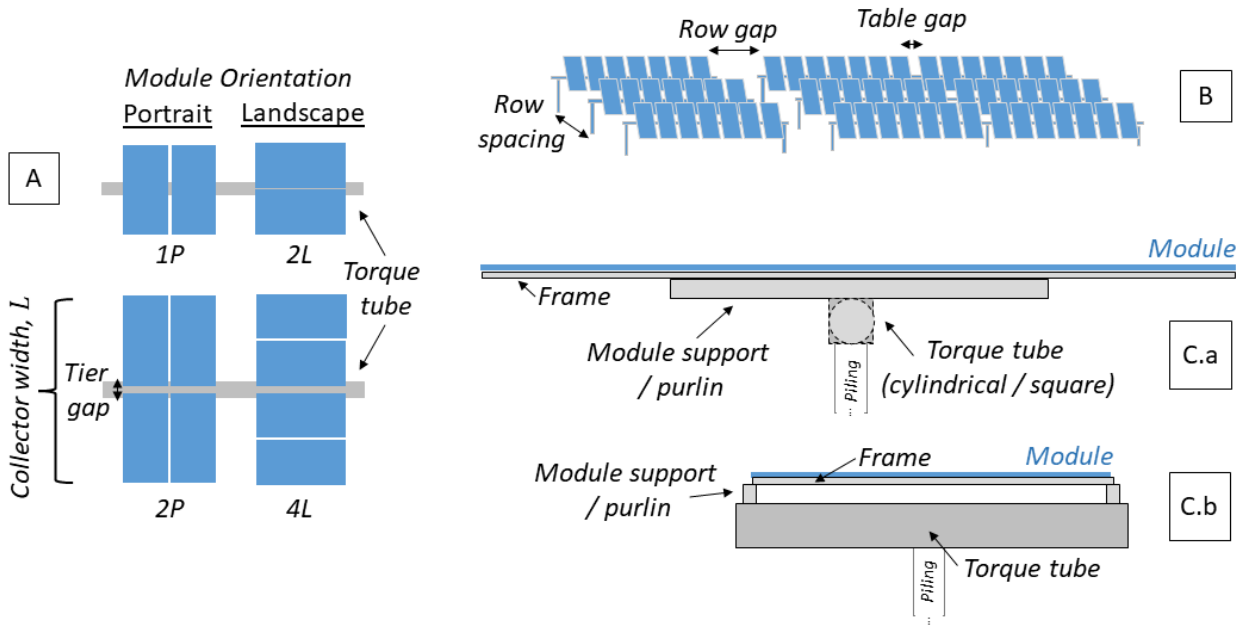


Figure 2.6: (A) Module orientation naming convention - P = portrait, L = landscape. (B) Multi-row array layout with row and table gaps. (C) Common supportive racking structures for single-axis tracking systems with C.a as cross-section of row and C.b as view from end of a single module column.

common. Fixed-tilt systems have longer tables with fewer gaps since they do not require slewing drives. Both fixed-tilt and SAT systems will feature *row gaps* more than one metre wide that allow service roads or personnel to pass between trackers. DAT systems feature several tables, or *tracker heads*, rotating freely from one another in the azimuthal axis.

All modules adjacent to a gap, or at the edge of a tracker head, will experience edge brightening due to additional reflected light from neighboring unshaded ground. Additionally, modules at the edge of a row experience less mutual shading - i.e., direct beam or diffuse occlusion due to adjacent rows - than central modules in the morning or evening. The effect of these gaps or row edges is not modelled in any software that assumes infinitely low rows.

Common supportive racking structures Each row sits on a supportive racking structure that holds the modules above the ground at a certain *ground clearance*. In fixed-tilt systems, this ground clearance is measured at the *leading* or lowest edge of the table (Fig. 2.5.A, bottom). In HSAT systems, the ground clearance is defined as the distance between the ground and either the underside of modules or the axis of rotation (Fig. 2.5.B, bottom). The following sections of this thesis

use the latter definition, specifying an additional *radius of rotation* between the rear of the modules and the axis of rotation as necessary. In early bifacial PV modelling, Asgharzadeh et al. [53] demonstrated a linear relationship between bifacial gain and ground clearance for multi-row fixed-tilt systems on a clear day with 1-3 m ground clearance.

Fig. 2.6.C shows common supportive racking structures seen in fixed-tilt and HSAT systems. In HSAT systems, the racking piece that runs along this axis of rotation, transferring torque from a motor to the modules is called a *torque tube*. These torque tubes have primarily cylindrical or rectangular cross-sections. The modules are attached to the torque tube with plane-of-array racking called *module supports* or *purlins*. These rails are commonly secured to the torque tube and to two adjacent modules. In fixed-tilt systems and DAT systems, modules are instead commonly secured to rails running parallel to the row which are in turn supported by purlins running perpendicular to the row.

All systems require *pilings* or vertical posts which are tethered to, or driven into the ground, at intervals along the row. Some pilings are positioned in table gaps while others are positioned within the length of the tables.

Finally, more than 90% of current modules are internally supported by an aluminum frame [17]; this frame surrounds the perimeter of the module, protruding from the rear of the module by $\sim$30 mm perpendicular to the rear backsheet or glass and wrapping back toward the center of the module by $\sim$30 mm in parallel to the module plane.

Row spacing The spacing between rows, or the row *pitch*, of a PV plant varies depending on the system configuration (i.e., module orientation, number of tiers, tracking type) and is defined as the distance between analagous points on adjacent rows. Another metric to define row spacing is the *ground coverage ratio* (GCR), defined as [54]:

$$\text{GCR} = \frac{L}{d} \tag{12}$$

where L is the collector width and d is the row spacing. As such, higher row spacing results in lower GCR. This metric allows comparison of row spacing regardless of system designs.

Wider row spacing results in higher energy yield for all systems: fixed-tilt systems with wider row-spacing mitigate row-to-row beam and sky dome shading; SAT systems with wider row-

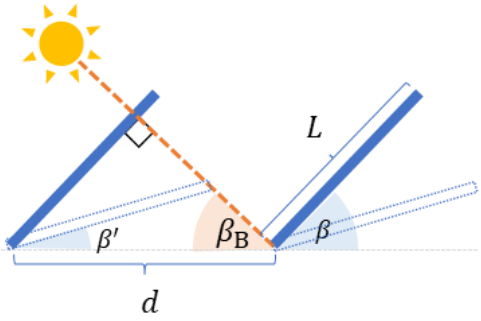


Figure 2.7: Backtracking adjusts single-axis tracking tilt angle, β, to a shallower angle, β', to avoid direct beam shading due to adjacent rows at sun elevation angle β_B. Figure adapted from [55].

spacing will operate *on-sun* for more hour of the year than systems with tighter row spacing, resulting in lower cosine losses. (See Backtracking). In practice, optimizing GCR for limited land area or AC capacity constraints may take precedence over optimizing for DC energy yield.

Backtracking During hours with low sun elevation, SAT systems move trackers to a tilt angle, β', that is shallower than the on-sun angle, β, as shown by the dotted collectors in Fig. 2.7; this *backtracking* angle is the largest possible tilt angle that does not result in row-to-row beam shading for the given sun position. This approach results in a higher angle of incidence between the beam and the plane-of-array than in on-sun operation but avoids the significant power loss resulting from harsh partial shading along the bottom cells in a row of modules. The Lorenzo et al. astronomical backtracking algorithm for flat ground [55] projects the sun beam into the row cross-section and uses the geometry of the sun position, collector width, and row spacing to determine beam shading and corrective backtracking angles for any given time and location. In [56], Anderson and Mikofski provide a backtracking for sloped ground. Several tracker companies have demonstrated "smart tracking" algorithms that adjust tilt angle based on sky-condition, forcing trackers to shallower angles during cloudy skies [57, 58].

For double-axis tracking, Section 4.3.1 describes Fernández-Humanda et al.'s algorithm [8] to determine whether direct beam shading occurs between tracker heads and to provide a corrective tilt angle. Lorenzo et al. [55] proposes a similar approach with azimuthal correction.

2.1.4 System electrical

Temperature effects The summation of temperature-dependent cell IV curves results in a temperature-dependent module IV curve. Thus, when modelling module power, we must calculate the cell temperature; in a ground-mount system, this cell temperature is strongly dependent on incident irradiance.

The empirical nominal operating cell temperature (NOCT) model [59] demonstrates approximately linear cell temperature gains or losses with increasing or decreasing incident irradiance as compared to outdoor ground-mount tests with 1 m/s wind speed and 800 $\mathrm{W/m^2}$ incident irradiance:

$$T_c = T_a + \frac{(T_{\text{NOCT}} - 20)}{800} G_c \tag{13}$$

where T_a is ambient temperature, T_{NOCT} is the nominal operating cell temperature specified by the module manufacturer, and G_c is the total irradiance incident on the cell. However, variable wind speed results in additional heating or cooling, and NOCT has been displaced as best practice by other empirical models such as Sandia [14], Faiman [15], or PVsyst [60] temperature models.

The Sandia cell temperature model features two empirical coefficients a and b and a correction factor for the temperature differential between the exterior of the glass and the cell (ΔT):

$$T_c = G_c \cdot e^{a+bW} + T_a + \frac{G_c}{G_{\text{STC}}} \Delta T \tag{14}$$

where G_c is the total cell irradiance, W is wind speed, T_a is ambient temperature, G_{STC} is 1000 $\mathrm{W/m^2}$. For bifacial modules with glass backing (*glass-glass modules*) the coefficients are a=-3.47 and b=-0.0594 and ΔT=3°C.

The Faiman module temperature model requires two coefficients - a constant heat transfer coefficient, U_0, and a convective heat transfer coefficient, U_1:

$$T_m = T_a + \frac{G_m}{U_0 + U_1 W} \tag{15}$$

where G_m is the average irradiance incident on the module. For glass-transparent backsheet modules the empirical coefficients were found to be U_0=23.5-26.5 $\mathrm{W/(m^2\,K)}$ and U_1=6.25-7.68

$\mathrm{W}/(\mathrm{m}^3\,\mathrm{K})$.

For comparison, a description of the PVsyst cell temperature model is available in [60]; however, this model is not explored in this thesis.

The above empirical models do not capture the effects of varied air currents within the plant. Additionally, a term can be added to these models account for radiative transfer with the sky dome [61]. Finally, transient, physical models are emerging as a preferred alternative to these steady state approaches for modelling sub-hourly calculations [62, 63].

Inter-module strings Once the modules are connected in a module string, the "module" itself becomes a functionaly obsolete concept. Instead, a series string of modules effectively becomes a series string of submodules, each with a parallel bypass diode. Irradiance non-uniformity across submodules causes similar current mismatch loss as described above for inter-module non-uniformity. At a forward bias greater than the cumulative V_{oc} of any unshaded, healthy submodules, low performing submodules will limit string current, reducing maximum power. Conversely, as mentioned in the above conversation on cells, submodules in a string experiencing edge brightening will result in an increased module string V_{oc} and a higher maximum power. This power is not proportional to the irradiance gain due to current mismatch losses; for example, Deline et al. [42] model an average 1% annual insolation gain for a single-axis tracking with a resulting 0.15% current-mismatch loss. See Section 3.4.1 for a demonstration of IV curve response to submodule shading and brightening and Section 4.1 for a study on inter-module edge brightening and current-mismatch loss.

DC-AC conversion In most utility-scale systems, module strings are combined in parallel for direct current (DC) to alternating current (AC) conversion at an *inverter* [43]. DC line losses proportional to the combined current occur at this stage, and the applied bias of the string is controlled by a maximum power point tracker that monitors the IV curves of each string or a parallel combination of strings. When the DC power exceeds the inverter's rated DC power (specified by a finite DC-to-AC capacity ratio), the AC power is reduced, or *curtailed*, to the maximum rated power - a power reduction known as *clipping loss*. Curtailment, in which the maximum power point tracker moves the string applied bias away from V_{mp} to reduce power, also occurs when the plant's generated power exceeds the power injection approved by the grid's system operator for a given time interval. This thesis deals primarily with the prediction of DC power prior to accounting for line

losses and AC conversion.

For a system with micro-inverters that avoid clipping losses and current mismatch loss, the module AC current will instead be combined in parallel and fed to a step-up transformer for transmission; however, this approach is costly and primarily limited to rooftop and small-scale systems.

2.2 Optical models for bifacial PV

The sun's radiation can be approximated as blackbody radiation. Wenham [64], Vignola [65], and Nelson [66] describe this approximation and the journey of this radiation through space and Earth's atmosphere to a PV module. The following section summarizes this physical process and the resulting radiation sources available to a PV module.

2.2.1 Radiation sources

A *blackbody* is an object that is at thermal equilibrium with its surroundings, absorbs all radiation without reflection,and emits energy in a spectrum that is based solely on its temperature. The spectrum of energy emitted by a black body is described by Plank's law which relates the per-wavelength energy of a blackbody to the temperature of the body and the given wavelength. While the sun is not an ideal blackbody, its surface temperature is approximately constant and it reflects a negligible fraction of incident radiation, resulting in a spectrum that closely follows black body radiation at 5778°K [64].

The intensity of the sun's radiation in space is inversely proportional to the square of the observer's distance from the sun. Thus, at 150 million km from the sun, the intensity of the broadband solar radiation incident on the external surface of the atmosphere known as the *extraterrestrial irradiance*, G_0 [$\mathrm{W/m^2}$], fluctuates between 1353-1392 $\mathrm{W/m^2}$ [49] at an average of 1361 $\mathrm{W/m^2}$ [67]. This fluctuation is primarily due to varying distance between Earth and the sun and the cycles in the sun's surface temperature.

Sunlight arrives at the surface of the atmosphere as a beam of *collimated* light with parallel rays. For the purpose of this thesis, a *ray* refers to a vector in the direction of the propagation of broadband light, perpendicular to the wavefront of the electromagnetic waves; we can also conceive of rays as the path of radiation transfer between a source point and an irradiated point.

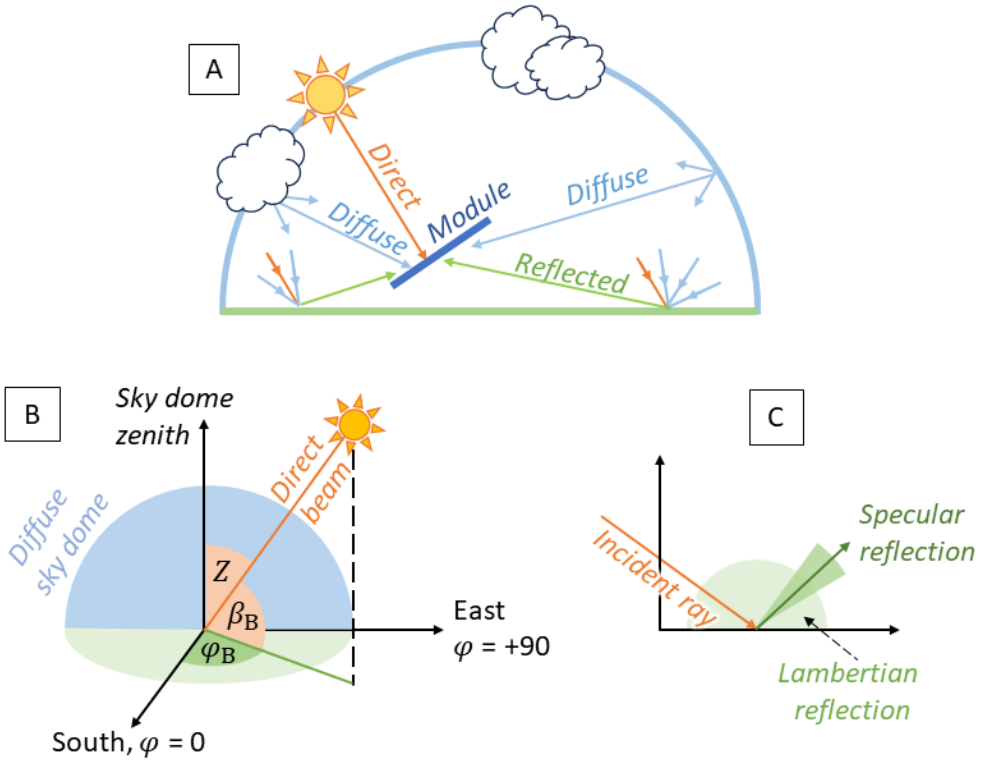


Figure 2.8: (A) Sources of radiation incident on bifacial PV including direct, diffuse and reflected irradiance. Figure adapted from [68]. (B) Sun position described by sun beam elevation β_B or zenith Z and sun beam azimuth φ_B. Figure adapted from [49]. (C) Ground reflection with Lambertian (magenta) and specular (green) components. Figure adapted from [69].

Since the waves that these rays represent will change speed and direction at a material boundary, the collimated sun beam refracts upon entry to the atmosphere. Additionally, ice crystals, aerosols, and water vapour within the atmosphere scatter the sun beam's shorter wavelength light. This process results in a *direct beam* with attenuated intensity in short wavelengths and within key atmospheric absorption bands, and a *diffuse sky dome* composed of primarily short wavelength radiation. The diffuse sky dome is the daylight hemisphere we see when we look up at the sky - the scattered and refracted radiation that reaches the Earth's surface after multiple interactions with atmospheric components. Shorter wavelengths scatter most rapidly and have the highest likelihood of reaching our eyes, which is - as our little Earthlings like to ponder - why the sky is blue. Radiation from the direct beam and diffuse sky dome are two of three sources of irradiance incident on a bifacial PV array shown in Fig. 2.8.A.

Another source of variation in the terrestrial solar spectrum is the *sun position* within the sky

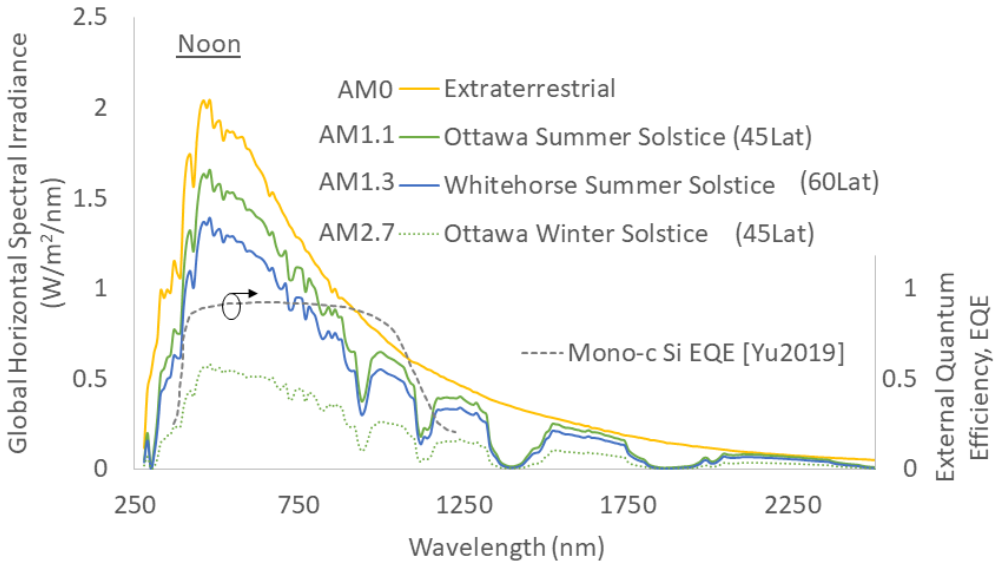


Figure 2.9: Clear sky spectral irradiance incident on a horizontal plane at noon in Ottawa at 45°N at summer solstice in green with air mass (AM) 1.1, Whitehorse at 60°N at summer solstice in blue with AM1.3, and Ottawa at winter solstice in dotted green with AM2.7, all beneath the extraterrestrial AM0 spectrum in yellow [7]. Mono-crystalline (mono-c) silicon (Si) external quantum efficiency (EQE) overlaid in dotted grey (right axis) [71].

dome. As the sun's *elevation angle*, β_B - subtended by vertical distance between the sun center and the horizon - decreases, the direct beam must travel a longer path through the atmosphere. The concept of *air mass* (AM) quantifies the relative length of the sun's optical path through the atmosphere, normalized to AM1 when the sun is directly overhead and increasing as the sun moves toward the horizon [49]. AM1.5G was chosen as the spectrum used for standard test conditions based on the average air masses of the contiguous US states [70]. Each sun position and associated optical path length results in a unique *spectrum* of sunlight with a specific intensity of radiation at each wavelength; since shorter wavelength light experiences more atmospheric scattering, longer optical paths result in red-shifted spectra in morning, evening and winter months. Fig. 2.9 demonstrates some of these varying spectra for different times of year in Ottawa at 45°N (green) and Whitehorse at 60°N (blue) as compared to the extraterrestrial irradiance spectrum (yellow) and overlaid with a mono-c Si cell EQE overlaid in dotted grey.

The total irradiance incident on a flat upward facing surface is known as the *global horizontal irradiance* (GHI, G_H) and is the combination of *direct normal irradiance* from the sun beam (DNI, G_B) adjusted for angle of incidence and the *diffuse horizontal irradiance* from the sky dome (DHI,

G_{D}). Due to Lambert's cosine law [72], the DNI contribution to GHI is modified by a cosine of the beam's angle of incidence (AOI) on the horizontal surface known as the solar *zenith angle*, Z, such that GHI (G_{H}) is:

$$G_{\mathrm{H}} = G_{\mathrm{B}} \cos(Z) + G_{\mathrm{D}} \tag{16}$$

For a given geographic location, meteorological datasets from ground measurements or satellites can provide timeseries for these three measures of irradiance. (See Section 2.3.1 on measurement devices). The ratio of DHI to GHI is the *diffuse ratio* which provides insight on sky conditions at the location; low diffuse ratios indicate clear skies while high diffuse ratios near 1 indicate purely overcast conditions with little to no direct light. The PV plant financing and design processes often require PV performance models to be run on two primary annual timeseries of irradiance, each with 8760 hours of data [73]:

- an irradiance timeseries which results in the plant's most likely energy yield (*p50*) for the given location - a yield against which the plant should overperform in 50% of operating years and underperform in the other 50%; and
- the irradiance timeseries which results in a conservative estimate of the plant's yield that the plant should exceed in 90% of operating years (*p90*).

The *typical meteorological year* (TMY) is a timeseries providing p50 yield that is available based on ground measurement in certain locations and on satellite data across the globe up to 75°N [74–77]. A TMY dataset consists of a concatenated set of 12 data-months selected to be statistically representative of each calendar month across 30 years of monitoring. For example, a location's June TMY data is the hourly data from the year in which June was most statistically representative of all Junes in the 30 year dataset. The applicability of the TMY approach to p50 generation is under review given changing regional and global weather patterns [78]. Access to historical weather datasets is valuable in assessing trends in a location's changing irradiance patterns.

2.2.2 Radiation source models

Extraterrestrial irradiance G_0 can be found based on the U.S. National Renewable Energy Laboratory (NREL) DISC model [79] as:

$$G_0 = \bar{G}_0(1.00011 + 0.034221\cos\eta + 0.001280\sin\eta \\ +0.000719\cos 2\eta + 0.000077\sin 2\eta) \tag{17}$$

$$\eta = 2\pi(n_\mathrm{d} - 1)/365 \tag{18}$$

where $\bar{G}_0$ is the average annual extraterrestrial irradiance of 1366 $\mathrm{W/m^2}$ [64], η is the *day angle* where n_d is the fractional day of the year unique to each timestamp.

Direct beam On a clear sky day, the direct beam intensity can be approximated as an exponential decay of extraterrestrial solar flux based on air mass and atmospheric optical depth [49]. However, such *clear sky models* are not sufficiently representative of true conditions to generate energy yield estimates for PV plant financing. Satellite or ground-measured DNI is the preferred direct beam input to PV performance models, representing the radiation of the sun and a *circumsolar region* of $\pm 2.5°$around the sun [80], as dictated by the acceptance angle of the pyrheliometer. (See Section 2.3.1 on measurement devices). If either DHI *or* DNI are missing on site, the missing timeseries can be calculated with minimal added uncertainty based on sun position in Eq. 16.

If DNI *and* DHI measurements are unavailable at a given location, *decomposition models* can be used to estimate these timeseries from ground or satellite GHI measurements [81]. Using the output of decomposition models as input irradiance timeseries in PV performance modelling introduces uncertainty into the final performance estimates; thus, higher mean absolute error between measured and modelled plane-of-array irradiance and energy yield results should be expected with this approach.

The sun position can be calculated based on the NREL Solar Position Algorithm [82] which accounts for variation in sun position across centuries, or with a simplified approach [49] where the

sun zenith, Z, is:

$$Z = \angle_{\text{lat}} - \delta_{\text{S}} \tag{19}$$

$$\delta_{\text{S}} = 23.45 \sin \frac{360}{365}(n_{\text{d}} - 1) \tag{20}$$

where $\angle_{\text{lat}}$ is the latitude, δ_{S} is the approximate *solar declination*. Fig. 2.8.B shows Z and sun azimuth, φ_{B}, calculated as:

$$\varphi_{\text{B}} = \arcsin \frac{\cos \delta_{\text{S}} \sin H}{\cos \beta_{\text{B}}} \tag{21}$$

$$\text{where } |\varphi_{\text{B}}| \leq 90^\circ \text{ if } \cos H \geq \frac{\tan \delta_{\text{S}}}{\tan \angle_{\text{lat}}}$$

$$\text{and } |\varphi_{\text{B}}| > 90^\circ \text{ if } \cos H < \frac{\tan \delta_{\text{S}}}{\tan \angle_{\text{lat}}}$$

where β_{B} is the sun beam elevation angle and H is the *hour angle* of the timestamp derived from the fractional hour of the day h in solar time.

$$\beta_{\text{B}} = 90 - Z \tag{22}$$

$$H = \frac{15}{\text{hour}}(12 - h) \tag{23}$$

See Masters [49] for conversion between solar and clock time such that the sun crosses location's equator-facing direction or *meridian* at solar noon. Note, the azimuth is here defined as 0° when equator facing and $\pm 180^\circ$ in the direction of the poles.

Diffuse sky Most PV performance models use the 1990 or 1993 anisotropic Perez sky model [13, 83] to calculate radiance distribution across the diffuse sky dome due to their superior tested performance [84–86]. These models provide the radiance at any point in the diffuse sky dome depending on elevation angle, β_s, and position with respect to the sun. Perez 1990 separates a bright circumsolar disc and horizon region from an isotropic sky dome, whereas 1993 provides a fully anisotropic radiance distribution.

The Perez 1993 algorithm [13] calculates sky clearness as:

$$\epsilon = \frac{(G_{\mathrm{D}} + G_{\mathrm{B}})/G_{\mathrm{D}} + 1.041Z^3}{1 + 1.041Z^3} \tag{24}$$

where G_{D} is the DHI and G_{B} is the DNI. Note: the sun zenith angle, Z, must be in radians here.

The brightness is calculated as:

$$\Delta = mG_{\mathrm{B}}/G_0 \tag{25}$$

where m is the air mass and G_0 is the extraterrestrial irradiance. (See Section 5.1 for discussion on air mass calculation).

The calculated sky clearness will fall within one of eight sky clearness bins. Each of these bins is associated with expressions for a set of coefficients $a - e$ that are based on Z, ϵ, and Δ and the empirical coefficients a_{1-4} through e_{1-4} provided in [13]. The resulting radiance at the point directly upward in the sky, or the *sky dome zenith* is G_{Z}:

$$G_{\mathrm{Z}} = G_{\mathrm{D}}(a + b\cos Z + c\exp(-3Z) + d\Delta) \tag{26}$$

and the radiance of any given point s on the sky dome is G_s:

$$G_s(Z, \gamma) = G_{\mathrm{Z}}\frac{f(Z, \gamma)}{f(0, Z)} \tag{27}$$

where γ is the angle between the sun and sky sample point s, and

$$f(Z, \gamma) = (1 + a\exp(b/cosZ))(1 + c\exp(d\gamma) + e\cos^2\gamma) \tag{28}$$

where $f(0, Z)$ is $f(Z, \gamma)$ at the sky dome zenith.

The resulting diffuse radiance at each sky sample point is normalized such that the total sky dome radiation incident on a flat horizontal surface is equal to the DHI entered as input to the model. The empirical coefficients for this model are based on measured irradiance data from 16,000 15-minute sky scans in Berkely, California; the Perez model has yet to be thoroughly validated against sky imaging for high latitudes.

Ground reflection Since ground-reflected irradiance comprises a significant portion of the irradiance incident on the rear of a bifacial PV module, an adequate ground reflectivity model is required for accurate energy yield estimations. In optics, the bi-directional reflectance distribution function model (BDRF) [87] describes reflections off of partially mirror-like - or *specular* - and partially diffuse surfaces that reflect in multiple directions. The BDRF predicts the intensity of a ray reflected in any given direction based on its direction with respect to the incident light, size of surface structures (roughness), and the spectrum of the incident radiation. The hemisphere of reflected rays thus consists of a specular grouping centered along a primary direction of reflection and a distribution of diffuse reflections in other directions. Fig. 2.8.C shows the ground reflection broken into a specular (green) and isotropic diffuse (magenta) component.

While ground reflections off ground materials such as dirt, grass, and gravel have a small specular component, most non-ray tracing bifacial PV models assume that the ground reflection is purely Lambertian, i.e., an isotropic reflection of equal intensity in all directions. Ernst et al. [88] have shown that varying the specularity of a 75% reflective flat rooftop surface from 15-50% increases the energy yield of 45°-tilt modules above the surface by 2.5%. The energy yield of modules above other ground surfaces with lower reflectivity, such as dirt and grass, will thus display <2.5% sensitivity to any smaller neglected specular component since the contribution of ground reflection to energy yield is less significant overall. The Gueymard model [89] with separate forward and backward reflection coefficients could be used as an alternative to assumed Lambertian reflection for applications with highly specular ground reflectivity such as floating PV, provided that any potential implementation has access to information on the direction of reflected radiation with respect to the incident beam.

Many PV models neglect spectral reflectivity of the ground when calculating reflected radiation, instead applying a broadband ground reflectivity known as the broadband *albedo* to all incident light. Broadband albedo, ρ is the ratio of upwelling vs. downwelling radiation at a given location where ρ=0 represents complete absorption and ρ=1 represents complete reflection [69]. (See Section 2.3.1 for further definition and measurement description).

2.2.3 Transposition and shading models

To predict the energy yield of a bifacial PV module, we must estimate the irradiance incident on the front and rear of the tilted module - also known as the front and rear *plane-of-array* (POA) irradiance. *Transposition models* estimate this POA irradiance by calculating the radiation transfer between the radiation sources discussed above and the front and rear module surfaces. Since adjacent rows and supportive racking structures in a real-life PV system will block radiation transfer to the module, bifacial PV performance models must combine transposition models with user-defined shading estimates or physics-based shading calculations. The resulting optical models can be categorized into three groups: two-dimensional (2D) view factor (VF) models; 3D non-ray tracing models including 3D VF, finite element, and hemicube models; and 3D ray tracing models. Table 1 summarizes some of the key differences between these modelling approaches which are explained in greater detail in the following paragraphs.

	2D VF	3D VF	Ray tracing
Supportive structure shading	User-defined parameter	Non-overlapping objects	Full calculation
Irradiance sampling	1D central sample line	2D profile	1D sample line or 2D profile
Approx. annual computation time* (non-HPC)	10 s - 5 min [86]	Scales with mesh density	12+h [86], scales with number of surfaces

*Dell 7400 laptop, Intel i7-8665U processor, 16 GB RAM [86].

Table 1: Comparison of transposition model types. (HPC = high performance computing; VF = view factor, 1/2D = 1/2-dimensional).

2D view factor A *view factor* (VF) is a unitless ratio that quantifies the radiation exchanged between two surfaces [90], assuming diffuse Lambertian emission or reflection from the source surface. For instance, view factor $F_{1,2}$ represents the fraction of energy emitted from surface S_1 that is incident on surface S_2. This value is always ≤ 1 and can be found as [90]:

$$F_{1,2} = \frac{1}{A_1 \pi} \int_{A_1} \int_{A_2} \frac{\cos\theta_1 \cos\theta_2}{R_{1,2}^2} \, dA_1 \, dA_2 \tag{29}$$

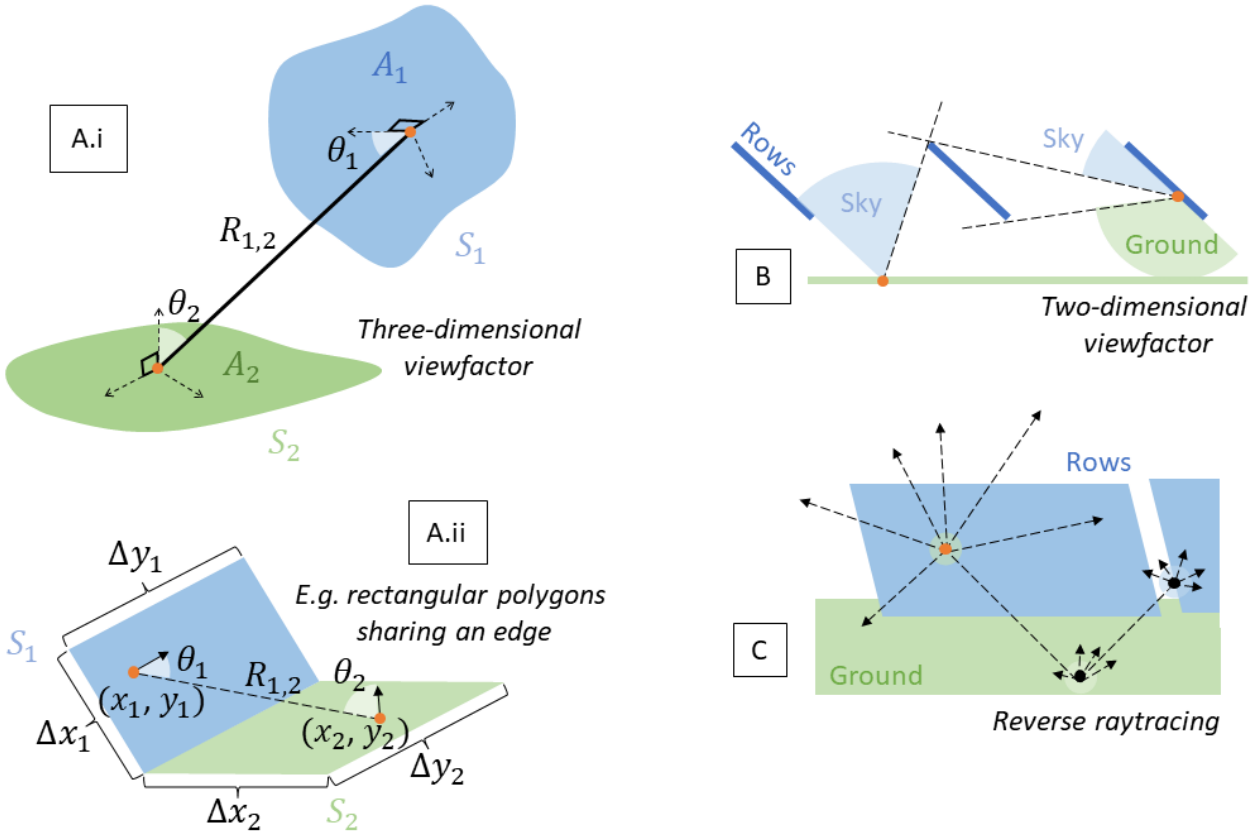


Figure 2.10: (A.i) Three dimensional view factor (3D VF). Figure adapted from Yusufoglu et al. [91]. (A.ii) Example of 3D VF in described in Eq. 30. Figure adapted from Muneer et al. [92]. (B) 2-dimensional VF collapses scenario in A.ii into a cross-section. Figure adapted from Hansen et al. [93]. (C) Reverse ray tracing probes the path of rays exiting the module sample point for intersection with surfaces, spawning additional rays at any intersection. Figure adapted from Retzlaff et al. [94].

where A_1 and A_2 are the total areas of the surfaces S_1 and S_2, and dA_1 and dA_2 are the variables of integration denoting integration across all continuous points on S_1 and S_2. $R_{1,2}$ is the length of a line segment between a set of points (x_1, y_1) and (x_2, y_2) on the two surfaces, and θ_1 and θ_2 are the angles of incidence between the line segment with length $R_{1,2}$ and the normals of S_1 and S_2 for each set of points.

To illustrate, we can take S_1 and S_2 to be rectangles with a parallel edge as in Fig. 2.10.A.ii. In this case, θ_1, θ_2, and $R_{1,2}$ in the integrand of Eq. (29) depend on the position of each set of points (x_1, y_1) and (x_2, y_2) within the coordinate frame of the planes over which the integration occurs. Thus, Eq. (29) for this scenario can be written as Eq. (30) where $\Delta x_{(1,2)}$ and $\Delta y_{(1,2)}$ are the side lengths of S_1 and S_2 [92].

$$F_{1,2} = \frac{1}{A_1 \pi} \int_0^{\Delta x_1} \int_0^{\Delta y_1} \int_0^{\Delta x_2} \int_0^{\Delta y_2} \frac{\cos\theta_1(x_1, y_1, x_2, y_2) \cos\theta_2(x_1, y_1, x_2, y_2)}{R_{1,2}(x_1, y_1, x_2, y_2)^2} \, dx_1 \, dy_1 \, dx_2 \, dy_2 \tag{30}$$

This radiation exchange scenario, and many others can be collapsed into 2D, simplifying the view factor integrals to expressions that depend exclusively on the surface dimensions and their position with respect to one another. John R. Howell has cataloged many such *2D view factors* [95]. PV performance models built on 2D VF optical models, such as PVsyst [40], SISIFO [96], pvfactors [97, 98], bifacial_VF [99] (and software using bifacial_VF source code such as SAM [100]), make use of 2D VFs by collapsing the 3D rows into a 2D cross-section assuming an infinite row length as in Fig. 2.10.B. This approach is sometimes referred to as an *infinite shed model* and results in a single line of irradiance samples along the collector width.

The infinite shed approach accounts for shading due to adjacent rows by calculating the portion of the sky within the module's field of view; however, it does not directly calculate lateral irradiance non-uniformity or supportive structure shading. Instead, these models require: (a) user-defined shading factors to attenuate plane-of-array irradiance calculated by the transposition models, and (b) user-defined current-mismatch loss factors to reduce the power due to irradiance non-uniformity introduced by edge effects and racking. There is little agreement on suitable values or geographic trends for these loss factors, and they are applied as an annual loss, limiting per-timestamp accuracy [42, 101–104]. Additionally, computing these factors for a given location requires a model with 3D shading capabilities, introducing unnecessary redundancy into the modelling process.

3D view factor In order to calculate shading while preserving the full effects of a 3D geometry, we must solve the 3D VF integrals in Eq. (29). However, as described by Modest and Mazumder [90], $F_{1,2}$ between two differential elements of arbitrary orientation in 3D space does not have an analytical solution. Instead, numerical approaches such as view factor algebra, finite element methods, or ray tracing are required to solve these view factors and to generate 2D irradiance maps across the full module face.

View factor algebra - explained at length in [90] - uses rules of energy conservation to compute unknown radiation transfer within an enclosed environment based on known view factors in the

scene. Yusufoglu et al. [91] and Araya Rojas [105] have demonstrated row-to-row shading and lateral irradiance non-uniformity across a row of modules using this approach. However, the 3D VF approach assumes that the VF of unshaded sky or ground seen from a module sample point is equal to 1 minus the sum of view factors from the module to all shading elements - known as the *summation* principle [90]. This assumption is only accurate if the shading elements do not overlap; hence, this 3D VF calculations does not allow for simultaneous simulation of supportive racking structures and multiple adjacent rows.

Finite element method One approach to the numerical solution of the view factor equation in Eq. (29) consists of splitting the emitting and receiving surfaces, S_1 and S_2, into a mesh of finite area patches or *elements* whose discrete central points acts as a proxy for all points within the element area. This *finite element method* is used within 3D VF models PV performance models to calculate radiation transfer between the shaded ground and the module. This thesis combines a finite element method with ray-object intersection to calculate direct, diffuse and reflected irradiance incident the plane-of-array.

Once emitting and receiving surfaces S_1 and S_2 are divided into a mesh, $F_{1,2}$ can then be approximated by the summation of partial view factors, or *coupling coefficients*, $C_{i,j}$:

$$F_{1,2} \approx \sum_{i=0}^{N_1} \sum_{j=0}^{N_2} C_{i,j} \tag{31}$$

where $C_{i,j}$ represents the radiation transfer between a set of coupled elements, (i, j), and N_1 and N_2 are the total number of mesh elements on S_1 and S_2, respectively. As the mesh density increases, the numerical solution of the view factor approaches the solution to the integral solution (i.e., the limit of Eq. (31) as N_1 and N_2 tend to infinity).

As shown in Fig. 2.11, the central points of element i and j now represent all points across the element, which forces the assumption that θ_i, θ_j, and $R_{i,j}$ are constant across the element area. This assumption holds as long as the area of the elements, A_i, A_j, are small with respect to the length of line segment connecting their centers, $R_{i,j}$. Since θ_i, θ_j, and $R_{i,j}$ are independent of the position on the element, these terms can be taken out of the integral of the view factor equation

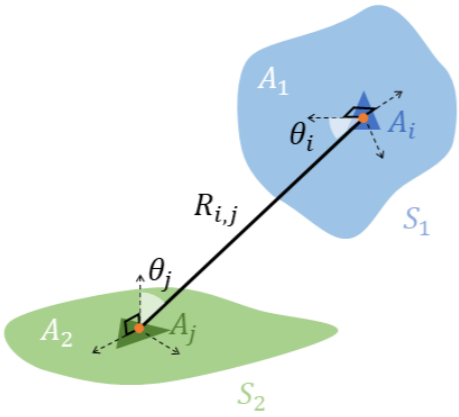


Figure 2.11: Finite element approach to solving view factor between two arbitrary surfaces S_1 and S_2 as the summation of coupling between i'th and j'th elements of finite area A_i, Aj.

(29). The product of the areas of all coupled elements, $A_i A_j$, now represents the integration across all points in the set of elements, regardless of the element shape. The coupling coefficient of each set of coupled elements is then:

$$C_{i,j} = \frac{1}{A_i} \frac{\cos\theta_i \cos\theta_j}{\pi R_{i,j}^2} \int_{A_i} \int_{A_j} dA_i \, dA_j \tag{32}$$

$$= \frac{1}{A_i} \frac{\cos\theta_i \cos\theta_j}{\pi R_{i,j}^2} A_i A_j \tag{33}$$

$$= A_j \frac{\cos\theta_i \cos\theta_j}{\pi R_{i,j}^2} \tag{34}$$

The angles of emission θ_i and the angle of incidence θ_j are calculated based on the normal vector of the emitting or receiving element, $n_{(\vec{i/j})}$, and the ray vector describing the line segment direction, $\vec{d_{i,j}}$, through the following relation exemplified for irradiated element j:

$$\theta_j = \arccos\left(\frac{\vec{n_j} \cdot \vec{d_{i,j}}}{|\vec{n_j}| \left|\vec{d_{i,j}}\right|}\right) \tag{35}$$

It follows that the irradiance incident on S_2 emitted by S_1 is:

$$G_2 = \frac{P_2}{A_2} = \frac{P_1}{A_2} F_{1,2} \approx \frac{1}{A_2} \sum_{i=0}^{N_1} \sum_{j=0}^{N_2} G_i A_i C_{i,j} \tag{36}$$

$$\approx \frac{1}{A_2} \sum_{i=0}^{N_1} \sum_{j=0}^{N_2} G_i A_i A_j \frac{\cos\theta_i \cos\theta_j}{\pi R_{i,j}^2} \tag{37}$$

$$\approx \frac{A_2}{\pi A_2} \sum_{i=0}^{N_1} \sum_{j=0}^{N_2} G_i \frac{A_i}{R_{i,j}^2} \cos\theta_i \cos\theta_j \tag{38}$$

$$\approx \frac{1}{\pi} \sum_{i=0}^{N_1} \sum_{j=0}^{N_2} G_i \Omega_{i,j} \cos\theta_i \cos\theta_j \tag{39}$$

$$G_2 \approx \frac{1}{\pi} \sum_{i=0}^{N_1} \sum_{j=0}^{N_2} G_i \Omega_{i,j_{\text{proj}}} \cos\theta_j \tag{40}$$

Here, P_2 is the power incident on S_2, which is a fraction of P_1 - the power emitted from S_1. As we have seen in Section 2.2.3, this fraction is represented by the view factor, $F_{1,2}$. The radiance emitted from each element of surface S_1 with area A_i is G_i. To further simplify the equation, we can group some terms into $\Omega_{i,j}$ and $\Omega_{i,j_{\text{proj}}}$ – the solid angle and projected solid angle, respectively, between elements i and j.

The finite element method approximates the view factor between two surfaces most accurately when the surface mesh densities of the coupled surfaces trend toward infinite (i.e., the line segment length becomes infinite with respect to mesh element area). Thus, the summation of coupling coefficients for a finite density of mesh in Eq. (31) will not be exactly equal to the theoretical solution of the view factor integral in Eq. (29). Chu Tu Li [1] demonstrates a *compensation factor* to account for the discrepancy between the summation of finite element coupling coefficients representing radiation transfer between a surface and a point and the theoretical view factor from that surface. This compensation factor is denoted by $\chi_{S_1,j}$,

$$\chi_{S_1,j} = \frac{F_{S_1,j}}{\sum_{i=1}^{N_{S_1}} C_{i,j}} \tag{41}$$

where: i is the i'th of N_{S_1} elements on the emitting surface S_1; j is the j'th mesh element on the irradiated surface S_2; $C_{i,j}$ is the coupling coefficient between elements i and j; and $F_{S_1,j}$ is the the-

oretical view factor between surface S_1 and point j on surface S_2. This compensation factor should be calculated for each element on the irradiated surface. As Masters describes in [6], theoretical 3D view factors between a tilted plane (representing a row of PV modules) and a hemisphere or horizontal plane (representing the sky and ground, respectively) collapse to 2D view factors with analytical solutions that substitute in for $F_{S_1,j}$.

The finite element approach does not inherently account for shade cast by objects in the path of radiation transfer; however, the approach can be combined with shading calculations that make use of spatial relationships between coupled elements and scene objects, as demonstrated in this thesis.

Hemicube Another unique non-ray tracing approach to 3D radiation transfer is the *hemicube model* in DNV's SolarFarmer [106]. In this approach - also borrowed from computer graphics rendering, a half-cube is projected from the surface of each module and ground sample point; the scene objects are then projected onto each hemicube face forming shaded and unshaded regions. These face-projections are then mapped back to the module's field of view for sky, ground, and direct beam shading. Neubert et al. [106] states that this model can account for shading objects, but the results shown in that text do not appear to include rack shading. Overall, this modelling approach aims to solve a similar question as this thesis: how to provide accurate shading with lower computational intensity than ray tracing.

Ray tracing To compute radiation transfer between radiation sources and surfaces in a 3D scene, *ray tracing* models - specifically *reverse ray tracing* models, described by Glassner in [107] - project a large number of rays away from each module sample point into the surrounding simulation environment in a stochastic distribution across the module's field of view. The simulation then follows these rays throughout the scene; at each intersection with a surface, additional rays are *spawned* into the scene with directions and intensities based on the reflectance, absorption, and transmittance of the surface and sub-surface properties of the material. Rays that meet a radiation source prior to a certain ray-spawning limit contribute to the irradiance incident on the module with an intensity calculated based on the radiation intensity of the source in the given direction and the attenuation along the full source-to-module ray path. Ray tracing models can be coupled with cell-level electrical models such as pvmismatch [41] to provide energy yield estimates that include shading and current-mismatch losses.

NREL's *bifacial_radiance* is an open-source Python wrapper for the RADIANCE ray tracing model - originally created to simulate indoor spaces based on artifical and natural light sources [108]. In this model, direct beam simulations are deterministic and all other radiation sources and reflections use the reverse ray tracing approach described above. Silvana Ayala Pelaez [109] and Amir Asgharzadeh Shishavan [110] demonstrated bifacial_radiance's capacity to form photorealistic 1D front and rear module irradiance sample lines.

To generate 2D irradiance profiles in a reasonable timeframe, ray tracing generally requires access to high performance computing resources that allows for parallel computation. PV Lighthouse's Sunsolve-Yield [111] provides a ray tracing model for PV performance prediction and analysis through cloud computing. Alternatively, MoBiDiG [112, 113] uses ray tracing only on the rear to reduce computational intensity.

2.2.4 Points of comparison

Incidence angle modification When light is incident on a PV module, less irradiance reaches the cell surface than reaches the module surface due to *Fresnel reflection* at the material boundaries within the module [114]. Each of the above modelling approaches accounts for this power loss differently; as shown in Riedel-Lyngskaer et al. [86], 2D VF models primarily employ the Sandia [14] or ASHRAE [115] incidence angle modifier (IAM) models or a simple Fresnel calculation at an air-glass interface for direct beam radiation. bifacial_radiance does not provide information on the angles of incidence of each incident ray; therefore, the default settings include irradiance samples on the external surface of the module. Ref. [116] shows a tutorial to modify bifacial_radiance simulations such that a glass surface is modelled above irradiance samples positioned at the cell level. Sunsolve samples irradiance below layers of glass and EVA at the cell surface [117].

Computational efficiency To date, Riedel-Lyngskaer et al. [86] provide the best available summary of computation time for a variety of models on the same computing architecture. The paper shows that 2D VF models are the most computationally efficient, calculating annual simulations with hourly timestamps in 10 seconds to 5 minutes. Comparatively, the ray tracing version of MoBiDiG took 12+h to run in the absence of high performance computing.

Typically, the computation time for radiation transfer calculations in 3D VF and finite element

models scales with surface mesh density [105]. Ray tracing computation time scales with number of rays and number of surfaces [108]. To reduce ray tracing computation without high performance computing, some implementations bin timestamps by tracker angles to reduce optical calculations [118]; the cumulative sky approach [119] sums the sky radiance for all timestamps in the same tracker angle bin to allow for a single optical calculation per bin. However, this cumulative sky approach loses temporal specificity since the results represent the entire period over which the sky radiance is summed, restricting the performance information available for analysis.

Modelling error Bifacial PV modelling comparisons aim to reduce investment risk by validating multiple PV models against the same measured data and by benchmarking the performance of models with respect to one another. In 2020, Riedel-Lyngskaer et al. [86] performed a modelling comparison of eight models against a year of measured data, demonstrating annual modelled-to-measured error of less than 3.5% for all models; however, for four of the eight models, monthly errors in some months exceeded 5% . The 2021 International Energy Agency Bifacial Modelling Comparison [2] provides a description and cross-comparison of twelve models, including the model described in this thesis, in two mandatory hypothetical scenarios (see Section 3.5.1) and two optional scenarios with associated measured field data. In the optional west-facing fixed-tilt scenario with one week of measured data, rear irradiance modelled in seven submissions showed a mean bias error (MBE) of -13% with a 15.2% standard deviation between models, and energy yield modelled in three submissions showed an MBE of +1.7% with a 3.2% standard deviation between models. The 2023 PV Performance Modeling Collaborative (PVPMC) Blind Modelling Comparison [18] received twenty-nine submissions, each modelling up to six of the defined fixed-tilt and single-axis tracking scenarios in one or more PV performance models. The results show a median annual energy yield error of -3.3% between modelled and measured data across all submissions and scenarios. The authors highlight that linearly-applied user-defined derate factors were a significant source of bias error, accounting for most of the energy yield underestimation and varying significantly between submissions. The two bifacial scenarios showed up to 99-150% rear irradiance error in some models at noon on a clear day; while the paper does not tie this error to user-defined derate-factors, such a deviation in submitted results indicates that the range of modellers lacked a collective understanding of expected rear irradiance behaviour.

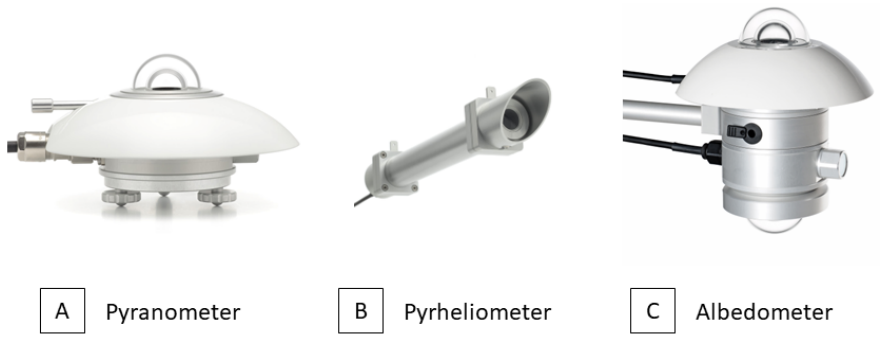


Figure 2.12: Irradiance measurement devices for DHI and GHI (A, pyranometer) and DNI (B, Pyrheliometer) and albedo (C, albedometer). Images by Hukseflux Thermal Sensors, licensed under CC BY 4.0.

2.3 Field measurements for PV model validation

To determine the accuracy of a PV performance model, modelled irradiance and energy yield must be compared to plane-of-array irradiance and energy yield measurements acquired from installed PV systems. The Task 13 IEA PVPS report on bifacial PV systems provides examples of test systems at research facilities around the world [2]. The following two sections highlight sensors required for meteorological data acquisition and irradiance measurements, and DC energy yield monitoring.

2.3.1 Meteorological and irradiance field measurements

In [120], Gostein et al. provide best practices for measuring irradiance in bifacial PV systems. Additionally, Vignola [121] provides in-depth descriptions of irradiance and meteorological measurement devices used in the field and discusses the merits and drawbacks of ground measurements vs. satellite-acquired data. The following paragraphs summarize the measurement devices and approaches relevant for PV performance modelling.

Direct normal irradiance (DNI) is commonly measured with a *pyrheliometer* - a device that measures the collimated radiation emanating from the circumsolar region $\pm 2.5°$ around the center of the sun [80]. The pyrheliometer consists of a *collimating tube* on a solar tracker that directs light from the circumsolar region onto a set of thermocouples calibrated to output an analog signal proportional to the incident direct beam irradiance.

Global horizontal irradiance (GHI) is measured using either a *pyranometer* or a silicon *reference cell*, both facing directly upward at the sky. The pyranometer consists of 1-2 glass domes with flat spectral transmission between 285-3000 nm sitting above a set of thermocouples; the domes provide 180° view of the sky dome while shielding the thermocouples from both precipitation and infrared radiation exchange with the atmosphere that can cause cooling. Silicon reference cells monofacial silicon PV cells packaged under glass and encapsulant layers to be weather-resistant. The output signals are calibrated to provide irradiance measurements relative to 1000 W/m^2 with the same angular acceptance as a PV module.

Diffuse horizontal irradiance (DHI) is measured with a pyranometer equipped with an additional *shadow band* or *shadow ball* that moves throughout the day to block light from the circumsolar region. A shadow band also blocks a thin portion of the sky dome, and thus a DHI pyranometer with a shadow band requires calibration to represent full DHI.

Plane-of-array (POA) irradiance can be measured using pyranometers or reference cells afixed to purlins or horizontal rails and facing away from the module plane to the front or rear. For instance, the NREL Bifacial Experimental Single-Axis Tracking field (NREL BEST) [122] provides rear plane-of-array irradiance measurements from a dummy-module with a set of silicon references cells strung such that the current of each row of cells is measured separately. The Technical University of Denmark (DTU) provided open source data from one rear-facing pyranometers on each of the tiers of a fixed-tilt and a single-axis tracking 2P system [123].

Albedo is the ratio of a downward-facing horizontal irradiance measurement by an upward-facing horizontal irradiance measurement (i.e., GHI). These measurements are sometimes referred to as *up-welling* and *down-welling* irradiance, respectively. The measurements can be achieved using two back-to-back pyramometers or reference cells facing in opposite directions at the same location. The ensemble is referred to as an *albedometer*, and best practices suggest that the downward-facing pyranometer or reference cell be installed 1.5 m above the ground [120] on an equator-pointing tripod armature, away from any significant sources of shade. It is also suggested that multiple locations within one site be tested throughout multiple seasons to account for variation in ground-cover.

Alternative devices have been developed over the past decades to provide simultaneous broadband and spectral irradiance measurements, such as the SolarSIM-D for DNI and SolarSIM-G for GHI [124]. All irradiance measurement devices are categorized by performance into Class A-C [125].

A variety of irradiance measurement issues can cause a bias in energy yield calculations. Uncalibrated, poorly installed, or rarely maintained irradiance sensors lead to persistent over- or underestimation. Sensor soiling or frost accumulation reduces irradiance measurements as compared to actual conditions, leading to an underestimation in modelled vs. measured energy yield. Sensor calibration, ventilation, and cleaning are therefore essential in maintaining a quality irradiance data set for PV performance model validation.

Meteorological stations are usually placed on a vertical *mast* - the height of which is based on the specific measurement devices. These devices may include an *anemometer* to measure wind speed and direction, a *rain* and/or *snow gauge* to measure precipitation, a *hygrometer* to measure relative humidity, a *thermometer* or *psychrometer* to measure dry bulb (ambient) temperature, and a *barometer* to measure pressure. Ground-accumulated snow depth is often measured using a *sonic sensor* or a measuring tape or ruler with manual-recording or image processing. While not a meteorological measurement, rear-side module temperature is another useful measurement for validating cell temperature models.

Satellite data can also be used in place of the above measurements, with varying degrees of certainty. Satellite irradiance measurements for a given location are interpolated based on images representing a large area (2-30x2-30km); therefore, localized weather patterns may not be captured at subhourly timestamps and instantaneous modelled energy yield may see significant error compared to measured energy yield at fine temporal resolutions. Additionally, differentiating between snow and cloud-cover in satellite images is not trivial [126], with any error resulting in added uncertainty in winter months at mid-to-high latitude. However, satellite data is particularly useful for locations or time frames in which on-site data is not available or requires additional validation.

2.3.2 Direct current (DC) electrical measurements

If the modules in a system are equipped with power optimizers or micro-inverters, PV performance models can be validated against the maximum DC power of each module. This isolates module performance from the effects of inter-module irradiance non-uniformity. Since AC power management in such a system is performed by a transformer, rather than by a large inverter, modelling validations can avoid discrepancies with measurement typically caused by clipping and curtailment in other systems.

However, systems with inter-module series stringing are more common. In small systems of this type, DC power measurements are available at the inverter where module strings are combined in parallel. In larger systems of this type, DC measurements may be available at the *combiner boxes* where module strings are connected in parallel prior to joining other combiner cables at inverter [43]. In the latter, access to combiner box data allows spatial specificity despite system size. However, in both system sizes, the inverter set-point dictates the DC voltage at which the module strings will be held; curtailment and clipping moves the module string operating point on the current-voltage curves away from the maximum power point, reducing measured DC power. Therefore, any PV performance model validation must either discard curtailed and clipped timestamps or adjusting the modelled DC power based on the apparent inverter set-point.

2.4 Software concepts

2.4.1 Primitives and rotations

In computer graphics rendering, the most fundamental surfaces and volumes that make up the objects in a 3D scene are known as *primitives*. In ray tracing, these primitives interact with rays in the scene to determine absorption, reflection, and refraction. Eric Haines' realtimerendering.com [127] hosts a list of the record fastest ray-primitive intersection algorithms, last updated 2021. Sample ray-primitive intersections are described in Appendix A of this thesis.

To form dynamic objects in a scene, defined primitives can be transformed by translation and *rotation matrices*. For example, Tait-Bryan matrices belong to a family of rotations called *Davenport chained rotations* which describe three sequential rotations around *body-fixed* axes X', Y', and Z' cite [128]. The body-fixed axes rotate with the primitive, staying in a fixed position relative

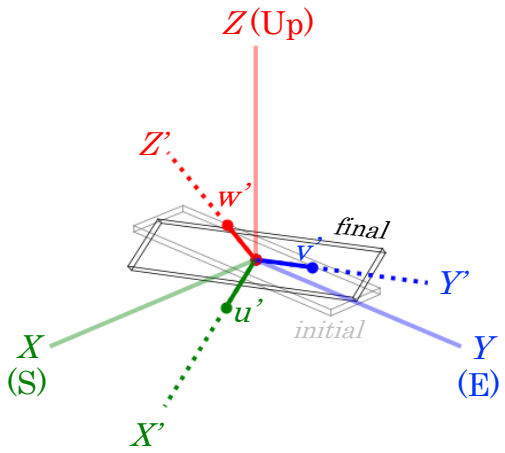


Figure 2.13: Example of the rotation of a volume from initial position in line with the global axes X, Y, Z to final position with unit vectors $u'v'w'$ in line with body-fixed axes $X'Y'Z'$. (S=south, E=east).

to each face as shown in Figure 2.13. In an initial position, prior to any rotation, unit vectors uvw are aligned with axes of the right-handed global coordinate frame, X, Y, Z. In the post-rotation position, unit vectors $u'v'w'$ transform from *uvw* based on a final rotation matrix, R – a sequential combination of matrices R_y, R_x, and R_z, each of which govern a rotation around one of the body-fixed axes, Y', X', and Z'.

As shown in Figure 2.14, R_y corresponds to rotation about the Y' axis by a *tilt* angle, β_p (also known as *pitch*), and R_z corresponds to rotation about the Z' axis by an *azimuth* angle, φ_p (also known as *yaw*). R_x corresponds to rotation about the X' axis by a roll angle, γ_p; for polygons representing rows of modules, γ_p is set to zero when the array is on flat ground. These angles describe a right hand rotation around each of the body-fixed axes shown as dotted lines in Figure 2.14, with a positive angle describing a counter-clockwise rotation when viewed from the infinite end of the each positive axis.

The order of Tait-Bryan rotations is important since each matrix rotates the body-fixed axes around which the next rotation(s) will occur. The above definition of angles and axes requires the following order and final rotation matrix, R, where c represents cosine, s represents sine. The generic subscript for primitive angles, p, has also been dropped for cleanliness, but these angles should not be confused with solar elevation (β_B), azimuth (φ_B), and sky element zenith angles (γ_s). Note also, these matrices are modified from standard Tait-Bryan matrices to align with the coordinate system in Figure 2.13 and definition of rotation angles in Figure 2.14.

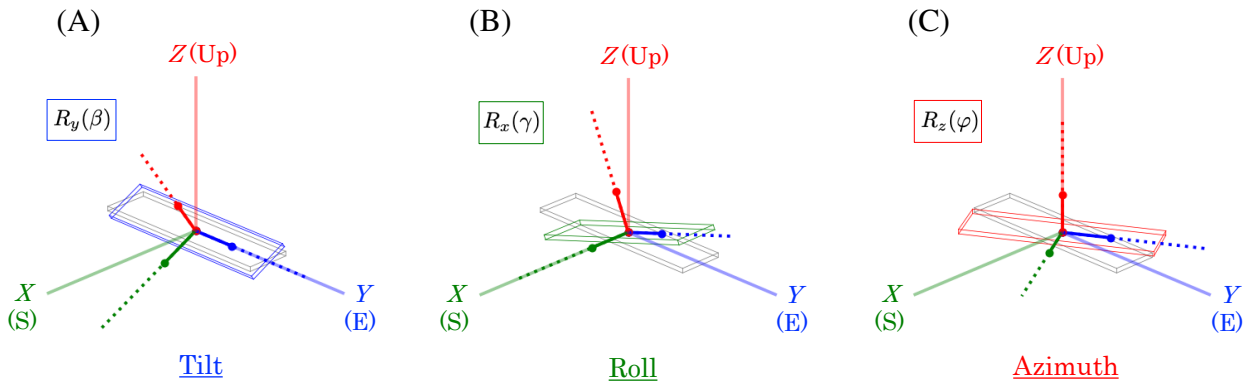


Figure 2.14: Tait-Bryan rotations: (A) $R_y(\beta)$ is the rotation by tilt angle β around the Y axis. (B) $R_x(\gamma)$ is the rotation by roll angle γ around the X axis. (C) $R_z(\varphi)$ is the rotation by roll angle φ around the Z axis. (S=south, E=east).

$$R_x(\gamma) = \begin{bmatrix} \mathrm{c}_\gamma & 0 & -\mathrm{s}_\gamma \\ 0 & 1 & 0 \\ \mathrm{s}_\gamma & 0 & \mathrm{c}_\gamma \end{bmatrix} \tag{42}$$

$$R_y(\beta) = \begin{bmatrix} 1 & 0 & 0 \\ 0 & \mathrm{c}_\beta & \mathrm{s}_\beta \\ 0 & -\mathrm{s}_\beta & \mathrm{c}_\beta \end{bmatrix} \tag{43}$$

$$R_z(\varphi) = \begin{bmatrix} \mathrm{c}_\varphi & \mathrm{s}_\varphi & 0 \\ -\mathrm{s}_\varphi & \mathrm{c}_\varphi & 0 \\ 0 & 0 & 1 \end{bmatrix} \tag{44}$$

$$R = R_y(\beta) \cdot R_x(\gamma) \cdot R_z(\varphi) \tag{45}$$

$$R(\beta, \gamma, \varphi) = \begin{bmatrix} \mathrm{c}_\beta \mathrm{c}_\varphi - \mathrm{s}_\beta \mathrm{s}_\gamma \mathrm{s}_\varphi & \mathrm{c}_\beta \mathrm{s}_\varphi + \mathrm{s}_\beta \mathrm{s}_\gamma \mathrm{c}_\varphi & -\mathrm{s}_\beta \mathrm{c}_\gamma \\ -\mathrm{c}_\gamma \mathrm{s}_\varphi & \mathrm{c}_\gamma \mathrm{c}_\varphi & \mathrm{s}_\gamma \\ \mathrm{s}_\beta \mathrm{c}_\varphi + \mathrm{c}_\beta \mathrm{s}_\gamma \mathrm{s}_\varphi & \mathrm{s}_\beta \mathrm{s}_\varphi - \mathrm{c}_\beta \mathrm{s}_\gamma \mathrm{c}_\varphi & \mathrm{s}_\beta \mathrm{c}_\gamma \end{bmatrix} \tag{46}$$

R is an orthogonal matrix; each column vector has length 1 and is orthogonal to all other column vectors. Thus, each column vector can be applied to the primitive's u, v, or w unit vectors to align

them as u', v', or w' with the X', Y', or Z' axes.

2.4.2 Bounding volume hierarchies

A bounding volume hierarchy (BVH) is an algorithmic structure that can be applied to improve computational efficiency in any 3D rendering technique involving rays. A BVH refers to a set of sequentially smaller volumes, ordered to form a decision tree that dictates which rays should be checked for intersection with which primitives. Each bounding volume in the hierarchy encompasses other groupings of sub-volumes or primitives; the algorithm only checks a given ray for intersection with a volume or primitive if if the ray intersects the bounding volume immediately above it in the hierarchy known as the *parent volume*.

For the example case in Fig. 2.15, a ray will be only checked for intersection with primitives B1-3 in pink if the same ray intersects with both volume A in green and B in blue, as in the case of Ray 2 and 4. Conversely, Ray 2 will not be checked against primitives C1-6, since it intersects with volume A, but not volume C in orange. The brute force approach to check all five rays in Figure 2.15 against primitives B1-3 and C1-6 requires 5×9, or 45 ray-volume or ray-primitive checks. In this example, and assuming ray-volume and ray-primitive checks are of approximately equal computational intensity, the bounding volume hierarchy approach saves $1 - (1 + 3 + 6 + 9 + 12)/45 = 31\%$ of the computation time for Rays 0-4.

As demonstrated by Ray 1 in Figure 2.15, which intersects with volume A but not sub-volumes B and C, it is important to minimize free space within the bounding volumes that is not occupied by a sub-volume to avoid unnecessarily passing to the next lowest level of the hierarchy. Additionally, bounding volumes should not contain too few sub-volumes or primitives as this would result in a high ratio of bounding volume checks to primitive checks, reducing savings. Neither should they contain too many spatially-disparate sub-volumes or primitives since a positive intersection check anywhere in the bounding volume will result in a check of all items contained within.

In a dynamic scene, some ray tracing software must re-generate the scene's bounding volume hierarchy for each timestamp to account for primitive transformations and changing bounding volumes. For example, the RADIANCE software [108] generates *octrees*, or ".oct" files, for each timestamp by recursively dividing the scene space around an origin point in eight until the smallest volumes contain a specified number of surfaces or reach a specified minimum volume. The

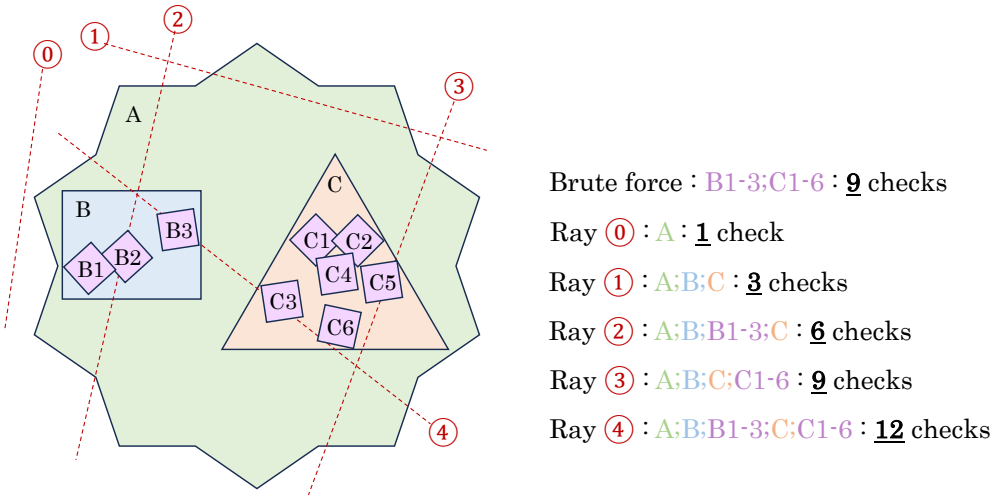


Figure 2.15: Example of a bounding volume hierarchy for volumes A in green, B in blue, and C in orange, primitive sets B1-3 and C1-6 in purple, and rays 0-4 in red. The primitive check lists to the right demonstrate that the bounding volume hierarchy for rays 0-3 require equal or less computation than the brute force method.

RADIANCE documentation [108] describes this computation time required by this process as a "fraction" of the overall optical simulation time; however, it is a noticeably non-negligible process, particularly for users without access to parallelized code and high performance computational resources.

2.4.3 Computational efficiency

Programming language Different programming languages offer different benefits to a developer. For example, Python has simple syntax, readily available libraries, and automatic memory management - all of which facilitate rapid prototype development [129]. Conversely, C is a faster, *compiled* language used in software such as the RADIANCE raytracer [108] which require significant computational resources per ray.

As Tucker and Noonan explain in [130], a *compiler* is a program that translates source code, which we can read and write, into an executable file of machine code which the computer's central processing unit (CPU) can understand. In C, a *static* or *ahead-of-time compiler* compiles the entire source code prior to execution; if there are syntax errors, all errors are shown at this stage, prior to executing any instructions. In contrast, a Python *interpreter* compiles source code into machine code line by line, immediately before each line CPU executes the line. This makes debugging easier

since errors can be caught at the source, but slows computation speed since any re-used functions must be re-compiled line-by-line.

C is also a *statically typed* language which requires that all variables be declared with their type (i.e., integer, float) at first usage [131]. In this way, all types are known at execution and no checks need be run during execution to determine a variable type. Python, however, is *dynamically typed*, meaning that the interpreter must infer the data type of the variables in each instruction [132]. Looping over elements of an array is particularly slow in Python since the interpreter must re-determine the type of variables in each line at each loop iteration. Using the *NumPy* Python library [133] reduces this burden somewhat since all elements of a NumPy array must share the same data type and operations can be carried out in NumPy's pre-compiled C code.

Vectorization Nested for-loops, which loop through elements of a multidimensional array, are particularly computationally inefficient in Python; for each iteration of the loop, the Python interpreter must determine the type of each variable in every line and load data from new memory addresses before executing the instructions in that line. To alleviate this computational burden, programmers can *vectorize* looped processes using array data structures from the NumPy Python library. Vectorization applies a given operation to all elements in an array through a single arithmetic operation or function call, removing any iteration from the source code and speeding up memory access. [134]. For example, to multiply two 3x3 NumPy arrays, a and b, the for-loop implementation would be:

```
for i in range(0, a.shape[0]):
        for j in range(0, a.shape[1]):
                c[i,j] = a[i,j]*b[i,j]
:7.71 µs ± 154 ns per loop
(mean ± std. dev. of 7 runs, 100,000 loops each)
```

and the vectorized implementation is:

```
c = a*b
:470 ns ± 2.06 ns per loop
(mean ± std. dev. of 7 runs, 1,000,000 loops each)
```

Using the %timeit IPython magic function, we can see the execution time for each of the above approaches under the code block. The vectorized implementation using NumPy surpasses the for-loop implementation in computational efficiency by an order of magnitude. All elements in the NumPy arrays have the same type, reducing the number of checks required to perform operations on all elements and improving computational speed. Additionally, NumPy arrays store elements in *contiguous memory* blocks which allows the CPU quicker access to multiple array elements at a time [135].

In many cases, vectorizing an operation requires that all NumPy arrays be of the same shape or share dimensions in one axis. A programmer must manually *broadcast* a variable to the correct shape by repeating vectors or arrays along new axes, or use a vectorization function or decorator to broadcast variables to the correct shapes [136, 137]. *NumPy.repeat* and *NumPy.newaxis* functions aid in this process, as exemplified below for the simple broadcasting of an n-dimensional vector, p, to a nxm array, q.

```
p_broadcast = np.repeat(p[:, np.newaxis], q.shape[-1])
p_broadcast.shape == q.shape
:True
```

This broadcasting approach has some drawbacks. It can introduce computational cost and should be monitored through profiling to ensure this cost is offset by efficiency gains from avoided for-loops. Additionally, broadcasting variables for operations with large arrays can quickly balloon the memory requirements of a program.

Just-in-time compiling Just-in-time (JIT) compiling is a compilation method aimed at improving the computational efficiency of interpreted languages with originally untyped variables. Like an interpreter, a *JIT compiler* compiles and runs code line by line; however, JIT compilers also cache compiled code for a subset of user-identified functions and simply re-run the compiled code in the event of repeated function calls. This approach reaps the computational efficiency benefits of ahead-of-time compilers, but maintains the syntax and structures of the original interpreted language. With this approach, there is computational overhead associated with compiling and caching machine code during the first call of any function [138]. Therefore, JIT decorators should mostly be applied to functions that are re-used frequently throughout the model.

To enable this approach, we must assign data types to the input and output variables of the given function so that the interpreter need not infer the variable types. In the JIT Python library called *Numba* [139], the programmer places @njit decorator signatures above the function [140] to be cached.

3 Model development and validation

As introduced in Chapter 1, and described in detail in Section 2.2, widespread access to accurate bifacial PV models will require a modelling tool that is both accurate at high spatial and temporal resolution and more computationally efficient than existing 3D approaches. This chapter defines one such model. The chapter begins with a re-production of a manuscript describing a finite element approach to PV optical modelling with 3D shading and provides a validation against field data for bifacial fixed-tilt and single-axis tracked systems. The subsequent sections of the chapter provide additional details on the simulated environment, optical model, and electrical model. These sections are followed by a description of two additional cross-software validations which situate the proposed model's performance with respect to 2D view factor and ray tracing approaches. The chapter ends with a discussion on the model's computational efficiency.

3.1 Novel energy yield model with 3-D shading for bifacial photovoltaic systems

ANNIE C. J. RUSSELL, CHRISTOPHER E. VALDIVIA, CÉDRIC BOHÉMIER, JOAN E. HAYSOM AND KARIN HINZER

Scope and Impact

The following text is a reproduction of a manuscript published in the November 2022 issue of the *IEEE Journal of Photovoltaics (JPV)*. The paper describes the a novel bifacial PV performance model, DUET, which combines finite element modelling and ray-object intersection to calculate shade-inclusive 2D front and rear module irradiance maps. This approach aims to reduce the computational intensity of 3D optical modelling compared to ray tracing while maintaining accuracy in simulated irradiance and energy yield.

The paper also contains a validation study comparing DUET's modelled outputs to open-access irradiance and energy yield measurements for a fixed-tilt system and a horizontal single-axis tracked (HSAT) system at the Technical University of Denmark [123]. The results of the validation demonstrate that:

1. The mean absolute error (MAE) between DUET's simulated average rear irradiance and measured values is 2.8-3.7 $\mathrm{W/m^2}$, falling within the range of error demonstrated by eight other software tested at this site in Riedel-Lyngskaer et al. [86]. The energy yield correlation coefficient between measured and modelled data exceeds 0.99 for both systems, demonstrating good agreement.

2. The spatial resolution of DUET's optical and electrical models contributes to decreased simulation error. For example, sampling irradiance at the specific coordinates of the rear-facing pyranometers reduces rear irradiance MAE by 0.44-1.4 $\mathrm{W/m^2}$ as compared to averaging across the rear of the modules (see Fig. 9.a). Additionally, DUET's cell-level current-voltage calculations decrease the magnitude of monthly relative fixed-tilt energy yield error for December - a month in which the fixed-tilt system sees harsh front-side shading of the direct beam - by 6.1% absolute as compared to the common 2D view factor approach which applies average rear side irradiance to every cell.

3. The model's non-optimized computation time for an annual simulation is 3.7 core-hours on a 3.9 GHz CPU, demonstrating improved computational efficiency as compared to 12+ hour, 1.9-4.8 GHz ray tracing simulation time reported in [86].

Note: The model used in this validation is the University of Ottawa SUNLAB's 2021 version, DUET v.uO-2021. Subsequent chapters will refer to the University of Ottawa DUET versions as DUET v.uO-20XX based on the year.

Copyright This manuscript was published in the IEEE Journal of Photovoltaics (JPV) in 2022. The Version of Record is available online at:

Annie C. J. Russell, Christopher E. Valdivia, Cédric Bohémier, Joan E. Haysom and Karin Hinzer, "DUET: A Novel Energy Yield Model With 3-D Shading for Bifacial Photovoltaic Systems," in IEEE Journal of Photovoltaics, vol. 12, no. 6, pp. 1576-1585, Nov. 2022, doi: 10.1109/JPHOTOV.2022.3185546.

Corrections The following text refers to DUET as a 3D view factor model with ray-object intersections; however, Section 3.3.1 clarifies that the equations within this text represent a finite

element method approximation of the view factor between arbitrary surfaces. Note also, Fig. 9 legend should cite Ref. [1] in the reproduced manuscript rather than Ref. [12].

1576 IEEE JOURNAL OF PHOTOVOLTAICS, VOL. 12, NO. 6, NOVEMBER 2022

DUET: A Novel Energy Yield Model With 3-D Shading for Bifacial Photovoltaic Systems

Annie C. J. Russell, Christopher E. Valdivia, Cédric Bohémier, Joan E. Haysom, and Karin Hinzer, *Senior Member, IEEE*

***Abstract*—Bifacial photovoltaic (PV) performance models strive to accurately quantify rear-incident irradiance. While ray tracing models are optically rigorous, they require significant computational resources; faster view factor (VF) models are widely adopted but require user-defined loss factors to approximate rear shading and irradiance nonuniformity, introducing uncertainty in energy yield predictions. This article describes DUET—a bifacial PV performance model that calculates optical and electrical performance based on a physically representative array geometry. DUET's novel shading algorithm pairs a 3-D VF model with deterministic ray-object intersections to capture 2-D shade-inclusive irradiance profiles while minimizing computational cost. Series and parallel combination of current–voltage curves capture irradiance nonuniformity throughout the module and array. This article provides validation against open-access system measurements from a test site in Roskilde, Denmark, and comparison to other software tested there [1]. DUET's modeled bifacial energy yield agrees with measured data within −1.56% for fixed-tilt and −0.65% for horizontal single-axis tracked (HSAT) systems. Mean absolute error (MAE) in hourly bifacial power is 14.2–15.0 mW/Wp for fixed-tilt and 17.3–18.3 mW/Wp for HSAT, depending on the module temperature model applied. Comparing modeled and measured rear irradiance of two rear-facing pyranometers, DUET's MAE values of 2.8 W/m^2 for fixed-tilt and 3.7 W/m^2 for HSAT are among the lowest errors reported for other software tested at this site. DUET provides computationally efficient bifacial performance modeling with geographic, temporal, and structural specificity to determine loss factors for use in other performance models or to be used directly in system design optimization.**

***Index Terms*—Albedo, bifacial, diffuse, electrical mismatch, energy yield, irradiance, photovoltaic (PV), ray tracing, shading.**

I. Introduction

BIFACIAL photovoltaic (PV) modules convert both front- and rear-incident light into electrical energy. The rear contribution leads to higher energy yields as compared to traditional one-sided, or *monofacial*, modules. This additional energy can reduce a system's levelized cost of energy, particularly when paired with horizontal single axis tracking (HSAT) [2]. However, uncertainty in bifacial yield prediction can impede design optimization and create a financial risk to project ownership [3]. The exact irradiance incident on the rear of a module depends on a complex set of factors such as the ratio of diffuse to direct light, the properties of the ground cover, and the position and shape of mounting structures [4]. In the absence of validated and accessible bifacial PV performance models and parameters, this complexity would manifest as uncertainty in rear irradiance modeling and inaccuracy in energy yield predictions, system costing, and forecasting.

Significant efforts are underway to increase confidence in bifacial PV modeling accuracy: existing software have undergone validation against field data [4]–[11]; cross-software comparisons provide technical and performance insights [1], [12]–[19]; and open-access field data is available in [20]–[22]. Despite these efforts, many optical models lack either computational efficiency or geographic and temporal specificity. For instance, annual calculations of hourly irradiance in ray tracing models [9]–[11], [14], [15], [17], [18], [23]–[25] typically exceed 12-h run times for HSAT systems unless high-performance computational resources are used [1]. These computationally intensive models capture complex shading and reflection by following a large collection of stochastic rays through multiple interactions with textured surfaces. Conversely, view factor (VF) models can efficiently compute the transfer of radiation between meshed surfaces in a scene [26] but treat shading more simply. While 2-D VF models [5]–[7], [24], [27]–[33] can simulate annual insolation in less than 5 min [1], they require user-defined loss factors to account for structure shade and irradiance nonuniformity along the width of a module or row. However, the geographic- and temporal-specificity of these loss parameters is still not well understood, leading to uncertainty in yield projections [1], [17], [34]. Three-dimensional (3-D) VF models [16], [35]–[38] inherently capture irradiance nonuniformity along the width of a module or row, and while BIGEYE [19], [35], [36] includes object shading, 3-D VF models typically rely on annualized, estimated factors to represent the effect of these structures. MobiDiG Hybrid [8], [24] computes front irradiance with VF and rear irradiance by ray tracing to improve computational efficiency while maintaining array design specificity.

Manuscript received 3 February 2022; revised 26 April 2022; accepted 13 June 2022. Date of publication 4 July 2022; date of current version 28 November 2022. This work was supported by the Natural Sciences and Engineering Research Council of Canada under Grant NSERC CREATE 497981 and Grant STPGP 521894. *(Corresponding author: Annie C. J. Russell.)*

Annie C. J. Russell, Christopher E. Valdivia, Cédric Bohémier, and Karin Hinzer are with SUNLAB, Centre for Research in Photonics, School of Electrical Engineering and Computer Science, University of Ottawa, Ottawa, ON K1N 6N5, Canada (e-mail: aruss100@uottawa.ca; valdivia@uottawa.ca; cbohe083@uottawa.ca; khinzer@uottawa.ca).

Joan E. Haysom is with SUNLAB, Centre for Research in Photonics, School of Electrical Engineering and Computer Science, University of Ottawa, Ottawa, ON K1N 6N5, Canada, and also with the J. L. Richards and Associates Ltd., Kingston, ON K7L 5N4, Canada (e-mail: jhaysom@jlrichards.ca).

Color versions of one or more figures in this article are available at https://doi.org/10.1109/JPHOTOV.2022.3185546.

Digital Object Identifier 10.1109/JPHOTOV.2022.3185546

This work is licensed under a Creative Commons Attribution 4.0 License. For more information, see https://creativecommons.org/licenses/by/4.0/

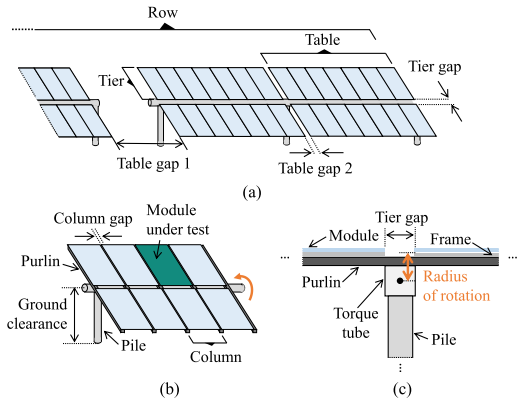


Fig. 1. Selection of DUET's input design parameters illustrated for: (a) row features and (b) table features in a generic 2-in-portrait (2P) system. (c) A close-up cross-section of a 2P system torque tube with user-defined features shown.

This article outlines our approach to fill the efficiency-specificity gap—Dual-sided Energy Tracer (DUET)—a numerical PV performance software with integrated optical and electrical models [39]–[41]. The optical model enhances the 3-D VF approach by checking a finite number of deterministic rays for intersection with objects in the scene and generates shade-inclusive 2-D front and rear module irradiance profiles. The electrical model captures current mismatch losses induced by irradiance nonuniformity across cells and provides module-, string-, or array-level energy yields based on a flexible wiring architecture. DUET is currently under active development in-house and was one of 13 models in the International Energy Agency (IEA) PV Power systems Programme (PVPS) Task 13 bifacial PV modeling comparison [12]. The following sections provide a detailed description of DUET and demonstrate field validation for fixed-tilt and HSAT systems at a test site in Denmark [22]. A list of symbols is available in Table I.

II. DUET Energy Yield Software

The DUET software computes the energy yield of monofacial and bifacial PV modules within a fixed-tilt or HSAT array. The array sits on a flat ground surface with time-varying albedo, ρ, and can consist of any number of rows, tables per row, and tiers or columns of modules per table. The optical model processes hourly or sub-hourly solar resource and meteorological data for the given geographic location. For each simulation, the user selects a single module under test from within the array and defines inputs relating to geography, array and table design, and optical and electrical parameters. A selection of the user-specified features in a row and table is illustrated in Fig. 1 and Table II.

The software separates the simulation into time-independent and time-dependent calculations [see Fig. 2(b) and (c)], the latter with hourly or sub-hourly timestamps. The novel shade model pairs ray-object intersection algorithms with the 3-D VF approach to generate detailed 2-D front and rear irradiance profiles for the selected module. The electrical model then calculates current–voltage (*IV*) curves for each cell and combines cell *IV* curves based on a user-specified wiring architecture to generate the module *IV* curve, including the effect of bypass diodes. Users can simulate multiple modules to construct *IV* curves for multimodule strings and arrays.

DUET provides cell- and module-level outputs for each timestamp as illustrated in Fig. 2(d), including: front and rear average irradiance, 2-D irradiance profiles, module average temperature, cell and module *IV* curves, maximum power, electrical mismatch, and bifacial gain. From these outputs, users can compute the loss factors required for use in 2-D VF models. The following sections provide further details on the DUET algorithm summarized in Fig. 2.

A. Optical Model

The optical model computes front and rear module irradiance based on three irradiance sources: direct radiation from the sun beam, anisotropic diffuse radiation from the sky, and reflected radiation from the ground. As in other 3-D VF models, the diffuse sky dome, ground, and module under test are meshed into patches to facilitate energy transfer calculations. After meshing, the HSAT module patch coordinates are rotated each timestamp based on tracker tilt. The energy that is emitted from one patch and incident on another depends on the area of the irradiated patch, the angle of incidence (AOI), and the solid angle between irradiated and emitting patches. In DUET, an object in the array can partially or completely attenuate energy transfer between two patches if it intersects with the ray that links the patch centroids. The resulting irradiance at the center of each module patch forms the module irradiance profile.

1) Shading Algorithm: The complex shading objects in a modern PV array, such as adjacent rows, mounting structures, and module frame, can be approximated by the combination of the three basic shapes, or *primitives* as shown in Fig. 3(a). These primitives consist of polygons, cylinders, and rectangular prisms. DUET uses ray-primitive intersection routines [42]–[45] to check whether a ray that links the centroids of an emitting source (e) and an irradiated patch (i) intersects with shading objects in the scene.

An intersection indicates that the emitting source may be obscured by a shading object, and we apply a multiplicative shading factor, $\delta_{e,i}$, to the ray's incident irradiance based on the transparency of the intersecting primitive. Intersection with an opaque primitive, such as the cylinder that forms the torque tube in Fig. 3(b), sets $\delta_{e,i}$ to zero. Intersection with a semi-transparent primitive sets $\delta_{e,i}$ to the pre-calculated transparency of the primitive, effectively dimming the ray. For example, the transparency of a polygon that represents a portion of a table is found as the fraction of the associated area that is covered by solar cells, adjusted for the given AOI to account for Fresnel transmittance of an air-to-glass and glass-to-air boundary. If no ray-primitive intersection is found, or if the ray intersects with a transparent primitive such as a a polygon representing a table gap or tier gap, $\delta_{e,i}$ is set to 1. Similarly, the model represents frame shading by setting $\delta_{e,i}$ to 0 for any rear-incident ray that does not pass through the transparent polygon formed by the innermost frame edges.

To decrease computation time, primitives are grouped into a hierarchy of bounding boxes around individual rows, sets of

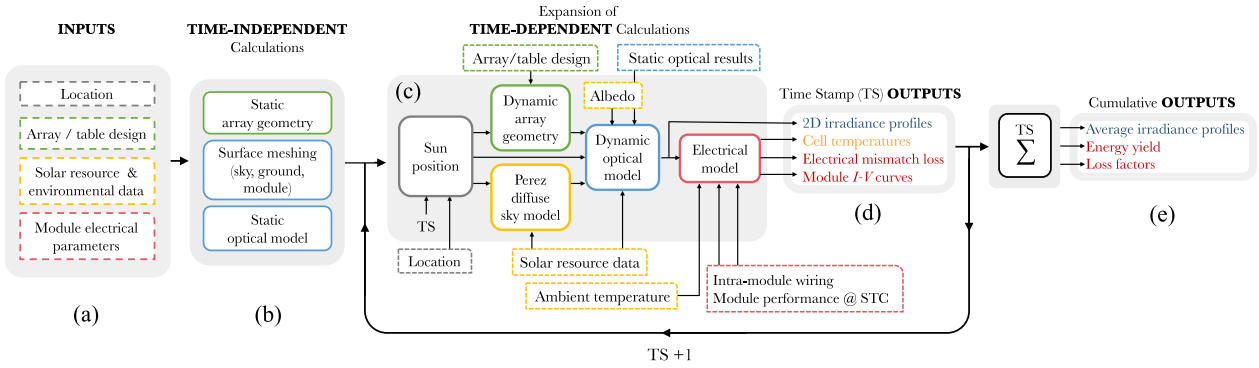


Fig. 2. Block diagram of DUET algorithm for module under test: (a) summary of inputs, (b) time-independent calculations, (c) expansion of time-dependent calculations, (d) timestamp outputs, and (e) cumulative outputs. TS = timestamp; STC = Standard Test Conditions; Grey = geography; green = array/table design; yellow = solar resource & environment; blue = optical model; red = electrical model.

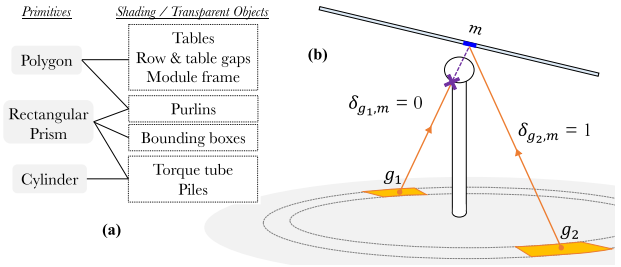


Fig. 3. (a) Composition of shading and transparent objects from primitives. (b) Cross-section of a single axis tracker with shading factors ($\delta_{g_1,m}$ and $\delta_{g_2,m}$) link emitting ground patches, g_1 (obscured) and g_2 (not obscured) with module patch m.

rows, and the full array. The extreme coordinates of the array or row form the corners of these boxes, and DUET checks rays for intersection with successively smaller bounding boxes until only the remaining eligible rays are checked for intersection with the primitives.

2) Ray Characteristics: All shading objects in DUET are considered absorbing and nonreflective, thus *reflections* off the mounting structure and frame are not captured. Since the ground is the sole reflecting surface, all rays in the simulation are deterministic and independent—an architecture that allows for parallel processing and vectorization to improve computational efficiency. This approach differs from recursive ray tracing, which can capture diffuse reflection from all defined surfaces. Recursive ray tracers follow stochastic rays away from the module to check for intersection with primitives in the scene, and each ray-primitive intersection "spawns" additional rays that emanate from the intersection point, which must also be checked for shading [46]. That process can repeat multiple times and requires significant computational resources.

DUET's deterministic rays can be classified into two groups: 1) static rays—in which all emitting sources, irradiated patches, and shading objects are stationary; and 2) dynamic rays—in which at least one of these components moves every timestamp. Fixed-tilt simulations are most computationally efficient since shading factors for diffuse and ground-reflected rays need only be calculated once in the time-independent static optical calculations in Fig. 2(b). Conversely, HSAT simulations are more computationally intensive since the predominantly dynamic rays require recalculation of shading factors each timestamp as part of the time-dependent dynamic optical calculations in Fig. 2(c).

3) Energy Transfer: DUET integrates these shading calculations with a 3-D VF model at each timestamp to predict the optical power incident on each of the cells in the module under test. The optical power on the rear of the c'th cell, $P_{c,\mathrm{r}}$, is

$$P_{c,\mathrm{r}} = \sum_{m=1}^{N_\mathrm{M}} G_{m,\mathrm{r}} \cdot A_m \tag{1}$$

where $G_{m,\mathrm{r}}$ is the *effective irradiance* incident on the rear (r) of the m'th module patch, consisting of the total incident irradiance less angle-dependent reflection losses; N_M is the number of module patches per cell and A_m is the area of the m'th module patch. The user defines the size and shape of the PV cells as well as the module patch resolution. For example, the validation in this article includes 156.75 mm pseudosquare cells, each meshed into a 4 × 4 grid of patches. $G_{m,\mathrm{r}}$ can be found as the sum of direct beam ($G^\mathrm{B}_{m,\mathrm{r}}$), diffuse sky ($G^\mathrm{D}_{m,\mathrm{r}}$), and ground-reflected ($G^\mathrm{R}_{m,\mathrm{r}}$) components

$$G_{m,\mathrm{r}} = G^\mathrm{B}_{m,\mathrm{r}} + G^\mathrm{D}_{m,\mathrm{r}} + G^\mathrm{R}_{m,\mathrm{r}}. \tag{2}$$

Equations analogous to (1) and (2) are used to find the effective irradiance incident on the front of the m'th module patch, $G_{m,\mathrm{f}}$, and the front (f) optical power of the c'th cell, $P_{c,\mathrm{f}}$. In the following explanation, front (f) and rear (r) subscripts are dropped to consider the irradiance incident on either side of the m'th module patch.

Direct beam effective irradiance incident on the m'th module patch is calculated as

$$G^\mathrm{B}_m = G_\mathrm{B} \cdot \cos\theta_{\mathrm{B},m} \cdot IAM(\theta_{\mathrm{B},m}) \cdot \delta_{\mathrm{B},m} \tag{3}$$

where $\theta_{\mathrm{B},m}$ and $\delta_{\mathrm{B},m}$ are the AOI and shading factor between the beam and the m'th module patch, respectively. *IAM* is the incidence angle modifier (IAM), governed by either the ASHRAE IAM model [47] or a user-defined sixth degree polynomial. Front and rear IAMs can be defined independently. The sun position

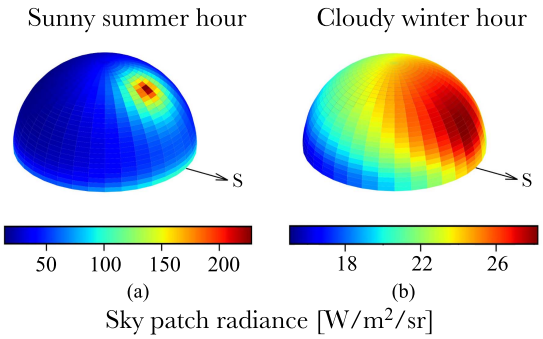


Fig. 4. Radiance of anisotropic diffuse sky based on Perez sky luminance distribution model [50] in Roskilde, Denmark during (a) a sunny 12:30 PM in summer (GHI: 851.5 $\mathrm{W/m^2}$, DHI: 126.7 $\mathrm{W/m^2}$), and (b) a cloudy 12:30 PM in winter (GHI: 73.5 $\mathrm{W/m^2}$, DHI: 71.4 $\mathrm{W/m^2}$).

is calculated with the NREL sky position algorithm [48] at the midpoint of each timestamp to accommodate timestamp-ending input data. For example, the sun position is set at 14:30 for an hourly timestamp labeled 15:00. The sun position dictates the tilt of HSAT modules, and a standard backtracking algorithm [49] adjusts HSAT module tilt away from beam normal incidence when row-to-row beam shading would otherwise be present.

Diffuse light is incident on both the front and rear of a bifacial module from a wide range of angles. DUET addresses this high angularity by meshing the entire diffuse sky dome into patches. Rays emanate from the centroid of each sky patch toward the module and ground patches. While the skydome is meshed into 36 equal azimuth divisions and 30 equal zenith divisions for the validation in this article, DUET's energy transfer framework would be compatible with an arbitrary number of mesh points and any meshing technique that provides the azimuth, zenith, and solid angles with respect to the origin.

The radiance of the s'th sky patch (L_s) is found via the 1993 Perez sky luminance distribution model [50] accounting for sky clearness, sky brightness, and the position of each patch with respect to the sun. This model generates a normalized radiance distribution for each timestamp, which is subsequently multiplied by the diffuse horizontal irradiance (DHI, or G_D) as shown in Fig. 4. For the timestamps when the sun is below the horizon and $G_\mathrm{D} > 0$, the diffuse sky is set as isotropic.

In both isotropic and anisotropic cases, the diffuse irradiance incident on the m'th module patch is calculated as

$$G_m^\mathrm{D} = \sum_{s=1}^{N_\mathrm{S}} G_s \cdot \Omega_{s,m} \cdot \cos\theta_{s,m} \cdot IAM(\theta_{s,m}) \cdot \delta_{s,m} \quad (4)$$

where N_S is the total number of sky patches; $\Omega_{s,m}$, $\theta_{s,m}$, $\delta_{s,m}$ are the solid angle, AOI, and shading factor between the s'th sky patch and the m'th module patch, respectively.

Ground-reflected light is also particularly important for bifacial energy yield calculations since both energy yield and bifacial gain scale with broadband ground reflectivity, or *albedo* [4]. To represent this irradiance source, DUET divides the flat ground surface into concentric rings which are centered below the module under test, with radial dimensions increasing away from the module. These rings are meshed into equal azimuth divisions such that the solid angles between the module and all ground patches are equal, with the highest resolution patches near the module under test. The validation simulations in this article are performed with 36 azimuth and 20 radial ground divisions.

The irradiance on the g'th ground patch (G_g) is calculated as the sum of direct beam (G_g^B) and diffuse (G_g^D) irradiance

$$G_g = G_g^\mathrm{B} + G_g^\mathrm{D} \quad (5)$$

$$G_g^\mathrm{B} = G_\mathrm{B} \cdot \cos Z \cdot \delta_{\mathrm{B},g} \quad (6)$$

$$G_g^\mathrm{D} = \sum_{s=1}^{N_\mathrm{S}} L_s \cdot \Omega_{s,g} \cdot \cos\theta_{s,g} \cdot \delta_{s,g} \quad (7)$$

where Z is the zenith angle of the sun and $\delta_{\mathrm{B},g}$ is the shading factor between the beam and the ground patch; $\Omega_{s,g}$, $\theta_{s,g}$, and $\delta_{s,g}$ are the solid angle, AOI, and shading factor between the s'th sky patch and the g'th ground patch, respectively.

The ground-reflected effective irradiance on the m'th module patch can be found as

$$G_m^\mathrm{R} = \rho \cdot \sum_{g=1}^{N_\mathrm{G}} G_g \cdot \Omega_{g,m} \cdot \cos\theta_{g,m} \cdot IAM(\theta_{g,m}) \cdot \delta_{g,m} \quad (8)$$

where ρ is the albedo and N_G is the total number of ground patches; $\Omega_{g,m}$, $\theta_{g,m}$, $\delta_{g,m}$ are the solid angle, AOI, and shading factors between the g'th ground patch and the m'th module patch, respectively. The base version of the model assumes a Lambertian ground reflection with equal intensity in all directions and does not account for the spectral shape of reflected light.

B. Electrical Model

The short circuit current for the c'th cell under standard test conditions (STC) is determined from

$$I_{\mathrm{sc},c} = (P_{c,\mathrm{f}} + P_{c,\mathrm{r}} \cdot \varphi) \cdot \Re \quad (9)$$

where φ is the current *bifaciality* constant, which accounts for the decreased probability of carrier collection from rear-incident light, and $\Re$ is the *broadband responsivity* of the cell at STC under the Air Mass 1.5 Global spectrum (AM1.5 G) in units of A/W. While DUET's baseline model calculates performance based on AM1.5 G at all hours, the true spectrum of module-incident light varies throughout the day and year with particular dependence on geographic location [51], [52] and ground-cover [53]. In [54] and [39], a version of DUET was modified to include an AM-dependent responsivity for an encapsulated Si heterojunction module, which impacted modeled annual energy yield by 0.5%–2.5% for a latitude range of 33–69° N.

The temperature-dependent short circuit current of each cell is adjusted using

$$I_{\mathrm{sc},c}(T_c) = I_{\mathrm{sc},c} \cdot (T_\mathrm{STC} - T_c) \cdot \mu_\mathrm{I} \quad (10)$$

where μ_I is the temperature coefficient of current and T_STC is the STC temperature of 25 °C. The cell temperature, T_c, is calculated based on the sum of front and rear cell average irradiances

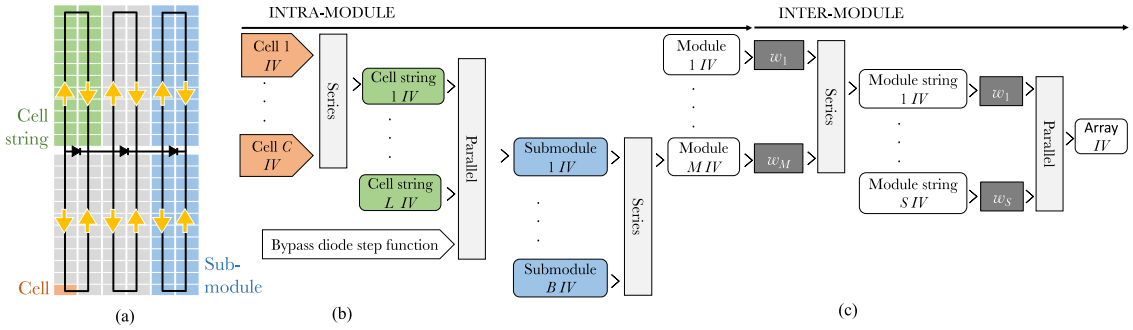


Fig. 5. (a) Intramodule wiring architecture for a half-cut cell module with cell, cell string and submodule identified, where yellow arrows indicate the direction of conventional current. (b) Electrical combination of *IV* curves within a module with *C* cells per inter-cell string, *L* inter-cell strings per submodule, and *B* submodules. (c) Intermodule *IV* curve combination with *M* modules per string and *S* module strings per array.

neglecting reflection losses ($G_{c,\mathrm{f}}, G_{c,\mathrm{r}}$)

$$G_c = G_{c,\mathrm{f}} + G_{c,\mathrm{r}} \tag{11}$$

the ambient temperature (T_a), and one of three module temperature models: the nominal operating cell temperature (NOCT) [55], Faiman [56], or Sandia [57] models. The latter two models are empirically derived functions of G_c, T_a, and wind speed.

For each timestamp, the software calculates the *IV* curve of each cell based on the single-diode model [58]

$$I_c = I_{\mathrm{sc},c}(T_c) - I_0(T_c)\exp\left[\frac{q(V_c + I_c R_\mathrm{s})}{nkT_c} - 1\right] - \frac{V_c + I_c R_\mathrm{s}}{R_\mathrm{sh}(G_c)} \tag{12}$$

where I_c and V_c are the cell current and voltage; the STC cell shunt and series resistances (R_s and R_sh), ideality factor (n), and dark saturation current (I_0) can be fit from the cell or module *IV* curves. Temperature-dependent $I_0(T_c)$ and irradiance-dependent $R_\mathrm{sh}(G_c)$ are found for each timestamp following the De Soto model approach [59].

The module *IV* curve is constructed from the combination of all cell *IV* curves based on a user-specified wiring architecture. Fig. 5(a) provides an example architecture with half-cut cells. Intermediate *IV* curves are calculated, as shown in Fig. 5(b), for: 1) strings of cells in series and 2) the parallel combination of one or more of these strings with a bypass diode into a *submodule*. Submodule *IV* curves are then combined in series to form the module *IV* curve. The flexible cell size and wiring architecture allows for simulation of emerging technologies such as large format modules with 182 or 210 mm cells or modules with multicut and shingled cells.

The series *IV* combination interpolates and sums the voltage of the cells or submodules at common current points. This procedure captures any current limitation due to the irradiance nonuniformity and could capture performance variation between cells. The parallel *IV* combination interpolates and sums current at common voltage points. As in the PVMismatch Python library [60], DUET approximates the bypass diode *IV* behavior as a step function in current at the diode's forward voltage threshold, typically ~ -0.7 V. This approach limits the negative voltage of each submodule and captures the reduced electrical mismatch loss enabled by the bypass diode. The module power under uniform average front and rear irradiance is also calculated at each timestamp to represent performance in the absence of electrical mismatch.

In 2-D VF models such as PVsyst [61], the array energy yield is estimated based on a single irradiance sample line at the center of an infinite row of modules, and the user defines loss factors to represent variations in module performance throughout the array. In DUET, users can obtain array results in a computationally efficient manner by weighting M module *IV* curves with coefficients w_1 to w_M based on the number of modules that each *IV* curve represents within a module string. As shown in Fig. 5(c), the series combination of multiple module *IV* curves generates the module string performance. The S module string *IV* curves can then be combined in parallel to form the array *IV* curve with weighting coefficients w_1 to w_S.

Importantly, this weighted summation of *IV* curves occurs *at each timestamp* allowing the extraction of maximum power of any subsection of the array at any given time. The instantaneous power is scaled by the timestamp duration to provide the energy generated during that timestamp, and the resulting time-series of output data [see Fig. 2(d)] provides insight into temporal performance variation. The summation of all timestamp energies provides the total energy yield for the module, string or array [see Fig. 2(e)].

III. Validation Methodology

A. Field Site

Results from DUET have been validated against open-access data from a bifacial PV test site in Roskilde, Denmark [see Fig. 6(a)] at 55.696°N, 12.104°E [22]. The site has 16 Soltec SF7 2P trackers: eight in HSAT configuration with north–south alignment and eight at a 25° fixed-tilt facing south. 8760 hourly on-site global horizontal irradiance (GHI), direct normal irradiance (DNI), and DHI measurements are available for April 2019–March 2020. Bifacial energy yield data is available during this period for one fixed-tilt and one HSAT row, consisting of four electrically parallel strings of 22 modules each as shown in Fig 6(b). The monthly average measured albedo ranges from 0.19 to 0.23, which did not include any periods of snow accumulation. Rear irradiance is provided from Feb. 21 to Mar. 31, 2020 as the average of two pyranometer measurements near

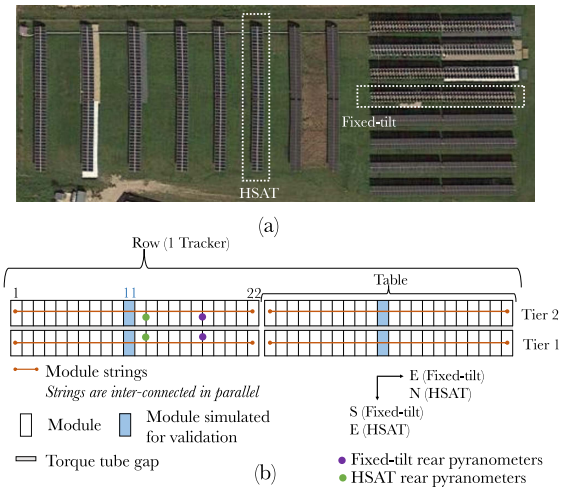


Fig. 6. (a) Satellite image of the test site in Roskilde, Denmark with measured bifacial rows in white boxes (Google Maps, Dec. 2021). (b) Physical and electrical layout of trackers and instrumentation.

the center of a table in each row of interest, on either side of the torque tube. The array geometry, including 2P mounting structure dimensions, is described further in [22]. The frameless bifacial modules are rated at 295 Watt-peak (Wp) with 60 passivated-emitter rear contact (PERC) cells and a bifaciality constant of 0.67. Module temperature coefficients and *IV* curves are available in the datasheet [62].

Riedel-lyngskaer *et al.* [1] provided an in-depth comparison of results from eight bifacial PV performance models against the measured rear irradiance data from this site: MoBiDiG Hybrid [8] with ray tracing based on bifacial_radiance [9], [23], MoBiDiG VF [24], PlantPredict [31], PVsyst [32], systems advisory model (SAM) [30], SolarFarmer [27], bifacialvf [6], and pvfactors [7]. In Section IV-C, we compare DUET's rear irradiance error to results in [1] for these software. We do not provide a direct comparison of energy yield error due to a 5-min time shift discovered in the measured power data after publication of [1]. The present validation compares DUET's modeled energy yield to Version 3 of the open-access data [22], whereas error values in [1] are based on a previous version of that dataset.

B. Simulation

The electrical stringing configuration in Fig. 6(b) shows that all modules within a module string are on the same tier and share the same ground clearance. Thus, we assume that the modules along the table share similar irradiance profiles, neglecting edge effects, and pilings for this validation. We simulated one module per string, shown in blue in Fig. 6(b), and multiplied its *IV* curve by 22 to get four module string *IV* curves. The results from these four strings were combined to find the energy of the row and then compared to the measured row yield. The electrical calculations were repeated for the three module temperature models—NOCT (44 °C [62]), Faiman, and Sandia. The Faiman model coefficients used are $U_0 = 31.0\ \mathrm{W/(m^2\,K)}$ and $U_1 = 1.6\ \mathrm{W\,s/(m^3\,K)}$ as derived by Soltec for this tracker at a site in California [63], and the Sandia coefficients are set for a glass-cell-glass module with open racking. Since seven of the eight models in [1] use the Faiman model, we present energy yield results for the Faiman model in the following sections, unless otherwise stated.

For comparison to measurements, we place an irradiance "sensor" sample point at the 3-D coordinate of each pyranometer [see Fig. 6(b)]. The piling adjacent to the fixed-tilt pyranometers is also modeled. The two-sensor average without IAM is then compared to the rear irradiance measurement, which is provided as the average of pyranometer irradiances.

C. Analysis

The analysis in [1] filters timestamps based on the following four criteria.

1) Sun elevation greater than 5°.
2) Tracker angle agreement between rows.
3) Availability of data acquisition systems.
4) Lack of morning shade on the bifacial HSAT.

For the sake of comparison, the present analysis also uses these same criteria, resulting in a total of 3370 energy timestamps for fixed-tilt and 2371 energy timestamps for HSAT. Filtered rear irradiance measurements are available for 375 and 207 timestamps for fixed-tilt and HSAT, respectively. The following sections compare modeled results (y) to measured data (x) over these sets of hourly timestamps using the metrics of relative error, MAE and mean bias error (MBE)

$$\text{Relative error} = \frac{\sum_{i=1}^{N} y_i}{\sum_{i=1}^{N} x_i} - 1 \tag{13}$$

$$\text{MAE} = \frac{1}{N}\sum_{i=1}^{N} |(y_i - x_i)| \tag{14}$$

$$\text{MBE} = \frac{1}{N}\sum_{i=1}^{N} (y_i - x_i) \tag{15}$$

where N is the number of timestamps.

IV. Results and Discussion

A. General Performance

Fig. 7 shows a comparison of modeled and measured data over the filtered timestamps for bifacial energy and rear insolation in the fixed-tilt [see Fig. 7(a), (b)] and HSAT [see Fig. 7(c), (d)] rows of interest. The blue and orange lines in each subplot represent the linear fit and perfect 1:1 lines, respectively, between DUET's modeled data and the measured data. The R^2 value for DUET's bifacial energy yield prediction is 0.995 or greater for both arrays, indicating good agreement with measurement. The modeled bifacial energy yield is 1.56% lower than measured data for fixed-tilt and 0.72% lower for HSAT. This relative error is less than the 4.5% combined uncertainty of summer clear sky hourly GHI and dc power measurements estimated in [1], as was the case for the six software simulating energy yield at the Roskilde site in that publication.

Modeled rear insolation in Fig. 7(b) and (d) also shows close agreement to pyranometer data with an R^2 of 0.987 for fixed-tilt

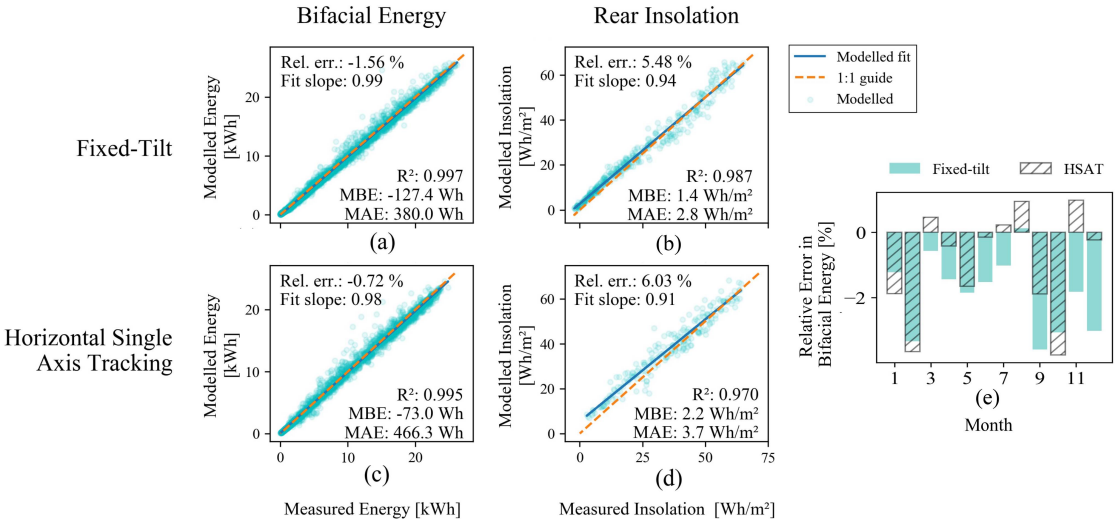


Fig. 7. Comparison of results modeled in DUET as a function of measured data for (a) fixed-tilt bifacial energy yield, (b) fixed-tilt rear insolation, (c) HSAT bifacial energy yield, and (d) HSAT rear insolation at the Roskilde, Denmark field site. Rel. err. = relative error. (e) Monthly relative error in DUET's modeled bifacial energy yield for fixed-tilt and HSAT systems. Energy reported here is modeled using the Faiman module temperature model.

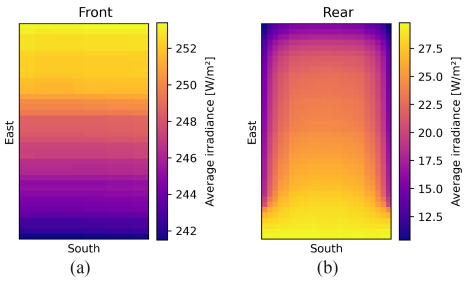


Fig. 8. Irradiance profiles for a frameless southern module in the fixed-tilt system, as generated by DUET. Average effective irradiance over 3370 hourly timestamps for the (a) front and (b) rear of the module.

and 0.970 for HSAT but overestimates in the many low irradiance hours resulting in 5.5% and 6.0% relative error, respectively. This low-irradiance overestimation is also present for all models in [1]. The hours with measured fixed-tilt rear insolation < 20 $\mathrm{Wh/m^2}$ have an average diffuse fraction of 86%, and 51% of these hours have DNI < 1, where diffuse shading from adjacent buildings or trees could have a significant impact. Relative humidity also rises to 82.2% in these low DNI hours producing the necessary conditions for rain and fog, which may impact ground-reflected light.

B. Irradiance Nonuniformity

With multiple sample points across the length and width of each cell, DUET's 2-D irradiance profiles capture nonuniformity across the full front and rear surfaces of the module. For example, Fig. 8(a) shows that modeled average front irradiance differs between the top and bottom of a southern module in the fixed-tilt row by approximately 13.2 $\mathrm{W/m^2}$. The irradiance gradient—primarily induced by inter-row diffuse shading—is relatively constant across the width of this module and could be represented by sampling a cross-section of irradiance down the center. In contrast, the rear irradiance profile in Fig. 8(b) shows shading on the sides and top due to the supporting purlins and torque tube, which would not be captured by cross-sectional irradiance sampling and which introduces a 18.0 $\mathrm{W/m^2}$ difference in average irradiance between the brightest and most shaded module patches.

While Fig. 8 shows an average irradiance profile across all filtered timestamps, DUET calculates energy yield based on a unique 2-D irradiance profile at each timestamp, thus capturing the temporal specificity of intercell current mismatch that cannot be represented by an annualized loss factor. In October to December, the monthly relative error between modeled and measured fixed-tilt energy yield drops from 6.6–9.2% to between -1.8% and -3.1% when current mismatch loss between cells is activated within DUET. These months feature many hours of low sun elevation when adjacent rows partially obscure the direct beam, and this significant error reduction indicates that DUET represents the resulting intercell current mismatch well. Overall, relative error for both fixed-tilt and HSAT ranges from $<1\%$ in magnitude in March to -3.75% in October [see Fig. 7(e)]—lower than the $>10\%$ fixed-tilt and $>5\%$ HSAT monthly error reported for some models in [1].

C. Cross-Software Comparison

The range of rear average insolation MAE for the eight other models is taken from the text of [1] and replotted as the light blue bars in Fig. 9(a). The MAE values in that paper were averaged over the filtered hourly timestamps and include the effect of an IAM as well as Soltec's recommended +0.7% shading factor [63] for the VF models. DUET's rear module irradiance sits within this range, both with and without an IAM applied, although close agreement with pyranometer data is not expected due to rack shading that does not affect the measurement device. The "sensor" approach samples the rear irradiance using the

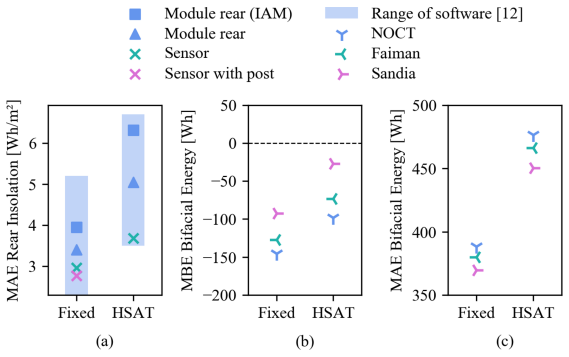


Fig. 9. Performance statistics for DUET and software from previous study [1] as compared to on-site measured data for fixed-tilt and HSAT systems. (a) MAE in modeled rear insolation. (b) MBE and (c) MAE in modeled bifacial energy yield for three temperature models. Wp = Watt peak (25.96 kW).

locations and size of the pyranometer, showing lower MAE than the module average by 0.44 $\mathrm{W/m^2}$ for fixed-tilt and 1.37 $\mathrm{W/m^2}$ for HSAT. The addition of the post adjacent to the fixed-tilt pyranometers further improves the MAE by 0.18 $\mathrm{W/m^2}$.

DUET's bifacial energy yield with the NOCT module temperature model shows an MBE of −146 Wh and −98 Wh for fixed-tilt and HSAT, respectively [see Fig. 9(b)]. This underestimation is partly due to module temperature overestimation, since accounting for wind cooling in the Faiman and Sandia models decreases the MBE magnitude by 18.3 and 53.0 Wh, respectively. The resulting MAE falls within 370–388 Wh (14.2–15.0 mW/Wp) for all three temperature models in fixed-tilt and 450–477 Wh (17.3–18.3 mW/Wp) in HSAT. When DUET's modeled energy yield error is calculated using measured data without the 5-min correction outlined in Section III-A, the resulting MAEs are lower than those reported for the six models in [1] by 23–107 Wh for fixed-tilt and 29–90 Wh for HSAT. The 5-min correction reduces DUET's MAE by 86 and 10.5 Wh, respectively. If we assume a similar corrective behavior for all models, DUET performs with lowest cumulative absolute error across all timestamps for both systems.

V. Conclusion

This article has presented a technical description of a new bifacial PV performance software, DUET, including a mathematical representation of optical and electrical numerical models. The novel shading algorithm combines a 3-D VF model with ray-object intersection to capture the effect of supportive structure shading, and the *IV* curve summation flexibly represents intra- and intermodule wiring and electrical mismatch loss between cells, modules, and module strings.

A validation against measured data from Denmark [22] shows that DUET predicts bifacial energy yield at −1.56% of measured yield for a fixed-tilt row over 3370 daylight hours and at −0.72% of measured yield for a HSAT row over 2731 daylight hours. The resulting MAE in bifacial power across the simulated daylight hours is 14.2–15.0 mW/Wp for fixed-tilt and 17.3–18.3 mW/Wp for HSAT, depending on the module temperature model. DUET's electrical model captures current mismatch due to irradiance nonuniformity, including partial direct beam shading during periods of low sun elevation in the fixed-tilt system. 2-D rear irradiance profiles also display nonuniformity caused by supportive racking that cannot be captured in a cross-sectional sample of module irradiance. For the subset of hours in which

TABLE I
List of Symbols

G_{H}	Global horizontal irradiance	$\mathrm{W/m^2}$
G_{B}	Direct normal (beam) irradiance	$\mathrm{W/m^2}$
G_{D}	Diffuse horizontal irradiance	$\mathrm{W/m^2}$
ρ	Albedo	unitless
N_{S}	Number of (No.) sky patches	unitless
N_{G}	No. ground patches	unitless
N_{M}	No. module patches per cell	unitless
e	Emitting source	-
i	Irradiated patch	-
$\delta_{e,i}$	Shading factor between e and i	unitless
$\theta_{e,i}$	Angle of incidence between e and i	°
$\Omega_{e,i}$	Solid angle between e and i	sr
c	Cell number	-
m	Module patch number	-
s	Sky patch number	-
g	Ground patch number	-
$P_{c,\mathrm{f}}$	Optical power on front of cell c	W
$P_{c,\mathrm{r}}$	Optical power on rear of cell c	W
A_m	Area of module patch m	$\mathrm{m^2}$
$G_{m,\mathrm{r}}$	Effective irradiance on rear of module patch m, including reflection losses	$\mathrm{W/m^2}$
G_m^{B}	Direct beam effective irradiance on module patch m, including reflection losses	$\mathrm{W/m^2}$
G_m^{D}	Diffuse effective irradiance on module patch m, including reflection losses	$\mathrm{W/m^2}$
G_m^{R}	Ground-reflected effective irradiance on module patch m, including reflection losses	$\mathrm{W/m^2}$
$G_{c,\mathrm{f}}$	Average irradiance on front of cell c neglecting reflection losses	$\mathrm{W/m^2}$
$G_{c,\mathrm{r}}$	Average irradiance on rear of cell c neglecting reflection losses	$\mathrm{W/m^2}$
G_c	Total average irradiance incident on both sides of cell c neglecting reflection losses	$\mathrm{W/m^2}$
L_s	Radiance of sky patch s	$\mathrm{W/m^2/sr}$
G_g	Irradiance incident on ground patch g	$\mathrm{W/m^2}$
Z	Sun zenith	°
$\Re$	Cell responsivity at STC	A/W
φ	Current bifaciality constant	unitless
$I_{\mathrm{sc},c}$	Short circuit current of cell c	A
I_c	Current of cell c	A
V_c	Voltage of cell c	V
q	Elementary charge	C
k	Boltzmann's constant	J/°C
n	Cell ideality factor at STC	unitless
I_0	Cell saturation current at STC	A
R_{sh}	Cell shunt resistance at STC	Ω
R_{s}	Cell shunt resistance at STC	Ω
T_{a}	Ambient temperature	°C
μ_{I}	Current temperature coefficient	%/°C
T_{STC}	Temperature at standard test condition	°C
T_c	Temperature of c	°C
w_M	Weighting coefficient of M'th module *IV*	No. modules
w_S	Weighting coefficient of S'th module string *IV*	No. strings

TABLE II
ADDITIONAL USER-DEFINED INPUTS

	Input	Unit or Option
Geo	Longitude	° (E>0)
	Latitude	° (N>0)
	Time zone	from UTC (E>0)
Array	Number of (No.) rows	-
	Pitch (row spacing)	m
	Array azimuth	° (S=0; E>0)
Table	Location of module	row, tier, column of the array
	Module orientation	portrait, landscape
	Torque tube shape	cylinder, rectangular prism
	Torque tube dimensions	m (radius or cross-sectional edges)
	Purlin shape, dimensions	rectangular prism, polygons ; m
	Pile shape	cylinder, rectangular prism
	Pile position, dimensions	m
	Tracker angle bounds	°, e.g. ±60
	Backtracking	on, off
Module	Cell type	full, half-cut, multi-cut
	Cell shape, dimensions	pseudo-square, rectangle; m
	Cell material bandgap	eV (e.g., 1.121 for Si)
	Bandgap temp. coeff.	%/°C
	No. cells, bypass diodes (BD)	-
	No. cell strings per BD	-
	Cell gap, margins	m (between cells, from edges)
	Incidence angle modifier	polynomial, ASHRAE [47]
	Module frame dimensions	m

*UTC = Coordinated Universal Time; temp. coeff. = temperature coefficient.

rear irradiance measurements were provided, the modeled irradiance at the location of two rear-facing pyranometers matches the measured data within 2.8 $\mathrm{W/m^2}$ for the fixed-tilt row and 3.7 $\mathrm{W/m^2}$ for the HSAT row—among the lowest errors reported for other software tested at this site in [1].

This article shows that DUET's shading algorithm performs with similar accuracy to other bifacial performance models—including a ray tracing model—while minimizing computational cost through deterministic ray-object intersections. With this approach, DUET provides computationally efficient bifacial performance modeling with geographic, temporal, and structural specificity—without reliance on estimated shading and electrical mismatch loss factors. The software can also be used to acquire, and better understand, such loss factors for use in other performance models or in system design optimization.

ACKNOWLEDGMENT

The authors would like to thank Henry P. Schriemer and Chu Tu Li for original concept work and early discussions, Nicholas Riedel-Lyngskær for correspondence regarding the Roskilde dataset, and Jill Tymchak for help with early validation. The University of Ottawa is on unceded Algonquin Territory. They recognize Indigenous self-determination as central to addressing climate change.

APPENDIX

A. Computation Time and Modeled Data

The HSAT annual energy yield calculations herein required 3.75 core-hours per module on a 3.9 GHz CPU. In general, DUET's computation time strongly depends on tracking type, patching resolution, size of array, and number of shading elements. Considerable speed improvements are expected through ongoing code refinements and improved algorithms.

The modeling results presented in this article are available for download in [64].

REFERENCES

[1] N. Riedel-lyngskaer et al., "Validation of bifacial photovoltaic simulation software against monitoring data from large-scale single-axis trackers and fixed tilt systems in Denmark," *Appl. Sci.*, vol. 10, no. 23, pp. 1–29, 2020.
[2] C. D. Rodríguez-Gallegos et al., "Global techno-economic performance of bifacial and tracking photovoltaic systems," *Joule*, vol. 4, pp. 1–28, 2020.
[3] R. Kopecek and J. Libal, "Towards large-scale deployment of bifacial photovoltaics," *Nature Energy*, vol. 3, no. 6, pp. 443–446, 2018.
[4] A. Asgharzadeh et al., "A sensitivity study of the impact of installation parameters and system configuration on the performance of bifacial PV arrays," *IEEE J. Photovolt.*, vol. 8, no. 3, pp. 798–805, May 2018.
[5] J. R. Ledesma et al., "A simulation model of the irradiation and energy yield of large bifacial photovoltaic plants," *Sol. Energy*, vol. 206, pp. 522–538, 2020. [Online]. Available: https://doi.org/10.1016/j.solener.2020.05.108
[6] B. Marion et al., "A practical irradiance model for bifacial PV modules," in *Proc. IEEE 44th Photovolt. Specialists Conf.*, 2017, pp. 1537–1542.
[7] M. A. Anoma et al., "View factor model and validation for bifacial pv and diffuse shade on single-axis trackers," in *Proc. IEEE 44th Photovolt. Specialist Conf.*, 2018, pp. 1549–1554.
[8] D. Berrian and J. Libal, "A comparison of ray tracing and view factor simulations of locally resolved rear irradiance with the experimental values," *Prog. Photovolt., Res. Appl.*, vol. 28, no. 6, pp. 609–620, 2020.
[9] S. A. Pelaez, C. Deline, P. Greenberg, J. S. Stein, and R. K. Kostuk, "Model and validation of single-axis tracking with bifacial PV," *IEEE J. Photovolt.*, vol. 9, no. 3, pp. 715–721, May 2019.
[10] K. R. McIntosh et al., "Simulation and measurement of monofacial and bifacial modules in a 1D tracking system," in *Proc. Conf. Rec. IEEE Photovolt. Specialists Conf.*, 2020, pp. 0366–0370.
[11] C. K. Lo, Y. S. Lim, and F. A. Rahman, "New integrated simulation tool for the optimum design of bifacial solar panel with reflectors on a specific site," *Renewable Energy*, vol. 81, pp. 293–307, 2015. [Online]. Available: http://dx.doi.org/10.1016/j.renene.2015.03.047
[12] J. S. Stein et al., "Bifacial PV modules & systems: Experience and results from international research and pilot applications. international energy agency photovoltaic power systems programme," 2021. [Online]. Available: https://iea-pvps.org/wp-content/uploads/2021/04/IEA-PVPS-T13-14_2021-Bifacial-Photovoltaic-Modules-and-Systems-report.pdf
[13] A. Driesse and N. Patel, "Cross-validation of PV system simulation software," in *Proc. 35th Eur. Photovolt. Sol. Energy Conf. Exhib.*, 2019, pp. 9–13.
[14] M. Chiodetti, J. Kang, C. Reise, and A. Lindsa, "Predicting yields of bifacial PV power plants – what accuracy Is possible?," in *Proc. 35th Eur. Photovoltaic Sol. Energy Conf. Exhib.*, 2018, pp. 1623–1629. [Online]. Available: https://www.eupvsec-proceedings.com/proceedings?paper=45942
[15] A. Asgharzadeh et al., "A benchmark and validation of bifacial PV irradiance models," in *Proc. IEEE 46th Photovolt. Specialists Conf.*, 2019, pp. 3281–3287.
[16] T. Capelle, F. Araya, F. Haffner, J. Sayritupac, and H. Colin, "A comparison of bifacial PV system modelling tools," in *6th BifiPV Workshop. Amsterdam: INES France*, 2019. [Online]. Available: http://npv-workshop.com/fileadmin/layout/images/bifiPV/presentations2019/bifiPV2019-CEA_INES_Capelle.pdf
[17] C. Zhao, J. Xiao, Y. Yu, and J.-N. Jaubert, "Accurate shading factor and mismatch loss analysis of bifacial HSAT systems through ray-tracing modeling," *Sol. Energy Adv.*, vol. 1, 2021, Art. no. 100004. [Online]. Available: https://doi.org/10.1016/j.seja.2021.100004
[18] M. Ernst, G. E. Conechado, and C.-A. Asselineau, "Accelerating the simulation of annual bifacial illumination of real photovoltaic systems with ray tracing," *iScience*, vol. 25, no. 1, 2021, Art. no. 103698. [Online]. Available: https://doi.org/10.1016/j.isci.2021.103698
[19] H. Nussbaumer et al., "Accuracy of simulated data for bifacial systems with varying tilt angles and share of diffuse radiation," *Sol. Energy*, vol. 197, 2019, pp. 6–21, 2020. [Online]. Available: https://doi.org/10.1016/j.solener.2019.12.071
[20] S. Ayala Peláez, "BEST field data—data and resources," 2021. [Online]. Available: https://datahub.duramat.org/dataset/best-field-data

[21] S. Ayala Pelaez, C. Deline, S. M. MacAlpine, and W. Marion, "Bifacial PV test-bed irradiance measurements," 2019. [Online]. Available: https://data.nrel.gov/submissions/125
[22] N. Riedel et al., "Data used in "validation of bifacial photovoltaic simulation software against monitoring data from large-scale single-axis trackers and fixed tilt systems in Denmark," 2021. [Online]. Available: https://doi.org/10.11583/DTU.13580759.v3
[23] S. A. Pelaez et al., "Comparison of bifacial solar irradiance model predictions with field validation," *IEEE J. Photovolt.*, vol. 9, no. 1, pp. 82–87, Jan. 2019.
[24] D. Berrian, J. Libal, M. Klenk, H. Nussbaumer, and R. Kopecek, "Performance of bifacial PV arrays with fixed tilt and horizontal single-axis tracking: Comparison of simulated and measured data," *IEEE J. Photovolt.*, vol. 9, no. 6, pp. 1583–1589, Nov. 2019.
[25] O. A. Katsikogiannis, H. Ziar, and O. Isabella, "Integration of bifacial photovoltaics in agrivoltaic systems: A synergistic design approach," *Appl. Energy*, vol. 309, no. Dec. 2021, Art. no. 118475. [Online]. Available: https://doi.org/10.1016/j.apenergy.2021.118475
[26] M. F. Cohen, D. P. Greenberg, D. S. Immel, and P. J. Brock, "An efficient radiosity approach for realistic image synthesis," *IEEE Comput. Graph. Appl.*, vol. 6, no. 3, pp. 26–35, Mar. 1986.
[27] M. A. Mikofski, R. Darawali, M. Hamer, A. Neubert, and J. Newmiller, "Bifacial performance modeling in large arrays," in *Proc. Conf. Rec. IEEE Photovolt. Specialists Conf.*, 2019, pp. 1282–1287.
[28] C. D. Rodríguez-Gallegos et al., "Monofacial vs bifacial Si-based PV modules: Which one is more cost-effective?," *Sol. Energy*, vol. 176, pp. 412–438, 2018. [Online]. Available: https://doi.org/10.1016/j.solener.2018.10.012
[29] M. Rouholamini, L. Chen, and C. Wang, "Modeling, configuration, and grid integration analysis of bifacial PV arrays," *IEEE Trans. Sustain. Energy*, vol. 12, no. 2, pp. 1242–1255, Apr. 2021.
[30] P. Gilman et al., "SAM PV model technical reference update," Nat. Renewable Energy Lab., Golden, CO, USA, Tech. Rep. NREL/TP-6A20-67399, 2018.
[31] Plant Predict Resource Centre, "Bifacial Modules," 2021. [Online]. Available: https://plantpredict.com/algorithm/irradiance-radiation/679-2/
[32] B. Wittmer, "Simulating bifacial fixed tilt and tracking systems with PVsyst," in *PV Mag. Webinar*, 2019. [Online]. Available: https://www.pvmagazine.com/webinars/pv-magazine-webinar-optimizing-bifacial-gain-and-balancinginvestment-costs/
[33] W. Gu, T. Ma, M. Li, L. Shen, and Y. Zhang, "A coupled optical-electrical-thermal model of the bifacial photovoltaic module," *Appl. Energy*, vol. 258, 2020, Art. no. 114075. [Online]. Available: https://doi.org/10.1016/j.apenergy.2019.114075
[34] K. R. McIntosh, M. D. Abbott, and B. A. Sudbury, "How the PVSyst inputs for bifacial systems depend on conditions," in *Proc. 7th bifiPV (virtual)*, 2020. [Online]. Available: https://www.dropbox.com/s/o4cx2xk3slastgl/T6A.-Keith.pdf?dl=0
[35] A. Burgers and B. van Aken, "BIGEYE–Simulation under shadow conditions," in *BifiPV Workshop*, Amsterdam, The Netherlands. 2019. [Online]. Available: http://npv-workshop.com/fileadmin/layout/images/bifiPV/presentations2019/bifiPV2019-_TNO_ECN_-_Burgers.pdf
[36] E. Barros, B. Van Aken, A. Burgers, L. Slooff-Hoek, and R. Fonseca, "Multi-objective optimization of solar park design under climatic uncertainty," *Sol. Energy*, vol. 231, pp. 958–969, 2022. [Online]. Available: https://doi.org/10.1016/j.solener.2021.12.026
[37] U. A. Yusufoglu et al., "Simulation of energy production by bifacial modules with revision of ground reflection," *Energy Procedia*, vol. 55, pp. 389–395, 2014. [Online]. Available: http://dx.doi.org/10.1016/j.egypro.2014.08.111
[38] D. Chudinzow, J. Haas, G. Díaz-Ferrán, S. Moreno-Leiva, and L. Eltrop, "Simulating the energy yield of a bifacial photovoltaic power plant," *Sol. Energy*, vol. 183, pp. 812–822, 2019. [Online]. Available: https://doi.org/10.1016/j.solener.2019.03.071
[39] M. R. Lewis et al., "Impact of air mass on energy yield calculation for bifacial silicon heterojunction photovoltaic modules in high-latitude conditions," in *Proc. Conf. Rec. IEEE Photovolt. Specialists Conf.*, 2020, pp. 0371–0375.
[40] C. E. Valdivia et al., "Bifacial photovoltaic module energy yield calculation and analysis," in *Proc. IEEE 44th Photovolt. Specialists Conf.*, 2017, pp. 1094–1099.
[41] C. T. Li, "Development of field scenario ray tracing software for the analysis of bifacial photovoltaic solar panel performance," Univ. Ottawa, Ottawa, ON, Canada, 2016. [Online]. Available: http://www.ruor.uottawa.ca/handle/10393/35523
[42] T. Moller and E. Haines, "Ray/Box Intersection - Intersection Test Methods," in *Real-Time Rendering*, 2nd ed. Natick, MA, USA: AK Peters/CRC Press, 2002, pp. 572–578.
[43] A. Williams, S. Barrus, R. K. Morley, and P. Shirley, "An efficient and robust ray-box intersection algorithm," *J. Graph. Tools*, vol. 10, no. 1, pp. 49–54, 2005.
[44] D. Sunday, "Line segment and convex polygon intersection," in *Practical Geometric Algorithms With C Code*, 2021. [Online]. Available: www.geomalgorithms.com/
[45] D. Sunday, "dist3D_Segment_to_Segment," in *Practical geometric algorithms with c code*, 2021. [Online]. Available: https://www.geomalgorithms.com/
[46] P. Shirley, "Global Illumination," in *Fundamentals of Computer Graphics*, 1st ed. Wellesley, MA, USA: A. K. Peters, 2005, ch. 23, pp. 551–560.
[47] A. F. Souka and H. H. Safwat, "Determination of the optimum orientations for the double-exposure, flat-plate collector and its reflectors," *Sol. Energy*, vol. 10, no. 4, pp. 170–174, 1966.
[48] I. Reda and A. Andreas, "Solar position algorithm for solar radiation applications (revised)," Nat. Renewable Energy Lab., Golde, CO, USA, Tech. Rep. NREL/TP-560-34302, 2005. [Online]. Available: https://www.nrel.gov/docs/fy08osti/34302.pdf
[49] E. Lorenzo, L. Narvarte, and J. Muñoz, "Tracking and back-tracking," *Prog. Photovolt., Res. Appl.*, vol. 19, no. 6, pp. 747–753, 2011.
[50] R. Perez, R. Seals, and J. Michalsky, "All-weather model for sky luminance distribution-preliminary configuration and validation," *Sol. Energy*, vol. 50, no. 3, pp. 235–245, 1993.
[51] K. A. Klise, C. W. Hansen, and J. S. Stein, "Dependence on geographic location of air mass modifiers for photovoltaic module performance models," in *Proc. IEEE 42nd Photovolt. Specialist Conf.*, 2015, pp. 1–5.
[52] E. M. Tonita et al., "Effect of air mass on carrier losses in bifacial silicon heterojunction solar cells," *Sol. Energy Mater. Sol. Cells*, vol. 230, 2021, Art. no. 111293. [Online]. Available: https://doi.org/10.1016/j.solmat.2021.111293
[53] N. Riedel-Lyngskær et al., "The effect of spectral albedo in bifacial photovoltaic performance," *Sol. Energy*, vol. 231, no. 2021, pp. 921–935, 2022.
[54] M. R. Lewis, "Performance of silicon heterojunction cells and modules in arctic applications: Impact of angle of incidence, Air Mass, and Spectra on Energy Yield," Univ. Ottawa, 2020. [Online]. Available: https://ruor.uottawa.ca/handle/10393/41164
[55] G. M. Masters, "Temperature-related PV derating," in *Renewable Efficient Electric Power Syst.*, 2nd ed. Piscataway, NJ, USA: Wiley, 2013, ch. 6.3.2, pp. 327–330.
[56] D. Faiman, "Assessing the outdoor operating temperature of photovoltaic modules," *Prog. Photovolt., Res. Appl.*, vol. 16, no. 1, pp. 307–315, 2008. [Online]. Available: https://doi.org/10.1002/pip.813
[57] D. L. King, J. a. Kratochvil, and W. E. Boyson, "Photovoltaic array performance model," *Online*, vol. 8, pp. 1–19, 2004. [Online]. Available: http://mauisolarsoftware.com/MSESC/PerfModel2003.pdf
[58] J. L. Gray, "The physics of the solar cell," in *Handbook of Photovoltaic Science and Engineering*,, 2nd ed., A. Luque and S. Hegedus, Eds. Hoboken, NJ, USA: Wiley, 2011, ch. 3.
[59] W. De Soto, S. A. Klein, and W. A. Beckman, "Improvement and validation of a model for photovoltaic array performance," *Sol. Energy*, vol. 80, no. 1, pp. 78–88, 2006.
[60] SunPower, "PVMismatch v4.1 Documentation," 2017. [Online]. Available: https://sunpower.github.io/PVMismatch/
[61] A. Mermoud and B. Wittmer, "Yield simulations for horizontal axis trackers with bifacial PV modules in PVsyst," in *Proc. 35th Eur. Photovoltaic Sol. Energy Conf.*, 2018, pp. 1929–1934. [Online]. Available: 10.4229/35thEUPVSEC 20182018--6CV.2.19
[62] Trina Solar"DUOMAX Twin 295-310 W," TSM-DEG5C.20(II), 2018.
[63] J. G. Pérez and J. N. Berbel, "BiTEC : How to simulate bifacial projects?," Soltec, Tech. Rep. BiTEC Results 2 - Fall 2018 . Winter 2019, 2019. [Online]. Available: https://lab.soltec.com/bifacial-trackers-ii/
[64] A. C. J. Russell, C. E. Valdivia, C. Bohémier, J. E. Haysom, and K. Hinzer, "Modelled data in "DUET: A novel energy yield model with 3D shading for bifacial photovoltaics systems," 2022. [Online]. Available: https://doi.org/10.5683/SP3/HLZ6JG

3.2 Details on simulated environment

3.2.1 Sky, ground and module meshing

As discussed in Section 3.1.II.A, the DUET v.uO-2024 algorithm meshes the module, sky and ground surfaces into patches of finite area, or finite *elements*. The area of each sky element, shown in the left of Fig. 3.1, is:

$$A_s = \frac{2\pi(\cos Z_{s,\mathrm{U}} - \cos Z_{s,\mathrm{L}})}{N_{\varphi_\mathrm{s}}}, \tag{47}$$

which describes the difference of the area of two spherical caps described by the lower and upper zenith angles of the sky element, $Z_{s,\mathrm{L}}$ and $Z_{s,\mathrm{U}}$ respectively, divided by the number of sky azimuth divisions N_{φ_s}. The upper and lower zenith angles of each sky element band are currently defined by an equal division of the 90° between the sky dome center, or *sky zenith*, and the horizon by a specified number of elevation divisions. This results in a concentration of sky elements toward the center of the dome. Future work should include testing other sky dome meshing schemes, including the Becker scheme which generates mesh elements of equal solid angle [141] or a sun path dependent meshing [142]. The model's coupling and shading algorithms would allow for any such substitution as long as sky elements are defined by their area and central point.

As shown in the right of Fig. 3.1, the area of each ground element is:

$$A_g = \frac{\pi(r_{g,\mathrm{O}}^2 - r_{g,\mathrm{I}}^2)}{N_{\varphi_\mathrm{G}}} \tag{48}$$

where $r_{g,\mathrm{O}}$ and $r_{g,\mathrm{I}}$ are the outer and inner radii of the ground element and N_{φ_G} is the number of ground azimuth divisions. The outer and inner radii of each element is currently calculated such that each ground element represents an equal solid angle with respect to the module for a user-specified number of radial divisions across the modelled ground surface. Future work should consider alternate meshing including triangular meshing which may improve computational efficiency since irradiance at central points in each triangle could be interpolated from fewer shared vertices. The ground coupling and shading algorithms would allow for any substituted meshing scheme that defines element area and central points.

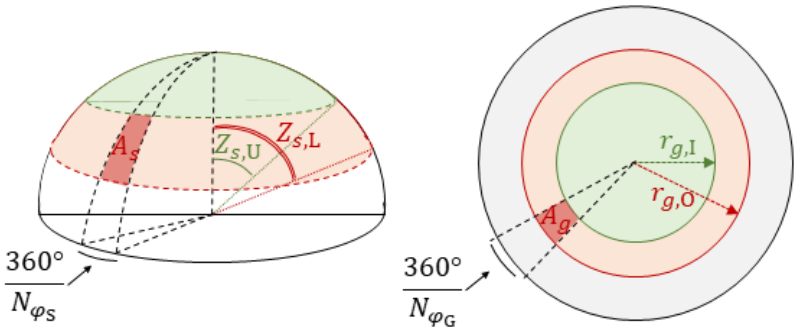


Figure 3.1: (Left) Side view of diffuse sky dome mesh element with area A_s, bound by upper and lower zenith angles $Z_{s,\text{U/L}}$ with an azimuthal angular range defined by the number of azimuthal sky mesh divisions N_{φ_S}; (Right) Birdseye view of ground mesh element with area A_g, bound by inner and outer radial dimensions $r_{g,\text{I/O}}$ with an azimuthal angular range defined by the number of azimuthal ground mesh divisions N_{φ_G}

The impact of mesh density on computation time and accuracy is described in Section 3.6.3. Compensation factors to account for low density meshes are described in Section 3.3.2.

3.2.2 Defining primitives

As shown in Fig. 3 in Section 3.1, basic shapes and volumes, or *primitives*, form the array shading elements in the 3D scene. Fig. 3.2.2 describes how these primitives themselves are defined.

Rectangular prisms are defined by a central coordinate, b_c, three unit vectors $\vec{u}'\vec{v}'\vec{w}'$ along body-fixed axes $X'Y'Z'$, and a half length along each unit vector dictating the dimensions, $h_{u,v,w}$. N-vertex **polygons** are defined by a set of corner coordinates, $P_{0-(N-1)}$, and a normal vector $\vec{n}$. **Cylinders** are defined by the start and end coordinates, c_0 and c_1, of the line segment delineating their central axis $\vec{c}$ and a radius r_c.

All primitives also have an associated transparency, α, from 0-1. The radiation assigned to any ray intersecting a primitive is attenuated by the primitive's transparency factor. **Rays** are described by an origin d_0 and direction vector $\vec{d}$ or as a line segment with two end coordinates and a defined length.

3.2.3 Rotation matrices

To generate the 3D coordinates of the objects in the PV array, the model uses Tait-Bryan rotation matrices [128] to orient primitives within the scene space as in Fig. 2.14. For example, the

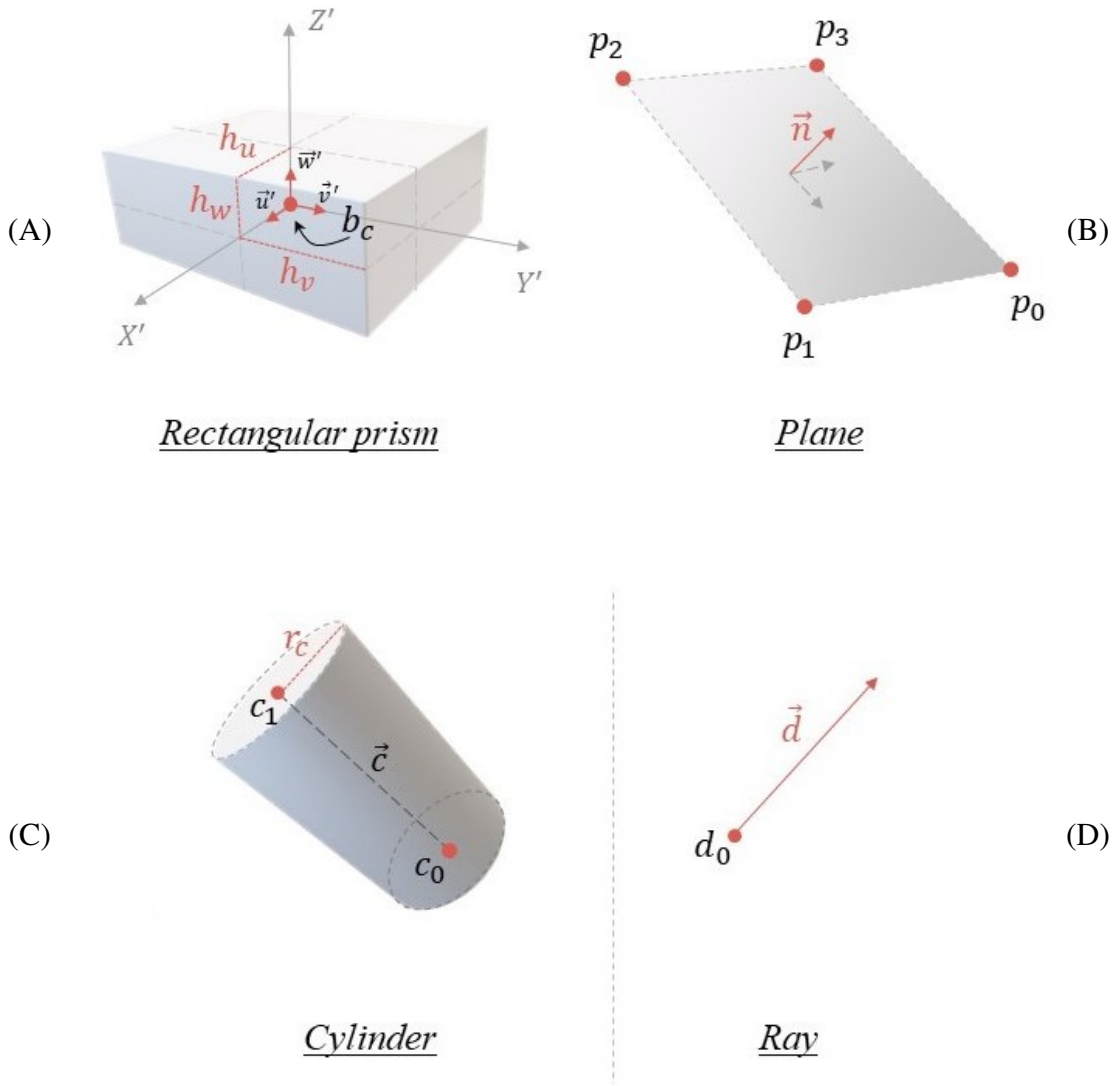


Figure 3.2: (A) Rectangular prism with central coordinate, b_c, three unit vectors $\vec{u}'\vec{v}'\vec{w}'$ along body-fixed axes $X'Y'Z'$, and half length dimensions $h_{u,v,w}$. (B) N-vertex polygons with corners $P_{0-(N-1)}$, and normal $\vec{n}$. (C) Cylinders with the start and end coordinates, c_0 and c_1, central axis $\vec{c}$ and a radius r_c. (D) Ray with origin d_0 and direction and length $\vec{d}$

.

plane-of-array tilt angle (β_{m}), azimuth angle (φ_{m}), and roll angle (γ_{m}) result in the rotation matrix $R(\beta_{\mathrm{m}}, \gamma_{\mathrm{m}}, \varphi_{\mathrm{m}})$ which aligns any dynamic primitives with the plane-of-array in single-axis tracking. The base version of the model described in this thesis assumes that all tables within the array have the same tilt, azimuth, and roll angles; this assumption holds for flat terrain.

3.3 Details on optical model

3.3.1 Finite element method

While Section 3.1 refers to DUET as a 3D view factor model, true 3D VF models use view factor algebra to calculate shading between objects and analytical view factors to calculate radiation transfer. Instead, DUET applies the finite element method (see Section 2.2.3) to approximate 3D view factors between irradiance sources and surfaces in the scene. Eq. 3-4 and 7-8 in Section 3.1 take the form of the finite element coupling coeffients described in Eq. (40) in Section 2.2.3 to quantify irradiance transfer between the sky and the panel, the sky and the ground, and the ground and the module. Of note, sky elements are assumed to be at an infinite distance from the ground and module with surfaces perpendicular to the ray $d_{s,g/m}$ with the angle of emission $\theta_{g/m,s} = 0$.

The finite element approach opens up the use of a deterministic ray-object intersection algorithm to account for shading due to overlapping objects within the PV array - a phenomena that view factor algebra inherently neglects. The combination of the finite element method with the ray-object shading approach also facilitates the vectorization of associated code as discussed in Section 3.6, improving computational efficiency. However, the accuracy of the finite element method scales with mesh density, and high-density simulations require prohibitive computation times. Section 3.6.3 demonstrates that an optimal setting must be found such that any reduction in computation time through reduced meshing density has minimal effect on energy yield results. The compensation algorithm described in Section 3.3.2 also helps mitigate the need for high density ground mesh.

3.3.2 Compensation algorithms

To maintain both the shading accuracy afforded by spatially discretizing the surface and the computational efficiency afforded by coarser surface meshing, the model described in this thesis uses

Li's compensation factors [1] to account for the discrepancy between the finite element and view factor approaches. (see Section 2.2.3). These factors are applied in two radiation exchanges: (1) between the sky and ground, and (2) between the ground and the module under investigation. For example, the irradiance incident on the g'th ground mesh element from the diffuse sky dome is:

$$G_g^{\mathrm{D}} = \sum_{s=1}^{N_{\mathrm{S}}} L_s \cdot C_{s,g} \cdot \chi_{\mathrm{S},g} \cdot \delta_{s,g} \tag{49}$$

where $C_{s,g}$ is the coupling coefficient between the s'th sky element and the g'th ground element and $\chi_{\mathrm{S},g}$ is the *sky-to-ground compensation factor* between the diffuse sky dome and the the g'th ground element. Analogously, $\chi_{\mathrm{G},m}$ is the *ground-to-module compensation factor* between the reflecting ground surface and the the m'th module element.

The remainder of this section demonstrates how these two compensation factors vary with tilt angle for a range of sky and ground mesh densities and for a range of radial distances to which the ground surface extends. An additional compensation factor between the sky dome and the module is also examined.

Sky to ground As shown in Figure 3.3, the base mesh density of the sky dome - consisting of 18 azimuthal divisions and 10 elevation divisions - slightly overestimates the theoretical sky-to-ground view factor, resulting in a $\chi_{\mathrm{S},g}$ of -0.2%. Increasing the elevation divisions by two fold to 20 divisions brings this compensation factor to near 1, as seen in the dark green line with triangular markers. Without the compensation factor, users must choose between tolerating the additional computation time required to double the sky elevation divisions or the additional 0.2% deviation from theoretical VF. (See Section 3.6.3 for more discussion on mesh density and run time). Using the compensation factor affords the option to keep the base sky mesh density the same while scaling the coupling factors from all sky elements by an equal 0.2%.

Applying an equal compensation factor to all sky element radiances assumes that all sky elements contribute equally to the deviation from the view factor. In reality, DUET v.uO-2024's sky meshing scheme concentrates sky elements near the top of the dome where the central point is more representative of the full element area than for the larger area elements at the base of the dome. Thus, an equal compensation factor may be unnecessarily dampening irradiance from higher parts

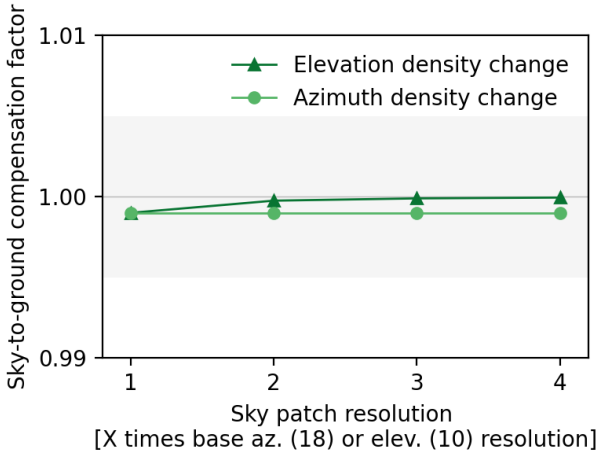


Figure 3.3: Sky-to-ground compensation factor vs. sky element resolution for changing elevation (elev.) and azimuth (az.) mesh density. Mesh density is normalized by the base density: 18 azimuth, 10 elevation.

of the sky. Future work should examine whether meshing schemes that provide equal solid angles per sky element would alleviate the need for this compensation factor, or whether a compensation factor for a subset of elevation tiers may be more appropriate.

Ground to module To examine the impact of ground meshing parameters on the ground-to-module compensation factor, we can look at the average $\chi_{\mathrm{G},m}$ across all N_{M} module elements, $\bar{\chi}_{\mathrm{G},m}$, for each tilt angle within a typical single axis tracking range. The following paragraphs discuss such an analysis for a single Eastern module in a 2P system with 5 rows and three tables of 21 modules per row. The module under investigation, centered in the array, is closest to the ground during the positive angles in the morning and farthest during the negative angles after noon. Around noon, the modules are almost flat with little or no view of the ground from the front and a full view of the ground on the rear. Compensation factors closer to 1 indicate that the finite element approaches the approximation of the view factor.

Figure 3.4 shows $\bar{\chi}_{\mathrm{G},m}$ for changing azimuth density with a stable 20 radial divisions and a last near-field ground element 10 m away from the least central edge of the array. Figure 3.5 shows $\bar{\chi}_{\mathrm{G},m}$ for changing radial division with a stable 18 azimuthal divisions and a last near-field ground element 10 m away from the least central edge of the array. Figure 3.6 shows the impact of changing both azimuthal and radial divisions (each by X-fold) while maintaining a last near-field ground element 10 m away from the least central edge of the array. Finally, Fig. 3.7 shows the

impact of changing the *ground extent*, or the radial distance between least central edge of the array and the last near-field ground element. All cases in this last figure use 36 azimuth and 200 radial divisions to reduce ringing and isolate the effect of the ground extent.

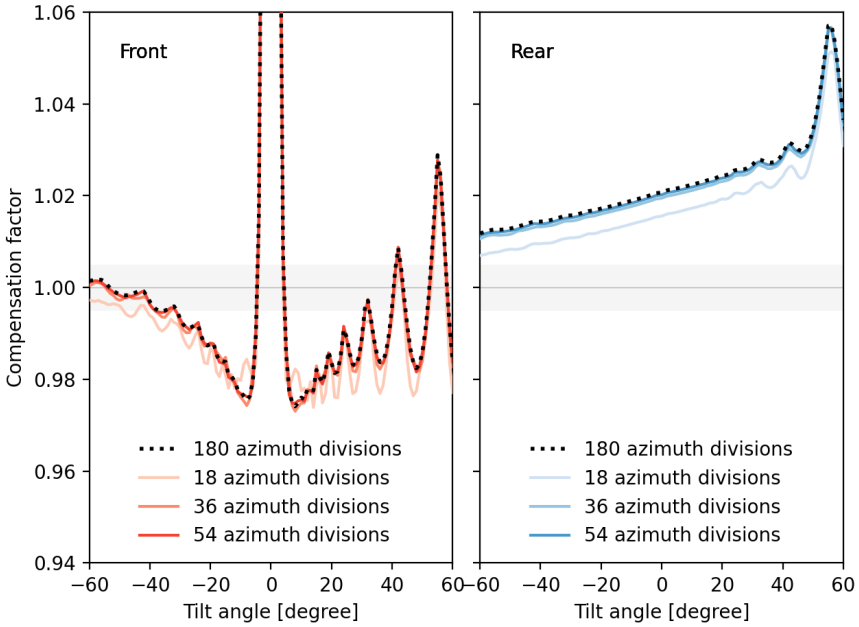


Figure 3.4: Front (left) and rear (right) ground-to-module compensation factor vs. tilt angle for varied azimuth mesh densities. Grey region is ±0.5%.

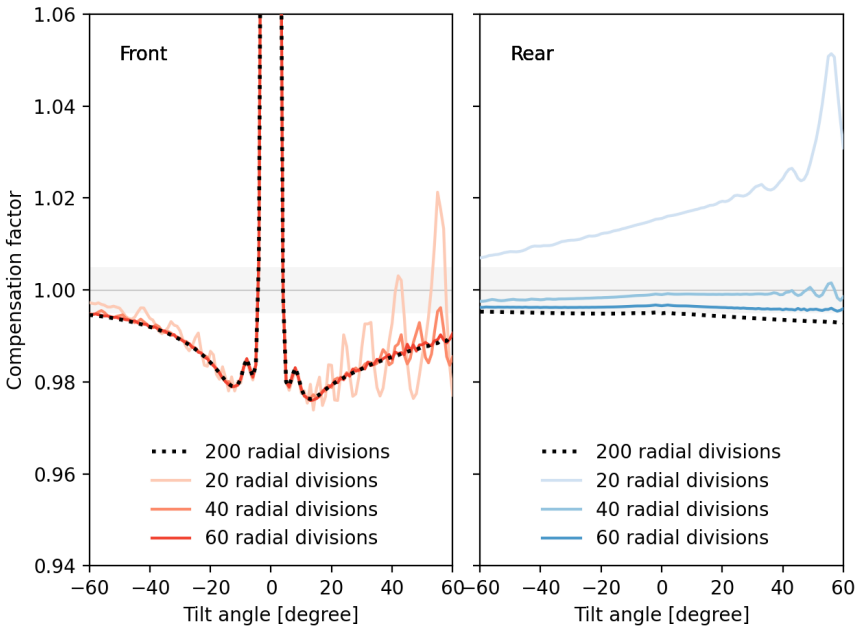


Figure 3.5: Front (left) and rear (right) ground-to-module compensation factor vs. tilt angle for varied radial mesh densities. Grey region is ±0.5%.

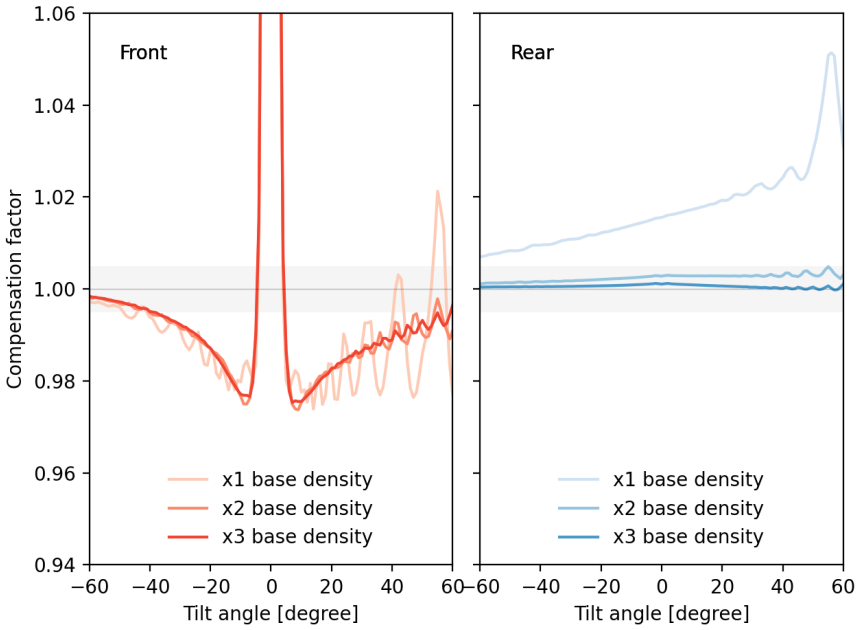


Figure 3.6: Front (left) and rear (right) ground-to-module compensation factor vs. tilt angle for varied ground mesh densities. E.g. 2x base density = 2(18), 2(20) = 36x40 ground mesh. Grey region is ±0.5%.

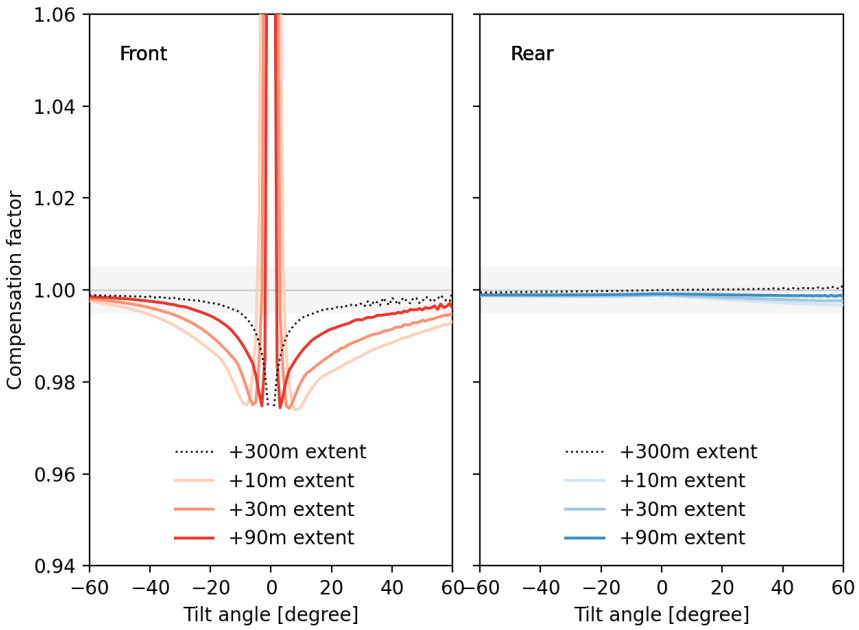


Figure 3.7: Front (left) and rear (right) ground-to-module compensation factor vs. tilt angle for varied ground surface extents. Grey region is ±0.5%.

Examining these figures, we can see that the radial mesh density has most significant impact on the discrepancy between finite element summation and the view factor. Doubling the base radial density to 40 in Fig. 3.5 brings the rear compensation factor within ±0.5% (shaded in grey) and collapses the front compensation factor to the high density case (dotted black) for most angles, which reduces the ringing. In contrast, doubling the azimuthal density does not bring the rear compensation factor within ±0.5% and does not mitigate the front-side ringing. It is interesting to note that increasing azimuthal density converges to a compensation factor greater than 1 (Fig. 3.4, dotted black), whereas increasing radial density converges to a compensation factor lower than 1 (Fig. 3.5, dotted black). When both the radial and azimuthal densities are increased by integer factors, as in Fig. 3.6, the rear compensation factor for 3x the base mesh divisions in both dimensions approaches 1, with the azimuthal and radial contributions from to the compensation factor appearing to cancel out.

Considering each dimension sequentially, we can also see that rear high density azimuth case (Fig. 3.4, dotted black) saturates at a magnitude that is only mitigated by increasing radial divisions in Fig. 3.5. Similarly, the rear high density radial case saturates at a magnitude below 1 that is only drawn closer to 1 by increasing the ground extent in Fig. 3.7.

The effect of ground extent is particularly clear for the front compensation factor which collapses to the same shape and magnitude with both high radial density and high combined azimuthal and radial densities but does not reduce in magnitude without increasing the ground extent. In these high density cases, more significant compensation is required at shallow tilt angles near zero when the modules see only the few, far field ground elements. Increasing the ground extent as in Fig. 3.7 makes more ground elements available at these angles, reducing the compensation factor; however, significantly increasing the ground extent requires a prohibitively large number of radial divisions to maintain adequately small mesh element areas for shading accuracy. Additionally, tilt angles approaching horizontal result in relatively low radiation transfer; as such, additional computation time would be largely wasted. The compensation factor, therefore, allows the model to approximate the view factor from an extended ground area while avoiding the computational cost of the additional radial divisions.

Future work should investigate the impact of the meshing scheme geometry on these compensation factors and on resulting irradiance and energy yield. Alternative approaches, such as triangular meshing could also reduce computation time allowing for higher density meshes. Just as for the sky-to-ground compensation factor, the ground-to-module compensation factor is applied equally across radiation from all ground elements. Further investigations are required to determine whether this assumption holds or whether $\chi_{\mathrm{G},m}$ should be modified based on the distance of each ground element from the module under investigation.

Sky to module A *sky-to-module compensation factor*, $\chi_{\mathrm{S},m}$, would account for the discrepancy between finite sky element summation and sky dome integration. However, the subplot to the left of Figure 3.8 shows that this sky-to-module compensation factor for the front of the module is less than $\pm 0.5\%$ for all tilt angles, suggesting that the finite element approach approximates the view factor well, even at the base mesh density. For the rear in the right subplot, the compensation factor exceeds $\pm 0.5\%$ at $\pm 29°$ for 10 sky elevation divisions in light blue and $\pm 21°$ for 20 sky elevation divisions in darker blue in Figure 3.8. At these angles, the theoretical sky-to-module rear view factors in dashed grey are $\sim$0.06 and $\sim$0.04, respectively, and adjacent rows will shade much of the diffuse sky dome from the rear of the module. Thus, we can expect that the significant compensation at shallower angles will have a minimal impact on total radiation transfer. Nevertheless, a rear

compensation factor could be applied with negligible computational cost should a motivation arise.

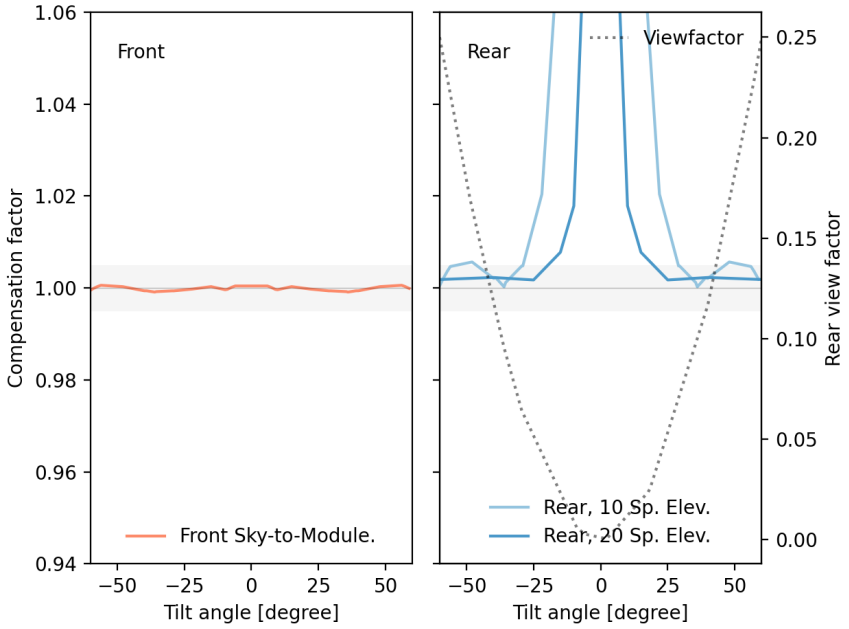


Figure 3.8: Front (left) and rear (right) sky-to-module compensation factor vs. tilt angle. Rear sky view factor is in dotted grey on the left. Results are shown for 10 and 20 sky elevation divisions for rear and 10 sky elevations for front. Grey region is $\pm 0.5\%$.

3.3.3 Bounding volume hierarchy

Once the model's coupling and compensation algorithms have calculated the energy transfer between emitting sources and irradiated elements, the model's shading algorithm determines whether the rays representing this transfer should be partially or fully shaded due to intersections with transparent or opaque objects in the array. The brute force solution to this problem would be to check all rays that are incident on the front or rear of the module against every single primitive in the array, resulting in a prohibitively long computation time. Instead, the model described in this thesis includes an adapted approach from computer graphics rendering to reduce the number of ray-primitive intersection checks, namely through the use of bounding volume hierarchies. (See Section 2.4.2).

The DUET v.uO-2024 bounding volume hierarchy is depicted in Fig. 3.9A and is composed of a hierarchy of polygons and rectangular prisms – the latter known as *bounding boxes* – which each enclose sequentially smaller volumes or primitives. Whereas ray tracing software typically group

primitives exclusively by spatial relationship [108], DUET v.uO-2024's bounding volume hierarchy is a streamlined decision tree logic based on an understanding of the layout and movement of typical PV arrays. As seen in Fig. 3.9B, rays are first checked for intersection with a bounding box around (1) the full array and subsequently around (2) front or rear row groups. (If the ray is incident on the ground, both front and rear bounding boxes are checked.)

Rays that intersect with front and/or rear row sets are then checked for intersection with the individual row bounding boxes within, as in Fig. 3.9(3). If a ray intersects with an individual row bounding box, this ray is also checked for intersection with all racking in the row that does not move with the plane-of-array, such as vertical pilings. Any ray intersecting with an opaque primitive is set to have a shading coefficient δ=0, fully-shading the ray and eliminating it from further checks.

All rays that intersect with an individual row bounding box are subsequently checked against the polygon that delineates the row plane-of-array surface as in Fig.3.9(4). Rays that have yet to be shaded and that intersect with the row polygon must be checked for intersection with (i) all dynamic racking that moved with the plane-of-array racking and (ii) the gaps in the table or row through which the ray could pass unobstructed as in Fig.3.9(5).

The handling of these gaps is where the described model's bounding volume hierarchy diverges most from conventional approaches; instead of simply checking for intersections between rays and surfaces, the model uses well-defined empty spaces between surfaces to reduce the number of intersection checks required. For example, for the 2P array shown in Fig. 3.9A with three tables, the algorithm checks rays for intersection with the row polygon, one tier gap polygon, and two row gap polygons for a total of 4 ray-polygon checks. This significantly reduces the 7 ray-polygon checks required in the brute force with a row polygon and six table polygon checks.

The validity of checking for ray intersection with table gaps, rather than tables, relies on the assumption that all tables are co-planar. This assumption holds for arrays on mostly flat or constantly-sloped ground. It will not hold for PV plants that follow rolling hills – a recent advancement in array deployment facilitated by improvements in tracker inflection points to avoid unnecessary ground levelling [143]. Thus, this portion of the bounding volume hierarchy must be adjusted for any case in which the plane-of-array changes for each table.

Finally, for rays incident on the rear of the module under investigation, the algorithm uses the same transparent primitive approach to calculate shading due to the module frame - an optional

feature in the modelled system. Since a module frame can be conceptualized as 4 rectangular surfaces perpendicular to the module plane and 4 rectangular surfaces parallel to the module plane, a brute force approach would require a ray-polygon intersection for each of the eight surfaces with each rear incident ray. However, the described algorithm makes use of the fact that the frame opening forms a polygon in green in Fig. 3.9A(6) through which all rear-incident must pass if they are not blocked by the frame surfaces. This reduces the computational intensity of the frame shading calculation by a factor of 16.

In summary, DUET v.uO-2024's PV-specific bounding volume decision tree:

- follows a single algorithm for all timestamps (i.e., independent of tracker angle, sun position);
- responds to user-defined PV array design (i.e., number of rows, tables, and tiers; position for the module under investigation); and
- is novel in its use of both a context-specific volume order and transparent primitives.

Section 3.6.1 describes vectorization of the model's bounding volume hierarchy – a computationally efficient approach that is possible since large sets of rays must follow the same logical checks. Section 4.2 discusses racking reflections, neglected in the above process due to the key assumption that the ground is the only reflective surface in the simulation environment.

Horizon mask In future, a horizon mask should be added to this bounding volume hierarchy. This additional shading element will block any direct or diffuse rays emanating from a sky element or sun position that is fully or partially obscured by far field objects such as buildings or mountain ranges. Adding a horizon mask may reduce the computation time since any fully obscured sky elements will be removed from shading calculations. Direct light calculations would also only be performed if the sun is above the elevation angle for the given azimuth range in which the sun position falls; however, these changes will only result in a mild benefit to computation speed and only locations with significant horizon shading like valleys, urban environments, or tree-lined sites.

Discrepancies in simulated results generated by models with and without a horizon mask will be most significant for satellite-derived input irradiance and during timestamps near sunrise and sunset or with very high diffuse fraction, excluding foggy conditions.

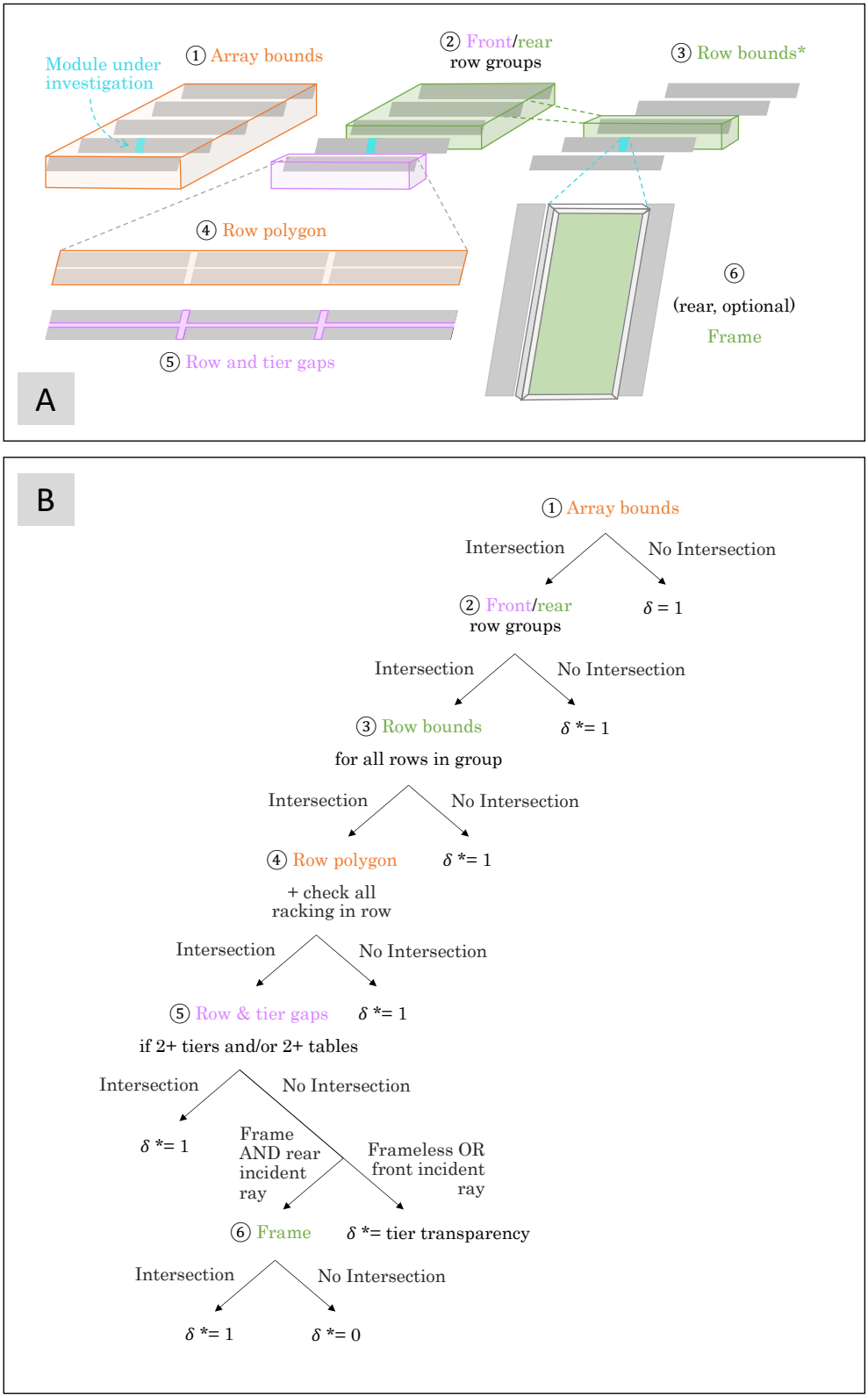


Figure 3.9: (A) DUET v.uO-2024 bounding volume hierarchy. (B) DUET v.uO-2024 bounding volume hierarchy decision tree.

3.3.4 Ray-primitive intersections

The bounding volume hierarchy and shading algorithms in DUET v.uO-2024's optical model rely on a set of ray-object intersection algorithms [9–12]. These algorithms determine whether rays representing radiation transfer between a source and a surface element intersect with an object in the PV array. The model's independent, deterministic rays allow ray-primitive intersection algorithms to be vectorized such that each instruction performs an operation for multiple rays at once. (See Section 3.6.1). The associated functions are also modular so that they may be replaced with more efficient algorithms over time.

Section 3.2.2 describes the primitives used in DUET v.uO-2024 to form shading objects, and Fig. 3.a in Section 3.1 and Fig. 3.9 demonstrate how the primitives come together to form the PV array objects and bounding volume hierarchy, respectively. Appendix B of this thesis describes sample ray-primitive intersection algorithms.

3.4 Details on electrical model

The following sections demonstrate the electrical model's response to partial shading and partial brightening within a module. An additional discussion on thermal modelling uncertainty in bifacial vs. monofacial systems can be found in Appendix C.

3.4.1 IV curve summation and partial shading

As described in Section 3.1II, DUET v.uO-2024 calculates current-voltage (IV) curves from cell- to -array level. The following section presents visualizations of the intermediate IV curves combined to find module maximum power and examines the behaviour under partial shading and brightening to illustrate the impact of cell breakdown voltage, bypass diode protection of submodule, and half-cut cells. To walk through these topics, we will refer to Fig. 3.10 which shows seven partial shading scenarios A-G with varied cell irradiance on one or more cells along with the electrical layout of cells and submodules across each bypass diode in grey. Figures 3.11-3.18 show the corresponding IV curves for cells (magenta), parallel strings across the bypass diodes in the half-cut cell case (green), submodules (blue), and the module itself (grey). The maximum power point of the module is provided as a golden dot at the highest power "knee" of the module IV curve. The bypass

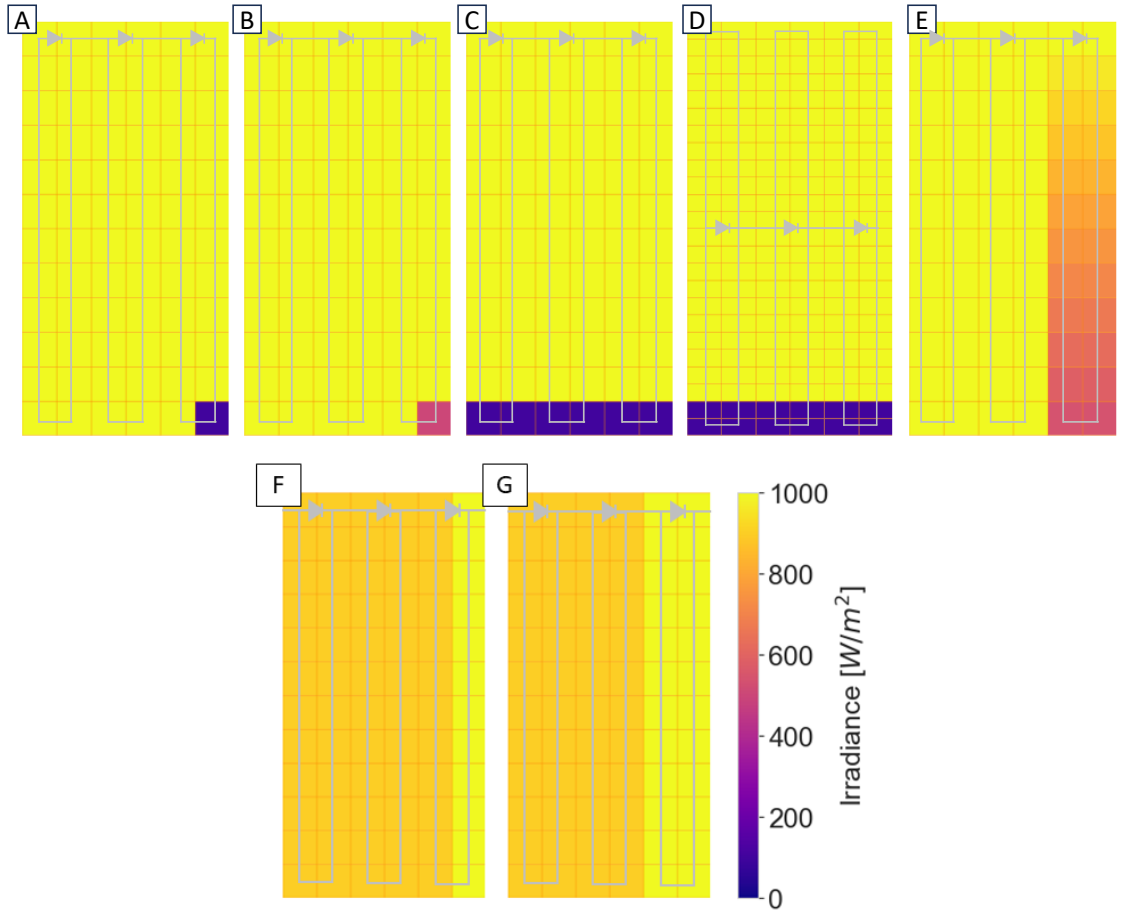


Figure 3.10: Module shading scenarios: (A) single cell with uniform 90% shading; (B) single cell with uniform 50% shading; (C) uniform 90% shading along bottom row of full cells; (D) uniform 90% shading along bottom two rows of half-cut cells; (E) gradual shading from 0-50% across full cells within a single submodule. Module edge brightening scenarios: (F) right-most column of full cells with 100 $\mathrm{W/m^2}$ brightening; (G) right-most submodule of full cells with 100 $\mathrm{W/m^2}$ brightening.

diode reverse bias and cell breakdown voltages are shown as vertical golden and grey dotted lines, respectively, in the negative portion of the voltage axis. These examples have a consistent 25°C cell temperature.

The first partial shading scenario, Case A, has a 10% uniform shading across a single cell. All but one of the cells have healthy first quadrant IV curves in Fig. 3.11; the shaded cell shows the expected 90% reduction in short circuit current and a negative bias that extends to the cell breakdown voltage, V_b (represented here by the step function at -15 V). The submodule IV curves in cyan show the series summation of cell IV curves with the submodule that contains the shaded cell clearly visible below the other two submodule IV curves.

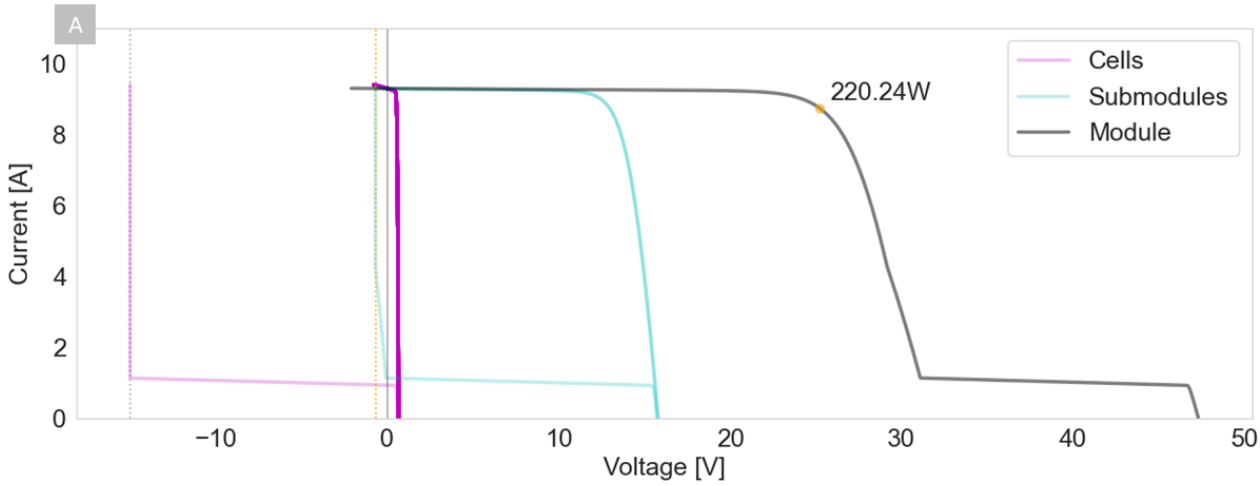


Figure 3.11: Current-voltage curves for module (dark grey), submodules (cyan), and cells (magenta) in *Shading Scenario A* with a single 90% shaded cell. Module maximum power is shown as gold dot on module IV curve. Bypass diode forward voltage is a vertical golden line at -0.7 V, and cell breakdown voltage is a vertical grey line at -15 V.

The bypass diode in parallel with the partially shaded submodule conducts current when the forward bias across the bypass diode, caused by irradiance non-uniformity within the associated string, exceeds the diode's forward voltage. This stops the current generated in the other two submodules from passing through the shaded cell. The knee of the resulting module IV curve sits at a lower voltage than it would in a fully unshaded module, but allows extraction of the higher current generated in the unshaded submodules.

The steep downward slant in the partially-shaded submodule current in cyan between the submodule forward voltage at -0.7 V and the short circuit current is characteristic of a string with a cell that has entered breakdown (see Section 2.1.1). In this case, the shaded cell enters breakdown due to the intense negative bias generated by the significant build up of carriers attempting to exit the string of 23 non-shaded, forward biased cells. In this state, current in excess of the generated photocurrent of the shaded cell flows through resistive shorts in parallel to the cell's drift current. Extended periods in breakdown will lead to overheating as power is dissipated. These hotspots are seen most often in harshly shaded regions of a module. This heating is neglected in DUET v.uO-2024's temperature-dependent IV curves, but the power dissipation and resulting power loss at the module terminals is captured in the IV curve summation.

Case B shows a similar single shaded cell, but this time with only 50% uniform shading as com-

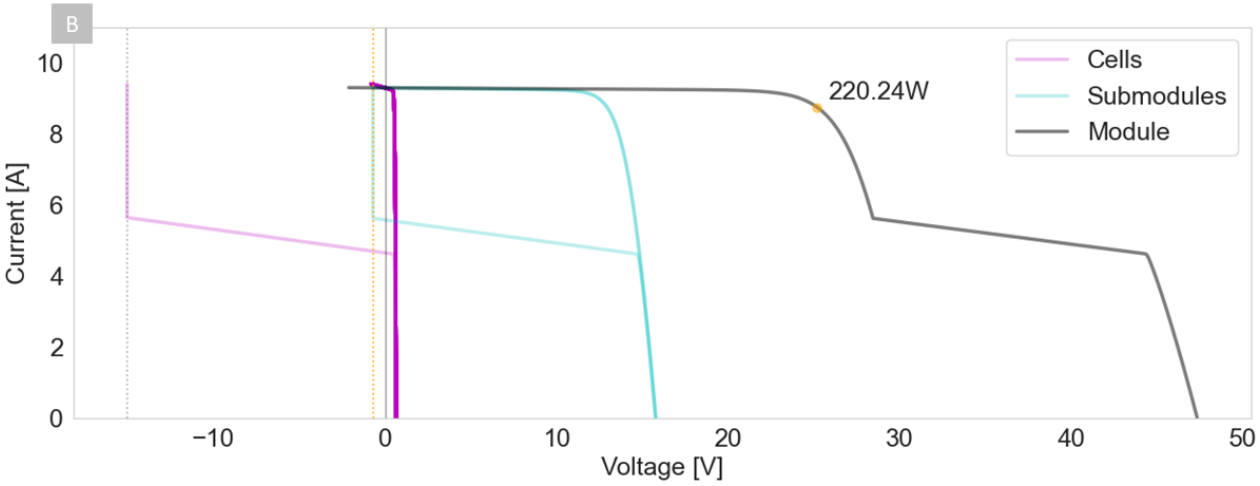


Figure 3.12: Current-voltage curves for module (dark grey), submodules (cyan), and cells (magenta) in *Shading Scenario B* with a single 50% shaded cell. Module maximum power is shown as gold dot on module IV curve. Bypass diode forward voltage is a vertical golden line at -0.7 V, and cell breakdown voltage is a vertical grey line at -15 V.

pared to the rest of the cells in the module. As seen in Fig. 3.12, the shaded submodule IV does not exhibit signs of cell breakdown since the slope defined by the cell shunt resistance is preserved all the way from the knee of the partially-shaded submodule IV curve back to the submodule forward voltage shown in the vertical dashed gold line. This illustrates that a harsh, localized shading resulting in severe imbalance between cell photocurrents is required for a module to experience breakdown caused by shading. Case E shows gradual shading across an entire submodule, resulting in a similar IV curve behaviour to Case B as shown in Fig. 3.13 since both are examples of moderate shading within a single submodule where bypass diodes have conducted excess current from other submodules around the shaded string.

Rear irradiance non-uniformity in ground-mounted bifacial modules is often a gradual penumbra due to obstruction of diffuse or reflected light and follows the IV curve archetype in Case E with mild non-uniformity within each submodule, rarely causing hotspots. High, uniform front irradiance also often lessens the impact of variations in rear irradiance. However, poorly installed wiring and junction boxes, or poorly optimized racking elements that are close to the rear surface, may cause harsher shading and greater current mismatch loss. Such shading would be relevant in cloudy conditions with high albedo in which rear irradiance makes up a greater portion of total irradiance and rear shadows from ground reflected light may be more harsh. Module frames also cause

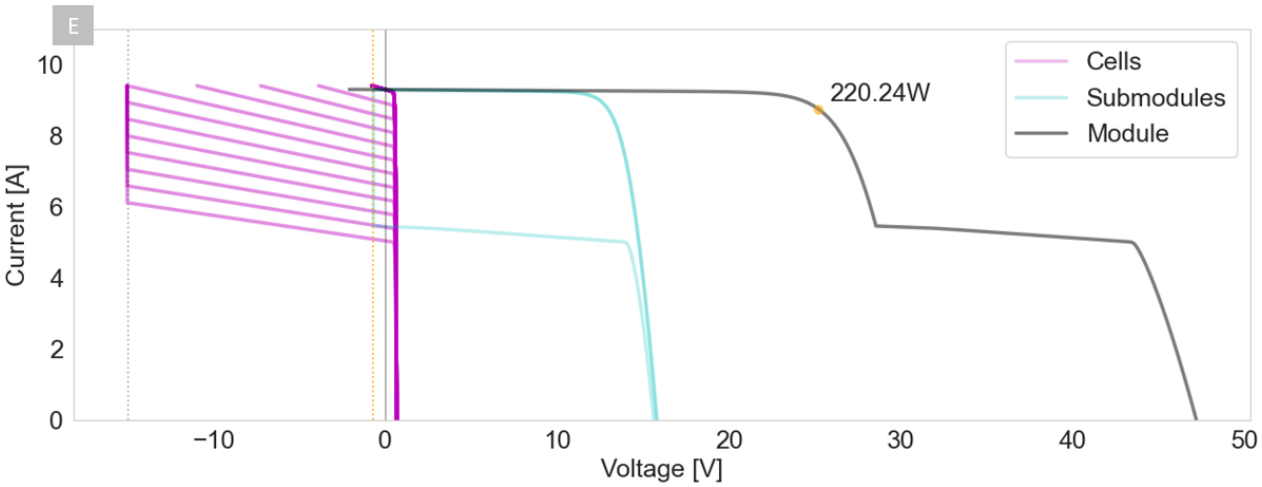


Figure 3.13: Current-voltage curves for module (dark grey), submodules (cyan), and cells (magenta) in *Shading Scenario E* with gradual 0-50% shaded cells within a single submodule. Module maximum power is shown as gold dot on module IV curve. Bypass diode forward voltage is a vertical golden line at -0.7 V, and cell breakdown voltage is a vertical grey line at -15 V.

mild non-uniformity across all submodules to a varying degree since the frame partially shades a portion of each edge cell.

Harsh front-side shading occurs most frequently at low sun elevation for fixed-tilt systems such as south-facing arrays and vertical east-west facing systems for agrivoltaics, when adjacent rows block the sun's rays from reaching part of the module under investigation. The full width of the lowest end of the module may be shaded in these cases, as in Case C. Figure 3.14 shows that uniform 10 % shading on 2 of 24 cells per submodule results in complete current limiting for all submodules. This case avoids breakdown conditions since there are two cells to share the reverse voltage applied by carrier buildup from the 22 unshaded cells. This shading across the bottom row of cells leads to a maximum power point at high voltage, but low current, with a maximum module power of only 41W.

At the system level, backtracking allows single-axis tracked (SAT) systems to avoid such harsh shading. But where harsh shading cannot be avoided, there are a few module-specific approaches to mitigate current mismatch loss and breakdown. For example, Calcabrini et al. [32] highlight that cell types with p-i-n junctions, such as interdigitated back contact (IBC) cells, are less resistant to reverse bias, resulting in breakdown voltages at -2 V to -5 V as compared to typical silicon breakdown voltages at -10 V to -30 V. Their study modelled the energy yield impact of these reduced

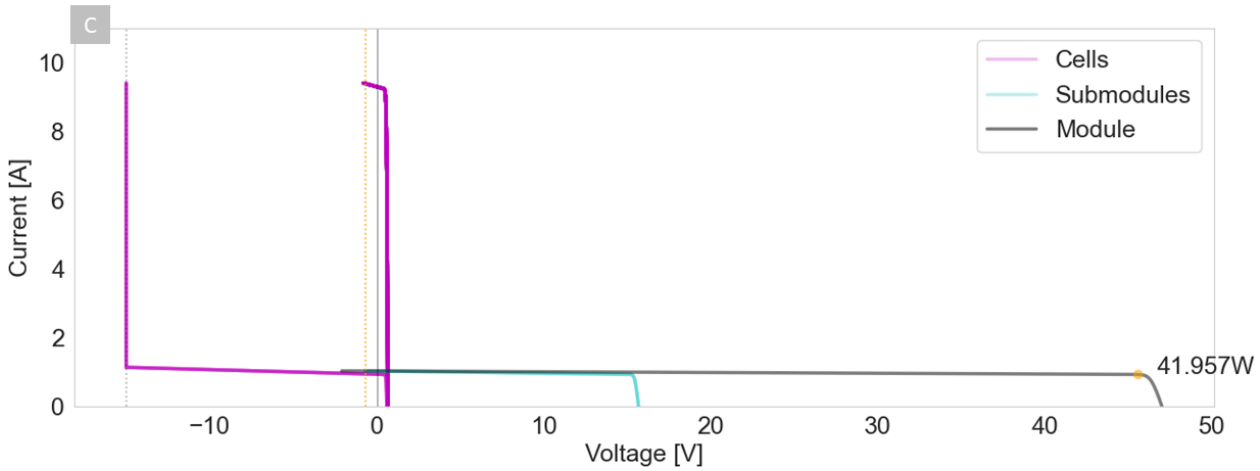


Figure 3.14: Current-voltage curves for module (dark grey), submodules (cyan), and cells (magenta) in *Shading Scenario C* with 90% shading across the bottom row of full cells. Module maximum power is shown as gold dot on module IV curve. Bypass diode forward voltage is a vertical golden line at -0.7 V, and cell breakdown voltage is a vertical grey line at -15 V.

breakdown voltages, suggesting that IBC cells were shade tolerant since low breakdown voltages mimic the electrical behaviour of a module with a bypass diode for every cell. The low magnitude breakdown voltages resulted in modelled energy yield gains for rooftop PV with adjacent shading objects of +6% for a module made of cells with -0.5 V breakdown voltage compared to a modules with cell breakdown voltages less than -10 V.

Figure 3.15 shows DUET v.uO-2024 IV curves for Case C with 10% shading across the bottom cells, but with a cell breakdown voltage of -0.7 V – equivalent to the bypass diode reverse bias. Very little power is lost to current mismatch as compared to the simulation with -15 V breakdown voltage in Fig. 3.14. The inset in Fig. 3.15 shows that breakdown voltages with magnitude less than 5 V begin to see a linear slope in power gain with respect to the 15 V Case C that reaches upward of 300% by -2.5 V. It should be noted that operating a module made of cells with low breakdown voltages under significant irradiance non-uniformity for prolonged periods would require that damage from operation in breakdown have minimal effect on module lifetime or be reversible at low cost.

Installing modules with half-cut cells is a more widely-adopted approach to mitigate harsh shading. As shown in Fig. 3.10D, these modules use cells that are half the height of full cells and wired such that the cells on either half of the module are electrically grouped into two sets of series strings that are connected in parallel across the bypass diode. Thus, the shaded cells limit the current

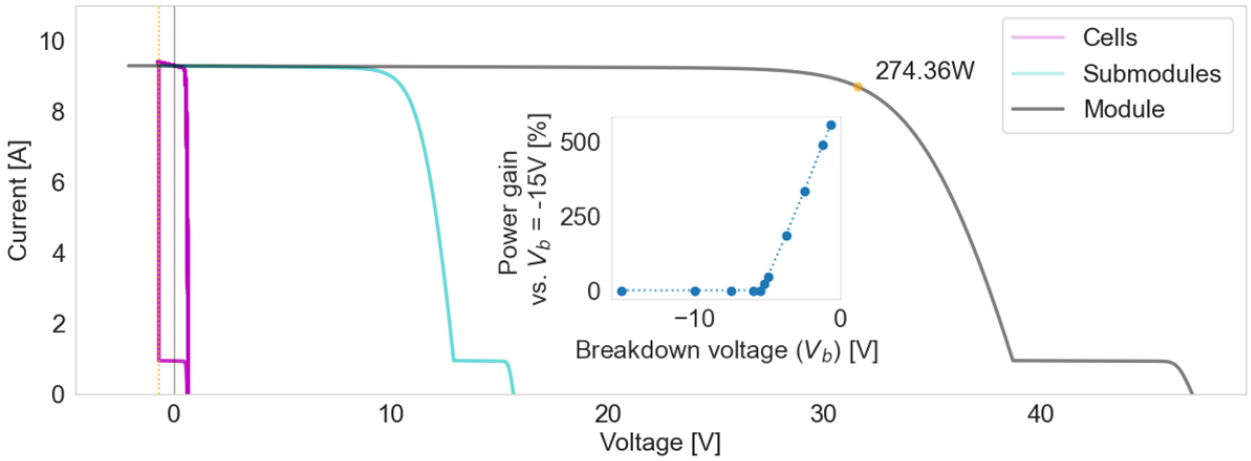


Figure 3.15: Outer figure: Current-voltage curves for module (dark grey), submodules (cyan), and cells (magenta) in *Shading Scenario C* with 90% shading across the bottom row of full cells and *-0.7 V cell breakdown voltage*. Module maximum power is shown as gold dot on module IV curve. Bypass diode forward voltage is a vertical golden line at -0.7 V. Inset: Power gain over -15 V breakdown voltage case vs. breakdown voltage.

within only their respective series string. Since submodule IV curves are a parallel summation of the string IV curves, the unshaded current from the top half of the module to contribute to the maximum power, unlimited by the shaded region.

Comparing the maximum power points of Case D with half-cut cells in Fig. 3.16 and Case C with the same full-width bottom cell shading, we can see that the half-cut module has a 360% higher power than the full cell module. Half-cut cells are thus beneficial for applications where harsh shading is expected. Their mainstream adoption is broadening the acceptable design landscape for array orientations and spacing, with the symbiotic benefit that the per-cell series resistance is also reduced due to the halved cell area. Half-cut cells have also been shown to reduce the need for backtracking in SAT systems which reduces cosine losses, improving the photogenerated current of the highest irradiance cells [144, 145].

3.4.2 IV curve summation and edge brightening

Localized brightening across a subset of cells or submodules leads to power gains with respect to uniform illumination across a module or module string. For example, we can consider the modules in scenarios F and G in Fig. 3.10 which show 100 $\mathrm{W/m^2}$ edge brightening on one column of cells and one submodule, respectively. The submodule IV curves in cyan in Fig. 3.17 show that the

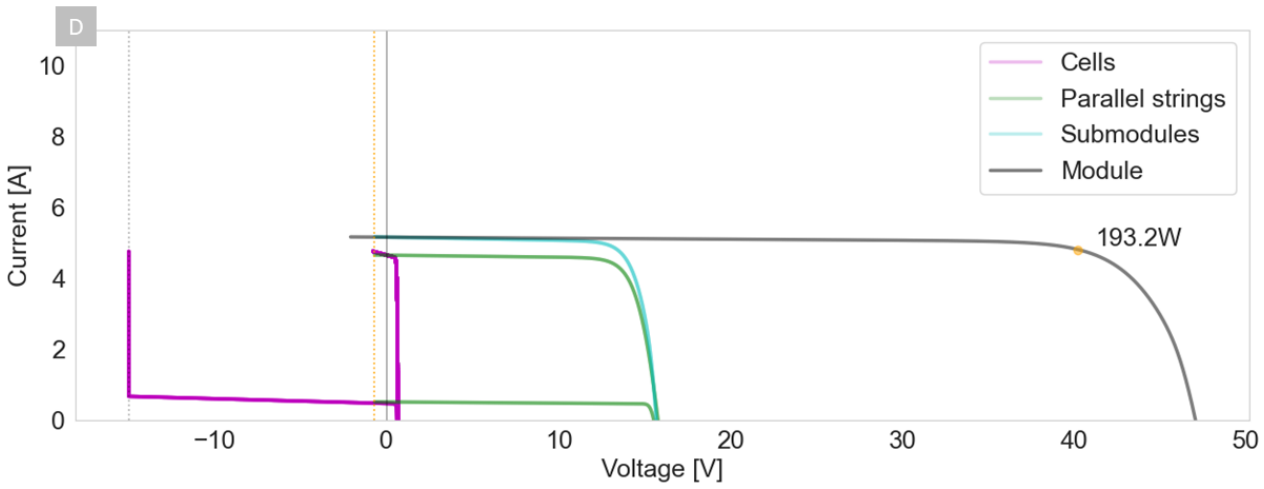


Figure 3.16: Current-voltage curves for module (dark grey), submodules (cyan), parallel strings across the bypass diodes (green), and cells (magenta) in *Shading Scenario D* with 90% shading across the bottom two rows of half-cut cells. Module maximum power is shown as gold dot on module IV curve. Bypass diode forward voltage is a vertical golden line at -0.7 V, and cell breakdown voltage is a vertical grey line at -15 V.

submodule with a single column of brightening in scenario F has a limited current due to the lower irradiance cells, but a higher voltage at maximum power due to the increased voltage contribution of the brighter cells to the series cell connection. The combination of all three submodule IV curves in series - shown in the gray module IV curve - then results in a slightly higher maximum power than would occur for uniform illumination, despite current limiting and the resulting current mismatch losses.

In Scenario G, the brightening is spread across the entire submodule. In this case, current limiting does not occur within the brighter submodule since all cells within have uniform illumination. The resulting bright submodule IV curve thus demonstrates a higher short circuit current than the other two submodules as shown in the cyan curves in Fig. 3.18. While most of this additional current cannot pass through lower irradiance cells to be extracted at the module terminals , the brighter submodule does contribute a higher voltage to the series summation of these three submodules at any currents less than the limiting I_{sc} and around the I_{mp} of the lower irradiance submodules. The resulting module IV curve in gray has a higher maximum power than would occur in uniform illumination. The power is also higher than in the single column brightening scenario F, since more cells generate excess light-generated carriers resulting in a greater forward bias at the limiting current. These examples underscore how both the intensity and the spatial breadth of edge brightening

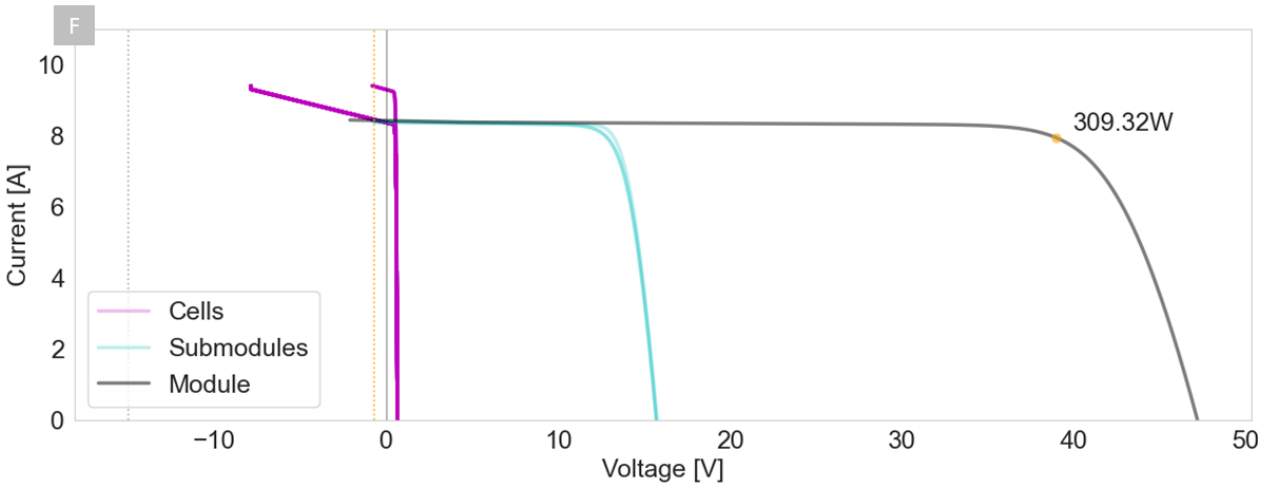


Figure 3.17: Current-voltage curves for module (dark grey), submodules (cyan), and cells (magenta) in edge brightening Scenario F with 100 $\mathrm{W/m^2}$ brightening across right-most column of full cells. Higher voltage in submodule with brightening seen as slight difference between submodule IV curve knees around 13 V.

affect the power of a module or module string.

Limitations The above implementation of IV curve generation neglects the temperature dependence of bypass diode forward voltage [146] and approximates the exponential curve of bypass diode conduction and cell breakdown [147] to step functions. These effects can be expected to have a sub-0.1% impact on annual energy yield. Therefore, future work should prioritize testing the validity of other assumptions with higher potential energy yield impact prior to testing the assumptions made here.

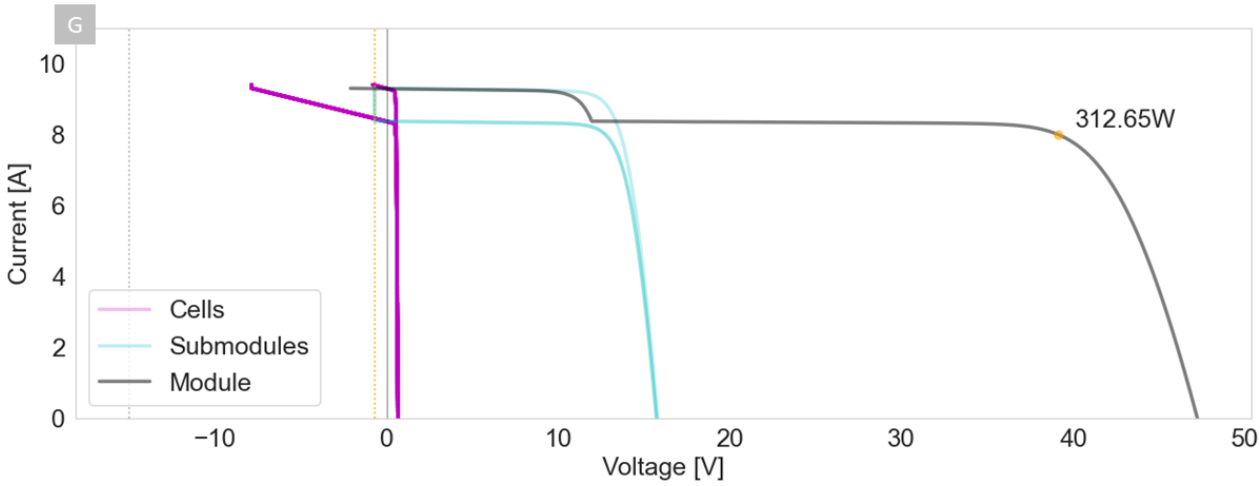


Figure 3.18: Current-voltage curves for module (dark grey), submodules (cyan), and cells (magenta) in edge brightening Scenario G with 100 $\mathrm{W/m^2}$ brightening across right-most submodule of full cells. Higher short circuit current and higher voltage at limiting current is seen in one of the three submodule IV curves.

3.5 Cross-software comparisons

In 2020, the International Energy Agency (IEA) PV Power Systems Programme (PVPS) Task 13 group requested submissions to a Bifacial PV Modelling Comparison. The aim was determine the degree to which existing bifacial PV performance models differed in output based on clearly defined simulation scenarios. DUET v.uO-2020 simulations were submitted for the two mandatory scenarios, S1 and S4, which emulate a fixed tilt and single-axis tracked system in three locations. The following sections discuss the results of the cross-software comparison and highlight areas for further investigation.

3.5.1 Software comparison - IEA Report

The IEA PVPS Bifacial Modelling Comparison required a minimum of two simulations - Scenario 1 (S1) and Scenario 4 (S4). S1 consists of a 7-row, 1L equator-facing system at a fixed 20° tilt with 0.62 albedo and neglecting all racking. S4 emulates a 10-row, 1P HSAT system with a torque tube with a 15 cm diameter running north-south and 0.25 albedo. The two simulation scenarios are described in further detail in the final IEA report [2]. These simulations were to be repeated using TMY data and geographical inputs for three locations detailed in Table 2. The locations span the northern and southern hemispheres and represent both highly-diffuse and highly direct

sky conditions.

City, Country	Latitude [°]	Longitude [°]	DNI [kWh/year]	Annual DNI/DHI	$\bar{T}_a$ [^{o}C]	Altitude [m]
Abu Dhabi, UAE	24.43	54.65	2295	0.26	27.1	27
Antofogasta, CL	-24.43	70.43	2044	0.33	17.0	120
Groningen, NL	53.13	6.58	625	0.97	9.1	4

Table 2: The three locations in the IEA PVPS Task 13 Bifacial Modelling Comparison (based on Table 16 in [2]). UAE: United Arab Emirates, CL: Chile, NL: The Netherlands, DNI: Direct normal insolation (annual), DHI: Diffuse horizontal insolation (annual), $\bar{T}_a$: Average ambient temperature.

The DUET v.uO-2020 front and rear irradiance reported in this section are a weighted average of the 1st, 10th, and 20th modules in the row - weighted as 1, 18, and 1 module(s), respectively (i.e. edge brightening on the two edge modules is considered). Irradiance for each module is sampled at 16 equally-spaced sampling points per cell for a total of 6912 irradiance sample points. For the bifacial power calculation - provided in the report but not discussed here, IV curves for the 1st, 10th, and 20th modules were similarly generated and combined in a series string based on a weighted voltages of 1, 18, and 1 module(s), respectively. The power of all 10 rows (strings) is assumed to be equal.

For scenarios S1 and S4, the IEA report shows three figures with anonymized simulation results for front or rear irradiance for the 12 participating models. Table 17 in the report [2] provides an in-depth comparison of the features of each participating model. In Fig. 3.19 in this text, a black line with circular markers is overlain on these anonymized figures to identify the DUET v.uO-2020 results. DUET is classified with the '3D view factor / Others' category, shown as a solid blue in the original report figure.

Fig. 3.19a shows that DUET v.uO-2020 front irradiance for the fixed-tilt scenario agrees with the dashed red bifacial_radiance ray tracing line to less than 10 $\mathrm{W/m^2}$ deviation throughout an entire clear day. DUET v.uO-2020 and bifacial_radiance v0.3 both show a minor morning overestimation and afternoon deviation from another ray tracing software in the solid red line – a pattern characteristic of a time or sun position shift. As noted in the IEA report, there is wide variation in front-side irradiance between models that can be mitigated by shifting certain results by $\pm$ 30 min-1 h, likely due to differing interpretations of what period the input irradiance timestamp represents.

With such temporal variation in front-side irradiance, it is unsurprising that there are significant

differences between modelled rear-side irradiance throughout the day for the fixed tilt system in Fig. 3.19b. In fact, 2D view factor models in green disagree by more than 50 $\mathrm{W/m^2}$ at peak irradiance. There is better agreement on peak rear irradiance between the *3D* VF models in blue, but the time of the peak varies between models. Unlike some 3D view factor models in blue, DUET v.uO-2020 reaches a peak at the same time of day as bifacial_radiance; however, DUET overestimates compared to that software by approximately 30 $\mathrm{W/m^2}$ at peak irradiance. Since front irradiance from these two models agreed so closely, the diffuse sky model is unlikely to be the source of this overestimation, leaving ground-reflected light as the likely source of discrepancy – particularly at 0.62 albedo. This could be the result of several factors such as differing modeled module transparencies casting differing shade beneath the panels or DUET ground mesh density affecting row-to-row shading of ground-reflected light.

Unlike the fixed-tilt case, DUET v.uO-2020 predicts rear irradiance to within 10 $\mathrm{W/m^2}$ of bifacial_radiance at all times of the sample day for the single-axis tracked system shown in Fig. 3.19c with 0.25 albedo. This is a closer agreement than is seen between bifacial_radiance and the two other ray tracing models at the peak of the day. From this close agreement, we can draw two conclusions: (1) the discrepancy in Fig. 3.19b is the result of one of the following unique to S1: DUET v.uO-2020's fixed-tilt model, single-tier landscape orientation, *or* high albedo; and (2) DUET v.uO-2020's ray-primitive intersection algorithm adequately captures shade cast by a fully absorptive torque tube with 0% reflectivity in a 1P system, as compared to the RADIANCE ray tracing engine. Given the relative computational efficiency of DUET v.uO-2021 vs. ray tracing approaches, the latter is a significant result.

Future work should focus on identifying any conditions under which DUET and bifacial_radiance differ significantly and determining the source of these discrepancies. Examining 2D irradiance profiles for identical simulation scenarios with isolated direct, reflected, and diffuse light modelling should illuminate the source of any discrepancies. In a brief foray into this work, we found and reported a bug [148] in Radiance implementation of the Perez model [13] that had been untouched since 1994. However, the updated bifacial_radiance code resulted in only a partial reduction in front and rear irradiance discrepancies. Thus, further investigation – including the variation of the reflective material properties of the ground and modules in bifacial_radiance – is required.

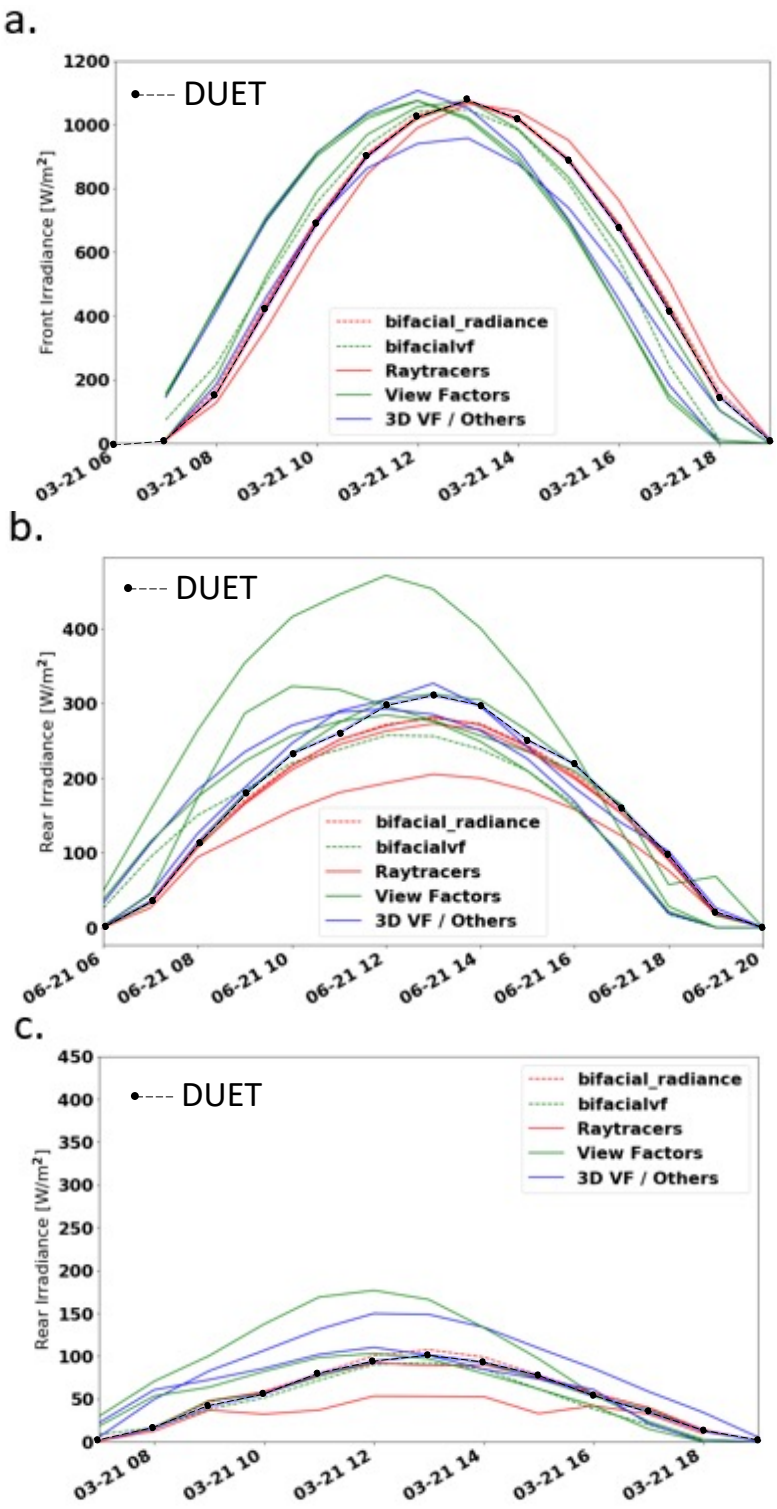


Figure 3.19: Selected IEA PVPS Task 13 Bifacial Modelling Comparison results with DUET v.uO-2020 results de-anonymized in black for (a) front irradiance in the S1 fixed-tilt system; (b) rear irradiance in the S1 fixed-tilt system; and (c) rear irradiance in the S4 single-axis tracked system with an opaque torque tube. Modified from Fig. 62 in [2]. DUET was classified as a 3D view factor model (blue lines) in the original results.

3.5.2 Software comparison - PVsyst

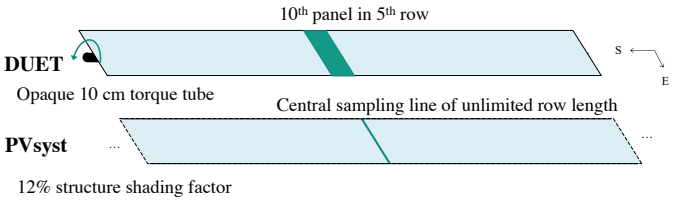
The following section compares central row approximations in PVsyst v6.86 [40, 149] and DUET v.uO-2020 for the S4 single-axis tracking annual simulation in the IEA PVPS Task 13 Bifacial Modelling Comparison [2] that is illustrated in Fig. 3.21. The DUET calculations represent the 10th module of 20 modules in the 5th row of 10 rows, including a 10 cm opaque torque tube with an axis of rotation 15 cm from the rear of the module. The PVsyst calculations represent the irradiance sampled at a central cross-section of an infinitely long row with a structure shading factor defining the rear irradiance blocked by the torque tube. Both of these approaches neglect row edge brightening, with the DUET results neglecting any irradiance non-uniformity beyond the width of the module under investigation. (See Section 4.1 for inter-module edge brightening and mismatch-loss effects.) While figures referenced in the following paragraphs compare DUET results in the y-axis to PVsyst on the x-axis, neither model can be considered a baseline; in the absence of field-data, such a comparison can only highlight deviations in model predictions and does not provide insight on either model's accuracy.

Fig. 3.20 shows a summary of PVsyst input parameters for the S4 HSAT scenario for Groningen. The factors underlined in yellow were computed from DUET v.uO-2020 calculations, including the 12.1% structure shading factor which rounded to the same value for all locations. In this case, the structure shading factor was found as the difference in annual rear insolation with and without torque tube shading, prior to IAM correction.

By comparing the irradiance results of the two models, we can determine that the optical models predict total annual front insolation to within a relative difference of -0.7% in Abu Dhabi, 0.33% in Antofagasta and 1.79% in Groningen. Abu Dhabi, a location dominated by direct-light sky conditions, shows an annual -2.1 $\mathrm{W/m^2}$ mean bias error (MBE) calculated from hourly irradiance, with average hourly MBE reaching -8 $\mathrm{W/m^2}$ and -10 $\mathrm{W/m^2}$; DUET v.uO-2020, therefore, has a tendency to underestimate with respect to PVsyst under these highly direct sky conditions, particularly mid-morning and mid-afternoon when tracker angles are farthest from horizontal (Fig. 3.22.A.ii). However, in Groningen where diffuse sky conditions dominate, DUET v.uO-2020 overestimates front irradiance compared to PVsyst under these same conditions and at these same times of day (Fig. 3.22.C.ii). Antofagasta displays the lowest discrepancy between the two models, with

Simulation parameters	System type	**Unlimited Trackers with backtracking**		
Tracking horizontal axis	Simplified model, unlimited	10tracker rows	Axis Azimuth	0°
Rotation Limitations	Phi min.	-60°	Phi max.	60°
	Tracking algorithm	Astronomic calculation		
Backtracking strategy	Nb. of trackers	10	Unlimited trackers	
	Tracker Spacing	5.70 m	Collector width	1.95 m
Inactive band	Left	0.02 m	Right	0.02 m
Backtracking limit angle	Phi limits	+/- 69.4°	Ground cov. Ratio (GCR)	34.2 %
Models used	Transposition	Perez	Diffuse	Imported
Horizon	Free Horizon			
Near Shadings	No Shadings			
Bifacial system	Model	Unlimited trackers, 2D calculation		
	Tracker Spacing	5.70 m	Tracker width	1.99 m
	Tracking limit angle	60°	GCR	34.9 %
	Ground albedo	25.0 %	Axis height above ground	1.20 m
	Module bifaciality factor	67 %	Rear shading factor	12.1 %
	Module transparency	12.6 %	Rear mismatch loss	7.3 %
User's needs :	Unlimited load (grid)			

Figure 3.20: PVsyst v6.86 simulation parameters for IEA Bifacial Modelling Comparison scenario S4 in Groningen, NL. Simulations performed by Jill Tymchak. Parameters underlined in yellow were pre-calculated in DUET. All other parameters were defined in the S4 brief and summarized in [2].



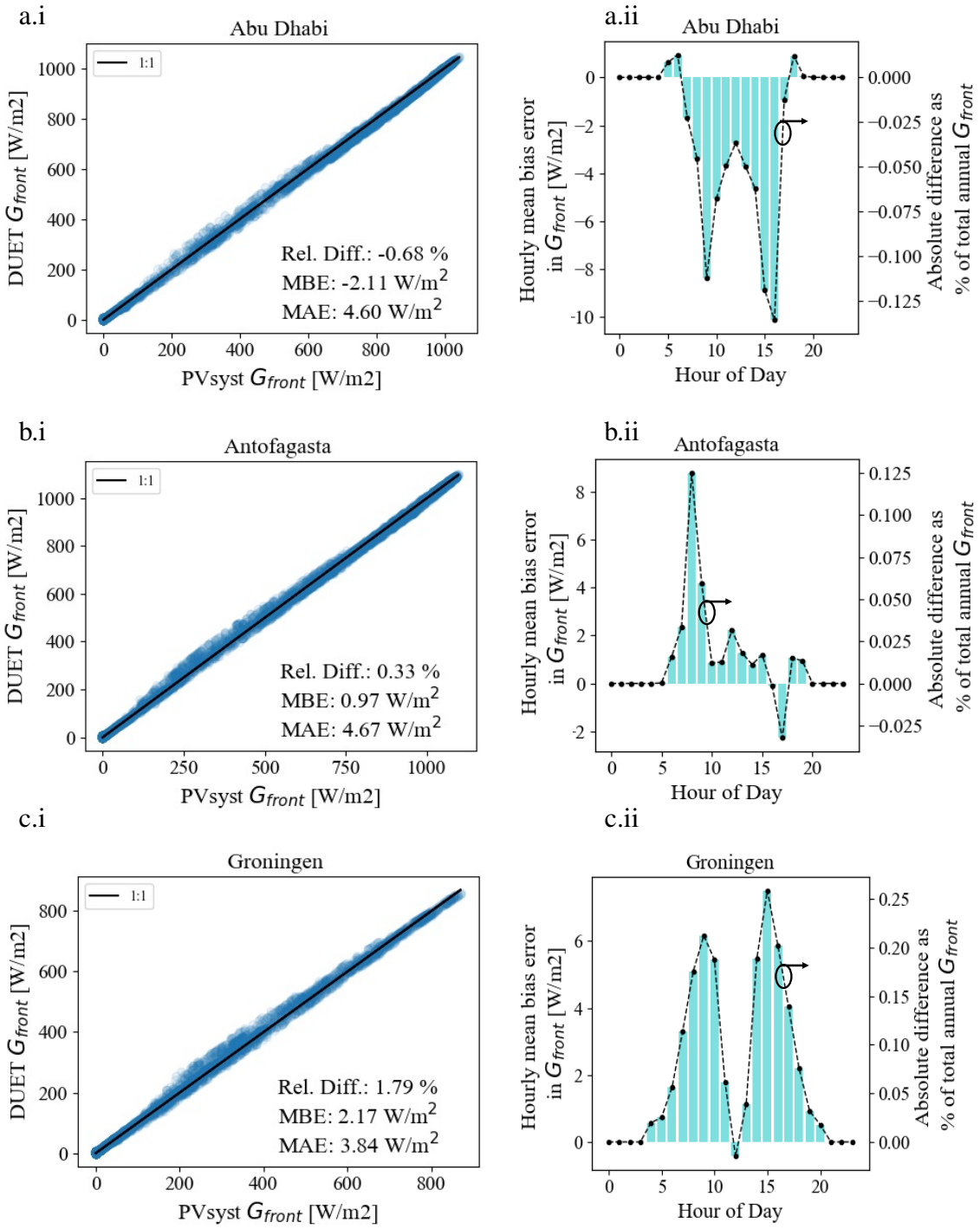
Horizontal N-S Single Axis Tracking
Albedo 0.25 (grass)
Row pitch = 5.7 m
Ground clearance = 1.2 m
10 rows, 20 modules per row
Typical Meteorological Year files

Figure 3.21: Description of IEA PVPS Task 13 Bifacial Modelling Comparison fixed-tilt Scenario 1 described in [2]. DUET v.uO-2020 irradiance results presented in Fig. 3.22 and 3.23 represent a single module at the center of an array. PVsyst v6.86 irradiance results represent a single sample line at the centre of a row of unlimited length [40, 149].

no symmetrical trend in hourly front irradiance MBE (Fig. 3.22.B.ii), perhaps due to sky conditions with significantly greater direct beam contribution than in Groningen but with a lower direct beam contribution than Abu Dhabi. If DUET v.uO-2020 underestimates direct beam irradiance contribution compared to PVsyst and overestimates diffuse contribution to front irradiance, then Antofagasta is an example of a location where these two discrepancies may largely cancel out for these specific parameters and this array geometry.

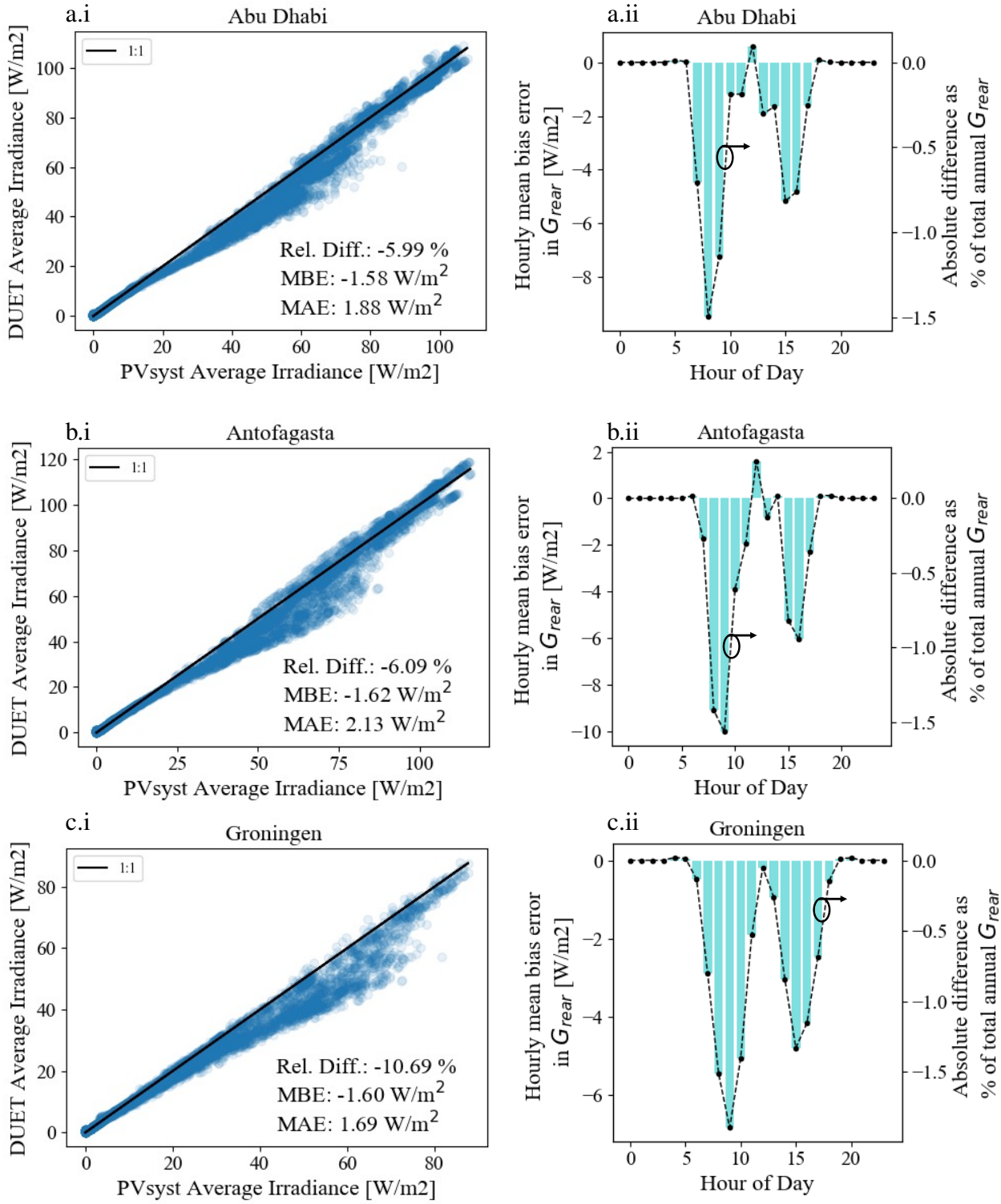
Considering the rear of the tracker in Fig. 3.23, DUET v.uO-2020 underestimates annual rear insolation compared to PVsyst by a relative -6 to -11% across the three locations. The average hourly MBE reaches -7 to -10 $\mathrm{W/m^2}$ depending on location, with all three demonstrating a similar shape in average hourly rear irradiance MBE across the day with peaks at hours with high tilt angle in the morning and afternoon. Upon visual inspection, this shape is analogous to the Groningen front irradiance MBE in Fig. 3.22.c.ii, but reflected across the *x*-axis. Since Groningen experiences highly diffuse conditions, the similar but opposing shapes in front and rear irradiance MBE suggest that the discrepancy between modelled rear plane-of-array irradiances in Fig. 3.23.a-c.ii might arise from a difference in radiance distribution across the sky dome or a difference in tracker angle. It is unlikely to result from a difference in inter-row shading calculation, such as differing row transparency, since DUET front and rear irradiance would *both* be overestimated or underestimated with respect to PVsyst in that case.

Tracker angle dictates the portion of the diffuse sky visible to the module, making this parameter a good candidate to explain such a discrepancy in diffuse contribution. If the DUET DUET v.uO-2020 tracker angles tended to be closer to horizontal on average than in PVsyst v6.86, DUET would overestimate front irradiance and underestimate rear irradiance compared to PVsyst. This tilt angle discrepancy would cause the front of the module to "see" more of the sky and the rear to see less – thereby increasing and decreasing the sky view factor in the front and rear cases respectively. This is the behaviour we seen in Figures 3.22.c.ii and 3.23.c.ii for the highly diffuse Groningen case. This tilt angle discrepancy could arise from a difference in sun position or from a difference between the module length and row spacing which all dictate the tilt angle through a backtracking algorithm. The sun position and the backtracking algorithms may themselves differ between DUET v.uO-2020 and PVsyst v6.86. Further comparison between models and intermediate outputs including sun position and tracker angle is required.



(Rel. Diff. = relative difference, MBE = mean bias error, MAE = mean absolute error)

Figure 3.22: Comparison between DUET v.uO-2020 and PVsyst v6.86 front irradiance for IEA Bifacial Modelling Comparison single-axis tracked scenario S4 [2] in three locations: (a-c.i, left) DUET (blue) vs. PVsyst average front irradiance. Black line indicates perfect agreement with PVsyst. (a-c.ii, right) Average hourly MBE in DUET vs. PVsyst average front irradiance on left y-axis; annual difference in front insolation by hour of day as a percent of total annual front insolation on right y-axis.



(Rel. Diff. = relative difference, MBE = mean bias error, MAE = mean absolute error)

Figure 3.23: Comparison between DUET v.uO-2020 and PVsyst v6.86 rear irradiance for IEA Bifacial Modelling Comparison single-axis tracked scenario S4 [2] in three locations: (a-c.i, left) DUET (blue) vs. PVsyst average rear irradiance. Black line indicates perfect agreement with PVsyst. (a-c.ii, right) Average hourly MBE in DUET vs. PVsyst average rear irradiance on left y-axis; annual difference in rear insolation by hour of day as a percent of total annual rear insolation on right y-axis.

Since PVsyst applies a static structure shading factor to each timestamp and DUET calculates dynamic per-timestamp rear shading, a residual rear irradiance deviation is expected. This deviation will peak at high tilt angles since the PVsyst annual structure shading factor applied is effectively the weighted average of DUET hourly shading factors. This weighted average biases the shading factor to be most physically-representative at noon hours that have significant GHI and low tilt angle; thus, the deviation between the models' rear irradiance predictions should be minimal near solar noon as is seen in Fig. 3.23.a-c.ii. However, DUET v.uO-2020's calculated hourly rear structure shading only varies by $\pm 0.8\%$ absolute throughout the day in all locations and thus cannot fully explain the discrepancy in average rear irradiance seen in Fig. 3.22.a-c.ii. Additionally, the temporal variation in DUET v.uO-2020's calculated structure shading is inconsistent across the three locations, unlike the consistent pattern in Fig. 3.23.a-c.ii.

Future comparisons between DUET and PVsyst should include:

- comparison of all available intermediate calculations and per-timestamp parameters to facilitate analysis of irradiance or yield discrepancies, in particular tracking angle and sky model comparison in PVsyst vs. DUET;
- comparison to a fixed-tilt analysis to determine whether discrepancies between software are unique to phenomena present in either a tracking or fixed cases;
- comparison to measured front and rear plane-of-array irradiance for a field site, where possible, to determine which software best matches measured data;
- comparison to a ray tracing software to quantify per-timestamp and annual discrepancies between 2D VF, 3D finite element, and ray tracing approaches; and
- comparison of modelled DC energy yield prior to light-induced degradation, soiling, potential induced degradation (PID) losses to determine the instantaneous impact of discrepancies in cell temperature, maximum power, and current mismatch loss calculations.

3.6 Computational efficiency

Computational speed is a key performance metric for PV performance prediction software. In PV array design, fast modelling allows for efficient work flow and in-depth optimization. As world-

wide installed PV capacity reaches multi-TW scale [150], performance models for design, financing, and monitoring will need to be as computationally efficient as possible to minimize the high performance computing requirements - and resulting operational costs and electricity demand - of the industry.

In addition to the architectural choices already mentioned in previous sections such as the bounding volume hierarchy, the software improvements described in the following section contributed significantly to decreases computation time in DUET v.uO-2021+. In particular, vectorization and just-in-time compiling alleviate the burden of data type inference and employ partial compiling to provide some of the efficiency benefits of a compiled language like C within a Python implementation of the model. (See Section 2.4.3 for further definition of these techniques). This section also discusses the computational intensity of varied surface mesh densities and the balance between accuracy and computational efficiency in finite mesh analyses.

3.6.1 Vectorization

In early version of the described model, the coupling, compensation and shading functions looped over each ray in the scene with nested for-loops. This inefficient structure resulted in prohibitively long computation time; for each iteration of the hundreds of for-loops in the program, the Python interpreter had to determine the type of each variable in every line and load data from new memory addresses before executing the instructions in that line.

However, all ray operations in DUET v.uO-2024 are deterministic and independent of one another; thus, the bounding volume hierarchy and ray-primitive intersection algorithms are perfect candidates for vectorizaton using the *NumPy* array data structure and functions from the *NumPy* Python library. All rays that follow same bounding volume hierarchy can be checked for shading through a single sequence of vectorized functions, significantly reducing computational intensity. Due to the broadcasting required for this implementation, the vectorized version of the model is memory-limited under extremely high surface mesh densities. However, these densities are much higher than is required for the simulations performed in this thesis.

To test the computational efficiency improvements of the fully vectorized code, we can consider a single day simulations for June 4 of the Typical Meteorological Year in Ottawa, ON, Canada in two versions of DUET v.uO-2024: (1) with the original for-loop functions, and (2) with vectorized

replacement functions. Just-in-time compiling is applied in both cases, and the simulation emulates a 2P single axis tracked system with 5 rows, 3 tables per row, a rectangular torque tube, and no vertical pilings. For this case, the vectorized version takes **90.1% less time** to run than the for-loop version.

3.6.2 Just-in-time compiling

When using the *Numba* Python library, the *JIT compiler* compiles functions with @njit decorators only once, caching the machine code for future execution in the event that the function is called again. We can consider the same single module in a 2P single axis tracked system with 5 rows, 3 tables per row, a rectangular torque tube, and no vertical pilings, and run a single day simulation for June 4 of the Typical Meteorological Year in Ottawa, ON, Canada in another two versions of DUET v.uO-2024: (1) with vectorized functions with JIT compiling through Numba and (2) with vectorized functions without JIT compiling, only the basic Python interpreter. For this case, running the simulation with JIT compiling takes **18.5% less time**.

3.6.3 Mesh density

While the source code is now vectorized and the JIT compiler caches some pre-compiled machine code for re-use, the size of the NumPy arrays representing the surface meshing still affects computation time. Figure 3.24 shows the computation times for a day-long simulation with a range of mesh densities for each of the module, ground, and sky surfaces. The simulation is for the same June 4 of the typical meteorological year in Ottawa, ON, Canada for a module in a 2P system with 5 rows, three tables per row, 21 modules per table, a module frame, and a rectangular torque tube. These times are normalized to the computation time of the base mesh density for each surface in DUET v.uO-2024: 4x4 mesh per solar cell, 18x20 ground mesh, and 18x10 sky mesh. For example, "2x" sky density refers to 2x18= 36 azimuth divisions and 2x10 = 20 elevation divisions.

Ground and module density have a similar impact on timing when divisions are doubled, with 3.4 and 3.6 times longer computation time than their base density cases, respectively. Doubling sky element divisions takes only 1.25x longer than base density since fewer shading and coupling calculations involve the sky mesh than the ground or module meshes. Importantly, decreasing the module mesh density by half to a 2x2 mesh while maintaining base sky and ground densities takes

0.28x as long as base density - a significant improvement in computational efficiency.

To test the impact of surface mesh density on energy yield, Figure 3.25 shows the energy yield for the same day-long simulation normalized to the highest density results for each of the surfaces. The module line in light green with star markers shows that the decrease in module mesh density to 2x2 has little effect on the energy yield and may provide a better computation-accuracy balance than the 4x4 mesh. Similarly, increasing sky mesh density has a negligible impact on energy yield, suggesting that the base density is sufficient for both speed and accuracy.

In contrast, the base density for the ground mesh results in an energy yield for this simulation day that is $>0.5\%$ above the highest resolution energy yield. This suggests that either: (a) the compensation factors in Section 3.3.2 are unable to fully account for the discrepancy between finite element and VF approaches or (b) the ground and module shading patterns converge around 2x ground mesh base density. The improved accuracy is almost entirely due to the increasing ground radial resolution; doubling the ground radial resolution but not the azimuthal resolution maintains the same accuracy as doubling both radial and azimuthal divisions and is only 1.75x slower than the base resolution case. Therefore, we can propose a new base density of a 2x2 cell mesh, 18x40 ground mesh, and 18x10 sky mesh for a computation speed that is twice as fast as the previous base density settings and which demonstrates improved energy yield accuracy.

Future work should include comparisons to measured field data under multiple sky conditions at multiple mesh densities as well as an assessment of computation time vs. density for other surface meshing schemes such as triangular ground meshing.

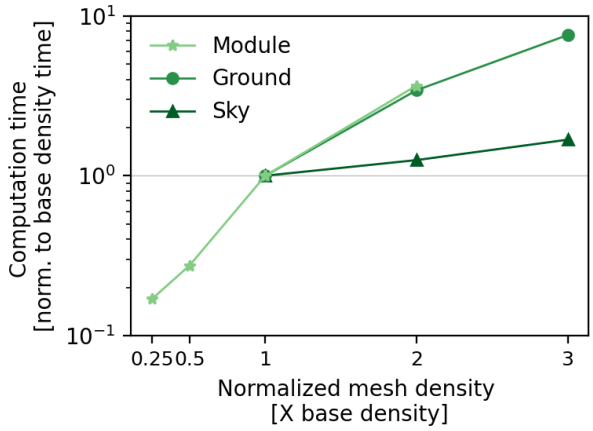


Figure 3.24: Normalized per-module *computation time* as a function of mesh density for a 2P single-axis tracked system for June 4th of the Ottawa Typical Meteorological Year. Mesh density is normalized to the base density: 4x4 mesh per solar cell, 18x20 ground mesh, and 18x10 sky mesh. E.g. 2x normalized sky mesh density = 36x40 sky elements. Computation time is normalized to base mesh density computation time in DUET v.uO-2024.

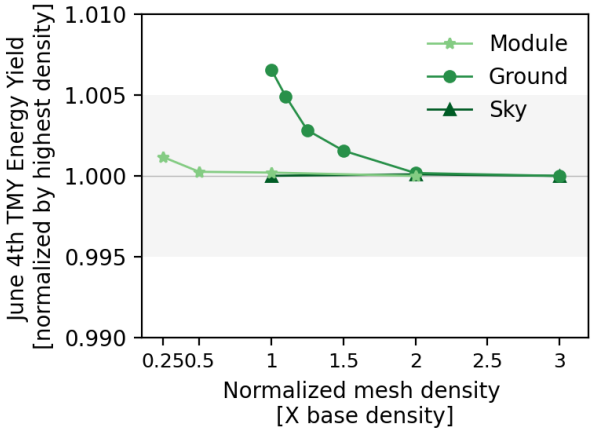


Figure 3.25: Normalized per-module *energy yield* as a function of mesh density for a 2P single-axis tracked system for June 4th of the Ottawa Typical Meteorological Year. Mesh density is normalized to the base density: 4x4 mesh per solar cell, 18x20 ground mesh, and 18x10 sky mesh. E.g. 2x normalized sky mesh density = 36x40 sky elements. Energy yield is normalized to base mesh density energy yield in DUET v.uO-2024.

4 Use-cases in tracking PV

In 2023, 40% of global crystalline silicon PV capacity was installed on single-axis trackers, and 35% of silicon PV module market share consisted of bifacial modules [17]. These two technologies have co-developed over the last decade, necessitating the development of new modelling tools, features, and parameters to quantify the performance of bifacial PV on trackers. The following three sections shed light on three question formed within this context:

1. How does irradiance non-uniformity across a row of trackers impact energy yield?
2. To what degree do reflections with high angles of incidence off of supportive racking structures contribute to energy yield?
3. How does introducing a second, azimuthal axis of rotation impact bifacial PV energy yield and bifacial gain?

4.1 Inter-module edge brightening and current mismatch loss

PV performance software that are built on 2D view factor models - such as PVsyst [40, 149] and NREL's System Advisory Model (SAM) [100] - calculate bifacial PV energy yield based on a cross-section of irradiance at the center of an infinite row or *shed* of PV panels, neglecting any gain or loss due to non-uniformity across the row. Most 2D view factor software allow a corrective factor to account for current mismatch loss which is the current loss due to non-uniform irradiance across cells within a module or modules within a string. For example, PVsyst bifacial "mismatch loss factor" [151] is meant to capture current mismatch loss to rear irradiance variation; the "module mismatch loss" is meant to capture the spread in standard test conditions performance for modules within a string [152], and the "string mismatch" tools are meant to quantify the effects of temperature or irradiance variation between multiple strings [153]. However, users must estimate these parameters or pre-compute them using other software that allow 3D irradiance sampling at the rows edges and near table gaps. Without widespread use of 3D performance models in industry, the range of acceptable values for these parameters is not yet well understood for all system types and sizes.

The graphical user interface for NREL's ray tracing software, *bifacial_radiance*, also defaults to sample a single cross-section of irradiance along the collector width at the center of 7 rows of 20 modules [154, 155]. However, researchers have modified this open-source software to provide irradiance maps for entire modules and rows [3, 42]. Zhao et al. [102] ran simulations in the Rhinoceros 3D ray tracing software for all 19-columns in a tracker, reporting a 0.22-0.24% current mismatch loss for 1P and 2P systems. Deline et al. [42] simulated a 5.8-8.3% increase in irradiance at the edge of a 20-module row in a 1-in-portrait array resulting in a 1% increase in total insolation annually. This study also showed that a 0.15% inter-module mismatch loss counteracts the energy yield gain due to this edge brightening. The authors note that this is an upper bound for expected edge brightening due to the small system size and that the topic warrants further investigation for other plant designs.

In this chapter, DUET v.uO-2022 simulations demonstrate the impact of inter-module irradiance non-uniformity and mismatch loss on energy yield for the fixed-tilt and horizontal single-axis tracked (HSAT) 2P test bed at 55°N at the Technical University of Denmark (DTU) [123]. This test site is described in Section 3.1.III and Ref. [86]. As seen in that section, DUET v.uO-2021's rear irradiance predictions were validated to a mean absolute error of less than 4 $\mathrm{W/m^2}$ at inner positions on tables at this site; additionally, a modelled energy yield with a mean absolute error from measured energy yield of 14.6 and 18.0 mW/Wp was found based on the assumption that central modules in each table were representative of the electrical response of the full table.

Riedel-Lyngskaer et al. [156] measured central and edge irradiance for a tracker in the same DTU system over grass, with 20 silicon reference cells spanning the collector width in both locations within the row. That study demonstrated approximately 50 $\mathrm{W/m^2}$ edge brightening for noon on a clear August day in Denmark. The authors also modelled the irradiance at each of the reference cells in bifacial_radiance. Applying measured irradiance to cell-level electrical calculations in *pvmismatch* [41], and assuming an irradiance equal to the average of edge modules and central modules for all unmeasured module columns, the electrical simulations showed a maximum current mismatch loss of 0.25% at solar noon on the clear day. Analogous current mismatch losses calculated with modelled irradiance agreed to within approximately 0.07% absolute.

The following sections quantify the energy yield gain – and the resulting improvement in energy yield accuracy – when modelling irradiance across all modules in the small test bed, as compared

to calculating energy yield using a central module approximation.

4.1.1 Methodology

This study compares three methods to model the energy yield of a row of modules. To calculate row energy using the three methods explained below, optical and electrical simulations were performed in DUET v.uO-2022 for each module within a row of HSAT and fixed-tilt modules in the DTU test bed. The DTU system rows are each composed of a single tracker with two tables, as shown in Fig. 4.1. The HSAT row is the 6th of 8 rows (counting from the west) and the fixed tilt row is the 4th of 8 rows (counting from the north). Further details on module electrical parameters and array geometry are available in Section 3.1 and [86, 123].

The three methods to calculate row energy yield are as follows:

1. ***Central module approximation:*** In this method, the central set of modules in each table of the tracker is considered to be representative of the electrical behaviour and energy yield of all modules in its associated string. Figure 4.1 shows the representative modules in light blue with their associated strings depicted as orange lines. Therefore, the row IV curve is found as the parallel combination of the 4 central module IV curves, each weighted by the number of modules per string. The annual energy yield is found through the annual summation of the maximum power points of the resulting row IV curve at each timestamp. Of the three approaches discussed here, this approach most closely aligns with the 2D view factor method which samples irradiance at the central line in an infinite shed.

2. ***Full row no mismatch loss:*** In this method, the per-timestamp row power is the summation of maximum power points for all modules in the tracker, demonstrating the available power including edge brightening prior to inter-module electrical interconnection. Thus, the result neglects any power loss due to irradiance non-uniformity between modules. The annual energy yield is then the annual sum of per-timestamp row energy yield.

3. ***Full row with mismatch loss:*** In the final method, the per-timestamp row IV curve is formed by the series and parallel summation of all per-timestamp module IV curves according to the electrical layout in Fig. 4.1 with 22 modules in series per string and 4 strings in parallel

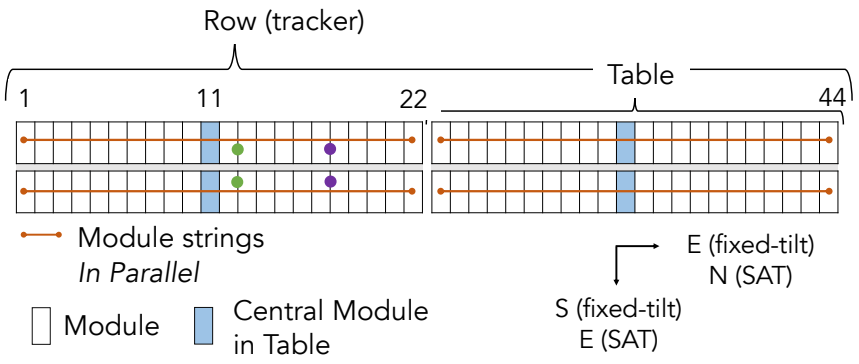


Figure 4.1: Birdseye view of a 2P row in the fixed-tilt and single-axis tracked (SAT) systems at the Technical University of Denmark (reproduction of Section 3.1 Fig.6b). Only blue modules are simulated in the *central module approximation method*. All modules are simulated in the *full row with no mismatch loss* and *full row with mismatch loss* methods; the latter represents the current mismatch losses due to interconnection across the four multi-module strings in orange.

per row. The annual energy yield is the annual sum of per-timestamp row IV curve maximum power. Of the three methods, this approach is the most physically representative and computationally intensive. In this study, the full row simulation in DUET included 202,752 irradiance sample points spread across the row in 4x4 meshes on the front and rear of each cell.

The comparison of approaches (2) vs. (1) quantifies the edge brightening gain in potential energy yield, illustrating the impact of additional front irradiance at the row edges due to reduced inter-row shading and additional rear irradiance at the edges due to reflections from unshaded ground extending beyond the array. The comparison of approaches (3) vs. (2) quantifies the current mismatch loss, demonstrating the power loss due to non-uniform photogenerated current throughout the row. Section 3.4.1 provides an example of module IV curves under such non-uniform illumination and discusses current mismatch principles that are also present in the series combination of inter-module IV curves. Finally, comparison of approaches (3) vs. (1) gives the net gain that accounts for both the edge brightening and current mismatch loss. These three gain metrics can be used to discuss the value of micro-inverters or power optimizers - which limit current mismatch losses by direct current (DC) to alternating current (AC) or DC-DC conversion prior to inter-module interconnection, or to quantify the electrical mismatch loss factors required for use in 2D view factor models.

The following section examines the resulting irradiance profiles, non-uniformity in module energy yield, and three gain metrics for the chosen rows. We will also consider the impact of these approaches on the error between modelled energy yield and measured field data.

4.1.2 Results & Discussion

Irradiance non-uniformity Based on the 200,000+ irradiance points sampled across the row in DUET v.uO-2022's optical simulation, Fig. 4.2 and 4.3 shows average hourly irradiance and non-uniformity, respectively, across all modules for the two systems. The front profiles appear at the top of these figures and the rear profiles at the bottom. Fixed tilt profiles are to the left, while HSAT profiles are to the right. Figure 4.2 shows average irradiance for fixed-tilt and HSAT irradiance with the same colour scale for direct comparison between system types, while Fig. 4.3 provides greater detail on irradiance non-uniformity.

Average front and rear irradiance in the fixed-tilt system range from 239-257 $\mathrm{W/m^2}$ and 8.9-37.1 $\mathrm{W/m^2}$ as shown in Fig. 4.2. This equates to a rear-to-front irradiance ratio ranging from 4-14%. With lower cosine losses than the fixed-tilt system, HSAT average front irradiance and rear irradiances range from 290-295 $\mathrm{W/m^2}$ and 9.5-42.3 $\mathrm{W/m^2}$ – a similar 3-14% rear-to-front irradiance ratio. While irradiance non-uniformity begins to appear across the rows in this figure – particularly on the rear, the edge brightening is more visible if we subtract the minimum average irradiance value from each row to find the average hourly absolute irradiance non-uniformity in $\mathrm{W/m^2}$, as in Fig. 4.3 with front and rear of both fixed-tilt and HSAT rows on the same colour scale.

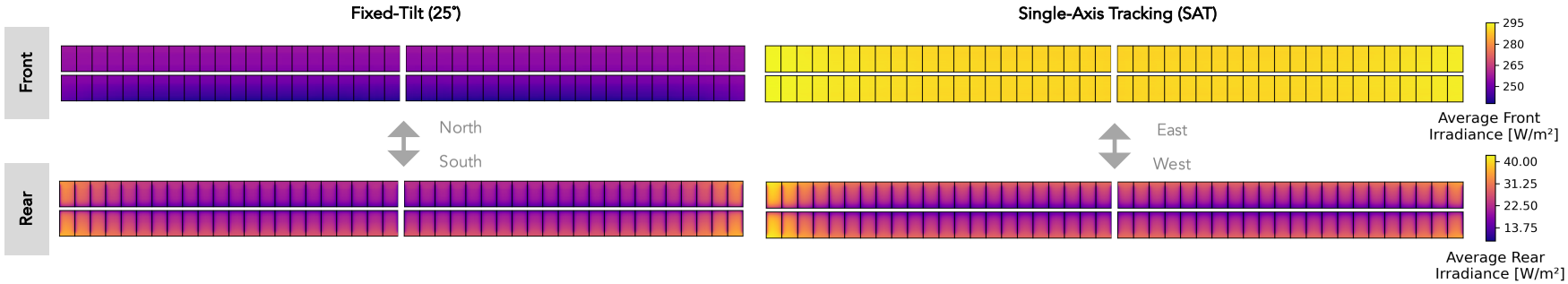


Figure 4.2: Average hourly modelled *irradiance* on front (top) and rear (bottom) of fixed 25° tilt row (left) and a single-axis tracking (SAT) row.

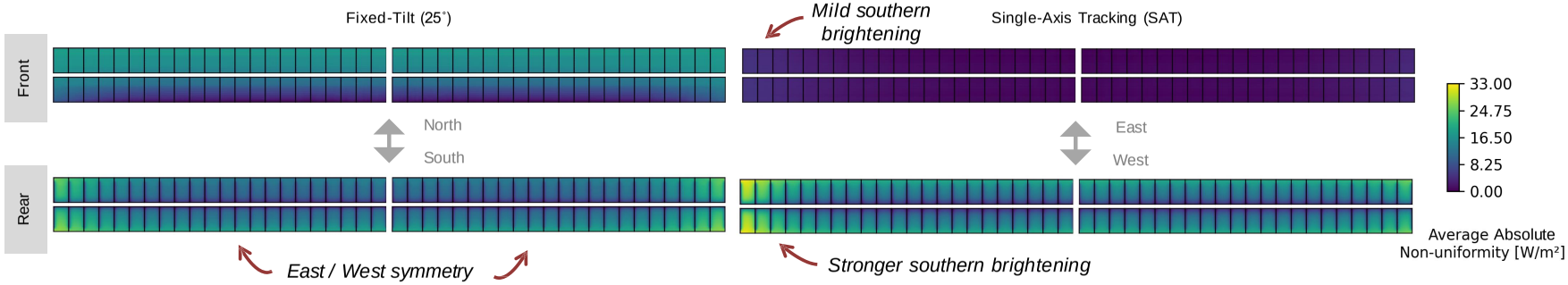


Figure 4.3: Average modelled *irradiance non-uniformity* on front (top) and rear (bottom) of fixed 25° tilt row (left) and a single-axis tracking (SAT) row (i.e., the irradiance in excess of the lowest irradiance point in the row).

For the 2P fixed systems in Fig. 4.3 (left), brightening is now visible at the western and eastern edges of the row by a maximum deviation of 18.3 $\mathrm{W/m^2}$ for the front and 28.2$\mathrm{W/m^2}$ for the rear. Average total irradiance for the row is 0.52% higher than the irradiance at the center of each of the two tables. Edge modules have a greater unshaded field of view of the sky than central modules, resulting in lower north-to-south front irradiance differential. Decreased ground shading at the row edges leads to rear side edge brightening that is relatively symmetrical to the east and west of the fixed-tilt system. These irradiance profiles show that edge brightening does indeed have a larger relative impact on bifacial rows than on monofacial rows due to the added rear brightening.

For the 2P HSAT system in Fig. 4.3 (right), a mild 5 $\mathrm{W/m^2}$ front edge brightening is only barely visible on the southern end of the row. The HSAT profile is relatively uniform due to backtracking that avoids inter-row shading of direct light. The rear profile shows the strongest brightening seen on either face of either system with 32.7 $\mathrm{W/m^2}$ of brightening on the southern end. The shadow cast on the ground by the row falls to the north, lessening the northern edge brightening on the rear. With this strong rear and mild front southern edge brightening, the average total irradiance for the row is 0.35% higher than the irradiance at the center of the each of the two tables. This HSAT profile shows a high degree of symmetry across east and west tiers for the average of all timestamps in the year; however instantaneous non-uniformity between the tiers is likely greater than shown here.

Energy yield The edge brightening seen in the above irradiance profiles results in higher photogenerated current in edge modules. If the modules were electrically isolated from one another, this current gain would lead to higher energy yield in edge modules. In the spirit of this thought exercise, Fig. 4.4 shows the relative gain in energy yield for each module in the row as compared to the energy yield of the central modules in each table, shown at the vertical black dotted lines.

While the edge modules in the eastern and western HSAT tiers show similar gains (Fig. 4.4, bottom), the fixed-tilt southern tier (top, magenta) experiences more non-uniformity than the northern tier (top, cyan). This is primarily due to front edge brightening that results from reduced inter-row shading, seen in the north-south irradiance gradient in Fig. 4.3. Figure 4.4 also shows the stronger southern gain in HSAT systems to the bottom left and an energy yield gain of less than +0.25% for modules north of the 40 cm slewing drive gap at the center of the row. Overall, edge modules in the

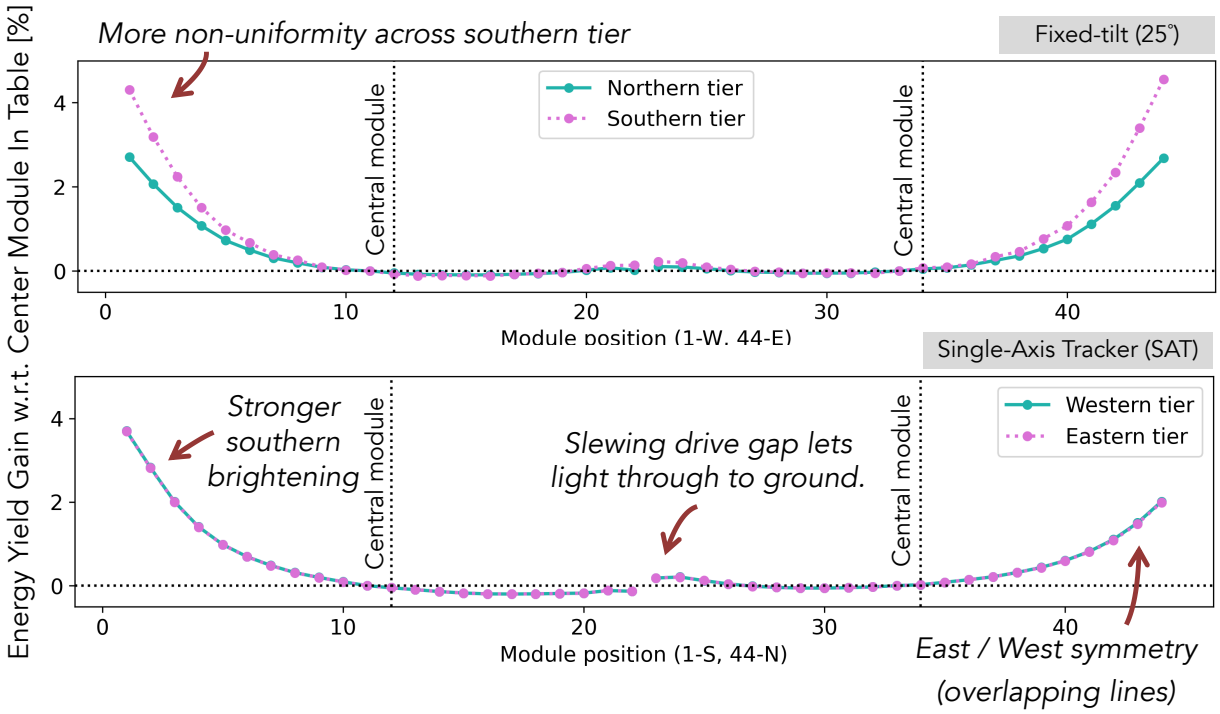


Figure 4.4: Annual energy yield gain with respect to (w.r.t.) center module in each table (vertical dotted line) for each module of the fixed-tilt row (top) and single-axis tracked row (bottom). (W = west, E = east, S = south, N = north).

fixed-tilt system generate 2.7-4.5% more energy annually than the central modules. For the HSAT system, the edge modules produce 1.9-3.7% more energy annually than central modules. This comparison allows us to understand the additional energy yield that edge modules would contribute to row energy yield if they were equipped with micro-inverters or power optimizers.

However, if the modules are connected in series across each tier in each table, as shown by the orange lines in Fig. 4.1 for the DTU site, some of this additional energy available due to edge brightening will be lost as heat. A large portion of the excess photogenerated carriers present in the edge modules will build up at the interface with the central lower irradiance modules, recombining before extraction at the string terminals. This current mismatch loss partially counteracts any edge brightening gain – an effect we can see by examining three gain metrics for the DTU rows. Table 3 shows a 0.51% and 0.24% edge brightening gain for fixed-tilt and SAT, respectively, when comparing the *full row no mismatch* method with the *central module approximation*. This non-uniformity results in a current mismatch loss of -0.21% and -0.09% for the two systems – the relative difference in yield for the *full row with mismatch* method compared to the *full row no mismatch* method.

		Energy Yield Comparison (Enhanced vs. Baseline)		
Baseline	Enhanced	Fixed-Tilt	SAT	
Centre Module Approximation	Full Row, No Mismatch	+0.51%	+0.34%	Edge Brightening Gain
Full Row, No Mismatch	Full Row, with Mismatch	-0.21%	-0.09%	Current Mismatch Loss
Centre Module Approximation	Full Row, with Mismatch	**+0.30%**	**+0.25%**	**Net Gain**

Like in PVsyst

Table 3: Energy yield comparison for the three row modelling methods described in 4.1.1. Edge brightening gain (green) and current mismatch loss (red) result in a net energy yield gain (green) with respect to the *central module approximation*.

As mentioned above, the mismatch loss can also be interpreted as the approximated avoided loss when using micro-inverters or power optimizers for a system of this scale, neglecting inverter or converter efficiency.

When comparing the most physically representative *full row with mismatch* loss method to the *central module approximation*, the net gain in energy yield is 0.3% and 0.25% for the fixed-tilt and SAT systems, respectively. This net gain also corresponds to the summation of the positive edge brightening gain and the negative current mismatch loss. Since the central module approximation approximates to the 2D view factor approach in this analysis, the net gain represents the relative energy yield difference that 2D view factor models, such as PVsyst, should aim to capture in user-defined mismatch factors. However, PVsyst v6.86 mismatch factors only allowed for a loss due to string irradiance non-uniformity, leaving no opportunity to implement a positive gain within a specified loss factor.

This 0.25-0.3% net gain should also be considered an upper bound for the effect of edge brightening gain and current mismatch loss in a 2P utility scale system at similar height and row spacing as the DTU site, since the ratio of edge modules to central modules is lower for utility-scale applications than for this small scale test. The analysis also neglects any shading from nearby buildings, combiner boxes, and pilings, which would contribute to increased current mismatch loss.

Validation The model validation in Section 3.1.III compares a modelled energy yield based on the *central module approximation* with a measured row energy yield that is the parallel summation of four parallel string yields, each composed of 22 modules. The resulting mean bias error (MBE) and mean absolute error (MAE) in bifacial energy yield is plotted in Section Fig. 4.5, with spread caused by the use of three different temperature models. For example, the Faiman cell temperature model gives -4.9 and -2.8 mW/Wp MBE and 14.6 and 18.0 mW/Wp MAE. Recomputing these error metrics using modelled energy yield based on the *full row with mismatch loss* method with the Faiman temperature model provides the -3.9 and -1.6 mW/Wp MBE and 14.3 and 17.6 mW/Wp MAE shown by the green circles in Figure 4.5. This corresponds to an absolute 0.3% improvement in relative error between measured and modelled data.

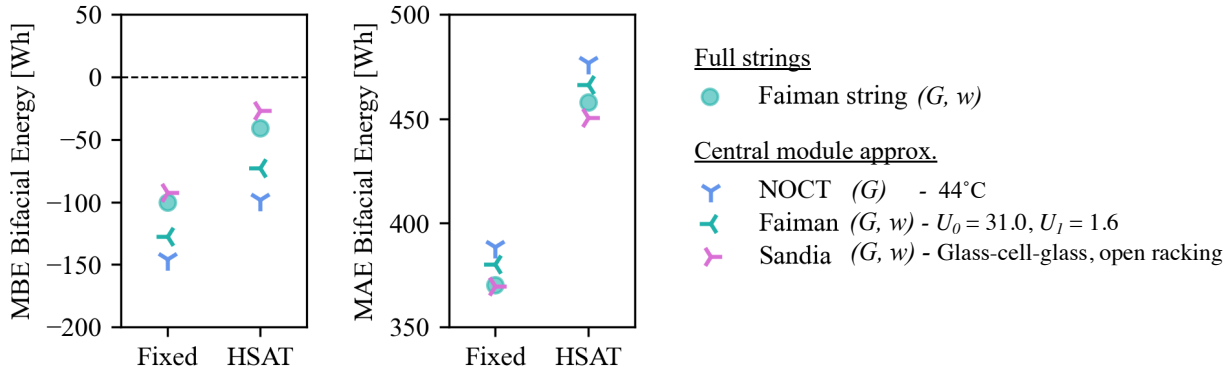


Figure 4.5: Mean bias error (MBE, left) and mean absolute error (MAE, right) between DUET v.uO-2022 modelled and measured data for the single-axis tracking row at the Technical University of Denmark. This image is a reproduction of Section 3.1 Fig. 9, modified to include the *full row with mismatch loss* method with the Faiman temperature model, labelled as "Faiman string" (green circle).

As demonstrated in Fig. 4.5, the accuracy improvement afforded by modelling all modules in the row falls within the uncertainty in energy yield introduced by the choice of cell temperature model (i.e., Faimain, Sandia or NOCT). While edge brightening and the resulting current mismatch loss has a diminishing effect with system size, temperature model uncertainty affects all modules in an array of any size. Thus, future research should focus on reducing temperature modelling uncertainty as a priority over further investigations into edge effects.

Conclusion & future work An analysis of irradiance uniformity across bifacial fixed-tilt and single-axis tracked test beds at 55°N showed edge brightening on both the front and rear faces of

both systems, resulting in +0.3% and +0.25% net energy yield gains, respectively, compared to conventional 2D view factor-style energy yield approximation (i.e., based on a central module or central irradiance sample line). This gain is the additive combination of a positive edge brightening gain and negative current mismatch loss, and it accounts for per-timestamp IV curve summation for the 88 modules in the simulated tracker. Since the small test bed in this study has a higher edge-to-center module ratio than rows in utility scale systems, these net gains should be considered an upper bound for all systems. The presented *full row with mismatch* method, which accounts for the optical and electrical behaviour of all interconnected modules, resulted in an absolute 0.3% improvement in relative error between measured and modelled data as compared to the relative error found using the *central module approximation*. The magnitude of this improvement is within the uncertainty introduced by differing models for cell operating temperature, exemplifying that future research should prioritize reducing uncertainty for modeled phenomena that affect all modules in a system of any size.

4.2 Supportive structure shading and reflection

In DUET v.uO-2024, all supportive racking structures are considered fully absorptive and are represented by primitives with a transparency factor of $\alpha = 0$. Therefore, reflections off racking components are not modelled. Contrary to this assumption, Pelaez et al. demonstrated in [157] that modelling a 44% reflectivity for the torque tube in a 2P system in Cairo in the bifacial_radiance ray tracing software reduces rear structure shading factor by more than 2% absolute for all tier gap dimensions. Additionally 5-13 cm tier gaps resulted in annual rear insolation *gains* compared to the no-racking scenario, suggesting that the reflection completely offsets torque tube shading on an annual basis in that location. Guerrero et al. [158] reported a similarly small 0.8% shading factor for a 2P system on a sunny day based on bifacial_radiance modelling with a reflective torque tube, suggesting that reflection almost entirely mitigated rear torque tube shading.

However, neither of these studies showed the impact of incidence angle and Fresnel reflections on the absorption of the additional rear irradiance. McIntosh et al. [117] used PV Lighthouse's Sunsolve Yield ray tracing program with encapsulated module layers to compare east and west modules in a 2P system and found that all non-ground reflections from racking of unspecified reflectivity had negligible impact on the difference in irradiance incident on the two modules; this

result suggests that any incidence angle modifier (IAM) -corrected reflection is either minimal or symmetrical east-to-west. Due to the conflicting non-IAM-corrected and IAM-corrected results in the above studies, it is of interest to the bifacial PV modelling community to quantify the IAM impact on light that is reflected off torque tubes and frames, reaching the module at shallow angles.

4.2.1 Methodology

In 2021, we undertook a study to test the impact of torque tube reflections on rear irradiance, electrical mismatch, and energy yield – including incidence angle effects [3]. Since users can set the reflectivity of any surface within bifacial_radiance, we selected this tool to generate 2D rear irradiance maps of torque tube reflected irradiance, prior to incidence angle modification. We selected DUET v.uO-2020 as the tool to test the impact of an externally-calculated torque tube reflection since the finite element coupling algorithm stores incidence angle data for each ray-surface combination and applies an IAM to each module-incident ray prior to the summation of all irradiance sources. Additionally, the built-in electrical model accounts for 2D irradiance non-uniformity.

For this study, Coathup and Lewis modified bifacial_radiance [155] to include a module frame and to output 2D irradiance maps with 2x4 sample points like those calculated in DUET v.uO-2020 and shown in Fig. 8 in Section 3.1.IV. Two simulations were performed for 1P and 2P single-axis tracked systems in Livermore, California with: (a) fully absorptive torque tubes, purlins, and frame, and (b) with these racking elements set to a reflectivity of 0.75, with 0.9 specularity and 0.2 roughness. The subtraction of irradiance at each sample point in the reflective scenario from each sample point in the absorptive scenario results in the 2D reflected irradiance map for input into DUET. The following algorithm details the approximation of the torque tube irradiance IAM at each module sample point and the introduction of the IAM-corrected irradiance map into DUET v.uO-2020's irradiance source summation.

IAM algorithm for torque-tube-reflected light

1. Find the angular range of torque tube seen by each module sample point in the north-south / east-west plane (assumed limited to the portion between the module purlins at the edge of each module). Divide this angular range into N_{TT} equal sub-angles to form torque tube mesh

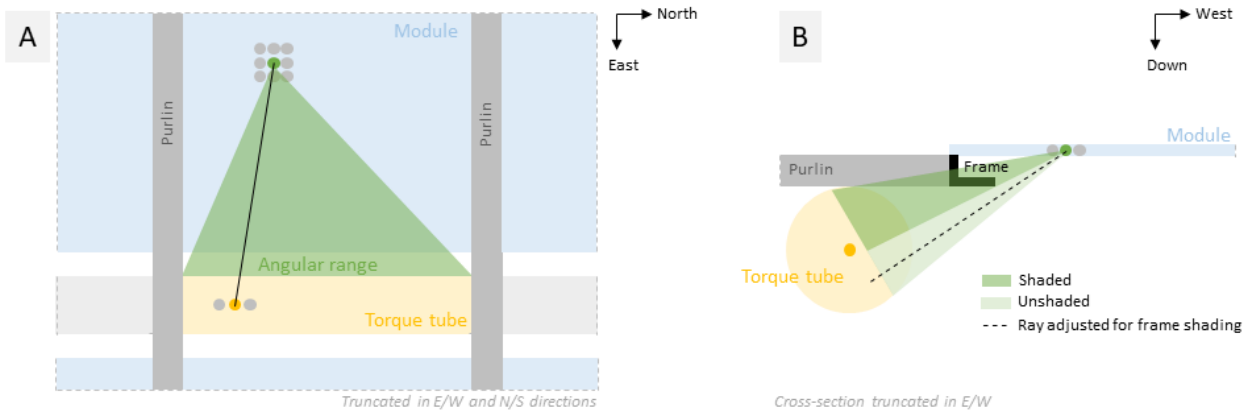


Figure 4.6: (A) Birdseye view in the north-east plane of of a 2P single axis tracker with black ray linking a green module mesh element and a yellow torque tube mesh element. The torque tube mesh elements span the angular range in green. (B) Cross-section of a portion of one module on a 2P tracker with a black ray adjusted to represent the unshaded angular range from the green module element to the yellow torque tube based on frame dimensions.

elements. Calculate the angle of incidence between rays linking each torque tube element from the axis of rotation to each module sample point (Fig. 4.6a).

2. Check whether the frame blocks the field of view from any module sample point to the torque tube in the up-down / east-west plane. Adjust the angle of incidence of frame-intersecting ray such that the adjusted ray represents only the unshaded angular range (Fig. 4.6b).

3. Apply the module IAM to the angle of incidence for each ray. The ASHRAE incidence angle modifier [115] was used for this study.

4. Take the average of the IAM from all torque tube elements for each module sample point, and multiply the resulting 2D IAM map by the 2D bifacial_radiance irradiance map.

5. Add the resulting incidence-angle-modified 2D irradiance map as an additional rear side irradiance source prior to application of the bifaciality factor in the short circuit current calculation.

Assumptions While the bifacial_radiance simulations were performed with a racking material specularity of 0.9 (i.e., a highly directional reflection), the directional information about module-incident irradiance is not available in bifacial_radiance; thus, we assumed a Lambertian reflection equal in all directions for IAM calculations.

This approach also assumes that the irradiance is emanating from an even distribution along the length of the torque tube. The bifacial_radiance shading maps demonstrate that this is not always true, since purlins that rest atop the torque tube block the low zenith beam in winter months, casting a shadow along the length of the torque tube and biasing the reflected light toward the north of the module. Since the geometry of the purlins and the beam is known at each timestamp, the applied IAM approach could be adjusted to account for purlin shading by shifting the southernmost torque tube point northward to the southernmost unshaded point.

4.2.2 Results & Discussion

This simulated results with the torque tube reflection included show that the IAM losses of module-incident, racking-reflected irradiance are indeed greater than the IAM losses of all other irradiance sources. Despite this irradiance reduction, the torque tube reflection at 0.75 reflectivity increases rear silicon-incident irradiance by 3% and 3.8% for 1P and 2P systems, respectively. At no point did the reflection entirely offset the structure shading losses. Interestingly, and perhaps intuitively, the racking reflections were concentrated toward the regions affected by structure shading; therefore, the racking reflections actually offset this shading, decreasing the irradiance non-uniformity across the module rear along with associated the current mismatch losses. The resulting 0.17% and 0.30% total annual irradiance gain from torque tube reflection provided an energy yield gain of 0.11% and 0.18%. (For context, a hypothetical system with 5% bifacial gain, 3% rear irradiance gain would provide a 0.15% gain in total energy yield). The highest hourly energy yield impacts, 0.8% for 1P and 0.4% for 2P, both occurred at high DHI or high zenith hours in which energy yield is already comparatively minimal; thus, both annual and instantaneous effects are comparatively small.

Conclusions & future work This exercise demonstrates how additional irradiance sources or reflective surfaces could be added to DUET with a sequence of meshing, coupling, shading, and IAM application. The sub-0.2% energy yield impact may not justify adding a reflective torque tube surfaces to DUET v.uO-2024's optical model due to additional computational burden. However, an empirical formula could be included if dominant parameters were determined. Since the torque tube, purlin and frame are fixed with respect to the module rear, the reflection is strongly dependent on front and rear plane-of-array irradiance; thus, future work should examine this relationship for

possible empirical formulae. Additionally, repeating this study with a range of reflectivity values would provide energy yield impacts for a range of materials and help determine the impact of torque tube soiling on any energy yield gain.

Finally, Lewis' recent study using bifacial_radiance [104] demonstrates that modelling a 74.5% reflectivity for torque tubes *and* purlins and the module frame in a 2P system in Livermore, California reduces non-IAM-corrected rear irradiance shading loss by 9.1% absolute as compared to fully absorptive racking, leading to an 0.3% energy yield gain and resulting in a final rear irradiance shading loss of 8.5%. Provided that such an analysis be repeated with IAM-correction and demonstrate a non-negligible impact on energy yield, future work should consider the addition of limited density surface meshing to the torque tube, module frame or purlins in DUET v.uO-2024+ to quantify reflected irradiance. These racking mesh elements could be considered as an additional irradiance source with a given reflectivity analogous to ground mesh elements with a modified bounding volume hierarchy.

4.3 Double-axis tracking at 45°N

Single-axis trackers are often selected over fixed-tilt systems when energy yield gain due to tracking decreases levelized cost of electricity despite additional tracker costs. With widespread adoption of bifacial PV on single-axis trackers, it is worth investigating whether double-axis tracking provides sufficient energy yield gain with respect to single-axis tracking to achieve this yield-cost balance. Rodríguez-Gallegos et al. [159] demonstrated that the modelled annual yield of double-axis tracked bifacial PV exceeds monofacial fixed-tilt PV by upward of 40% across all latitudes on average. When considering 2020 estimated installation costs, the authors showed that the levelized cost of electricity for double-axis tracked bifacial PV approaches that of single-axis tracked bifacial PV at latitudes north of 60° N - suggesting possible high latitude applications. However, that analysis neglected energy yield reductions due to adjacent rows, backtracking, or supportive rack shading. Burnham et al. [160] measured a 14% annual bifacial gain and >30% bifacial gain in some winter months for double-axis trackers in Vermont at 44° N. Stein et al. [161] showed instantaneous bifacial gains of 2.5-25% in 6 days of initial data from the trackers at the same site. Few other studies on double-axis tracked bifacial PV exist.

The bifacial PV modelling comparison in the 2021 IEA PVPS Task 13 report showed that none

of the models participating in the modelling comparison could, at that time, model double axis tracking [2]. To the author's knowledge, the following section describes the first implementation of a double-axis tracking bifacial PV performance model with multiple rows, supportive racking, and backtracking - features that would be required to assess whether the additional yield afforded by the secondary axis of rotation offsets additional cost or land-use. The following section describes changes made to DUET v.uO-2023 to allow double-axis tracking and provides a validation and a preliminary tracking comparison at 45° N for Sherbrooke, Québec and Ottawa, Ontario, respectively. In future, higher latitude simulations could be performed to acquire levelized costs of electricity updated with recent installation cost estimates and yield estimates including effects of rack shading and full arrays.

4.3.1 Methodology

Most of the DUET architecture described in Section 3 - namely the racking structures, bounding volume hierarchy, and shading algorithms - was designed to require minimal changes to allow for double-axis tracking implementation. The changes that were necessary impact array geometry, front and rear row set definitions, and backtracking, as described below.

Array geometry A double-axis tracking PV plant commonly consists of multiple rows of tracker heads rotating independently. The tracker heads are spaced out along the length of the row and are often offset in a checkerboard pattern such that a tracker in one east-to-west row aligns with the tracker head two rows away in a north-to-south line as shown in Fig. 2.5.

To achieve this geometry in DUET v.uO-2023, the coordinates of a base tracker head with a specified number of module columns and tiers are calculated at the origin of the scene with a certain tilt and azimuth angle every timestamp. These base coordinates are then duplicated and translated throughout the scene as necessary to form the full array of tracker heads. This allows for an east-west offset in any given row, and spacing between tracker heads, facilitating the checkerboard spacing pattern. Any substantial gaps between tiers in these tracker heads are checked for ray-polygon intersections, but any column gaps between modules are accounted for in the tracker head transparency.

In the bounding volume hierarchy and shading algorithms, these tracker heads are equivalent

to rows in fixed-tilt and single-axis tracking models; each "effective row" is composed of a single table with no table/row gaps. This approach allows the bounding volume hierarchy explained in Fig. 3.9 to remain unchanged; the algorithm first checks rays for intersection with front and rear row-sets (now tracker-head sets) and then for intersection with the individual tracker heads. The bounding volumes for each tracker head are originally set as the maximum possible coordinates in each global coordinate axis for sky-to-ground static shading calculations (i.e, the widest distance across the tracker head polygon plus a radius of rotation) and then updated each timestamp using the coordinates of the polygon corners.

Front and rear row sets In single-axis tracking, the front and rear row-sets can be identified based on the plane-of-array tilt angle; a positive or negative tilt angle dictates the direction that the modules are facing and which rows fall to the front or rear. With an additional azimuthal axis of rotation in double-axis tracking, a different approach is required to determine which tracker heads are in front of the module under investigation and which are behind for any given timestamp.

To determine front and rear row sets, we must first define a single point at an analogous position on all tracker heads. For example, the point of rotation through which the axes of azimuth and tilt rotation intersect. For tracker head i in Fig. 4.7, all tracker heads in front will satisfy the following condition [162]:

$$(p_{j,x} - p_{i,x})(B_{i,y} - p_{i,y}) - (p_{j,y} - p_{i,y})(B_{i,x} - p_{i,x}) > 0 \tag{50}$$

where $p_{i,x/y}$ are the x and y coordinates of the rotation point on the tracker head under investigation, $p_{j,x/y}$ are the x and y coordinates of the rotation point on any other tracker head, and $B_{i,x/y}$ are the x and y coordinates of point B at the farthest edge of a tracker such that point p_i and B form a line parallel to the ground. Rear tracker heads can be grouped as the tracker heads that do not satisfy this condition, including the tracker head under investigation. If all rotation matrices are pre-calculated for all timestamps as a time-independent function, front and rear rows for all timestamps can be determined in a single, time-independent function call resulting in minimal additional computational cost compared to single-axis or fixed-tilt bounding volume hierarchy implementations.

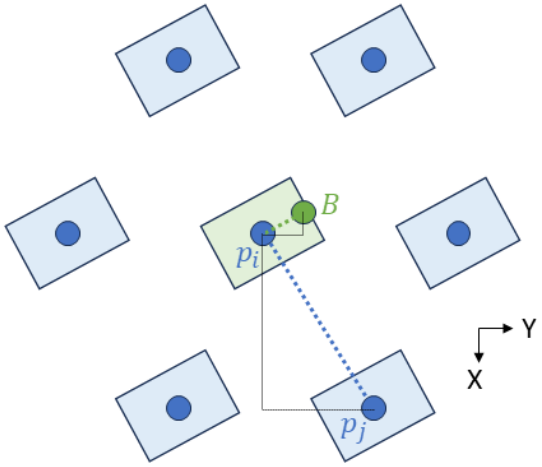


Figure 4.7: A schematic of the tracker under investigation (green) with adjacent tracker heads (blue). Eq. (50) determines whether the blue tracker heads are behind or in front of the green tracker head based on analogous points p_i and p_j on the two trackers in question and point B on the green tracker plane with no z-axis displacement from p_i.

DUET v.uO-2023+ then generates an axis-aligned bounding box around the most extreme coordinates of each set of front and rear tracker heads. In future, oriented rectangular prisms or another more suitable volume should replace these axis-aligned prisms to reduce the empty space within the bounding volume and thereby reduce the unnecessary ray-object intersection checks.

Backtracking Backtracking should occur when direct beam light incident on a tracker head becomes partially shaded by another tracker head. Due to the additional azimuthal axis of rotation, backtracking could be achieved by rotating the trackers off-sun toward a shallower tilt angle, as in single-axis tracking, or by adjusting the azimuth angle. The initial implementation of double-axis backtracking is based on the Fernandez-Humanda et al. [8] and adjusts tilt angle; future work could compare performance with any algorithm that outputs a corrected tilt and/or azimuth angle based on sun position and tracker coordinates.

For each tracker head, p_i again represents the rotation point of the tracker under investigation, while point p_j represents the analogous point on another tracker head. As seen in Fig. 4.8A, to project tracker head i onto the plane of tracker head j with normal $\vec{n}$, we find the distance τ along the sun unit vector $\vec{s}$ that results in an intersection point d at a vector d_j from the point p_j in the plane of tracker head j, where:

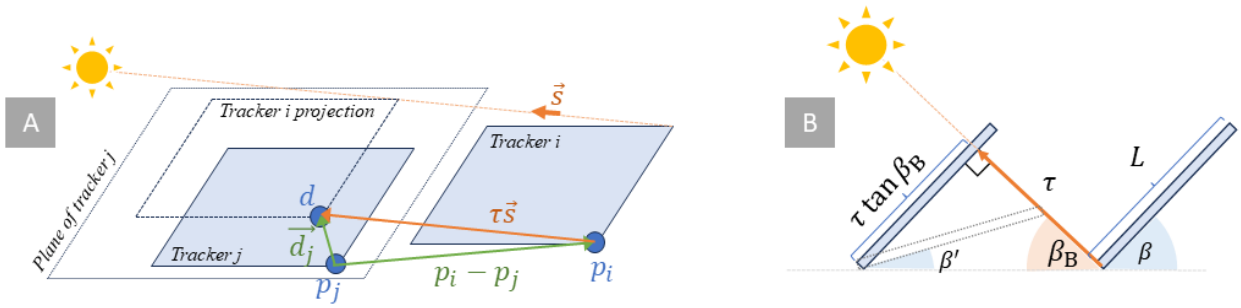


Figure 4.8: Schematics of backtracking checks for double-axis tracking. (A) The sun beam that is incident on tracker i at p_i intersects the extended plane of tracker j at point d. $\vec{d_j}$ separates d from point p_j on tracker j (that is analogous to p_i on tracker i), and components of $\vec{d_j}$ projected in the plane of tracker j are used to determine whether tracker j shades tracker i. $p_i - p_j$ is parallel to the ground. Figure adapted from [8]. (B) Adjusted backtracking angle β' is based on τ - the distance along the sunbeam path between trackers, the tier-wise collector width L, and the sun elevation angle φ_B.

$$\tau = \frac{(p_i - p_j) \cdot \vec{n}}{\vec{s} \cdot \vec{n}} \tag{51}$$

$$\vec{d_j} = (p_i - p_j) + \tau\vec{s} \tag{52}$$

We can convert d_j into the coordinate system of the plane j using the rotation matrix components R_x and R_y that govern its orientation. Then $d_{j,x}$ must be less than or equal to the tier-wise height of the tracker head, L, and $d_{j,y}$ must be less than or equal to the column-wise width for shading to occur. In this case, a more shallow tilt angle can be determined to avoid shading. This corrected tilt angle shown in Fig. 4.8B is:

$$\beta' = \beta - \arccos(\frac{\tau \tan\beta_B}{h}) \tag{53}$$

where β_B is the sun elevation, derived from the right angle triangle formed between sun vector and a cross-section of tracker heads i and j such that the unshaded potential along the tracker head is greater than L, or: $\tau \tan\beta_B > L$.

A simpler approach would be to determine whether $\tau \tan\beta_B > L$, and if not, to correct to a backtracking angle regardless of whether the ray falls between the gap between tracker heads (as

can be determined by the $d_{j,y}$ check). This results in more backtracking and lower energy yield, but assures no shading. The preliminary simulations in Section 4.3.2 use of this simplified approach, but the full $d_{j,y}$ check should be used in future simulations.

4.3.2 Results & Discussion

Double-axis tracked bifacial PV validation To assess the accuracy of the double-axis tracking implementation, the following section provides a validation comparing DUET v.uO-2023's modelled DC energy yield against the measured DC energy yield of 6 double-axis tracked modules [163] with power-optimizers at the University of Sherbrooke at 45.2°N.

The field, illustrated in Fig. 4.9, contains a row of 8 monofacial trackers to the south and 9 bifacial trackers to the north. This analysis considers 6 modules within the tracker head that sits second from the westernmost end of the bifacial row, shown in green. Fig. 4.10 shows the location of these 6 modules within the tracker head in yellow, with blue regions representing the supportive structure (not modelled in this study). On-site irradiance data is measured for GHI, DNI, and DHI with a Kipp & Zonen RaZON+. Ambient temperature and wind speed are also measured.

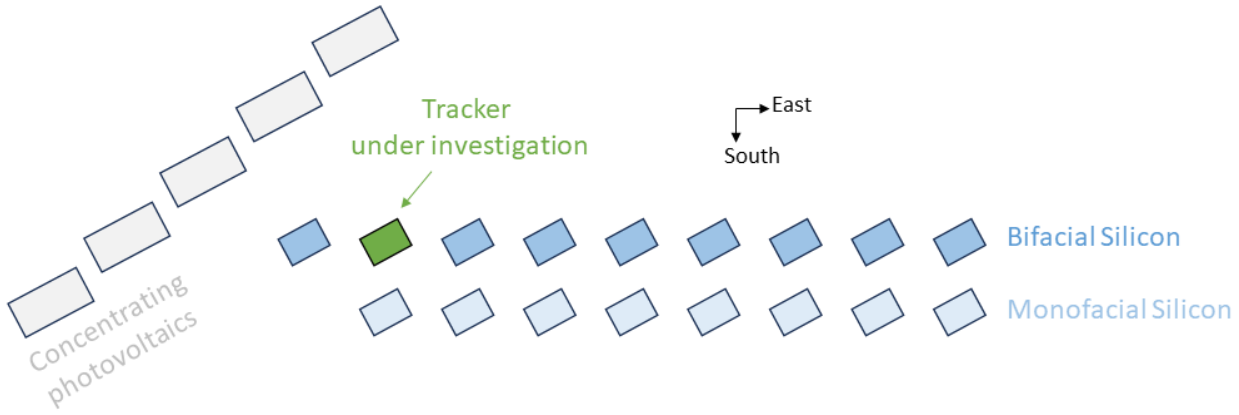


Figure 4.9: Layout of the Université de Sherbrooke double-axis tracking site with a row of 9 bifacial tracker heads north of a row of 8 monofacial tracker heads. Tracker investigated in this study is shown in green. A diagonal row of concentrating PV tracker heads sits to the west.

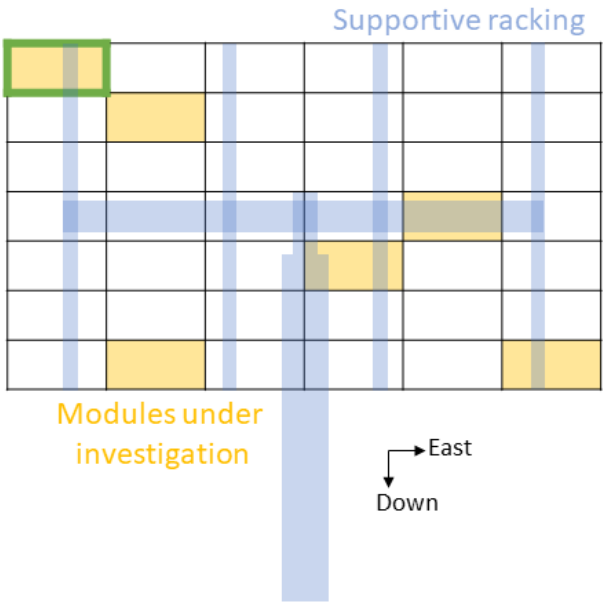


Figure 4.10: A 7L, 6-column double axis tracker head at the Université de Sherbrooke site with modules investigated in this study in yellow and supportive racking (not modelled) in light blue. Modelled vs. measured results for green outlined module are shown in Fig. 4.11.

For August 2022, Fig. 4.11 shows a plot of modelled power vs. measured power at 1-5 min intervals for the single module outlined in green at the top left of Fig. 4.10. This comparison omits timestamps with sun zenith lower than 10° and uses measured irradiance as model input for each available measured energy yield timestamp. At this timescale, some spread is expected during intermittently cloud due to the distance between the onsite irradiance measurement and the tracker head. However, the orange clustered line of points below the black line denoting unity with measured data demonstrates a consistent negative bias in modelled energy yield, particularly during clear or sunny (orange) hours with a Perez sky clearness index $\epsilon > 4$. This underestimation results in a relative error of -6.7% between measured and modelled energy yield for the month.

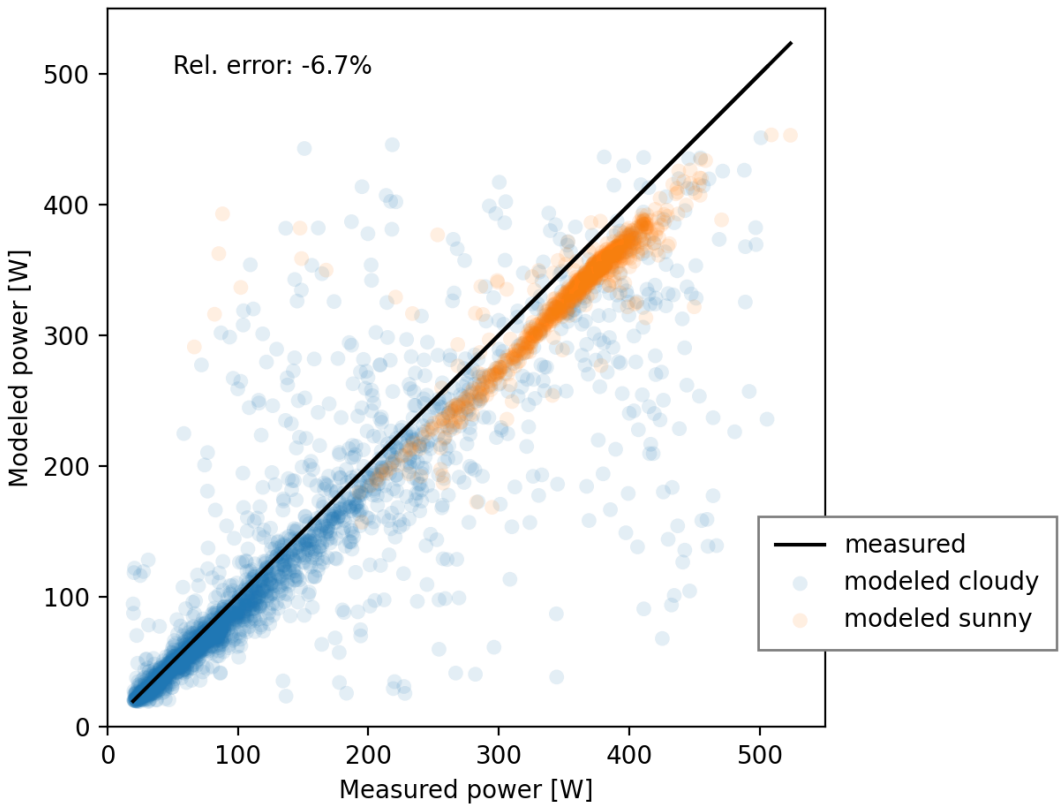


Figure 4.11: Modelled vs. measured power for the module outlined in green in Fig. 4.10 in the 7L, 6-column green tracker head in Fig. 4.9 for August 2022. Black line indicates perfect agreement. Orange dots represent timestamps with a Perez sky clearness index $\epsilon > 4$, blue dots represent $\epsilon < 4$ (where clear = 8, overcast = 1). Rel. = relative.

This underestimation is also clearly visible in the black lines in the left subplot of Fig. 4.12, representing the bifacial modelled power timeseries for the 6 modules on a clear-sky August 20th. The cyan lines represent the measured data for the same modules, displaying a similar production curve to the modelled data but with a positive bias. Such a consistent modelling underestimation is commonly due to sensor soiling or miscalibration, differences in modelled and measured module temperature, inaccurate modelled shading or radiation coupling, or reflections on-site that are not modelled.

Satellite irradiance data from Solcast [164] for the same day provides irradiance values within 20 $\mathrm{W/m^2}$ of on-site measured GHI on average, suggesting that sensor soiling is likely not the primary cause of this underestimation. However, the on-site 10 m ambient temperature is warmer in the morning and cooler in the afternoon compared to the Solcast data. The pattern of deviation is

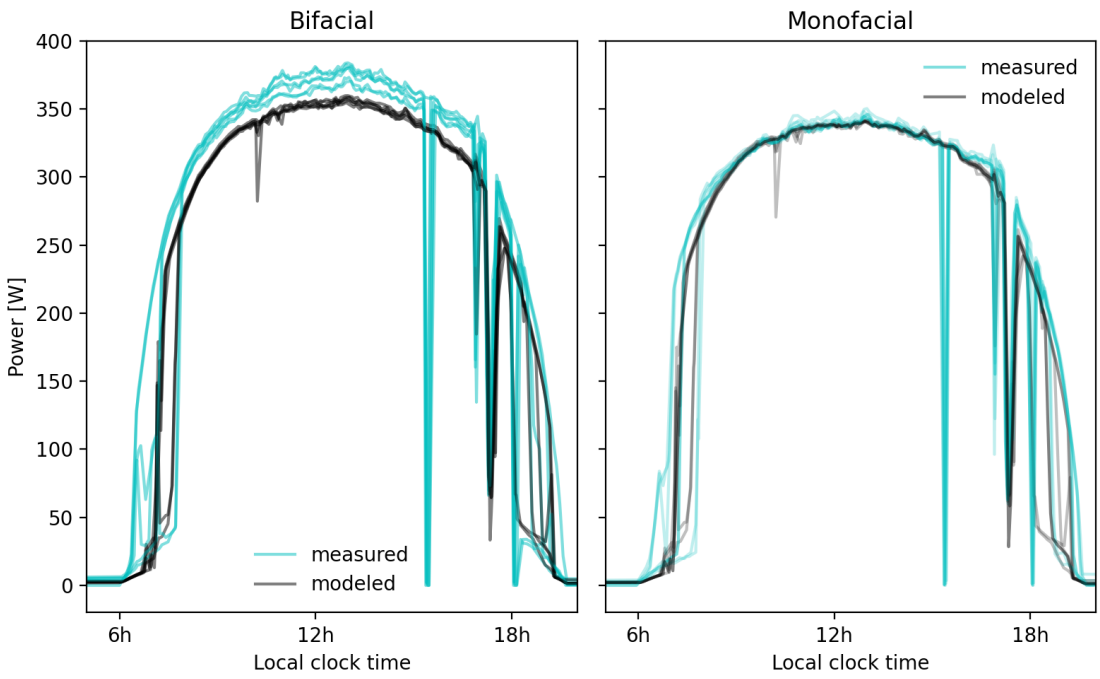


Figure 4.12: Modelled (black) and measured (cyan) power timeseries for the six yellow modules in Fig. 4.10 for bifacial (left) and monofacial (right) trackerheads on a clear August 20, 2022.

characteristic of a time-offset between the datasets; using the satellite temperature and wind speed data does offer a reduction in modelled energy yield error. However, this temperature discrepancy does not fully explain the -6.7% bias.

Decreasing the temperature coefficient of power by 0.1% absolute or increasing the STC efficiency by 1% absolute would each separately bring modelled data to within the measured data. Flash-testing the modules after time in the field or collecting rear module temperature and analyzing power at various plane-of-array irradiance would confirm STC performance and temperature coefficients, ruling these out as the source of discrepancy. Additional effects have already been ruled out, including: removing all modelled shading, increasing albedo by 5% absolute increase in albedo, and increasing DHI by a relative 15% as a liberal estimate of any possible pyranometer shading or soiling. Without further information, we cannot estimate the diffuse and direct light reflected off the concentrating PV tracker heads that are situated to the west of the silicon trackers in Fig. 4.9, but this reflection is a potential source for the approximate 60 $\mathrm{W/m^2}$ discrepancy seen at noon on a clear day in this bifacial tracker head at this western edge of the row.

Again considering the left subplot of Fig. 4.12, we can see that the measured bifacial data in

cyan for the 6 modules demonstrates a larger performance spread than the modelled data. Since this magnitude of spread is not seen in the measured monofacial data in cyan on the right subplot, this spread is likely due to a rear-side effect. It appears that the variation is related to distance from the ground since the yield is grouped roughly into three sets of two modules, with modules in each set being within one tier of each other within the tracker head; the highest yield results from the modules farthest from the ground. Additional simulations at high ground mesh density and large ground extent - both parameters that could impact the radiation coupling and irradiance non-uniformity from the top to the bottom of the tracker head - did not introduce a spread into the modelled data.

The large torque tube can also be expected to have a differing rear shading impact based on module distance from the ground, introducing a spread in energy yield. While DUET v.uO-2023+ *can* simulate the racking for this double-axis tracked system, the racking was not included in these simulations; thus, any spread due to rear-side structure shading is not captured in the modelling. Future work should include simulations with racking to determine its impact. Additional future work should target the explanation for the modelling underestimation and performance spread, including: measuring module backside temperature across multiple tiers, measuring plane-of-array irradiance using Si reference cell or pyranometer to compare to modelled results; simulating different date ranges and different tracker heads within the system, farther from the concentrating PV; further reviewing the double-axis bounding volume hierarchy; and building a ray tracing scene with specialized geometry and orientation to test individual timestamps for direct comparison.

Simulated tracking comparison The following section presents preliminary simulations for fixed-tilt, single-axis and double-axis tracked systems in Ottawa, ON at 45° N using a typical meteorological year [75]. In all cases, the simulated row spacing is set to achieve 5% row-to-row electrical shading loss with half-cut cells and backtracking in the tracking cases, either through optimization simulations or through the latitude-dependence shown by Tonita et al. [5]. The fixed-tilt and single-axis tracked simulations represent a central module in a 1P row with three tables with 10, 11, and 10 module columns. The double-axis tracked simulations represent a module at the center of a 1P, 3 column tracker head. The tracker head itself is at the center of an array with 5 rows, each with 5 tracker heads offset such that they form a checkerboard pattern similar to that

in Fig. 4.7. This lightweight double-axis tracker head design was chosen due to its application in higher-latitude areas with permafrost where pile driving is not possible. It is similar to the Morgan Solar Inc. Savanna tracker [165] but with wider spacing to achieve the 5% row-to-row shading.

Fig. 4.13 shows the daily energy yield profiles for each tracking type with 5% row-to-row shading loss, averaged for the six months around summer and winter solstice (top and bottom, respectively). The golden shaded region represents the bifacial PV power gain on a double-axis tracker within an full array of tracker heads. Both energy yield and bifacial gain peak at noon for the DAT system. The DAT system also offers higher peak energy yield than the SAT system (blue) due to avoided cosine losses, but we can note that backtracking causes a similar yield profile for DAT and SAT systems during the morning and afternoon. Thus, applying the additional capital required for double axis trackers to build increased SAT capacity may provide the broadest curve for any given cost. Future comparisons should consider that cost equivalence.

The grey line corresponding to the right axis in Fig. 4.13 plots the average hourly wholesale energy price for the province of Ontario (HOEP) for 2016-2022. If a PV plant sells electricity directly on a real-time energy market, the plant's annual revenue neglecting curtailment can be simplified as the annual sum of the per-timestamp energy yield weighted by the per-timestamp wholesale electricity price for the relevant market, with the ten highest-price hours ignored. By this definition, the left-most points on Fig. 4.14 shows the gain in annual revenue between tracker types on a per kWp basis, given no land constraints.

The double-axis tracked bifacial PV with multiple rows and backtracking yields 35.7% more revenue than fixed-tilt (gold) and 20.2% more than single-axis tracked (black) for 0.2 albedo and equivalent 5% row-to-row shading. A number of factors affect the accuracy and relevance of this tracking gain estimate; for example, neglecting racking leads to overestimated double-axis tracked rear irradiance, while the simplified backtracking method and negative bias seen in Section 4.3.2 may result in underestimated double-axis yield.

For additional context, the right-most points on Fig. 4.14 show that the row spacing required for 5% row-to-row loss across all systems results in energy yield loss with respect to fixed-tilt systems for both the SAT and DAT systems; therefore, even accounting for rack shading, the 3 column, 1P tracker heads with the row spacing examined in this modelling would not be competitive on a basis of revenue per land area at 45°N. Other densities and row-spacing should be tested before

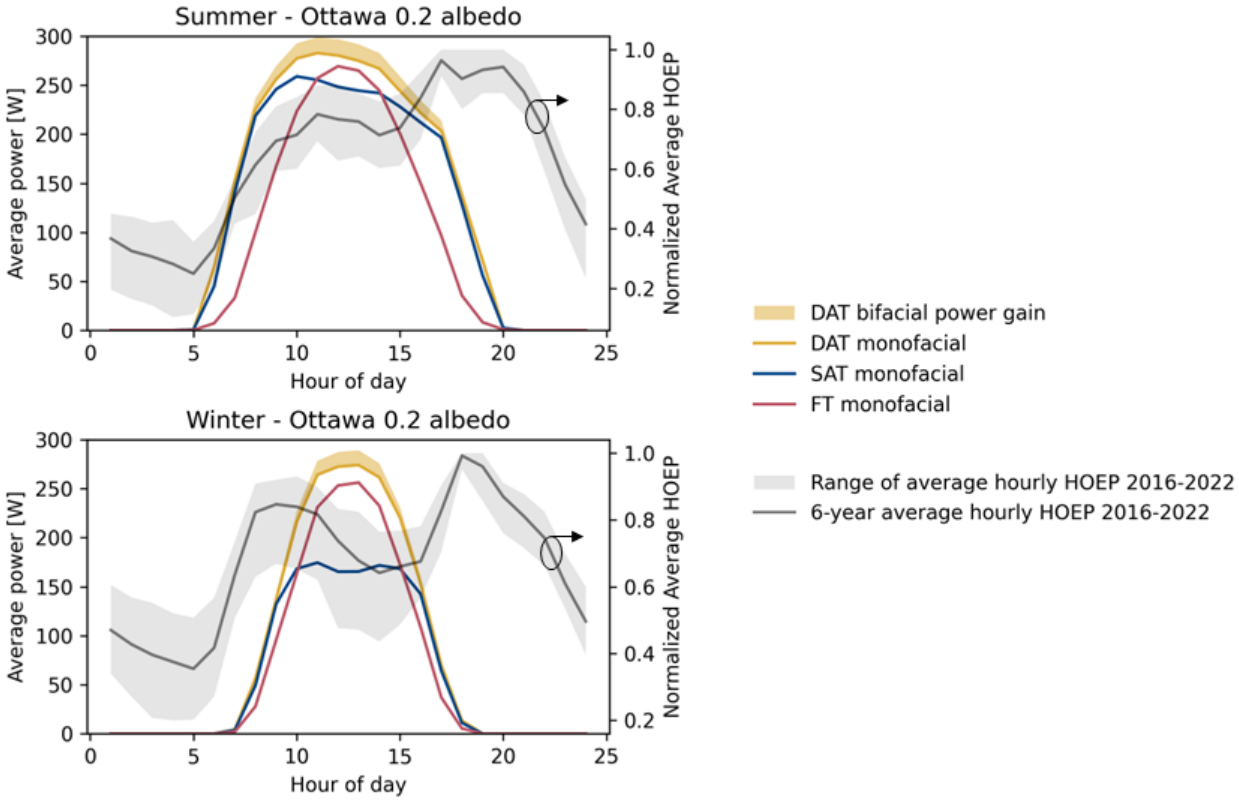


Figure 4.13: Summer (top) and winter (bottom) average energy yield profiles for double-axis tracked (DAT) monofacial PV (gold line), single-axis tracked (SAT) monofacial PV (blue line), and fixed-tilt (FT) monofacial PV (red line), all with 5% row-to-row loss. Shaded gold region shows average bifacial power gain for DAT PV with 5% row-to-row loss. Grey line shows average Hourly Ontario Energy Price (HOEP) for 2016-2022; the shaded grey region shows the range of average HOEP prices across 2016-2022.

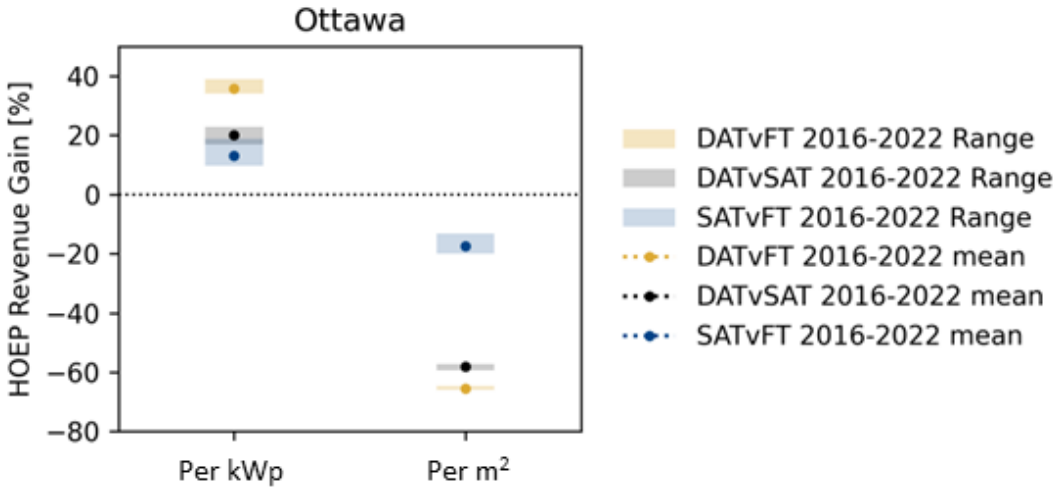


Figure 4.14: Tracking gain in revenue per kWp (left) and per m^2 of land (right) based on the Hourly Ontario Electricity Price (HOEP). Bifacial PV performance with double-axis tracking (DAT) vs. fixed-tilt (FT) is in gold; double-axis tracking (DAT) vs. single-axis tracking (SAT) is in grey; and single-axis tracking (SAT) fixed-tilt (FT) is in blue. Dotted lines show mean of 2016-2022 gains; shaded regions show range in 2016-2022 gains.

conclusions on the general viability of bifacial PV on double-axis trackers can be made, since single-axis systems are frequently chosen over fixed-tilt at land-constrained mid-latitude locations but demonstrate an energy yield loss per land area based on the equivalent row-to-row shading case here.

For a double-axis tracker to outperform the energy yield of any other system based on energy yield per land area, the following expression must hold:

$$\frac{EY_{\mathrm{DAT}}}{EY_{\mathrm{X}}}\frac{L_{\mathrm{DAT}}}{L_{\mathrm{X}}} > 1 \tag{54}$$

where $EY_{\mathrm{DAT/X}}$ are the energy yield per installed capacity $[\mathrm{Wh/Wp}]$ and $L_{\mathrm{DAT/X}}$ installed capacity per land area $[\mathrm{Wp/m^2}]$ for each of the systems.

Finally, if we consider a denser DAT system with approximately 10% row-to-row shading loss, Fig. 4.15 shows that albedo remains a significant driver of *bifacial gain* - or the improvement in bifacial energy yield vs. monofacial energy yield - for double axis trackers. The systems in this figure are not directly comparable to one another since the SAT and fixed-tilt systems have 5% row-to-row shading, but all three systems are included here as a reference for the trend of bifacial gain with albedo. Increasing albedo from 0.2 to 0.4 results in a 3.7% absolute increase in average

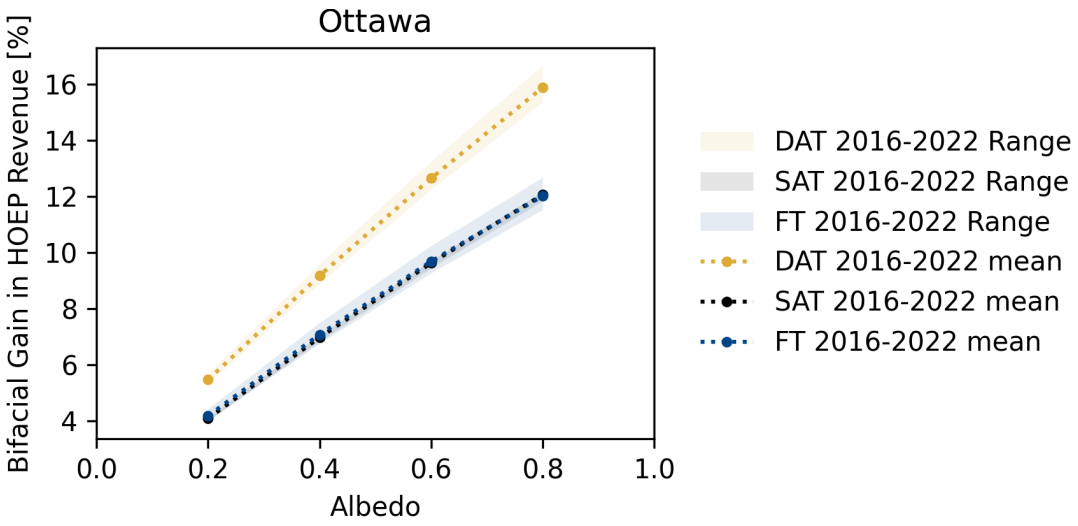


Figure 4.15: Bifacial gain in revenue based on the Hourly Ontario Electricity Price (HOEP) and bifacial and monofacial PV performance in double-axis tracking (DAT), single-axis tracking (SAT), and fixed-tilt (FT) systems. Dotted lines show mean of 2016-2022 gains; shaded regions show range in 2016-2022 gains. Note: DAT system has 10% row-to-row shading while FT and SAT systems have 5%.

bifacial revenue gain for the double-axis tracked system in 2016-2022. Due to the already elevated cost of double-axis tracked systems, artificially enhancing albedo through albedo engineering is an unlikely option; instead, seasonal increases in albedo from 0.2-0.8 during snowy seasons at mid-high latitude could deliver part of the 10% absolute increase in bifacial gain shown here.

5 Use-cases in mid-to-high latitude PV

The meteorological and PV operating conditions at mid-to-high latitude locations diverge substantially from the low-latitude conditions for which accurate and validated physical and/or empirical modelling has existed for decades. The three following sections explore the energy yield impacts of three phenomena of interest in mid-to-high latitude locations, namely: air mass, latitude-dependent row spacing, and ground-accumulated snow. The use of the proposed model within these studies demonstrates: (a) how flexible, highly parameterized PV performance models allow examination of physical phenomena of importance to emerging PV markets; and (b) how latitude-dependent physical modelling reduces the uncertainty that user-defined loss parameters have previously introduced into widespread geographical studies.

5.1 Air mass impact on short circuit current

At mid-to-high latitudes, the sun spends more time closer to the horizon than it does at low latitudes. Therefore, the spectrum of the available light at higher latitudes shifts toward a balance of longer wavelengths, since shorter wavelengths are absorbed in the sunlight's comparatively long path through the atmosphere. These spectral differences are shown in the varying shape of air mass (AM) spectra, both with latitude and throughout the day and year. (See Section 2.2.1).

However, the base version of DUET v.uO-2024 assumes that all light sources (diffuse sky, direct beam, and ground-reflected) radiate with the AM1.5G spectral shape at all times. The model applies the PV module's rated short-circuit current measured at standard test conditions under AM1.5G to calculate the cell responsivity, $\Re$, in $\mathrm{A/W}$ of incident light. Since this assumption is not fully physically representative, we undertook a study to quantify the impact of neglecting air mass on energy yield prediction in two mid-to-high latitude locations [4].

5.1.1 Methodology

This study compares the energy yield of fixed-tilt tracked systems simulated with and without an air mass modifier (AMM) in a modified version of DUET v.uO-2020. An AMM modifies the AM1.5G short circuit current of a PV cell or module to account for an air-mass-specific spectrum [166]. The

approach outlined in this study requires the simulation of air mass spectra for AM0-40 for a given geographic location and a modeled or measured EQE for an encapsulated silicon cell from which the spectral responsivity $\Re(\lambda)$ can be found in A/W/nm. The AMM for each AM bin 0-40 is then taken as the ratio between (1) the integration of the per-wavelength product of the AM spectrum (scaled to the same total irradiance as the AM1.5G spectrum) and $\Re(\lambda)$ and (2) the integration of the per-wavelength product of AM1.5G spectrum and $\Re(\lambda)$ [167]. The resulting AMM lookup table can then be accessed based on per-timestamp AM.

The algorithm to access and apply the AMM each timestamp is as follows:

1. Calculate the per-timestamp air mass based sun zenith, Z, through Eq. 55 [168].

$$m = \frac{1}{\cos Z + 0.50572 * (96.07995 - Z)^{-1.6364}} \tag{55}$$

2. Interpolate the per-timestamp AMM from the AMM lookup table based on the timestamp's air mass.

3. Multiply the AM1.5G responsivity by the timestamp's AMM to adjust the short circuit current of all cells prior to input into the temperature-dependent single diode model.

5.1.2 Results & Discussion

The study finds that including the AMM in modelling increases annual energy yield predictions for the fixed-tilt system by 2.1% at 69.1° N, 0.8% at 45.4° N, and 0.3% increase at 33° N. A monthly comparison shows that neglecting air mass underestimates energy yield in some months by greater than 6.8% at 69.1° N and 3.6% at 45.4° N while modestly overestimating in some summer months for the lower of the two latitudes. The magnitude of these effects suggests that modelling PV energy yield without considering air mass provides a safe conservative performance estimate but is not fully representative of most likely system performance. For high latitude systems, this underestimation may be resulting in unnecessary system over-sizing based on annual predictions and unexpected curtailment in some months.

Modelling air mass and other spectral impacts - i.e., cloudiness, precipitable water [169], and aerosol optical depth [170] - will become more important across all latitudes with increased deployment of thin films and tandem devices which have a more spectrally-dependent performance

than silicon devices and are set to reduce the material demands of the energy transition. Since irradiance contributions from individual irradiance sources are calculated and saved separately in DUET v.uO-2024, separate responsivities could be applied to direct, diffuse, and reflected light, in an approach similar to the above exercise for air mass. Alternatively, Tonita et al. applied a different method in DUET v.uO-2022 to adjust for spectral albedo [171]; rather than changing the responsivity for ground-to-module light, the authors directly apply an albedo value that is the integration of the per-wavelength product of spectral albedo and the module's EQE to ρ in Section 3.1 Eq. (8). This albedo value could change for each timestamp, seasonally, or simply for testing varied ground material, as in Ref. [172].

5.2 Latitude impact on optimal row spacing

In addition to causing a spectral shift in sunlight, the low sun elevation at higher latitudes also results in more frequent inter-row shading in fixed-tilt systems and more frequent backtracking in single axis tracked (SAT) systems. Thus, row spacing and *ground coverage ratio* (GCR) – i.e., the ratio between collector width and row spacing – should vary with latitude for optimal performance. While one can approximate optimal GCR for fixed-tilt systems based on shading conditions at winter solstice [173], the existing studies on optimal GCR for tracking systems consider only a few low-latitude locations [174–177]. Additionally, there is little existing guidance on optimal spacing for bifacial systems vs. monofacial systems. To address this gap in geographically-specific bifacial PV array design optimizations, we undertook a study using DUET v.uO-2022 to find the optimal row spacing for fixed-tilt, SAT and vertical east-west (E-W) facing systems across 17-75° N [5].

5.2.1 Methodology

This study included energy yield simulations in DUET for 31 locations in North America (17-75° N) using typical meteorological year files. The optimal fixed-tilt angle for each location was found prior to row spacing optimization. A parameter sweep of row spacing for all three system types at all locations then allowed the identification of the ground coverage ratio (GCR) required to achieve 5%, 10%, and 15% energy yield loss with respect to the performance of a single row of modules (i.e., *inter-row loss*).

This wide-ranging geographic study was possible due to both DUET's geographically-specific

shading algorithm and the model's relative computational efficiency. While the simulations could have been performed more quickly in a 2D VF model, such an approach would have required an understanding of the latitude-dependence of rear structure shading factors and electrical mismatch loss factors for the three systems at all 75 latitudes. Instead, since DUET's optical and electrical models calculate shading and electrical mismatch losses at each timestamp for any location, the results are inherently latitude-dependent without adding additional uncertainty of a user-defined factor. Additionally, the analysis could have been performed using ray tracing; however, the computational load would have required a significantly longer run time or greater access to high performance computing resources.

5.2.2 Results & Discussion

The analysis reveals that optimal GCR range from 17-75° N for 5% inter-row loss case varies more for fixed-tilt systems than SAT systems at 0.68-0.15 GCR vs. 0.32-0.17 GCR, respectively. Here, lower GCRs indicate wider row spacing. Vertical E-W requires wide row spacing to avoid shading regardless of latitude, showing the lowest variation in optimal GCR at 0.16-0.11 for this latitude range. The results also demonstrate that bifacial systems require wider optimal row spacing than monofacial systems to allow more diffuse and reflected light to reach the rear, but only by 0.03 GCR on average. Therefore, monofacial and bifacial GCR can ostensibly be considered equally viable in highly constrained land use scenarios.

The trend lines shown in Figure 5.1 can be used to predict the location-specific optimal GCR for any of the three system types based on North American latitude. The associated equations and fitting parameters are given in the study [5]. The standard deviation in residuals between these trend lines and the location-specific optimal GCR data points is ± 0.03 for fixed-tilt and ± 0.01 for HSAT and vertical systems. Since meteorological conditions will be the primary source of spread in yield between two different locations at the same latitude, these standard deviations (calculated as the square root of variance in residuals between data and fit) suggest that meteorological conditions have the greatest effect on fixed-tilt optimal GCR; as such, meteorological variation across latitude should be considered when highly optimized GCR is required for such systems. These trend lines also show that the design process for mid-high latitude PV plants requires a fundamentally different set of decision-making criteria than for low-latitude plants, since fixed-tilt and SAT systems in the

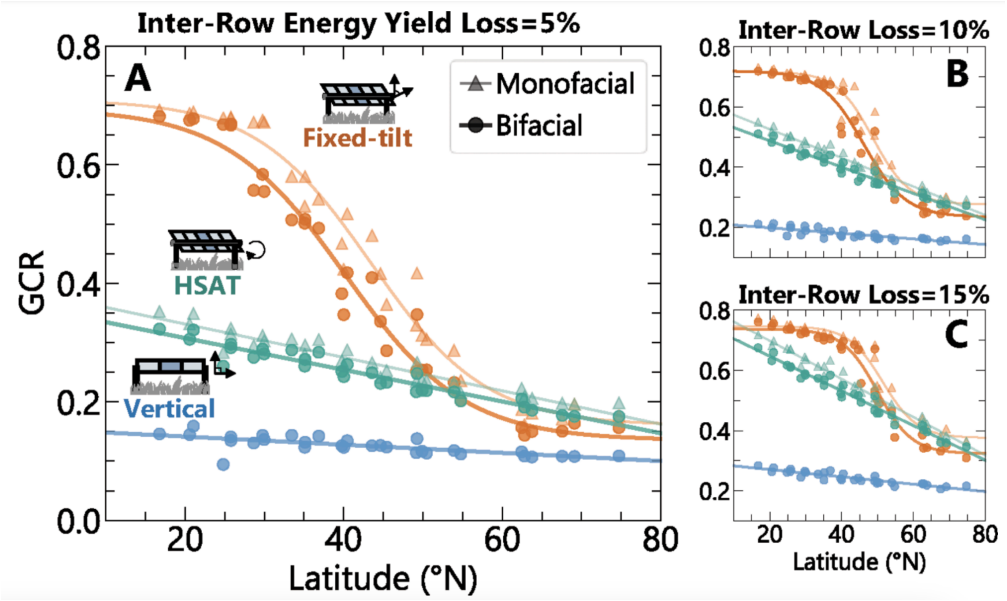


Figure 5.1: Trends in optimal ground coverage ratio (GCR) for fixed-tilt, horizontal SAT (HSAT) and vertical E-W systems for (A) 5%, (B) 10%, and (C) 15% inter-row loss cases. Figure reproduced from Tonita et al. [5].

5% inter-row loss case require approximately equal GCR for latitudes $\geq$50°N. This frees decision makers to focus on other criteria such as energy yield, cost, maintenance, and reliability, rather than land-use when deciding between system types.

5.3 Snow-dependent ground clearance

ANNIE C. J. RUSSELL, CHRISTOPHER E. VALDIVIA, JOAN E. HAYSOM AND KARIN HINZER

Scope and Impact

The following text is a reproduction of a conference proceeding from the *2022 IEEE 49th Photovoltaics Specialists Conference (PVSC)*. The proceeding describes a modelling study that examines the impact of ground-accumulated snow on irradiance and energy yield in single-axis tracked bifacial systems. The text demonstrates how DUET v.uO-2021 was modified to allow dynamic ground clearance such that the reflective ground, which representing the snow surface in this case, rises closer to the module as snow accumulates on the ground. This is the first demonstration of dynamic ground clearance in bifacial PV modelling known to the author. The approach is possible due to DUET's highly-parameterized array geometry and its flexible shading algorithm in which

rays can be re-classified as static or dynamic and functions that handle bounding volumes, coupling coefficients, and ray-primitive intersection can be re-called as necessary each timestamp.

This exercise demonstrates that, for a single-axis tracked system at 45° N, the simulated daily energy yield loss due to ground-accumulated snow scales linearly with snow depths up to 30 cm, before saturating at greater depths. The text includes a derate factor that can be applied based on daily snow depth for similar latitudes. The snowy season impact of ground-accumulated snow on rear irradiance and energy yield in two locations at greater than 45°N is comparable to the impact of rear structure shading and electrical mismatch loss, which are commonly applied in modelling across all latitudes.

The simulated snowy season energy yield impact is 0.3-0.7% which is non-negligible compared to commonly-applied annual derate factor for electrical mismatch (0.2-0.9% [42]); the 3-10% rear insolation loss is on-par with annual insolation loss due to a metallic torque tube (2-10% [157]). This initial investigation suggests that modellers should consider a derate factor for ground-accumulated snow during snowy seasons at mid-to-high latitudes. This finding contributes to improving agreement between measured and modelled performance during spring and fall shoulder seasons in which a considerable solar resource overlaps with high albedo snow cover. Improving energy yield prediction accuracy during these periods is crucial to facilitating PV integration in any electricity grid that relies on carbon-intensive fuel and/or hydro-power with freezing periods; in these contexts, under-performance will significantly impact the financial and societal value of a solar PV plant and the reliability of the electricity grid.

Copyright

This conference proceeding was published as part of the 2020 IEEE Photovoltaic Specialist Conference proceedings on IEEE Xplore. The Version of Record is available online at:

A. C. J. Russell, C. E. Valdivia, J. E. Haysom and K. Hinzer, "Impact of Snow Depth on Single-Axis Tracked Bifacial Photovoltaic System Performance," *2022 IEEE 49th Photovoltaics Specialists Conference (PVSC)*, Philadelphia, PA, USA, 2022, pp. 1-4,
doi: 10.1109/PVSC48317.2022.9938750.

Impact of Snow Depth on Single-Axis Tracked Bifacial Photovoltaic System Performance

Annie C. J. Russell[1], Christopher E. Valdivia[1], Joan E. Haysom[1,2], and Karin Hinzer[1]

[1] SUNLAB, Centre for Research in Photonics, University of Ottawa, Ottawa, Ontario, Canada
[2] J. L. Richards & Associates Limited, Ottawa, Ontario, Canada

***Abstract*— Photovoltaic (PV) capacity is rapidly expanding in mid-to-high latitude jurisdictions due to drastic decreases in PV system cost and global decarbonization efforts. However, uncertainty around performance impacts of latitude-specific conditions, such as ground-accumulated snow, contribute to investment risk. In this work, we employed DUET, our custom bifacial PV modelling tool, to study variable ground clearance resulting from snow accumulation. We model the impact of snow depth on a module in four generic, 2-in-portait single-axis tracked (SAT) systems with baseline ground clearances ranging from 1.6-2.8 m. Over the snowy season in Ottawa, Ontario (45˚N) and Cambridge Bay, Nunavut (69˚N), Canada, rear insolation and energy yield decrease by 3.4-9.6% and 0.36-0.69%, respectively – comparable to annual structure shading and electrical mismatch loss factors. The average daily energy yield loss in both locations is 0.034% per centimeter of accumulated snow. When hourly energy yield loss throughout the snowy season is binned by hour of day, hourly averages peak at 1.2-1.4% loss, suggesting implications for real-time and short-term forecasting.**

Keywords—bifacial, albedo, model, ground clearance, energy yield, rear irradiance, derate, forecasting, high latitude, Northern

2022 IEEE 49th Photovoltaics Specialists Conference (PVSC) | 978-1-7281-6117-4/22/$31.00 ©2022 IEEE | DOI: 10.1109/PVSC48317.2022.9938750

I. Introduction

Competitive photovoltaic (PV) system costs and global electricity decarbonization efforts are driving PV installation at increasingly higher latitudes [1,2]. In Canada, for example, the population – and thus, the demand for affordable, renewable energy – spans latitudes of 41.7-82.3˚N. PV systems in such regions, where extended summer daylight hours offset low winter light conditions, benefit from colder average yearly temperatures. In snowy months, *bifacial* PV systems in particular benefit from both high albedo and preferential snow shedding as compared to monofacial modules [3]. However, the dominant factors influencing mid-to-high-latitude PV performance remain uncertain, since performance models have historically been designed and validated for low-latitude regions. For example, rear irradiance of a single bifacial module has been shown to increase with ground clearance [4], but the impact of varying snow depth on multi-row systems in high albedo snowy months is still unknown. Understanding performance under mid-to-high latitude conditions reduces uncertainty in energy yield predictions for this region and, consequently, reduces financial risk for companies and communities looking to invest in bifacial PV [5].

In this work, we used the University of Ottawa SUNLAB's bifacial PV modelling tool DUET [6, 7] which has been validated against field data from 2-in-portrait (2P) fixed-tilt and single-axis tracked (SAT) systems at 55˚N [8]. DUET was customized to enable variable ground clearance at each timestamp. We paired this feature with snow depth data to model a time-varying distance between the top surface of accumulated snow and the modules. We compare modelled rear irradiance and energy yield for this snow-dependent ground clearance method against the traditional fixed ground clearance method for a SAT system at 69˚N and 45˚N during the snowy season. Since forecasting, performance monitoring, and project financing require energy yield predictions at varied timescales, we present a discussion of the hourly, daily, and seasonal impacts of snow depth.

II. Methodology

DUET's 3D optical model calculates the irradiance incident on the front and rear of each PV cell in a module based on the geometry of the array. This includes the ground clearance, defined here for a SAT system as the distance between the ground and the center of rotation of the torque tube. Eq. 1 and Fig. 1 demonstrate the *snow-dependent ground clearance* ($C_s(t)$) as the difference between a fixed ground clearance (C_f) and snow depth ($S(t)$) at a given time, t:

$$C_s(t) = C_f - S(t) \quad (1)$$

We investigated snow depth impacts at two Canadian locations: Cambridge Bay, Nunavut at 69˚N and Ottawa, Ontario at 45˚N. The daily snow depth data for each location was retrieved from [9] for all available years in 1990-2020. The average snow depth for each day of the year is found from this 30-year dataset, and the *snowy season* is defined as the period

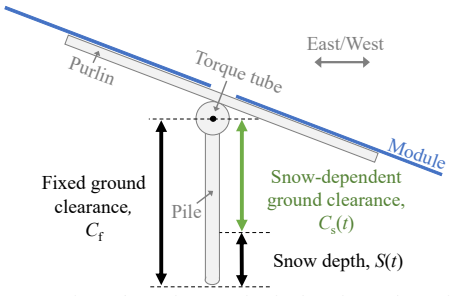


Fig. 1: Cross-section of a 2-in-portrait single-axis tracker with snow-dependent ground clearance as the difference between fixed ground clearance and snow depth for time, *t*.

Authorized licensed use limited to: University of Ottawa. Downloaded on July 19,2023 at 19:31:12 UTC from IEEE Xplore. Restrictions apply.

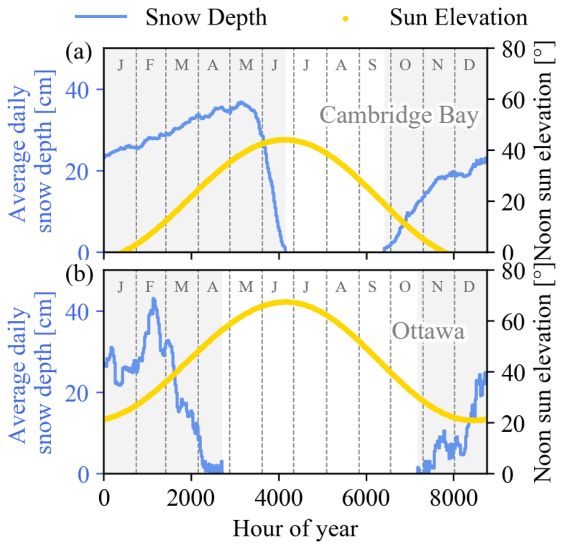


Fig. 2: Hourly snow depth and noon sun elevation for (a) Cambridge Bay, Nunavut and (b) Ottawa, Ontario. The gray region shows the snowy season.

between the first and last snowfall, including days with 0 cm snow depth. Fig. 2 shows that the resulting snowy season runs from September 25 - June 22 (271 days) in Cambridge Bay and October 27 - April 23 (179 days) in Ottawa. The average daily snow depth ranges from 0-37 cm and 0-43 cm for each location, respectively. For the following analysis, the snow depth of a given hour is set equal to the average snow depth on that day.

Hourly irradiance and temperature are taken from the Typical Meteorological Year in each location. In both ground clearance methods, the albedo for each hour is based on [10] with the following values:

(1) 0.8 (fresh snow) for $S(t) \geq 2$ cm;
(2) 0.5 for 2 cm $> S(t) > 0$ cm; and
(3) 0.2 (grass / brown dirt) for $S(t) = 0$.

We simulated the eastern and western modules in the center row of a 5-row, 2-in-portrait (2P) SAT system with ±60° tracking angle and backtracking. The morning performance of a western string is approximately equivalent to the afternoon performance of an eastern string, and vice versa. The full system performance can be approximated by the average of irradiance and the sum of power for eastern and western modules.

The simulations are executed for all hours in the snowy season with both the fixed ground clearance and the snow-dependent ground clearance methods for four C_f: 1.6, 2.0, 2.4, and 2.8 m. While a true snow surface may be shaped by ground elevation profile, blowing snow, site operation and maintenance, and snow shedding from the front of the panels, these simulations assume a flat snow surface.

This analysis does not account for snow cover on the front of modules. Ground-accumulated snow will have a significant impact on energy yield during these periods since rear-incident light is the primary remaining irradiance source; therefore, the following analysis provides a conservative baseline for performance impacts across the snowy season.

III. Results & Discussion

A. Hourly impact

Since hourly energy yield estimates are required for near real-time forecasting, we investigate the hourly performance impact of snowy conditions. We define the hourly performance impact of snow depth as:

$$\Delta(\mathrm{t})\ [\mathrm{absolute}] = X_s(t) - X_f(t) \quad (2)$$

$$\Delta(\mathrm{t})\ [\mathrm{relative}] = \frac{X_s(t)}{X_f(t)} - 1 \quad (3)$$

where $X_s(t)$ is either the hourly irradiance or the power with a snow-dependent ground clearance at time, t; $X_f(t)$ is the same quantity with a fixed ground clearance.

To demonstrate the impact of snow depth across the day, we bin the hourly performance impacts throughout the snowy season by hour of day for the $C_f = 2$ m case. Figure 3 shows the average of each bin as a solid line and provides the minimum and maximum value in each bin as the bounds of the shaded region. This figure demonstrates eastern module performance,

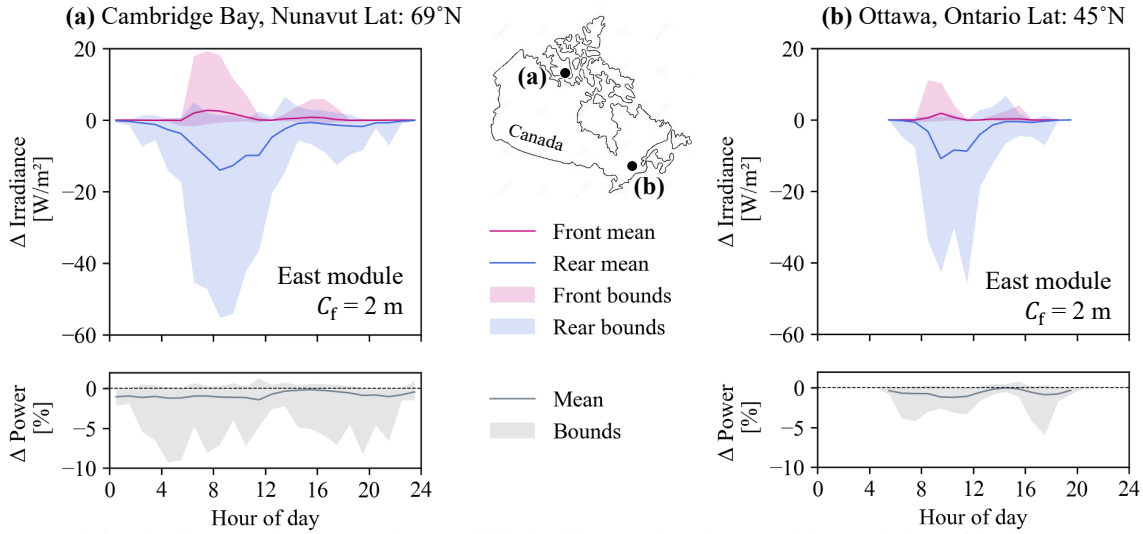


Fig. 3: Change (Δ) in front irradiance, rear irradiance, and energy yield induced by snow-dependent ground clearance by hour of day for an eastern module in a 2P bifacial SAT system in (a) Cambridge Bay, Nunavut, and (b) Ottawa, Ontario. Bounds indicate the highest and lowest change in each metric for a given hour.

Authorized licensed use limited to: University of Ottawa. Downloaded on July 19,2023 at 19:31:12 UTC from IEEE Xplore. Restrictions apply.

but the western module performance can be approximated as the mirror image of Fig. 3, flipped about solar noon. The absolute increase in front irradiance and absolute decrease in rear irradiance both peak mid-morning when the module is closest to the ground, which suggests that low-lying fixed-tilt modules would be subject to these peak changes at most hours of the day. The average change in rear irradiance peaks at −14.0 W/m^2 for Cambridge Bay and −10.8 W/m^2 for Ottawa. The average change in electrical power peaks at −1.4% and −1.2%, respectively.

In the days with deepest snow, the maximum absolute hourly change in rear irradiance for the eastern module is −55.1 W/m^2 in Cambridge Bay and −46.0 W/m^2 in Ottawa, corresponding to 44.7% and 22.5% rear irradiance loss and 2.0% and 2.8% power loss, respectively. The maximum relative module power losses – 9.2% in Cambridge Bay and 5.6% in Ottawa – are found in a different set of highly-diffuse evening hours in which rear irradiance contributes 20-25% of total irradiance in the fixed ground clearance case. Since snow depths in this analysis are 30-year averages, larger-than-average snowfalls would see higher hourly impacts than those reported here.

As seen in Fig. 3, higher snow depths can also *increase* module power under some conditions. In the afternoon, for example, reducing the ground clearance of a multi-row array shifts the ground shading pattern in a direction that can increase both front and rear irradiance on the eastern module. However, any afternoon power gain for the higher eastern modules coincides with a more significant power loss for the lower western modules, resulting in an overall negative performance impact to the array during most of these hours. When the eastern and western module performance are combined to represent the full system behavior, the mean impact of snow-dependent ground clearance is more stable throughout the day. Figure 4 shows this full-system relative energy yield loss with a slight peak in the mean at -1.1%.

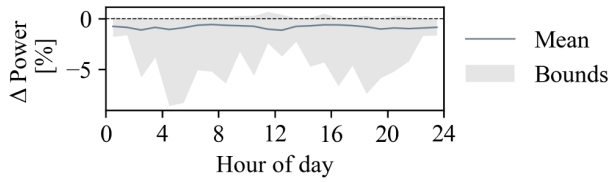


Fig. 4: Relative change in energy yield induced by snow-dependent ground clearance by hour of day for a 2P bifacial SAT system in (a) Cambridge Bay, Nunavut.

B. Daily impact

The snow-dependent ground clearance decreases daily energy yield of the full system by an average of 0.79% in Cambridge Bay and 0.57% in Ottawa across the snowy season. Therefore, adjusting for ground accumulated snow in day-ahead forecasting could avoid mild overestimation of supply. Such a procedure would require an energy yield derate based on accumulated snow depth. Interestingly, daily energy yield losses amount to an average 0.034% per cm of accumulated snow for both locations. Figure 5 shows the spread of daily relative energy yield loss around the loss calculated using the average loss/cm/day derate (dark grey line) in Ottawa. Since Cambridge Bay sees between 0 and 24 hours of daylight

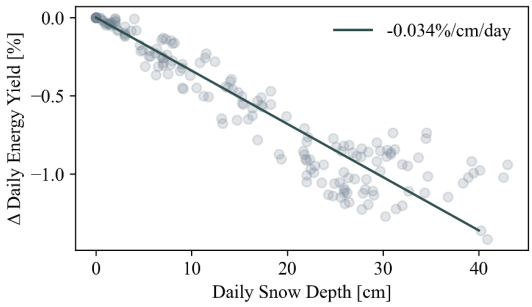


Fig. 5: Daily relative change in energy yield by snow depth in Ottawa, Ontario. Dark gray line shows loss calculated using the -0.034%/cm average derate.

throughout the year, the daily losses are spread more widely around this line than in Ottawa, suggesting that this simple derate may be less useful for forecasting applications at higher latitudes.

C. Seasonal impact

The overall impact of ground-accumulated snow on full-system snowy season insolation is shown in Table 1 for the range of fixed ground clearances, C_f. Rear insolation over the snowy season is 3.4-9.6% lower depending on location and C_f. This irradiance reduction is comparable to the 0-9% shading factors estimated for torque tubes in SAT bifacial PV systems [11]. Figure 6 shows that the absolute decrease in rear irradiance is offset slightly by an increase in front insolation, resulting in 0.37-0.69% energy yield loss in Cambridge Bay and 0.36-0.52% energy yield loss in Ottawa across the snowy season – on-par with annual electrical mismatch loss for SAT systems [12]. Since snow-dependent ground clearance affects energy yield and rear irradiance to a similar degree as widely adopted derate factors like structure shading and electrical mismatch loss, snow depth may be an equally important consideration in modelling applications that rely on accurate yield estimates in snowy months such as storage capacity planning for microgrids.

IV. Conclusion

Over the 179- and 271-day snowy seasons in two Canadian locations at 69˚N and 45˚N, modelling snow-dependent ground clearance for a 2P SAT bifacial system increases front insolation by 0.02-0.37% and decreases rear insolation by 3.4-9.6%, as compared to a fixed ground clearance. The hourly impact of snow depth on front and rear irradiance of a 2P

Table 1: Change (Δ) in front/rear insolation and energy yield for snow-dependent ground clearance with respect to fixed ground clearance over each snowy season.

	C_f	Δ Front Insolation		Δ Rear Insolation		Δ Energy Yield	
	m	%	kWh/m^2	%	kWh/m^2	%	Wh/W$_p$
Cambridge Bay	1.6	0.37	3.2	-8.8	-11.5	-0.37	-3.6
	2	0.20	1.7	-9.6	-14.3	-0.69	-6.7
	2.4	0.14	1.1	-7.0	-11.6	-0.58	-5.7
	2.8	0.04	0.3	-5.5	-9.9	-0.54	-5.3
Ottawa	1.6	0.19	1.0	-6.5	-6.1	-0.40	-2.5
	2	0.11	0.6	-6.2	-6.5	-0.52	-3.2
	2.4	0.07	0.4	-4.1	-4.8	-0.38	-2.4
	2.8	0.02	0.1	-3.4	-4.3	-0.36	-2.3

Authorized licensed use limited to: University of Ottawa. Downloaded on July 19,2023 at 19:31:12 UTC from IEEE Xplore. Restrictions apply.

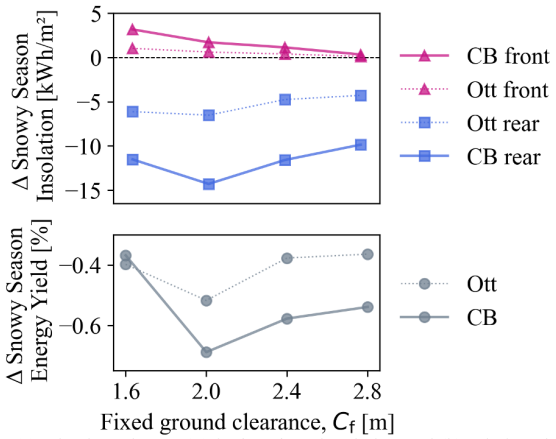


Fig. 6: (a) Absolute change (Δ) in front/rear insolation and (b) relative change (Δ) in energy yield for snow-dependent ground clearance with respect to fixed ground clearance over the full snowy season in each location. CB = Cambridge Bay. Ott = Ottawa.

tracked module is most significant whenever the module is closest to the ground, suggesting that deep snow would affect the lowest lying modules in a fixed tilt system throughout the day. When power loss is binned by hour of day, the average per-bin loss peaks at 1.2-1.4%, suggesting implications for real-time and short-term forecasting.

The snow depth results in an average daily energy yield loss of 0.034% per cm of accumulated snow for both sites. The impact on energy yield over the snowy season ranges from a 0.36-0.69% loss which is comparable to typical annual electrical mismatch and structure shading losses. Thus, a snow depth derate may be warranted for snowy season energy yield predictions. Further research is required to understand impact of snow depth on fixed-tilt and 1-in-portrait SAT systems, and knowledge of site operation, maintenance, and snow-drift patterns would be beneficial for a full analysis of a given site.

REFERENCES

[1]. International Renewable Energy Agency, “Renewable Capacity Statistics”, March 2020. ISBN: 978-92-9260-239-0

[2]. International Renewable Energy Agency, “Renewable power generation costs in 2020”, 2021, ISBN: 978-92-9260-348-9

[3]. K. S. Hayibo, A. Petsiuk, P. Mayville, L. Brown, and J. M. Pearce, “Monofacial vs Bifacial Solar Photovoltaic Systems in Snowy Environments,” *SSRN Electron. J.*, vol. 193, pp. 657–668, 2022.

[4]. C. Deline et al., "Assessment of Bifacial Photovoltaic Module Power Rating Methodologies—Inside and Out,” *IEEE JPV*, Mar. 2017.

[5]. R. Kopecek and J. Libal, “Towards large-scale deployment of bifacial photovoltaics,” *Nature Energy*, 2018.

[6]. C. E. Valdivia et al., “Bifacial Photovoltaic Module Energy Yield Calculation and Analysis,” in *44th IEEE PVSC*, 2017.

[7]. J. S. Stein et al., *Bifacial PV modules & systems: Experience and Results from International Research and Pilot Applications*. IEA PVPS, 2021.

[8]. A. Russell et al., “DUET: A novel energy yield model with 3D shading for bifacial photovoltaic systems”, *under review*.

[9]. Historical Weather Data, Environment & Climate Change Canada, 2021. [Online]. Available: https://climate.weather.gc.ca/historical_data/search_historic_data_e.html

[10]. Perovich, D. “Light reflection and transmission by a temperate snow cover,” *Journal of Glaciology, 53*(181), 2007, 201-210.

[11]. S. A. Pelaez, et al., “Effect of torque-tube parameters on rear-irradiance and rear-shading loss for bifacial PV performance on single-axis tracking systems,” *46th IEEE PVSC,* 2019.

[12]. C. Deline et al., “Estimating and parameterizing mismatch power loss in bifacial photovoltaic systems,” *Prog. PV. Res. Appl.*, no. Dec 2019, pp. 1–13, 2020.

Authorized licensed use limited to: University of Ottawa. Downloaded on July 19,2023 at 19:31:12 UTC from IEEE Xplore. Restrictions apply.

6 Summary and outlook

This thesis focuses on the author's contributions to the development, validation, and application of a bifacial PV performance model. The model's 3D optical simulations combine a finite element method with ray-object intersection algorithms to provide shade-inclusive 2D irradiance sampling across the front and rear surfaces of any PV module within a simulated array. This approach centers on the use of: (a) deterministic and independent rays and (b) a PV-specific hierarchy of intersection checks between rays and shading objects. These methods allow for higher computational efficiency than reverse ray tracing models and avoid the need for the user-defined shading and current-mismatch loss factors required in 2D and 3D view factor models. The resulting irradiance profiles act as input for the model's cell-to-array level electrical simulations which account for irradiance non-uniformity within and between modules based on a flexible electrical architecture that will allow for emerging PV module designs. This thesis provided a validation against measured field data for fixed-tilt, single-axis tracking systems, and double-axis tracked systems.

The text also describes the author's contribution to several modelling studies using the proposed model to investigate the energy yield impact of tracking- and latitude-specific effects. These studies demonstrate the applicability of the proposed model to the evolving questions in growing or emerging PV markets. Table 4 ranks the novel or additive modelling approaches that were demonstrated in this thesis by impact on annual or seasonal energy yield, as parsed by latitude. The air mass modified short circuit current dominates annually at mid-to-high latitudes, followed by inter-module mismatch in the context of a small test bed. For lower latitudes, torque tube reflection had less than half the impact of applying an air mass modifier. While it has no significant impact on *annual* energy yield, snow-dependent ground clearance has a larger impact than inter-module mismatch within the snowy season, which demonstrates that the ordered priority of these effects may change when considering shorter, non-annual timescales for planning purposes. Apart from spectral correction at high latitude, all modelling approaches resulted in annual or seasonal impact of less than 1%. The energy yield and accuracy impact of these and any novel modelling approach should be weighed against computational cost prior to wider adoption within bifacial PV modelling tools.

A few caveats to the above comparison should be noted: these effects were not tested at identical

	Energy yield impact (%)				
	33-37 °N	**45 °N**	**55 °N**	**69 °N**	Time Period
Air-mass modified short circuit current	0.3	0.8	-	2.1	**Annual**
Snow-dependent ground clearance	-	*0.36-0.52*	-	*0.37-0.69*	***Snowy season**
Inter-module irradiance non-uniformity	-	-	0.25-0.30	-	**Annual**
Torque tube reflection	0.11-0.18	-	-	-	**Annual**

Gain with respect to baseline modelling approach
Loss with respect to baseline modelling approach

Table 4: Annual and seasonal energy yield impacts of novel modelling approaches demonstrated in this thesis. Green represents gain with respect to baseline modelling approach and red represents loss. Results are listed with same precision as they were reported within their respective chapters.

locations and on identical systems which would be required for exact prioritization of impact; inter-module non-uniformity will vary by system size and edge-to-central module ratio with non-rectangular systems experiencing the largest impact; double-axis tracking is not here included as gains are an artefact of system behaviour rather than modelling approach.

To highlight the impact of the work described above, the following sections summarize key results and recommended future work for each of the thesis' major themes: model development, validation, and applications in tracking and mid-to-high latitude systems. The last section identifies future areas of study relevant to bifacial PV modelling.

6.1 Model development

The author developed a flexible, parameterized 3D model of a PV array using oriented 3D objects, such as polygons, cylinders, and rectangular boxes, to define PV rows and supportive racking structures. For tracking systems, the orientation and coordinates of any dynamic components in this 3D model update each timestamp, requiring updated shading calculations. Sections 3.1-3.4 describe the optical and electrical models developed in-depth, including:

- a novel PV-specific approach to ray-object intersections and bounding volume hierarchies which yields 2D shade-inclusive irradiance profiles (Section 3.3.3);
- a demonstration of the electrical model response to irradiance non-uniformity within and across submodules (Sections 3.4.1 & 3.4.2); and

- guidance on finite element surface mesh density to maximize the computational efficiency while minimizing compensation factors. (Section 3.6.3)

Future model development should consider alternative meshing schemes for sky, ground, and module, assessing both the computational efficiency and accuracy of these changes. Ground meshing is a priority given the higher compensation factors at low mesh densities. The following algorithmic and implementation improvements could also reduce computation time: tilt angle binning, further bounding volume hierarchy development, and hybridization with other modelling acceleration; and computational parallelization and translation to a statically-typed and compiled programming language.

Double-axis tracking development

To the author's knowledge, this thesis describes the first double-axis tracked bifacial PV model to include shading due to adjacent tracker heads and racking and a backtracking algorithm. Section 4.3 describes the algorithm to identify tracker heads to the front and rear of the module under investigation and briefly summarizes the Fernández-Ahumada backtracking algorithm used [8]. Future changes could include alternative backtracking approaches and non-rectangular tracker head shapes.

6.2 Model validation

To assess the accuracy of the proposed model, this thesis provided validations of fixed-tilt, single-axis tracking and double-axis tracking system simulations against measured field data.

Fixed-tilt and single-axis tracking validation

The validation in Section 3.1 compares modelled to measured data for plane-of-array irradiance and power within a string of modules in a fixed-tilt and single-axis tracked system at 55.7° N at the Technical University of Denmark. The comparison shows a mean absolute error (MAE) in rear plane-of-array irradiance within 2.8 $\mathrm{W/m^2}$ for fixed-tilt and 3.7 $\mathrm{W/m^2}$ for single-axis tracking – a result at the lower end of the modelled irradiance error given for eight models tested at the same site in Riedel-Lyngskaer et al. [86]. A central module approximation of string power using the Sandia

temperature model [14] yielded the lowest MAE in power of three tested temperature models at 14.2 mW/Wp for fixed-tilt and 17.3 mW/Wp for single-axis tracking, outperforming NOCT and Faiman models for the particular parameters tested. A brief investigation in Appendix C showed that the choice of cell temperature model introduced < 0.02% additional uncertainty in bifaical vs. monofacial temperature for both system types. Validation against measured rear-side temperature would allow for a better overall analysis of modelling uncertainty and would help isolate sources of error.

Double-axis tracking validation

A preliminary validation of the double-axis tracking model in Section 4.3.2 shows consistent underprediction of bifacial PV power at 1-5 min intervals throughout a sunny day as compared to measured data from the University of Sherbrooke, Québec, with 6% underestimation for the month of August 2022. This validation also shows a spread between performance of modules at the bottom and top of the tracker that is not captured in the preliminary modelling, possibly due to shade from the substantial supportive racking neglected in this initial work. Future validation is required to determine the sources of discrepancy between modelled and measured data. In particular, future validations will require measured plane-of-array irradiance and rear-side temperature data to allow for separate optical and electrical validations and to assess temperature variability across the tracker head.

Field measurements

Ideally, field measurements for future validations would include front and rear plane-of-array irradiance in multiple locations along the collector width, rear-side module temperature measurements, and redundancy in irradiance and albedo measurements where possible. Additionally, input meteorological data timeseries should be filtered for non-physical values and plotted for inspection to avoid errors such as time-shifts and daylight savings – the two most common data issues noted in the course of this work. An understanding of the location in question, or access to typical meteorological year, is ideal for determining whether measured values are reasonable, beyond whether a value is physically possible (e.g. frequency of fog, high winds, and intermittent cloud, seasonal temperature patterns). Comparison of ground and satellite data also provides a useful secondary

check for measured meteorological values.

Additional cross-software comparison

Beyond the cross-software validation in Section 3.1 afforded by comparison to Riedel-Lyngskaer et al.'s modelling comparison results at the DTU site [86], Sections 3.5.1 and 3.5.2 provide brief comparisons between the proposed model and other PV performance software. Results from the 2021 International Energy Agency (IEA) Photovoltaic Power Systems Task 13 Bifacial Modelling Round Robin show that the proposed model's rear irradiance results for a single-axis tracked system with an opaque torque tube closely follow the results from a ray tracing software, bifacial_radiance, for a given sunny day. Conversely, fixed-tilt rear irradiance without supportive racking deviates from the ray tracing result around midday. A comparison of 8760 hourly results for the same IEA scenarios shows the proposed model underestimating rear irradiance with respect to a 2D view factor model, PVsyst, by 6-11% on an annual basis underestimation. The highest deviation between the two models occurs systematically at high tilt angles and with a magnitude that cannot be attributed to PVsyst's static shading or current mismatch losses. Without measured data, these comparisons identify conditions of agreement and deviation between models but do not allow comparison of modelling error.

Future cross-software comparisons should seek to identify the specific sources of discrepancy between modelled irradiance generated by the modelling approach described in this thesis and ray tracing and 2D view factor models. This comparison could be achieved by: (1) isolating direct, reflected and diffuse light, and (2) comparing a full set of per-timestamp intermediate values (e.g. sun position and tilt angle) and pre-loss plane-of-array irradiance. In addition, such investigations should include a comparison to measured data to determine how these discrepancies translate to modelling error. Where possible, modelled irradiance should be sampled at the specific location of the irradiance measurement device to avoid averaging effects across a region of the plane-of-array that does not represent the given sensor. Modelling irradiance with and without an incidence angle modifier can also help distinguish discrepancies between plane-of-array irradiance measured on silicon reference cells and pyranometers.

6.3 Applications in tracked PV systems

Since 40% of new mono-crystalline PV modules are now installed on single-axis tracked systems, this thesis examined the impact of three concepts of interest on bifacial PV energy yield in tracked systems: (1) inter-module irradiance non-uniformity for fixed-tilt and single-axis tracking systems, (2) reflections off the torque tube in the supportive racking structure, and (3) addition of a secondary axis of rotation in double axis tracking.

Inter-module irradiance non-uniformity (edge brightening)

Building on the model validation performed against publicly available data from the Technical University of Denmark PV test bed, Section 4.1 presents modelling for all cells within the central 2-in-portrait rows of the fixed-tilt and single-axis tracking systems (i.e., across 88 modules). This full row analysis reveals a 0.3% and 0.25% net energy yield gain with respect to a central module approximation for each of the systems, respectively. This gain is the combined result of a 0.3-0.5% edge brightening gain and a 0.09-0.21% current-mismatch loss. This finding suggests that 2D view factor models should allow a positive gain to account for the net effect of edge brightening. However, gain for larger, utility scale systems will be lower than 0.3% due to a lower proportion of edge modules than in this test bed. Future research should therefore prioritize quantifying physical phenomena affecting the majority of modules in a system – such as temperature modelling uncertainty – over further investigation of edge effects.

Torque tube supportive racking reflections

The author contributed to a study that used the proposed model to quantify incidence angle losses on any energy yield gained from light reflecting off the torque tube in a single-axis tracked system. This study showed that torque-tube-reflected light experienced higher IAM losses than all other light sources and reduced current-mismatch losses by offsetting shading, resulting in 0.11-0.18% energy yield gain for a 74.5% reflective torque tube. While this impact is minimal, Lewis et al.'s most recent modelling work [104] without incidence angle modification has shown that reflection off the full supportive structure excluding pilings (i.e., 74.5% reflective torque tube, purlins / module supports, and frame) increases annual energy yield in California by 0.3%. Future investigations

should examine IAM losses from those sources with various reflectivity to account for soiling. Any remaining significant energy impact would justify implementing either an empirical adjustment or a finite element approach with rays linking low resolution racking meshes to ground, sky and module meshes.

Simulated energy yield comparison for tracking types

To determine the energy yield impact of a secondary, azimuthal tracking axis, the simulated tracking comparison in Section 4.3.2 compared fixed-tilt, single-axis tracking and double-axis tracking systems. In Ottawa, Ontario at 45° N, double-axis tracking showed a 20.2% gain in wholesale electricity revenue per module vs. single-axis tracking for the configuration modeled and assumptions in this section which consist of: spacing to achieve 5% row-to-row shading loss; 1x3 module double-axis tracker head; and 0.2 albedo. This gross revenue does not account for permitting, balance-of-system, land, or operations and maintenance costs. In fact, this 5% row-to-row shading loss configuration results in a loss in revenue per land area for tracking systems compared to fixed-tilt. This loss suggests that future studies should consider different equivalences between tracking types for land constrained systems and consider alternative DAT tracking configurations and spacing.

6.4 Applications in mid-to-high latitude PV systems

As PV system costs have decreased, PV installations have become more economically viable in mid-to-high latitude locations. This thesis presented a summary of three studies that use the proposed model to quantify the energy yield impacts of air mass, row spacing, and snow depth on mid-to-high latitude PV installations.

Short circuit current modification for hourly air mass

The spectral shape of incident light shifts toward longer wavelengths as the sun elevation decreases, resulting in a red shift that increases in intensity with latitude. To capture this effect, Section 5.1 demonstrates the application of a per-timestamp air mass modifier to the proposed model which increases or decreases cell short-circuit current based on sun position. The air mass modifier results

in a 0.3-2.1% impact on annual energy yield for 33-69° N. This work suggests that technology-specific incidence angle modifiers or empirical factors should be used for mid-to-high latitude simulations. Future work should model the energy yield impacts of latitude-dependent spectra for systems with emerging cell technologies.

Row spacing optimization

Conventional guidance on optimal row-spacing has focused on monofacial PV at low-to-mid latitudes. Section 5.2 describes a row-spacing optimization study using the model described in this thesis; the model was was chosen for its geographically-specific shading and current mismatch loss calculations. The results for 5-15% row-to-row shading demonstrate that optimal fixed-tilt and single-axis row spacing are roughly equivalent between 50-55°and >70°N. This result suggests that land-use need not be the major design consideration when choosing between the two systems at these latitudes.

Ground accumulated snow simulations

To the author's knowledge, this thesis provides the first demonstration of variable ground clearance in PV modelling to quantify the impact of ground-accumulated snow throughout the snowy season in two locations in Canada. The results in Section 5.3 demonstrate a 0.36-0.69% snowy season loss, which is comparable to annual current-mismatch loss factors, and a daily loss factor of 0.034%/cm of accumulated snow at 45° N.

This analysis requires future validation. A similar analysis could be repeated for fixed-tilt systems and varied latitude. Future studies of variable snow depth should include front-side snow-shedding models. Access to meteorological and plane-of-array irradiance data at mid-to-high latitudes, and to validated snow shedding models, would allow greater certainty in bifacial PV performance predictions under snowy conditions and help de-risk future PV projects in these regions.

6.5 Looking ahead

As the PV market expands into new greographic regions and evolving applications, the PV modelling community should seek to quantify the energy yield impact of all neglected physical effects

and operating conditions. Such an effort will ensure that emerging PV markets benefit from accurate PV modelling and financial certainty. PV model validations should be as varied as the geography, climate, and system types in which models are applied, and field data from these validations should be examined for widespread geographical and climatic trends. As tracking, module, and cell technologies evolve to reduce costs and diversify materials, PV modelling must be responsive to new developments; field data acquisition and model validations must be ongoing.

Beyond the topics discussed in this thesis, future efforts in bifacial PV energy yield modelling should expand on emerging questions within the PV market and within our changing electricity grid. These include:

- modelling trackers installed on undulating terrain to reduce the impacts of land grading on soil and ecosystems [56];
- quantifying spectrally-resolved ground irradiance for various array configurations in agrivoltaics [52];
- expanding electrical models to represent the behaviour of tandem, thin film, and emerging cell technologies [178];
- validating models at high temporal resolution to inform PV energy yield forecasting for grid integration studies and PV-storage operation [179, 180]; and
- maintaining computational efficiency to ensure access in the face of the rapidly-accelerating demand for computational resources [181].

7 Appendices

References

[1] C. Li, "Development of field scenario ray tracing software for the analysis of bifacial photovoltaic solar panel performance," M.A.Sc thesis, University of Ottawa, 2016. [Online]. Available: http://www.ruor.uottawa.ca/handle/10393/35523

[2] J. Stein, C. Reise, J. Castro, G. Friesen, G. Mauger, E. Urrejola, S. Ranta, M. Alam, M. Anoma, S. Ayala Pelaez, D. Berrian, E. Bertrand, M. Chiodetti, D. Chudinzow, H. Colin, I. Devoto, R. French, E. Fuentealba, F. Haffner, A. Halm, J. Haysom, K. Hinzer, I. Horvath, H. Huerta, M. Khan, M. Klenk, R. Kopecek, J. Libal, M. Lindh, B. Marion, M. Mikofski, R. Molinero, M. Monarch, A. Neubert, M. Patel, A. Petersson, G. Poulin, S. Ramesh, O. Rhazi, N. Riedel-Lyngskær, D. Riley, A. Russell, A. Schneider, C. Stark, T. Timofte, D. Tune, J. Tymchak, C. Valdivia, F. Valencia, and M. Wang, "Bifacial Photovoltaic Modules and Systems: Experience and Results from International Research and Pilot Applications: Report IEA-PVPS T13-14:2021," International Energy Agency, Tech. Rep., 2021. [Online]. Available: https://iea-pvps.org/wp-content/uploads/2021/04/IEA-PVPS-T13-14_2021-Bifacial-Photovoltaic-Modules-and-Systems-report.pdf

[3] T. J. Coathup, M. R. Lewis, A. C. J. Russell, J. E. Haysom, C. E. Valdivia, and K. Hinzer, "Impact of torque tube reflection on bifacial photovoltaic single axis tracked system performance," *Opt. Express*, vol. 31, no. 4, pp. 6143–6155, Feb 2023. [Online]. Available: https://opg.optica.org/oe/abstract.cfm?URI=oe-31-4-6143

[4] M. R. Lewis, A. C. J. Russell, C. E. Valdivia, J. E. Haysom, M. I. Bertoni, and K. Hinzer, "Impact of air mass on energy yield calculation for bifacial silicon heterojunction photovoltaic modules in high-latitude conditions," in *2020 47th IEEE Photovoltaic Specialists Conference (PVSC)*, 2020, pp. 371–375.

[5] E. M. Tonita, A. C. J. Russell, C. E. Valdivia, and K. Hinzer, "Optimal ground coverage ratios for tracked, fixed-tilt, and vertical photovoltaic systems for latitudes

up to 75°n," *Solar Energy*, vol. 258, pp. 8–15, 2023. [Online]. Available: https://www.sciencedirect.com/science/article/pii/S0038092X23002682

[6] G. M. Masters, "Ch 5 - Photovoltaic Materials and Electrical Characteristics," in *Renewable and Efficient Electric Power Systems*, 2nd ed. John Wiley and Sons, 2013.

[7] PV Lighthouse, "Solar spectrum calculator," 2014. [Online]. Available: https://www2.pvlighthouse.com.au/calculators/solar%20spectrum%20calculator/solar%20spectrum%20calculator.aspx

[8] L. Fernández-Ahumada, J. Ramírez-Faz, R. López-Luque, M. Varo-Martínez, I. Moreno-García, and F. Casares de la Torre, "A novel backtracking approach for two-axis solar pv tracking plants," *Renewable Energy*, vol. 145, pp. 1214–1221, 2020. [Online]. Available: https://www.sciencedirect.com/science/article/pii/S0960148119308900

[9] D. Sunday, "Line Segment and Convex Polygon Intersection," in *Practical Geometric Algorithms with C++ code*, 2021. [Online]. Available: www.geomalgorithms.com/

[10] ——, "dist3D_Segment_to_Segment," in *Practical Geometric Algorithms with C++ code*, 2021. [Online]. Available: https://www.geomalgorithms.com/

[11] A. Williams, S. Barrus, R. K. Morley, and P. Shirley, "An Efficient and Robust Ray-Box Intersection Algorithm," *Journal of Graphics Tools*, vol. 10, no. 1, pp. 49–54, 2005.

[12] T. Möller and E. Haines, "Ray/Box Intersection - Intersection Test Methods," in *Real-Time Rendering*, 2nd ed. AK Peters / CRC Press, 2002, pp. 572–578.

[13] R. Perez, R. Seals, and J. Michalsky, "All-weather model for sky luminance distribution-Preliminary configuration and validation," *Solar Energy*, vol. 50, no. 3, pp. 235–245, 1993.

[14] D. L. King, J. A. Kratochvil, and W. E. Boyson, "Photovoltaic array performance model," Sandia National Laboratories, Tech. Rep. December, 2004. [Online]. Available: doi.org/10.2172/919131

[15] D. Faiman, "Assessing the Outdoor Operating Temperature of Photovoltaic Modules," *Progress in Photovoltaics: Research and Applications*, vol. 16, no. 1, pp. 307–315, 2008. [Online]. Available: https://doi.org/10.1002/pip.813

[16] International Energy Agency, "Net Zero by 2050: A Roadmap for the Global Energy Sector," Tech. Rep., 2021. [Online]. Available: https://www.iea.org/reports/net-zero-by-2050

[17] VDMA, "International Technology Roadmap for Photovoltaics (ITRPV) 2022 Results," Tech. Rep., 2022. [Online]. Available: https://www.vdma.org/international-technology-roadmap-photovoltaic

[18] M. Theristis, N. Riedel-Lyngskær, J. S. Stein, L. Deville, L. Micheli, A. Driesse, W. B. Hobbs, S. Ovaitt, R. Daxini, D. Barrie, M. Campanelli, H. Hodges, J. R. Ledesma, I. Lokhat, B. McCormick, B. Meng, B. Miller, R. Motta, E. Noirault, M. Parker, J. Polo, D. Powell, R. Moretón, M. Prilliman, S. Ransome, M. Schneider, B. Schnierer, B. Tian, F. Warner, R. Williams, B. Wittmer, and C. Zhao, "Blind photovoltaic modeling intercomparison: A multidimensional data analysis and lessons learned," *Progress in Photovoltaics: Research and Applications*, vol. 31, no. 11, pp. 1144–1157, 2023. [Online]. Available: https://onlinelibrary.wiley.com/doi/abs/10.1002/pip.3729

[19] M. Bolinger, J. Seel, C. Warner, and D. Robson, "Utility-Scale Solar, 2022 Edition: Empirical Trends in Deployment, Technology, Cost, Performance, PPA Pricing, and Value in the United States." Lawrence Berkeley National Laboratory, Tech. Rep., 2022. [Online]. Available: https://emp.lbl.gov/sites/default/files/utility_scale_solar_2023_edition_slides.pdf

[20] H. Mori, "Radiation energy transducing device - US Patent No. 3278811," 1966.

[21] A. Moehlecke, I. Zanesco, and A. Luque, "Practical high efficiency bifacial solar cells," in *Proceedings of 1994 IEEE 1st World Conference on Photovoltaic Energy Conversion - WCPEC (A Joint Conference of PVSC, PVSEC and PSEC)*, vol. 2, 1994, pp. 1663–1666 vol.2.

[22] S. R. Wenham, M. A. Green, M. E. Watt, R. Corkish, and A. Sproul, *Applied Photovoltaics*, 3rd ed. Earthscan, 2013.

[23] J. Nelson, *The physics of solar cells*. Imperial College Press, 2003.

[24] C. Hu, *Modern semiconductor devices for integrated circuits*. Upper Saddle River, N.J: Prentice Hall, 2010.

[25] C. Honsberg and S. Bowden, "Bias of P-N junctions," pveducation.org, 2019. [Online]. Available: https://www.pveducation.org/pvcdrom/pn-junctions/bias-of-pn-junctions

[26] S. R. Wenham, M. A. Green, M. E. Watt, R. Corkish, and A. Sproul, "Ch 2 - Semiconductors and P-N Junctions," in *Applied Photovoltaics*, 3rd ed. Earthscan, 2013.

[27] J. Nelson, "Ch 6 - Analysis of the P-N Junction," in *The physics of solar cells*. Imperial College Press, 2003.

[28] J. Libal and R. Kopecek, *Bifacial Photovoltaics*. Stevenage, England: Institution of Engineering and Technology, Dec. 2018.

[29] S. R. Wenham, M. A. Green, M. E. Watt, R. Corkish, and A. Sproul, "Ch 4 - cell properties and design," in *Applied Photovoltaics*, 3rd ed. Earthscan, 2013.

[30] J. Nelson, "Ch 4 - Generation and Recombination," in *The physics of solar cells*. Imperial College Press, 2003.

[31] S. R. Wenham, M. A. Green, M. E. Watt, R. Corkish, and A. Sproul, "Ch 3 - the behavior of solar cells," in *Applied Photovoltaics*, 3rd ed. Earthscan, 2013.

[32] A. Calcabrini, P. Procel Moya, B. Huang, V. Kambhampati, P. Manganiello, M. Muttillo, M. Zeman, and O. Isabella, "Low-breakdown-voltage solar cells for shading-tolerant photovoltaic modules," *Cell Reports Physical Science*, vol. 3, no. 12, p. 101155, 2022. [Online]. Available: https://www.sciencedirect.com/science/article/pii/S2666386422004660

[33] T. Markvart and L. Castañer, "Ch. I-1-A - Principles of Solar Cell Operation," in *McEvoy's Handbook of Photovoltaics (Third Edition)*, third edition ed., S. A.

Kalogirou, Ed. Academic Press, 2018, pp. 3–28. [Online]. Available: https://www.sciencedirect.com/science/article/pii/B978012809921600001X

[34] J. Nelson, "Ch 7 - Monocrystalline Solar Cells," in *The physics of solar cells*. Imperial College Press, 2003.

[35] C. S. Ruschel, F. P. Gasparin, and A. Krenzinger, "Experimental analysis of the single diode model parameters dependence on irradiance and temperature," *Solar Energy*, vol. 217, pp. 134–144, 2021. [Online]. Available: https://www.sciencedirect.com/science/article/pii/S0038092X21000931

[36] W. De Soto, S. A. Klein, and W. A. Beckman, "Improvement and validation of a model for photovoltaic array performance," *Solar Energy*, vol. 80, no. 1, pp. 78–88, 2006.

[37] J. Nelson, "Ch 1 - Introduction," in *The physics of solar cells*. Imperial College Press, 2003.

[38] A. M. Gabr, A. H. Trojnar, M. Wilkins, T. J. Hall, R. N. Kleiman, and K. Hinzer, "Optimization of anti-reflection coatings for bifacial solar cells with upconversion layers," in *2014 IEEE 40th Photovoltaic Specialist Conference (PVSC)*, 2014, pp. 2230–2233.

[39] S. Guo, J. P. Singh, I. M. Peters, A. G. Aberle, and T. M. Walsh, "A quantitative analysis of photovoltaic modules using halved cells," *International Journal of Photoenergy*, vol. 2013, p. 1–8, 2013. [Online]. Available: http://dx.doi.org/10.1155/2013/739374

[40] PVsyst, "Pvsyst 7.4 documentation," 2023. [Online]. Available: https://www.pvsyst.com/help/index.html?contents_table.htm

[41] M. Mikofski, B. Meyers, and C. Chaudhari, "PVMismatch Project," SunPower Corporation, Tech. Rep., 2018. [Online]. Available: https://sunpower.github.io/PVMismatch/

[42] C. Deline, S. Ayala Pelaez, S. MacAlpine, and C. Olalla, "Estimating and parameterizing mismatch power loss in bifacial photovoltaic systems," *Progress in Photovoltaics: Research and Applications*, vol. 28, no. 7, pp. 691–703, 2020. [Online]. Available: https://onlinelibrary.wiley.com/doi/abs/10.1002/pip.3259

[43] G. M. Masters, "Ch 6 - Photovoltaic Systems," in *Renewable and Efficient Electric Power Systems*, 2nd ed. John Wiley and Sons, 2013.

[44] J. Lopez-Garcia, E. Ozkalay, R. P. Kenny, L. Pinero-Prieto, D. Shaw, D. Pavanello, and T. Sample, "Implementation of the IEC TS 60904-1-2 Measurement Methods for Bifacial Silicon PV Devices," *IEEE Journal of Photovoltaics*, vol. 12, no. 3, pp. 787–797, 2022.

[45] Trina Solar, "TSM-DEG5C.20(II) (295-310 W) Datasheet." [Online]. Available: https://static.trinasolar.com/sites/default/files/PS-M-0647%20A%20Datasheet_Duomax%20M%20Twin_DEG5C%2020%28II%29__EN.pdf

[46] California Energy Commission, "PV Module List," 2024. [Online]. Available: https://www.energy.ca.gov/media/2367

[47] C. B. Jones and C. W. Hansen, "Single diode parameter extraction from in-field photovoltaic I-V curves on a single board computer," in *2019 IEEE 46th Photovoltaic Specialists Conference (PVSC)*, 2019, pp. 0382–0387.

[48] C. W. Hansen, "Parameter estimation for single diode models of photovoltaic modules," Sandia National Laboratories, Tech. Rep., 2015. [Online]. Available: https://www.osti.gov/servlets/purl/1177157

[49] G. M. Masters, "Ch 4 - The Solar Resource," in *Renewable and Efficient Electric Power Systems*, 2nd ed. John Wiley and Sons, 2013.

[50] G. Qiu and S. B. Riffat, "Optimum tilt angle of solar collectors and its impact on performance," *International Journal of Ambient Energy*, vol. 24, no. 1, pp. 13–20, 2003.

[51] G. Lewis, "Optimum tilt of a solar collector," *Solar and Wind Technology*, vol. 4, no. 3, p. 407 – 410, 1987. [Online]. Available: doi.org/10.1016/0741-983X(87)90073-7

[52] M. Trommsdorff, S. Gruber, T. Keinath, M. Hopf, C. Hermann, and F. Schönberger, "Agrivoltaics: Opportunities for agriculture and the energy transition," Fraunhofer Institute for Solar Energy Systems ISE, Tech. Rep., 2022. [Online]. Available: https://www.ise.fraunhofer.de/content/dam/ise/en/documents/publications/studies/APV-Guideline.pdf

[53] A. Asgharzadeh, B. Marion, C. Deline, C. Hansen, J. S. Stein, and F. Toor, "A sensitivity study of the impact of installation parameters and system configuration on the performance of bifacial PV arrays," *IEEE Journal of Photovoltaics*, 2018.

[54] K. Doubleday, B. Choi, D. Maksimovic, C. Deline, and C. Olalla, "Recovery of inter-row shading losses using differential power-processing submodule dc–dc converters," *Solar Energy*, vol. 135, pp. 512–517, 2016. [Online]. Available: https://www.sciencedirect.com/science/article/pii/S0038092X1630192X

[55] E. Lorenzo, L. Narvarte, and J. Muñoz, "Tracking and back-tracking," *Progress in Photovoltaics: Research and Applications*, vol. 19, no. 6, pp. 747–753, 2011.

[56] K. Anderson and M. Mikofski, "Slope-aware backtracking for single-axis trackers," National Renewable Energy Laboratory, Tech. Rep., 2020. [Online]. Available: https://www.nrel.gov/docs/fy20osti/76626.pdf

[57] D. Gun and A. A. Shishavan, "Enhancing energy yields with truecapture," Nextracker LLC, Tech. Rep., 2022. [Online]. Available: https://info.nextracker.com/hubfs/Whitepaper%202022/Nextracker_Whitepaper_TrueCapture_2002.pdf

[58] DNV-GL, "Field testing and model validation of array's smartrack tm shade mitigation technology," Tech. Rep., 2020. [Online]. Available: https://arraytechinc.com/products/smartrack/smartrack-backtracking/

[59] J. R. G. Ross and M. I. Smokler, "Flat-plate solar array project final report," U.S. Department of Energy Jet Propulsion Lab, Tech. Rep., 1986. [Online]. Available: https://www.osti.gov/biblio/6802984

[60] PVsyst, "Array Thermal Losses: PVsyst 7.4 Documentation." [Online]. Available: https://www.pvsyst.com/help/thermal_loss.htm

[61] A. Driesse, J. S. Stein, and M. Theristis, "Improving common pv module temperature models by incorporating radiative losses to the sky," Sandia National Laboratory, Tech. Rep., 2022. [Online]. Available: https://www.osti.gov/servlets/purl/1884890

[62] M. Prilliman, J. S. Stein, D. Riley, and G. Tamizhmani, "Transient weighted moving-average model of photovoltaic module back-surface temperature," *IEEE Journal of Photovoltaics*, vol. 10, no. 4, pp. 1053–1060, 2020. [Online]. Available: doi.org/10.1109/JPHOTOV.2020.2992351

[63] M. K. Fuentes, "A simplified thermal model for flat-plate photovoltaic arrays," Sandia National Laboratory, Tech. Rep., 5 1987. [Online]. Available: https://www.osti.gov/biblio/6802914

[64] S. R. Wenham, M. A. Green, M. E. Watt, R. Corkish, and A. Sproul, "Ch 1 - The Characteristics of Sunlight," in *Applied Photovoltaics*, 3rd ed. Earthscan, 2013.

[65] F. Vignola, J. Michalsky, and T. Stoffel, "Ch 2 - Solar Spectral Measurements," in *Solar and Infrared Radiation Measurements*. CRC Press: Taylor & Francis Group, 2012.

[66] J. Nelson, "Photons In, Electrons Out: Basic Principles of PV," in *The physics of solar cells*. Imperial College Press, 2003.

[67] C. A. Gueymard, "A reevaluation of the solar constant based on a 42-year total solar irradiance time series and a reconciliation of spaceborne observations," *Solar Energy*, vol. 168, pp. 2–9, 2018, advances in Solar Resource Assessment and Forecasting. [Online]. Available: https://www.sciencedirect.com/science/article/pii/S0038092X18303463

[68] G. Corbellini and V. Medici, "Modeling of Bifacial PV Modules," in *4th PV Performance Modelling Collaborative*, 2015. [Online]. Available: https://www.slideshare.net/sandiaecis/41-corbellini-analysisandmodellingofbifacialpvmodules

[69] F. Vignola, J. Michalsky, and T. Stoffel, "Ch 9 - Albedo," in *Solar and Infrared Radiation Measurements*. CRC Press: Taylor & Francis Group, 2012.

[70] International Organization for Standardization, "Solar energy — Reference solar spectral irradiance at the ground at different receiving conditions — Part 1: Direct normal and hemispherical solar irradiance for air mass 1,5," Tech. Rep., 2022. [Online]. Available: https://www.iso.org/standard/67464.html

[71] C. Yu, J. Chai, S. Han, Z. Liu, X. Li, and J. Yao, "Field performance evaluation of various crystalline silicon photovoltaic technologies in Pingshan, China," *Energy Reports*, vol. 5, pp. 525–528, 2019. [Online]. Available: https://www.sciencedirect.com/science/article/pii/S2352484719300551

[72] F. Vignola, J. Michalsky, and T. Stoffel, "Ch 5 - Measuring Global Irradiance," in *Solar and Infrared Radiation Measurements*. CRC Press: Taylor & Francis Group, 2012.

[73] F. E. Vignola, A. C. McMahan, and C. N. Grover, "Ch 5 - Bankable Solar-Radiation Datasets," in *Solar Energy Forecasting and Resource Assessment*, J. Kleissl, Ed. Boston: Academic Press, 2013, pp. 97–131. [Online]. Available: https://www.sciencedirect.com/science/article/pii/B978012397177700005X

[74] T. Cebecauer and M. Suri, "Typical meteorological year data: Solargis approach," *Energy Procedia*, vol. 69, pp. 1958–1969, 2015. [Online]. Available: https://www.sciencedirect.com/science/article/pii/S1876610215005019

[75] Natural Resources Canada, "Canadian Weather Year for Energy Calculation (CWEC)," Government of Canada, 2023-05-18. [Online]. Available: https://open.canada.ca/data/en/dataset/55438acb-aa67-407a-9fdb-1cb21eb24e28

[76] S. Wilcox and W. Marion, "Users Manual for TMY3 Data Sets," National Renewable Energy Laboratory, Tech. Rep., 2008. [Online]. Available: https://www.nrel.gov/docs/fy08osti/43156.pdf

[77] EU Science Hub, "Photovoltaic Geographical Information System," European Commission, 2022-03-01. [Online]. Available: https://re.jrc.ec.europa.eu/pvg_tools/en/#TMY

[78] H. Jiang, N. Lu, L. Yao, J. Qin, and T. Liu, "Impact of climate changes on the stability of solar energy: Evidence from observations and reanalysis," *Renewable Energy*, vol. 208, pp. 726–736, 2023. [Online]. Available: https://www.sciencedirect.com/science/article/pii/S0960148123004172

[79] E. L. Maxwell, “A quasi-physical model for converting hourly global horizontal to direct normal lnsolation,” US DOE Solar Energy Research Institute, Tech. Rep., 1987. [Online]. Available: https://www.nrel.gov/docs/legosti/old/3087.pdf

[80] P. Blanc, B. Espinar, N. Geuder, C. Gueymard, R. Meyer, R. Pitz-Paal, B. Reinhardt, D. Renné, M. Sengupta, L. Wald, and S. Wilbert, “Direct normal irradiance related definitions and applications: The circumsolar issue,” *Solar Energy*, vol. 110, pp. 561–577, 2014. [Online]. Available: https://www.sciencedirect.com/science/article/pii/S0038092X14004824

[81] M. Lave, W. Hayes, A. Pohl, and C. W. Hansen, “Evaluation of global horizontal irradiance to plane-of-array irradiance models at locations across the united states,” *IEEE Journal of Photovoltaics*, vol. 5, no. 2, pp. 597–606, 2015. [Online]. Available: doi.org/10.1109/JPHOTOV.2015.2392938

[82] I. Reda and A. Andreas, “Solar Position Algorithm for Solar Radiation Applications (Revised),” National Renewable Energy Laboratory, Tech. Rep., 2005. [Online]. Available: https://www.nrel.gov/docs/fy08osti/34302.pdf

[83] R. Perez, P. Ineichen, R. Seals, J. Michalsky, and R. Stewart, “Modeling daylight availability and irradiance components from direct and global irradiance,” *Solar Energy*, vol. 44, no. 5, pp. 271–289, 1990. [Online]. Available: https://www.sciencedirect.com/science/article/pii/0038092X9090055H

[84] K. Alshaibani, D. Li, and E. Aghimien, “Sky luminance distribution models: A comparison with measurements from a maritime desert region,” *Energies*, vol. 13, no. 20, 2020. [Online]. Available: https://www.mdpi.com/1996-1073/13/20/5455

[85] D. Yang, “Solar radiation on inclined surfaces: Corrections and benchmarks,” *Solar Energy*, vol. 136, pp. 288–302, 2016. [Online]. Available: https://www.sciencedirect.com/science/article/pii/S0038092X16302432

[86] N. Riedel-Lyngskaer, D. Berrian, D. A. Mira, A. A. Protti, P. B. Poulsen, J. Libal, and J. Vedde, “Validation of bifacial photovoltaic simulation software against monitoring data

from large-scale single-axis trackers and fixed tilt systems in Denmark," *Applied Sciences*, vol. 10, no. 23, pp. 1–29, 2020. [Online]. Available: https://doi.org/10.3390/app10238487

[87] Y. Qu, "Sea Surface Albedo," in *Comprehensive Remote Sensing*, S. Liang, Ed. Oxford: Elsevier, 2018, pp. 163–185. [Online]. Available: https://www.sciencedirect.com/science/article/pii/B9780124095489103719

[88] M. Ernst, X. Liu, C.-A. Asselineau, D. Chen, C. Huang, and A. Lennon, "Accurate modelling of the bifacial gain potential of rooftop solar photovoltaic systems," *Energy Conversion and Management*, vol. 300, p. 117947, 2024. [Online]. Available: https://www.sciencedirect.com/science/article/pii/S0196890423012931

[89] C. Gueymard, "An anisotropic solar irradiance model for tilted surfaces and its comparison with selected engineering algorithms," *Solar Energy*, vol. 38, no. 5, pp. 367–386, 1987. [Online]. Available: https://www.sciencedirect.com/science/article/pii/0038092X87900090

[90] M. F. Modest and S. Mazumder, "Ch 4 - View Factors," in *Radiative Heat Transfer*, 4th ed., M. F. Modest and S. Mazumder, Eds. Academic Press, 2022, pp. 127–159. [Online]. Available: https://www.sciencedirect.com/science/article/pii/B9780128181430000122

[91] U. A. Yusufoglu, T. H. Lee, T. M. Pletzer, A. Halm, L. J. Koduvelikulathu, C. Comparotto, R. Kopecek, and H. Kurz, "Simulation of energy production by bifacial modules with revision of ground reflection," *Energy Procedia*, vol. 55, pp. 389–395, 2014. [Online]. Available: http://dx.doi.org/10.1016/j.egypro.2014.08.111

[92] T. Muneer, S. Ivanova, Y. Kotak, and M. Gul, "Finite-element view-factor computations for radiant energy exchanges," *Journal of Renewable and Sustainable Energy*, vol. 7, no. 3, May 2015. [Online]. Available: http://dx.doi.org/10.1063/1.4921387

[93] C. W. Hansen, J. S. Stein, C. Deline, S. MacAlpine, B. Marion, A. Asgharzadeh, and F. Toor, "Analysis of irradiance models for bifacial pv modules," in *2016 IEEE 43rd Photovoltaic Specialists Conference (PVSC)*, 2016, pp. 0138–0143. [Online]. Available: https://doi.org/10.1109/PVSC.2016.7749564

[94] M.-G. Retzlaff, J. Hanika, J. Beyerer, and C. Dachsbacher, "Physically based computer graphics for realistic image formation to simulate optical measurement systems," *Journal of Sensors and Sensor Systems*, vol. 6, no. 1, pp. 171–184, 2017. [Online]. Available: https://jsss.copernicus.org/articles/6/171/2017/

[95] J. R. Howell, "A catalog of radiation heat transfer configuration factors," 2020. [Online]. Available: http://www.thermalradiation.net/tablecon.html

[96] J. Ledesma, R. Almeida, F. Martinez-Moreno, C. Rossa, J. Martín-Rueda, L. Narvarte, and E. Lorenzo, "A simulation model of the irradiation and energy yield of large bifacial photovoltaic plants," *Solar Energy*, vol. 206, pp. 522–538, 2020. [Online]. Available: https://www.sciencedirect.com/science/article/pii/S0038092X20306071

[97] M. A. Anoma, D. Jacob, B. C. Bourne, J. A. Scholl, D. M. Riley, and C. W. Hansen, "View factor model and validation for bifacial pv and diffuse shade on single-axis trackers," in *2017 IEEE 44th Photovoltaic Specialist Conference (PVSC)*, 2017, pp. 1549–1554.

[98] Sunpower Corporation, "pvfactors," Tech. Rep., 2021. [Online]. Available: https://sunpower.github.io/pvfactors/

[99] B. Marion, S. MacAlpine, C. Deline, A. Asgharzadeh, F. Toor, D. Riley, J. Stein, and C. Hansen, "A practical irradiance model for bifacial PV modules," *IEEE 44th Photovoltaic Specialists Conference (PVSC)*, no. June, 2017. [Online]. Available: https://www.nrel.gov/docs/fy17osti/67847.pdf?gathStatIcon=true

[100] N. Blair, A. Dobos, J. Freeman, T. Neises, M. Wagner, T. Ferguson, P. Gilman, and S. Janzou, "System Advisor Model, SAM 2014.1.14: General Description," National Renewable Energy Laboratory, Tech. Rep., 2014. [Online]. Available: www.nrel.gov/docs/fy14osti/61019.pdf

[101] K. R. McIntosh, M. D. Abbott, B. A. Sudbury, and J. Meydbray, "Mismatch loss in bifacial modules due to nonuniform illumination in 1-d tracking systems," *IEEE Journal of Photovoltaics*, vol. 9, no. 6, pp. 1504–1512, 2019. [Online]. Available: https://doi.org/10.1109/JPHOTOV.2019.2937217

[102] C. Zhao, J. Xiao, Y. Yu, and J.-N. Jaubert, "Accurate shading factor and mismatch loss analysis of bifacial hsat systems through ray-tracing modeling," *Solar Energy Advances*, vol. 1, p. 100004, 2021. [Online]. Available: https://www.sciencedirect.com/science/article/pii/S2667113121000048

[103] S. A. Pelaez, C. Deline, P. Greenberg, J. S. Stein, and R. K. Kostuk, "Corrections to "model and validation of single-axis tracking with bifacial PV"," *IEEE Journal of Photovoltaics*, vol. 9, no. 6, pp. 1880–1880, 2019. [Online]. Available: https://doi.org/10.1109/JPHOTOV.2019.2943086

[104] M. R. Lewis, T. J. Coathup, A. C. J. Russell, C. E. Valdivia, and K. Hinzer, "Quantifying Structural Shading & Reflection Effects on Single Axis Tracked Bifacial Photovoltaic System Performance," *Advanced Energy and Sustainability Research*, Accepted April 2024.

[105] F. Araya Rojas, "Predictive modelling of bifacial PV plants performance and diagnostic," Ph.D. Dissertation, Université Grenoble Alpes, 2022. [Online]. Available: https://theses.hal.science/tel-03828423

[106] A. Neubert, M. Hamer, and J. Lopez-Lorente, "Shading in utility-scale photovoltaic plants: A hemicube approach for efficient shading calculations," *Solar RRL*, vol. 7, no. 19, p. 2300473, 2023. [Online]. Available: https://onlinelibrary.wiley.com/doi/abs/10.1002/solr.202300473

[107] A. S. Glassner, "Ch 1 - An Overview of Ray Tracing," in *An Introduction to Ray Tracing*. GBR: Academic Press Ltd., 1989. [Online]. Available: https://www.realtimerendering.com/raytracing/An-Introduction-to-Ray-Tracing-The-Morgan-Kaufmann-Series-in-Computer-Graphics-.pdf

[108] G. J. Ward, "Hierarchical Octrees for Spatial Subdivision," in *The RADIANCE Lighting Simulation and Rendering System*. Berkely Labs, US Department of Energy, 2003. [Online]. Available: https://floyd.lbl.gov/radiance/papers/sg94.1/octree.html

[109] S. Ayala Pelaez, "Bifacial solar panels system design, modeling, and performance," Ph.D. dissertation, The University of Arizona, 2019. [Online]. Available: http://hdl.handle.net/10150/631283

[110] A. Asgharzadeh Shishavan, "Bifacial photovoltaic (PV) system performance modeling utilizing ray tracing," Ph.D. dissertation, University of Iowa, 2019. [Online]. Available: https://doi.org/10.17077/etd.wb36-bytp

[111] K. R. McIntosh, M. D. Abbott, B. A. Sudbury, J. Nagyvary, K. Lee, L. Creasy, J. Sharp, J. Crimmins, and D. Zirzow, "Simulation and measurement of monofacial and bifacial modules in a 1D tracking system," in *Conference Record of the IEEE Photovoltaic Specialists Conference*, 2020. [Online]. Available: https://doi.org/10.1109/PVSC45281.2020.9300620

[112] H. Nussbaumer, G. Janssen, D. Berrian, B. Wittmer, M. Klenk, T. Baumann, F. Baumgartner, M. Morf, A. Burgers, J. Libal, and A. Mermoud, "Accuracy of simulated data for bifacial systems with varying tilt angles and share of diffuse radiation," *Solar Energy*, vol. 197, no. December 2019, pp. 6–21, 2020. [Online]. Available: https://doi.org/10.1016/j.solener.2019.12.071

[113] D. Berrian and J. Libal, "A comparison of ray tracing and view factor simulations of locally resolved rear irradiance with the experimental values," *Progress in Photovoltaics: Research and Applications*, vol. 28, no. 6, pp. 609–620, 2020.

[114] M. Pharr, W. Jakob, and G. Humphreys, "Ch. 8 - Reflection Models," in *Physically Based Rendering: From Theory to Implementation*, 3rd ed. San Francisco, CA, USA: Morgan Kaufmann Publishers Inc., 2016.

[115] A. F. Souka and H. H. Safwat, "Determination of the optimum orientations for the double-exposure, flat-plate collector and its reflectors," *Solar Energy*, vol. 10, no. 4, pp. 170–174, 1966.

[116] S. Ayala Pelaez, "Tutorial: Modeling modules with glass - bifacial_radiance documentation," National Renewable Energy Laboratory Webinar. [Online]. Available: https:

//bifacial-radiance.readthedocs.io/en/latest/tutorials/13%20-%20Modeling%20Modules%20with%20Glass.html?highlight=incidence%20angle#13---Modeling-Modules-with-Glass

[117] K. R. McIntosh, M. D. Abbott, G. Loomis, B. A. Sudbury, A. Mayer, C. Zak, and J. Meydbrey, "Irradiance on the upper and lower modules of a two-high bifacial tracking system," in *2020 47th IEEE Photovoltaic Specialists Conference (PVSC)*, 2020, pp. 1916–1923. [Online]. Available: https://doi.org/10.1109/PVSC45281.2020.9300838

[118] M. Ernst, G. E. Conechado, and C.-A. Asselineau, "Accelerating the simulation of annual bifacial illumination of real photovoltaic systems with ray tracing," *iScience*, vol. 25, no. 1, p. 103698, 2022. [Online]. Available: https://www.sciencedirect.com/science/article/pii/S2589004221016680

[119] D. Robinson and A. Stone, "Irradiation modelling made simple: the cumulative sky approach and its applications," in *The 21st Conference on Passive and Low Energy Architecture*, September 2004. [Online]. Available: https://doi.org/10.1109/PVSC.2016.7749836

[120] M. Gostein, S. A. Pelaez, C. Deline, A. Habte, C. W. Hansen, B. Marion, J. Newmiller, M. Sengupta, J. S. Stein, and I. Suez, "Measuring irradiance for bifacial pv systems," in *2021 IEEE 48th Photovoltaic Specialists Conference (PVSC)*, 2021, pp. 0896–0903. [Online]. Available: https://doi.org/10.1109/PVSC43889.2021.9518601

[121] F. Vignola, J. Michalsky, and T. Stoffel, *Solar and Infrared Radiation Measurements*. CRC Press: Taylor & Francis Group, 2012.

[122] S. Ovaitt, "BEST Field Data - Data and Resources," National Renewable Energy Laboratory, 2021. [Online]. Available: https://datahub.duramat.org/dataset/best-field-data

[123] N. Riedel, D. Berrian, D. Alvarez Mira, A. A. Protti, P. B. Poulsen, and J. et al. Libal, "Data used in "Validation of Bifacial Photovoltaic Simulation Software against Monitoring Data from Large-Scale Single-Axis Trackers and Fixed Tilt Systems in Denmark"," 2021. [Online]. Available: https://doi.org/10.11583/DTU.13580759.v3

[124] V. Tatsiankou, K. Hinzer, H. Schriemer, S. Kazadzis, N. Kouremeti, J. Gröbner, and R. Beal, "Extensive validation of solar spectral irradiance meters at the world

radiation center," *Solar Energy*, vol. 166, pp. 80–89, 2018. [Online]. Available: https://www.sciencedirect.com/science/article/pii/S0038092X18302767

[125] International Organization for Standardization, "Solar energy — Specification and classification of instruments for measuring hemispherical solar and direct solar radiation," Tech. Rep., 2018. [Online]. Available: https://www.iso.org/standard/67464.html

[126] C. Richiardi, P. Blonda, F. M. Rana, M. Santoro, C. Tarantino, S. Vicario, and M. Adamo, "A revised snow cover algorithm to improve discrimination between snow and clouds: A case study in gran paradiso national park," *Remote Sensing*, vol. 13, no. 10, 2021. [Online]. Available: https://www.mdpi.com/2072-4292/13/10/1957

[127] E. Haine, "Ray Tracing Resources Page," 2021. [Online]. Available: https://www.realtimerendering.com/intersections.html

[128] P. Corke, "Representing position and orientation," in *Robotics, Vision and Control: Fundamental Algorithms In MATLAB®*, 2nd ed. Cham: Springer International Publishing, 2017, pp. 17–62. [Online]. Available: https://doi.org/10.1007/978-3-319-54413-7_2

[129] S. Gowrishankar and A. Veena, *Introduction to Python Programming*, 1st ed. Boca Raton, FL: Chapman and Hall/CRC, 2018 - 2019.

[130] A. B. Tucker and R. Noonan, *Programming languages : principles and paradigms*, 2nd ed. Boston: McGraw-Hill Higher Education, 2007.

[131] T. Budd, *An introduction to object-oriented programming*, 3rd ed. Boston, MA: Addison-Wesley, 2002.

[132] P. Mccaffrey, "Ch 11 - A selective introduction to Python and key concepts," in *An Introduction to Healthcare Informatics*, P. Mccaffrey, Ed. Academic Press, 2020, pp. 145–157. [Online]. Available: https://www.sciencedirect.com/science/article/pii/B9780128149157000119

[133] NumPy, "NumPy Documentation Version 1.26." [Online]. Available: https://numpy.org/doc/stable/index.html

[134] R. Johansson, "Vectors, Matrices, and Multidimensional Arrays," in *Numerical Python: A Practical Techniques Approach for Industry*. Berkeley, CA: Apress, 2015, pp. 25–62. [Online]. Available: https://doi.org/10.1007/978-1-4842-0553-2_2

[135] T. E. Oliphant, "Contiguous memory layout," in *Guide to NumPy*. CreateSpace Independent Publishing Platform, 2006.

[136] NumPy, "Broadcasting and Vectorization," Unidata. [Online]. Available: https://unidata.github.io/python-training/workshop/NumPy/numpy-broadcasting-and-vectorization/

[137] Numpy, "numpy.vectorize Version 1.26," 2023. [Online]. Available: https://numpy.org/doc/stable/reference/generated/numpy.vectorize.html

[138] C. von Csefalvay, "JIT fast! Supercharge tensor processing in Python with JIT compilation," 2019. [Online]. Available: https://medium.com/starschema-blog/jit-fast-supercharge-tensor-processing-in-python-with-jit-compilation-47598de6ee96

[139] Numba, "Compiling python code with @jit," 2023. [Online]. Available: https://numba.readthedocs.io/en/stable/user/jit.html

[140] Numba, "Types and Signatures." [Online]. Available: https://numba.readthedocs.io/en/stable/reference/types.html#numba-types

[141] B. Beckers and P. Beckers, "Fast and accurate view factor generation," in *An International Conference on Urban Physics*, Quito-Galápagos, Ecuador, 2016, pp. 22–31. [Online]. Available: https://www.researchgate.net/publication/315292615_Fast_and_accurate_view_factor_generation

[142] T. Leduc, "Quantify sun exposure: a visual-based approach combining meshed sky vault and moving light source," in *International Research Seminar at Laboratorio di Simulazione Urbana - Fausto Curti*, no. November, Milano, Italy, 2015. [Online]. Available: https://doi.org/10.13140/RG.2.1.1012.1048

[143] C. Crowell, *How solar trackers overcome undulating terrain - and avoid grading costs*. Solar Builder Magazine, 2021. [Online]. Available: https://solarbuildermag.com/solar-trackers/how-solar-trackers-overcome-undulating-terrain-and-avoid-grading-costs/

[144] D. S. Dolan, V. Prodanov, P. Salter, F. Cheein, and J. Dolan, "Reducing performance loss due to backtracking error through use of half cut cell modules," in *2019 9th International Conference on Power and Energy Systems (ICPES)*, 2019, pp. 1–4.

[145] F. Cheein, D. S. L. Dolan, and S. H. Patrick, "Effective backtracking algorithm for half-cut cell solar panels," in *The 9th Renewable Power Generation Conference (RPG Dublin Online 2021)*, vol. 2021, 2021, pp. 355–358.

[146] E. Than, "Diode-based temperature measurement SBOA277A," Texas Instruments, Tech. Rep., 2019. [Online]. Available: https://www.ti.com/lit/an/sboa277a/sboa277a.pdf?ts=1703035191586&

[147] J. Bauer, J.-M. Wagner, A. Lotnyk, H. Blumtritt, N. Zakharov, and O. Breitenstein, "Physical mechanisms of electrical breakdown in silicon solar cells," Max Planck Institute of Microstructure Physics, Tech. Rep., 10 2009.

[148] A. Russell, "Incorrect solid angle in gendaylit diffuse normalization factor?" 2020. [Online]. Available: https://discourse.radiance-online.org/t/incorrect-solid-angle-in-gendaylit-diffuse-normalization-factor/5402/2

[149] B. Wittmer, "Simulating Bifacial Fixed Tilt and Tracking Systems with PVsyst," in *PV Magazine Webinar*, 2019.

[150] J. Chase, "Global PV Market Outlook, 4Q 2023," Bloomberg New Energy Finance, Tech. Rep., 2023. [Online]. Available: https://about.bnef.com/blog/global-pv-market-outlook-4q-2023/

[151] PVsyst, "Bifacial Systems Procedure: PVsyst 7.4 Documentation," 2023. [Online]. Available: https://www.pvsyst.com/help/index.html?bifacial_procedure.htm

[152] ——, "Module mismatch loss: Pvsyst 7.4 documentation." [Online]. Available: https://www.pvsyst.com/help/module_mismatch_loss.htm

[153] ——, "Mismatch principles: Pvsyst 7.4 documentation." [Online]. Available: https://www.pvsyst.com/help/mismatch_principles.htm

[154] S. Ayala Pelaez and C. Deline, *Bifacial_Radiance Training - Part 1: NREL Webinar*. National Renewable Energy Laboratory Webinar, Oct. 17, 2019. [Online]. Available: https://www.nrel.gov/docs/fy20osti/75218.pdf

[155] C. Deline and S. Ayala Pelaez, "Bifacial_radiance," US DOE Office of Energy Efficiency and Renewable Energy (EERE), Solar Energy Technologies Office (EE-4S)., 17 Dec. 2017. [Online]. Available: https://www.osti.gov/doecode/biblio/6869

[156] N. Riedel-Lyngskær, M. Petit, D. Berrian, P. B. Poulsen, J. Libal, and M. L. Jakobsen, "A spatial irradiance map measured on the rear side of a utility-scale horizontal single axis tracker with validation using open source tools," in *2020 47th IEEE Photovoltaic Specialists Conference (PVSC)*, 2020, pp. 1026–1032. [Online]. Available: https://doi.org/10.1109/PVSC45281.2020.9300608

[157] S. Ayala Pelaez, C. Deline, J. S. Stein, B. Marion, K. Anderson, and M. Muller, "Effect of torque-tube parameters on rear-irradiance and rear-shading loss for bifacial pv performance on single-axis tracking systems," in *2019 IEEE 46th Photovoltaic Specialists Conference (PVSC)*, vol. 2, 2019, pp. 1–6. [Online]. Available: https://doi.org/10.1109/PVSC40753.2019.9198975

[158] J. Guerrero Pérez and J. Navarro Berbel, "BiTEC : How to simulate bifacial projects?" Soltec, Tech. Rep., 2019. [Online]. Available: https://lab.soltec.com/bifacial-trackers-ii/

[159] C. D. Rodríguez-Gallegos, H. Liu, O. Gandhi, J. P. Singh, V. Krishnamurthy, A. Kumar, J. S. Stein, S. Wang, L. Li, T. Reindl, and I. M. Peters, "Global Techno-Economic Performance of Bifacial and Tracking Photovoltaic Systems," *Joule*, vol. 4, pp. 1–28, 2020. [Online]. Available: https://doi.org/10.1016/j.joule.2020.05.005

[160] L. Burnham, D. Riley, B. Walker, and J. M. Pearce, "Performance of bifacial photovoltaic modules on a dual-axis tracker in a high-latitude, high-albedo environment," in *2019 IEEE 46th Photovoltaic Specialists Conference (PVSC)*, 2019, pp. 1320–1327. [Online]. Available: https://doi.org/10.1109/PVSC40753.2019.8980964

[161] J. S. Stein, D. Riley, M. Lave, C. Hansen, C. Deline, and F. Toor, "Outdoor field performance from bifacial photovoltaic modules and systems," in *2017 IEEE 44th Photovoltaic Specialist Conference (PVSC)*, 2017, pp. 3184–3189. [Online]. Available: https://doi.org/10.1109/PVSC.2017.8366042

[162] J. R. Shewchuk, "Adaptive Precision Floating-Point Arithmetic and Fast Robust Geometric Predicates," *Discrete & Computational Geometry*, vol. 18, no. 3, pp. 305–363, Oct. 1997. [Online]. Available: https://www.cs.cmu.edu/~quake/robust.html

[163] LG, "LG390N2T-A5 (390-395 W) Datasheet." [Online]. Available: https://www.lg.com/us/business/solar-panels/lg-LG390N2T-A5

[164] Solcast, "Solcast API and Weather Forecasting Tool - Historical and TMY," 2024. [Online]. Available: https://solcast.com/historical-and-tmy

[165] Morgan Solar Inc., "Morgan Solar Timeline," 2023. [Online]. Available: https://morgansolar.com/timeline

[166] K. A. Klise, C. W. Hansen, and J. S. Stein, "Dependence on geographic location of air mass modifiers for photovoltaic module performance models," in *2015 IEEE 42nd Photovoltaic Specialist Conference (PVSC)*, 2015, pp. 1–5. [Online]. Available: https://doi.org/10.1109/PVSC.2015.7355939

[167] A. Lewis, "Performance of Silicon Heterojunction Cells and Modules in Arctic Applications: Impact of Angle of Incidence, Air Mass, and Spectra on Energy Yield," M.A.Sc thesis, University of Ottawa, 2020. [Online]. Available: https://ruor.uottawa.ca/items/4e374013-19a8-4300-8bab-6e3d74277d26

[168] F. Kasten and A. T. Young, "Revised optical air mass tables and approximation formula," *Appl. Opt.*, vol. 28, pp. 4735–4738, 11 1989. [Online]. Available: https://opg.optica.org/ao/abstract.cfm?URI=ao-28-22-4735

[169] M. Lee and A. Panchula, "Spectral correction for photovoltaic module performance based on air mass and precipitable water," in *2016 IEEE 43rd Photovoltaic*

Specialists Conference (PVSC), 2016, pp. 1351–1356. [Online]. Available: https://doi.org/10.1109/PVSC.2016.7749836

[170] J. A. Caballero, E. F. Fernández, M. Theristis, F. Almonacid, and G. Nofuentes, "Spectral corrections based on air mass, aerosol optical depth, and precipitable water for pv performance modeling," *IEEE Journal of Photovoltaics*, vol. 8, no. 2, pp. 552–558, 2018.

[171] E. M. Tonita, C. E. Valdivia, A. C. J. Russell, M. Martinez-Szewczyk, M. I. Bertoni, and K. Hinzer, "A general illumination method to predict bifacial photovoltaic system performance," *Joule*, vol. 7, pp. 5–12, 2023. [Online]. Available: https://www.sciencedirect.com/science/article/pii/S2542435122005761

[172] E. M. Tonita, C. E. Valdivia, A. C. J. Russell, and K. Hinzer, "Impact of spectral versus broadband albedo on bifacial silicon heterojunction photovoltaic devices across north america (conference presentation)," in *Physics, Simulation, and Photonic Engineering of Photovoltaic Devices XII*, A. Freundlich, S. Collin, and K. Hinzer, Eds., vol. PC12416. SPIE, 2023, p. PC124160G. [Online]. Available: https://doi.org/10.1117/12.2650155

[173] G. M. Masters, "Shading analysis using shadow diagrams," in *Renewable and Efficient Electric Power Systems*, 2nd ed. John Wiley and Sons, 2013.

[174] J. Appelbaum, "Bifacial photovoltaic panels field," *Renewable Energy*, vol. 85, pp. 338–343, 2016. [Online]. Available: https://www.sciencedirect.com/science/article/pii/S0960148115300732

[175] A. A. B. Baloch, S. Hammat, B. Figgis, F. H. Alharbi, and N. Tabet, "In-field characterization of key performance parameters for bifacial photovoltaic installation in a desert climate," *Renewable Energy*, vol. 159, pp. 50–63, 2020. [Online]. Available: https://www.sciencedirect.com/science/article/pii/S096014812030879X

[176] A. Al-Quraan, M. Al-Mahmodi, K. Alzaareer, C. El-Bayeh, and U. Eicker, "Minimizing the utilized area of pv systems by generating the optimal inter-row spacing factor," *Sustainability*, vol. 14, 2022. [Online]. Available: https://www.mdpi.com/2071-1050/14/10/6077

[177] P. H. A. Veríssimo, R. A. Campos, M. V. Guarnieri, J. P. A. Veríssimo, L. R. do Nascimento, and R. Rüther, "Area and lcoe considerations in utility-scale, single-axis tracking pv power plant topology optimization," *Solar Energy*, vol. 211, pp. 433–445, 2020. [Online]. Available: https://www.sciencedirect.com/science/article/pii/S0038092X20310239

[178] M. A. Green, *Third Generation Photovoltaics : Advanced solar energy conversion*. Berlin: Springer, 2003.

[179] H. Jain, M. Sengupta, A. Habte, and J. Tan, "Quantifying solar pv variability at multiple timescales for power systems studies," in *2020 47th IEEE Photovoltaic Specialists Conference (PVSC)*, 2020, pp. 0180–0185. [Online]. Available: https://doi.org/10.1109/PVSC45281.2020.9300658

[180] R. Tang, K. Abdulla, P. H. W. Leong, A. M. Vassallo, and J. Dore, "Impacts of Temporal Resolution and System Efficiency on PV Battery System Optimisation," in *17th Annual Asia Pacific Solar Research Conference*, 2017. [Online]. Available: https://api.semanticscholar.org/CorpusID:218840664

[181] A. de Vries, "The growing energy footprint of artificial intelligence," *Joule*, vol. 7, no. 10, p. 2191–2194, Oct. 2023. [Online]. Available: http://dx.doi.org/10.1016/j.joule.2023.09.004

[182] PVsyst, "PVsyst Release Notes," 2024. [Online]. Available: https://www.pvsyst.com/release-notes/

[183] G. M. Masters, "Temperature-Related PV Derating," in *Renewable and Efficient Electric Power Systems*, 2nd ed., 2013, pp. 327–330.

[184] S. P. Aly, S. Ahzi, N. Barth, and A. Abdallah, "Using energy balance method to study the thermal behavior of PV panels under time-varying field conditions," *Energy Conversion and Management*, vol. 175, pp. 246–262, 2018. [Online]. Available: https://www.sciencedirect.com/science/article/pii/S0196890418310033

[185] J. Appelbaum and T. Maor, "Dependence of PV module temperature on incident time-dependent solar spectrum," *Applied Sciences*, vol. 10, no. 3, 2020. [Online]. Available: https://www.mdpi.com/2076-3417/10/3/914

[186] S. E. Smith, B. Viggiano, N. Ali, T. J. Silverman, M. Obligado, M. Calaf, and R. B. Cal, "Increased panel height enhances cooling for photovoltaic solar farms," *Applied Energy*, vol. 325, p. 119819, 2022. [Online]. Available: https://www.sciencedirect.com/science/article/pii/S030626192201090X

[187] kWh Analytics, "Solar Generation Index," Tech. Rep., 2022. [Online]. Available: https://www.kwhanalytics.com/sgi

[188] R. Kennedy, *Solar assets are underperforming expectations by 8%, what is the root cause?* pv magazine, 2023. [Online]. Available: https://pv-magazine-usa.com/2023/05/03/solar-assets-are-underperforming-expectations-by-8-what-is-the-root-cause/

Appendix A

The flowcharts in this section describe the ray-primitive intersection algorithms for a single ray.

Ray-polygon intersection Daniel Sunday [9] provides an algorithm to determine whether a ray with direction $\vec{d}$ and origin d_0 intersects with an N-vertex polygon with corners $p_{0-(N-1)}$. The calculations require the normal of the plane described by the polygon corners, $\vec{n}$, to determine the intersection point p_{x} between an infinite line extending along $\vec{d}$ and the polygon plane. If p_{x} is within a length of $\vec{d}$ from the ray origin d_0, the sum of the areas of N triangles formed between p_{x} and $N-1$ pairs of polygon corners, A_{x}, is found. As shown in Fig. 7.1, if A_{x} is less than or equal to the area of the polygon in green, A_{p}, then the ray intersects the polygon.

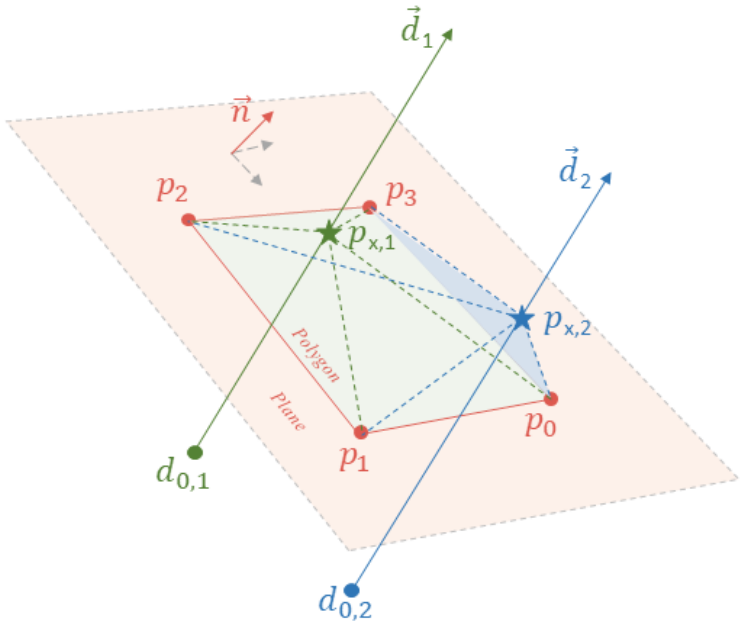


Figure 7.1: Rays $\vec{d_1}$ and $\vec{d_2}$ intersect with the plane defined by normal $\vec{n}$. Ray $\vec{d_1}$ intersects with the N-vertex polygon lying on the plane defined by corners $p_{0-(N-1)}$ since the collective area of the triangles formed by the intersection point $p_{x,1}$ and corners sets $p_{0,1}, p_{1,2}, p_{2,3}, p_{3,0}$ is $\leq$ the polygon area in green. Ray $\vec{d_2}$ does not intersect since this collective sum for intersection point $p_{x,2}$ exceeds the polygon area by the blue highlighted region.

The algorithm is described in further detail in Fig. 7.2.

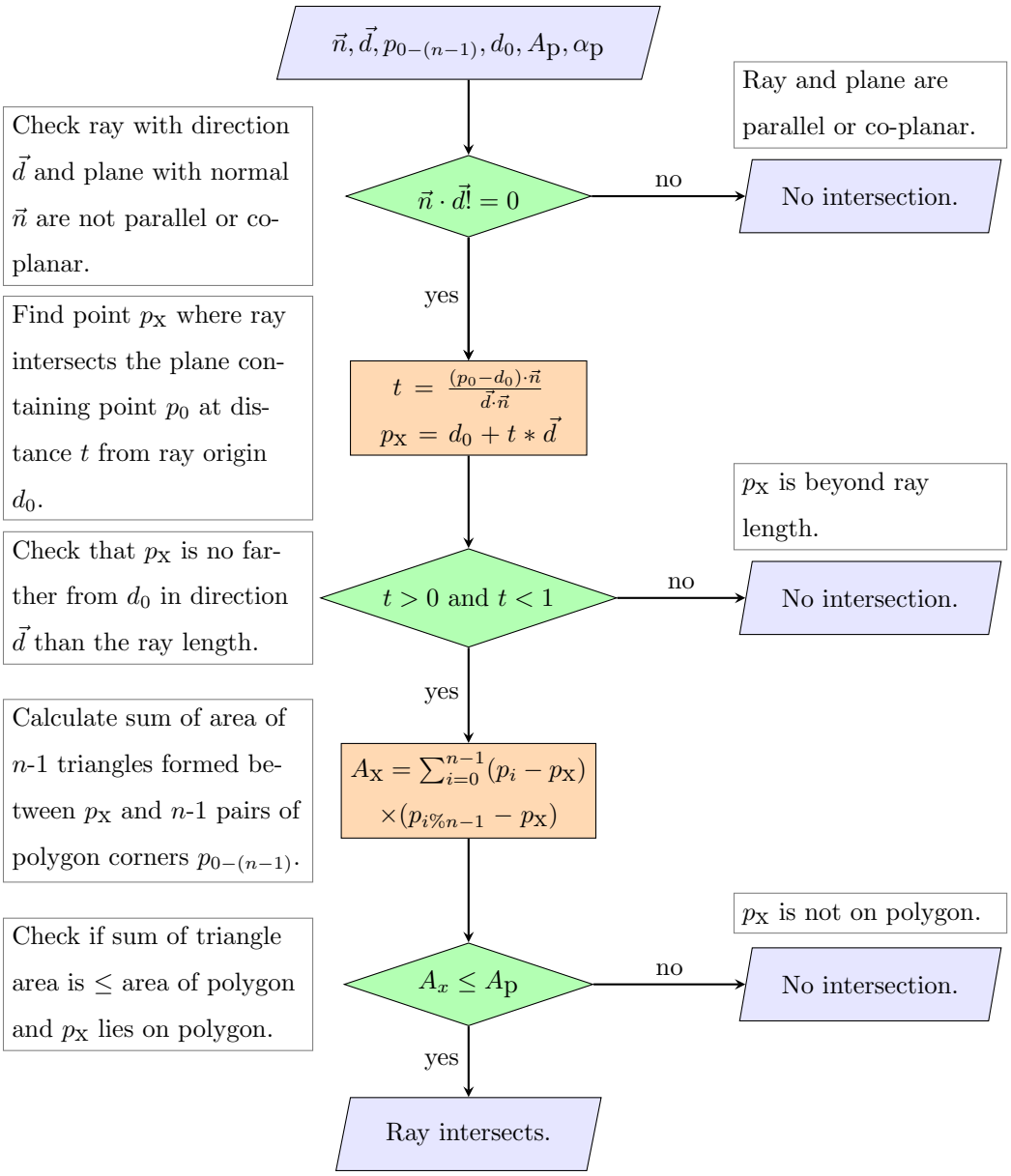


Figure 7.2: Flowchart for ray-polygon intersection [9]

Ray-cylinder intersection Sunday also provides a ray-cylinder intersection test [10]. The cylinder can be described as the volume bound by a radial distance r_c from a line segment with origin c_0 and direction and length $\vec{c}$. To determine whether a ray passes within this volume, the algorithm finds the distances s and t along $\vec{d}$ and $\vec{c}$ that result in the shortest distance between the line segments. This distance is l or the magnitude of the vector between the closest points $\vec{dP}$ (i.e., l_1 and l_2 in Fig. 7.3 for rays $\vec{d_1}$ and $\vec{d_2}$.

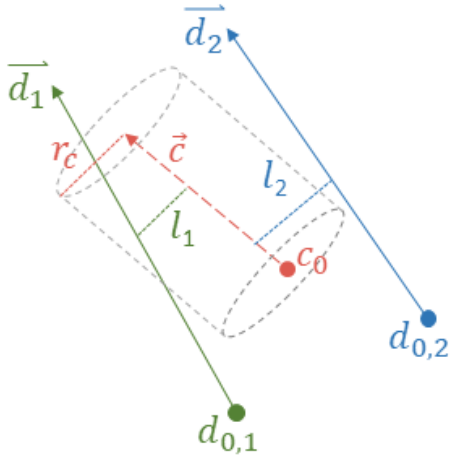


Figure 7.3: Ray $\vec{d_1}$ intersects with the cylinder defined by central axis $\vec{c}$ and radius r_c, while ray $\vec{d_2}$ does not, since l_1 (the shortest distance between $\vec{c}$ and d_1) < r_c but $l_2 > r_c$.

Since the $\vec{dP}$ represents the shortest distance between the ray and the cylinder line segment, distances s and t can be found from the solution to the set of linear equations Eq. (57)-58 that describe the projections of Eq. (56) onto $\vec{d}$ and $\vec{c}$. Here $\vec{w_0}$ is the vector between the origins of the ray and cylinder line segment.

$$\vec{dP} = \vec{w_0} + s\vec{d} - t\vec{c} \tag{56}$$

$$s(\vec{d}\cdot\vec{d}) - t(\vec{d}\cdot\vec{c}) = -\vec{d}\cdot\vec{w_0} \tag{57}$$

$$s(\vec{c}\cdot\vec{d}) - t(\vec{c}\cdot\vec{c}) = -\vec{c}\cdot\vec{w_0} \tag{58}$$

$$as - bt = -d \tag{59}$$

$$bs - ct = -e \tag{60}$$

The coefficients $a - e$ of this set of equations can be used to form the solution of the equation set as $s = sN/sD$ and $t = tN/tD$. These numerators and denominators must be adjusted if distances s and t are negative or greater than 1, since the intersection point is not within the line segment or

ray.

$$sN = \begin{vmatrix} -d & -b \\ -e & -c \end{vmatrix} \tag{61}$$

$$tN = \begin{vmatrix} a & -d \\ b & -e \end{vmatrix} \tag{62}$$

$$D = sD = tD = \begin{vmatrix} a & -b \\ b & -c \end{vmatrix} \tag{63}$$

$$\tag{64}$$

The algorithm is described in further detail in the flowcharts in Fig. 7.4-7.6.

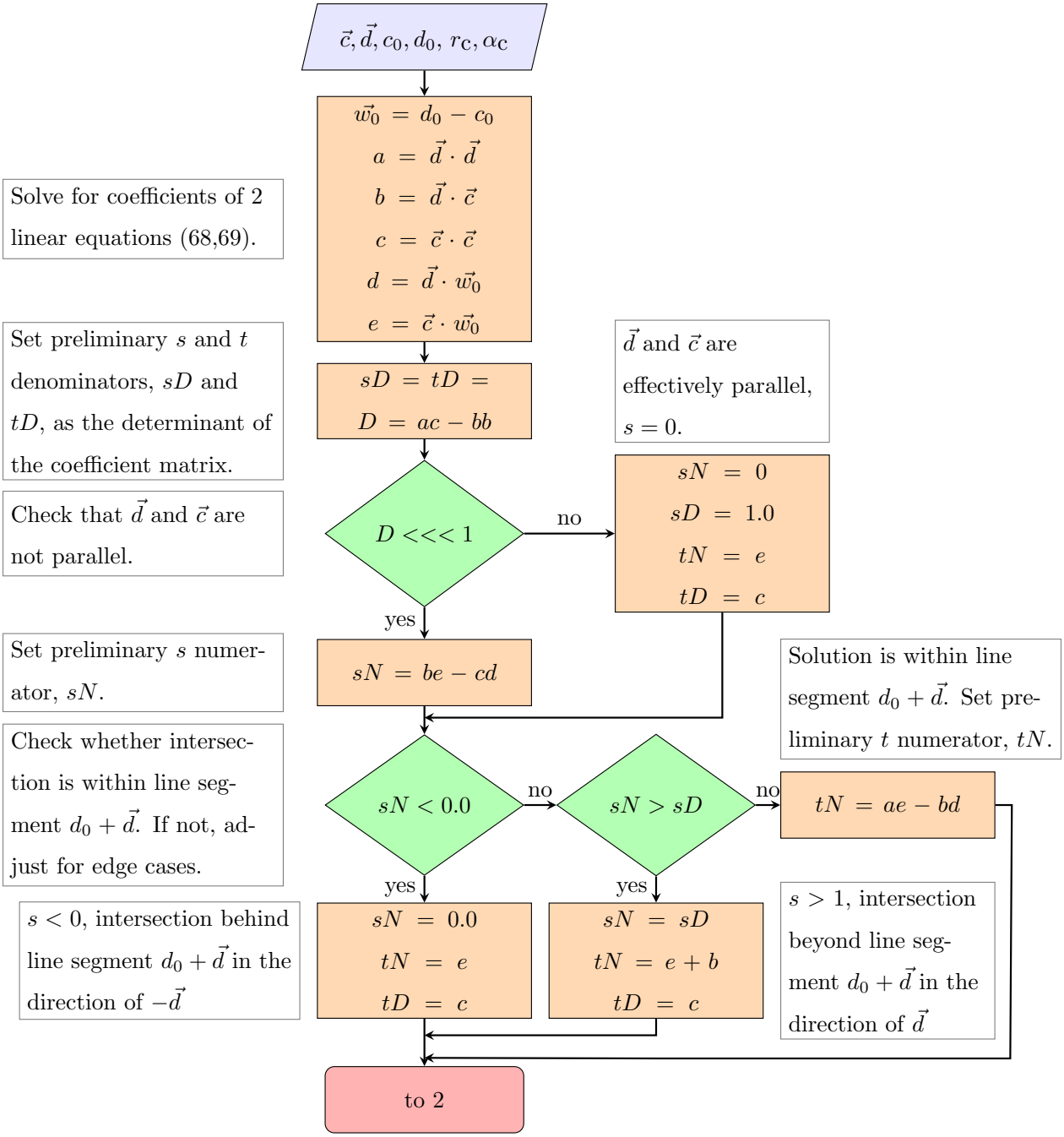


Figure 7.4: Flowchart for ray-cylinder intersection (Part 1) [10]

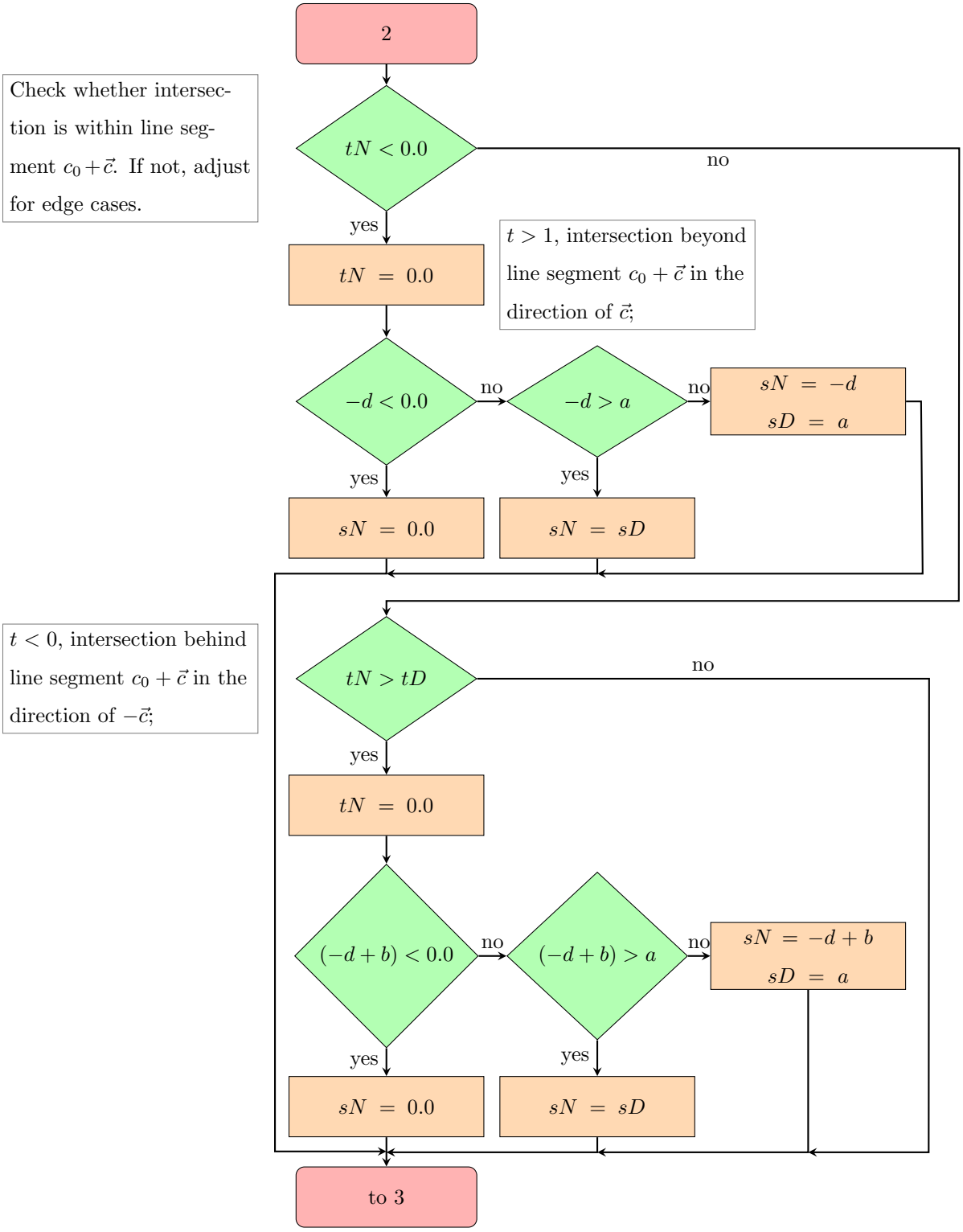


Figure 7.5: Flowchart for ray-cylinder intersection (Part 2) [10]

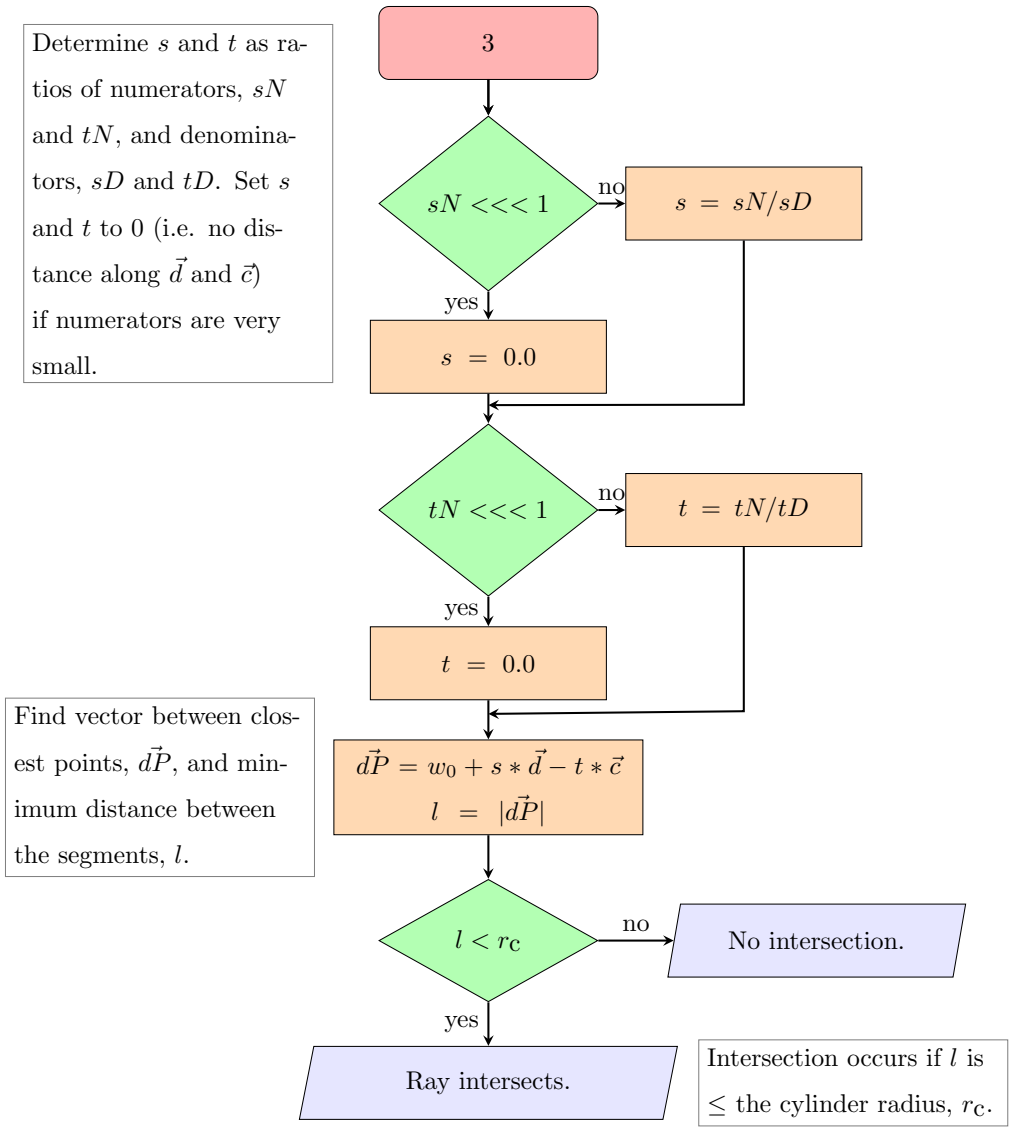


Figure 7.6: Flowchart for ray-cylinder intersection (Part 3) [10]

Ray-prism intersection: axis-aligned rectangular Williams et al. [11] describe an algorithm to determine whether a ray $d_0 + \vec{d}$ intersects with a rectangular prism with faces that are aligned with the scene axes X, Y, Z. The prism is defined by the extreme coordinates of each face where $b_{0,x-z}$ is the minimum bounds in X, Y, and Z and $b_{1,x-z}$ is the maximum bound, based on an origin at $(0, 0)$. For a given ray, the distance along $\vec{d}$ from d_0 at which the ray crosses the closest bound to d_0 for a given axis is found as $t_{\text{min},x-z}$. The next bound crossing in the given axis is found as $t_{\text{max},x-z}$. The closest and farthest bounds along $\vec{d}$ are dictated by the sign of $\vec{d}$ in the given axis. When considering two dimensions, for example X and Y in Fig. 7.7, the ray only intersects the

projection of the prism in the X-Y plane if the bound crossing points alternate between one axis and the other, as in d_1. For this alternation to occur and for an intersection to be possible in the X-Y plane, $t_{\text{min},x}$ must be shorter than $t_{\text{max},y}$ and $t_{\text{min},y}$ must be shorter than $t_{\text{max},x}$. If an intersection is possible in the X-Y plane, the subspace of the original prism projection in the X-Y plane in which intersection can occur provides the constraining ray-bound crossing points that must alternate with the Z-bound crossing points along $\vec{d}$.

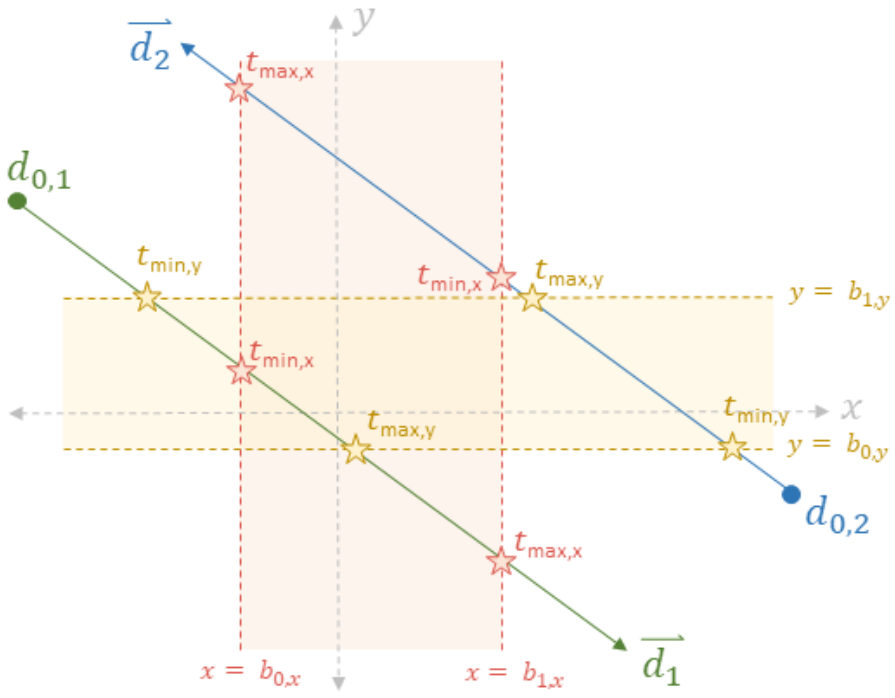


Figure 7.7: Ray-prism (axis-aligned) intersection projected in the xy plane. Green ray $\vec{d_1}$ intersects with the rectangular prism defined by unit vectors b_u, central point b_c, and dimensions b_h, while blue ray $\vec{d_2}$ does not. Stars indicate points where rays cross the bounds of a slab. (Figure adapted from [12]).

The algorithm is described in further detail in the flowchart in Fig. 7.8.

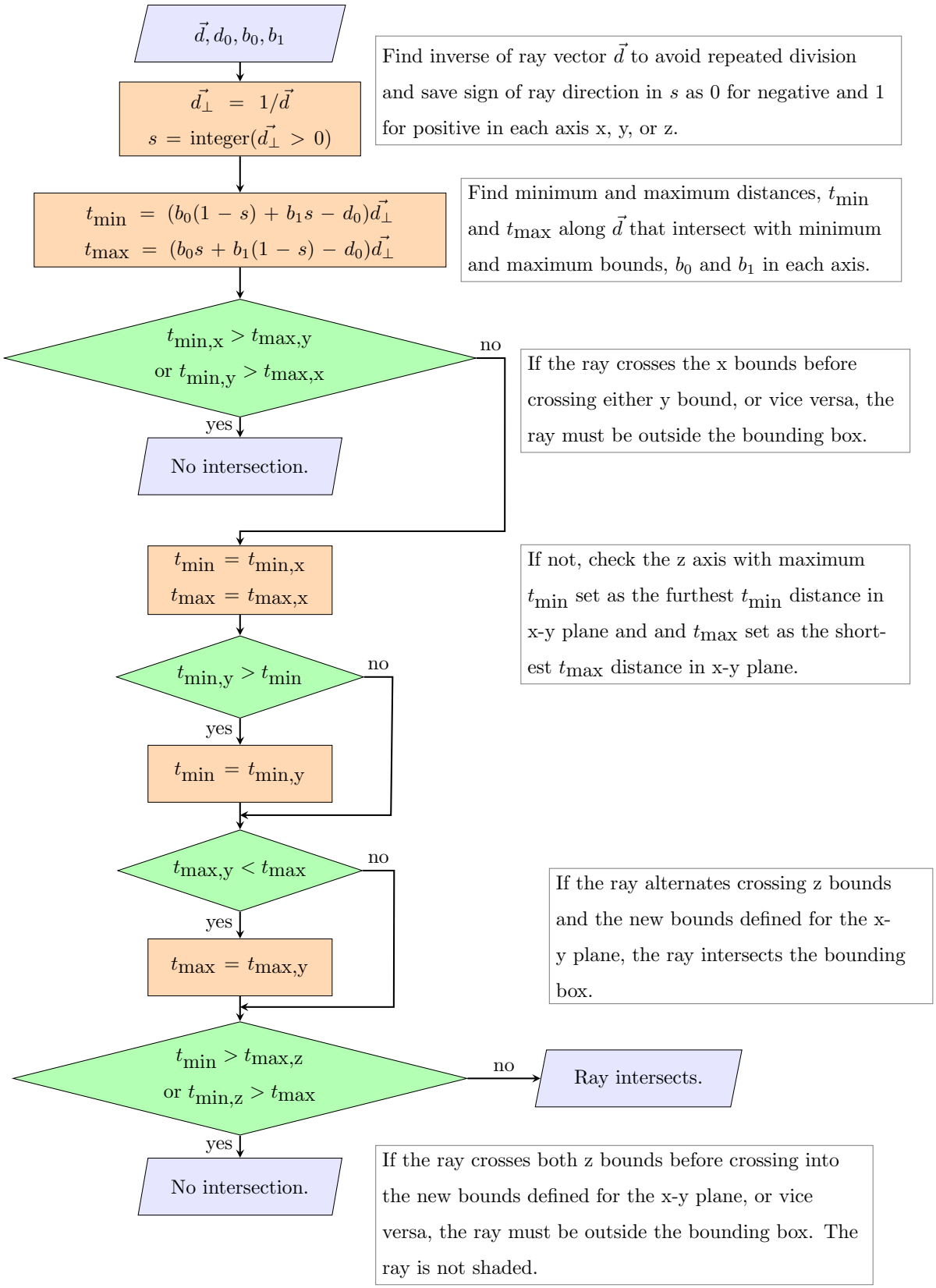


Figure 7.8: Flowchart for ray-prism intersection : axis-aligned rectangular prisms [11]

Ray-prism intersection: arbitrarily-oriented rectangular Möller et al. [12] describe an algorithm to check for intersection between rays and arbitrarily-oriented rectangular prisms. This process follows a similar approach to the axis-aligned rectangular prism, requiring the ray to cross the bounds in two axes in an alternating fashion for intersection to be possible. However, the bounds are now defined based on positive and negative half-lengths, $\pm b_h$, along the direction of unit vectors b_u in three axes of the oriented prism that point away from a central origin point, b_c. The area between the projections of the prism faces onto each of the unit vectors b_u is also known as a *slab*, in orange and yellow in Fig. 7.9.

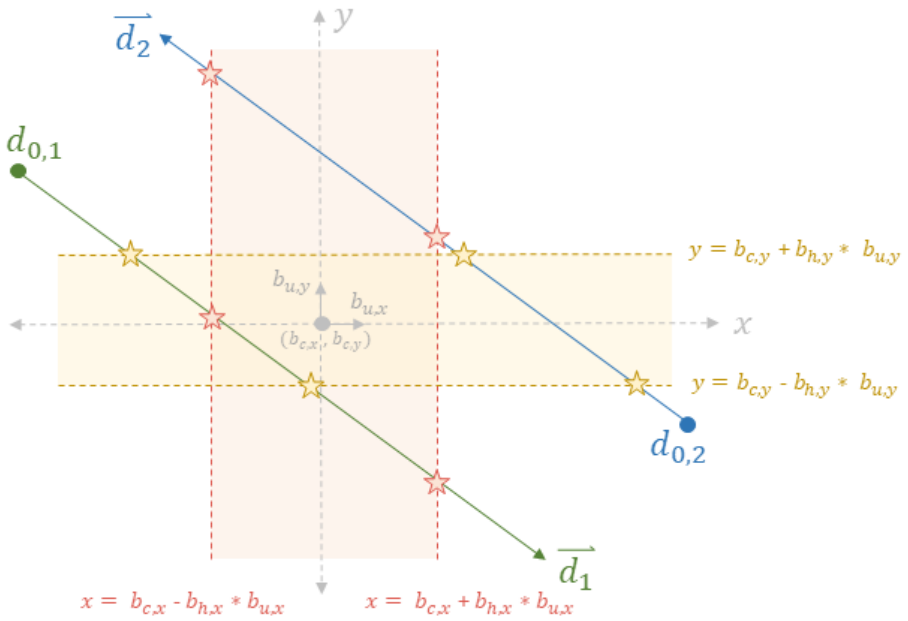


Figure 7.9: Ray-prism (arbitrarily oriented) intersection projected in the xy plane. Green ray $\vec{d_1}$ intersects with the rectangular prism defined by extreme coordinates in each axis $b_0/1, x/y$, while blue ray $\vec{d_2}$ does not. Stars indicate points where rays cross the bounds of a slab. (Figure adapted from [12]).

The algorithm finds the bounds-crossing points t_1 and t_2 along $\vec{d}$ such that $t_1 < t_2$. If a ray does not intersect the projection of the prism for a certain dimension (i.e., only non-alternating bounds-crossings are found), the ray cannot intersect the prism, even if intersections are possible in other dimensions. If ray intersections are possible in all dimensions, the ray necessarily intersects the prism.

The algorithm is described in further detail in the flowchart in Fig. 7.10.

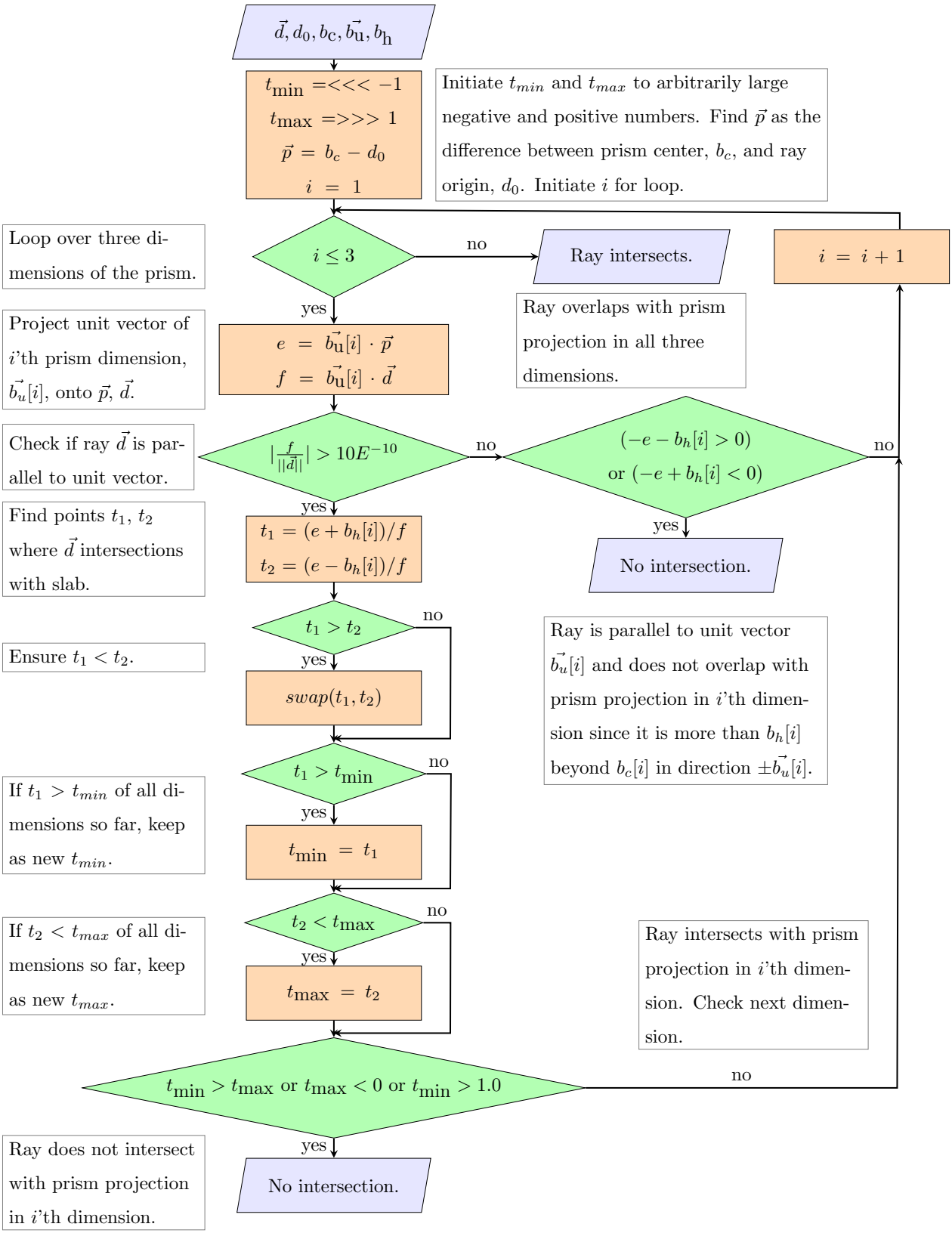


Figure 7.10: Flowchart for ray-prism intersection : arbitrarily-oriented rectangular prisms [12]

Appendix B

While the DUET and PVsyst energy yield results are not presented in Section 3.5.2, they are presented in the energy yield summary of the International Energy Agency report [2]. Thus, a brief discussion on bifacial mismatch loss factor, M_{PVsyst}, is warranted. This static loss factor is intended to represent the annual energy yield loss due to rear irradiance non-uniformity and is applied to energy yield at each timestamp. It is labelled as "Mismatch loss factor" in the PVsyst v6.86 bifacial input pane, "Rear mismatch loss" in the PVsyst report input parameter section (Fig. 3.20), and "Mismatch for back irradiance" in the PVsyst report loss diagram. The suggested default value for this parameter is 10%, but PVsyst documentation [151] states that this value is a rough estimate that is not based on modelling or calculation.

An analysis of outputs from a PVsyst v6.86 simulation reveals the following formula for the bifacial mismatch loss factor:

$$M_{\text{PVsyst}} = \frac{1 - \frac{P_1}{P_0}}{BG_{\text{PVsyst}}} \tag{65}$$

$$BG_{\text{PVsyst}} = \frac{\bar{G}_{\text{r}}}{\bar{G}_{\text{f}} + \phi \bar{G}_{\text{r}}} \tag{66}$$

where ϕ is the module bifaciality factor, $\bar{G_{\text{(f/r)}}}$ is the per-timestamp average front/rear irradiance, and BG_{PVsyst} represents a form of bifacial irradiance gain. For the central module approximation, P_1 is the module power accounting for current mismatch losses within the module and P_0 is the module power with an average irradiance applied across all cells (i.e., the sum of cell maximum power points under non-uniform illumination [42]).

Note: Release notes for PVsyst v7.4.6 [182] state that "the bifacial factor of the PV module is now considered when computing the rear mismatch loss" - a correction which suggests that the bifacial irradiance gain *may* now be the following, which has *not* been verified:

$$BG_{\text{PVsyst}} = \frac{\phi \bar{G}_{\text{r}}}{\bar{G}_{\text{f}} + \phi \bar{G}_{\text{r}}} \tag{67}$$

While M_{PVsyst} is meant to represent loss due to rear irradiance non-uniformity, it is a non-trivial task to separate the effects of front and rear non-uniformity. Deline et al. [42] report a combined

current mismatch loss due to front and rear non-uniformity. Additionally, annual front and rear non-uniformity are of similar magnitude for fixed-tilt systems, as demonstrated in Fig. 4.3 and Section 3.1 Fig. 8; therefore, completely neglecting front uniformity would underestimate current mismatch loss.

Based on DUET v.uO-2020 calculations of M_{PVsyst} for Abu Dhabi, we applied a 3.7% bifacial mismatch loss factor accounting for front and rear irradiance non-uniformity in the PVsyst v6.86 simulations to achieve the -0.30% annual loss. Bifacial mismatch factors for Antofagasta and Groningen were 4.2% (-0.36% loss) and 7.3% (-0.83% loss), respectively.

Appendix C

As seen in Section 3.1.III, the choice between three common cell or module temperature models impacts modelled bifacial power mean absolute error by 0.8-1 mW/Wp on an annual basis. This result indicates relatively close agreement between the *Faimain* [15], *Sandia* [14], and *NOCT* [183] temperature models over an extended time period. Based on these same three temperature models, the following section examines the difference between modelled bifacial and monofacial cell temperature for the central modules in the fixed-tilt and horizontal single-axis tracked (HSAT) systems at the Technical University of Denmark as described in Section 3.1. The analysis compares the temperature, and power and energy yield uncertainty introduced by the choice of temperature model in bifacial vs. monofacial systems, quantifying the additional uncertainty introduced when modelling rear side temperature effects.

To examine the impact of incident rear irradiance on cell temperature, Fig. 7.11 shows the hourly absolute difference in bifacial vs. monofacial cell temperature as a function of rear irradiance for the three models. The additional temperature ranges from 0-2.5°C for a range of 0-85 $\mathrm{W/m^2}$ of rear irradiance. The NOCT model in orange neglects the cooling effects of wind and thus shows marginally higher temperatures than the other two models. For both the Faiman and Sandia models, we see a spread of cell temperatures at each irradiance due to differing wind speed at timestamps with similar irradiance. This analysis neglects monofacial heating due to any minimal rear incident radiation absorbed through the highly reflective white backsheet.

While east and west single-axis tracked tiers in Fig. 7.11 A and C show relatively similar additional temperature and irradiance ranges, the south-facing fixed-tilt systems experience more

rear irradiance on the lowest southern tier (Fig. 7.11D) and than on the highest northern tier (Fig. 7.11B). This differential between fixed-tilt tiers in the 2P system corresponds to an approximate 20 $\mathrm{W/m^2}$ difference in maximum rear irradiance and an approximate 1°C difference in maximum additional temperature as compared to the monofacial case.

The coefficient of variation (CV) in cell temperature across the three models can represent the uncertainty that the differing temperature models introduce into the calculation of this additional bifacial temperature. The per-timestamp CV is:

$$CV = \frac{\sigma}{\mu} \tag{68}$$

where σ is the standard deviation between outputs predicted using the three temperature models, and μ is the average.

For both tiers in both systems, the average per-timestamp CV in cell temperature ($\bar{\mathrm{C}}\mathrm{V}$ in Δ_{T_c}) is 4.5%. Propagating this temperature uncertainty based on the average cell temperature, $\bar{\Delta}T_c$, and a -0.39%/°C temperature coefficient of power, μ_P, the estimated additional uncertainty in bifacial vs. monofacial power is 0.01% for the average timestamp. This result is shown in the rightmost column in Table 5 that is the row-wise product of the other columns. This estimated difference in bifacial vs. monofacial power uncertainty is confirmed by the *calculated* absolute difference in the average CV ($\bar{\mathrm{C}}\mathrm{V}$) in bifacial power vs. average CV in monofacial power (P_{bi}, P_{mono}), as in Table 6.

The bifacial and monofacial CV in annual energy yield across the three modules are 0.27 and 0.25-0.26%, respectively, as shown in Table 7 (CV in EY_{bi} and EY_{mono}). The difference between these CV, shown in the third column, is 0.016-0.020% absolute. This additional bifacial-PV-specific uncertainty is negligible with respect to the total 0.25-0.27% energy yield CV introduced by the choice of temperature model for both monofacial and bifacial systems. Since the differences in bifacial vs. monofacial modelling uncertainty for cell temperature, power, and energy yield are all less than 0.02%, this analysis indicates that the cell temperature gains induced by rear-incident irradiance for the Technical University of Denmark site introduce negligible additional modelling uncertainty in the bifacial PV modelling pipeline.

Site-specific conditions may impact these findings. For example, the monthly albedo values

provided for this site ranged from 0.19-0.23, which is typical for grass or dirt and satisfies the range seen in many low-to-mid latitude locations with such ground cover. Locations with snow will see higher rear irradiance contributions which will cause additional cell heating, albeit during periods of colder ambient temperature. Any resulting increase in rear irradiance contribution would lead to additional uncertainty not accounted for here.

The above analysis has demonstrated that the three empirical models show relatively close agreement and introduce low bifacial-specific uncertainty. However, modeled module temperature may still vary from measured data and should be validated against field data in future work. Time- and wind-dependent models [184–186] should also be explored to capture transient effects as well as air currents unique to each row spacing and tilt angle. Validating temperature models is of particular interest since module temperature has yet to be ruled out as a factor in the 8% under-performance in mainland U.S. solar plant production compared to modelling [187, 188].

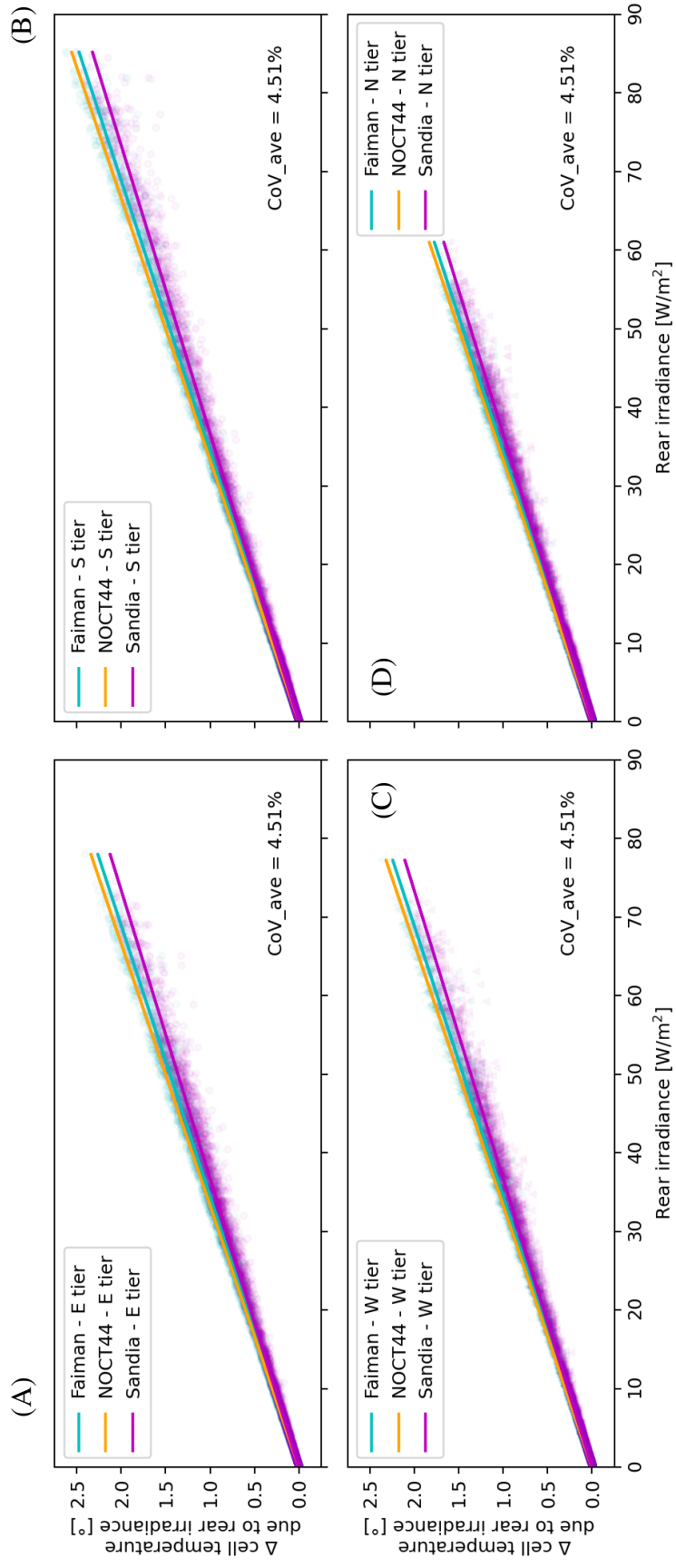


Figure 7.11: Modelled change in (Δ) cell temperature due to rear irradiance for three cell temperature models and four modules: (A) HSAT east, (B) fixed-tilt north, (c) HSAT west, and (D) fixed-tilt south.

	$\bar{\Delta}T_c$ [°C]	$\bar{\text{CV}}$ in ΔT_c [%]	μ_P [%/°C]	Estimated $\Delta\bar{\text{CV}}$ in P [%, bi. vs. mono.]
HSAT E	0.63	4.5	-0.39	0.01
HSAT W	0.62	4.5	-0.39	0.01
Fixed S	0.61	4.5	-0.39	0.01
Fixed N	0.54	4.5	-0.39	0.01

Table 5: *Estimated* absolute difference in bifacial vs. monofacial average coefficients of variation in power ($\Delta\bar{\text{CV}}$ in P), across three temperature models. $\bar{\Delta}T_c$: average difference in bifacial vs. monofacial cell temperature; $\bar{\text{CV}}$ in ΔT_c: average CV in difference between bifacial and monofacial cell temperature; μ_P: temperature coefficient of power.

	$\bar{\text{CV}}$ in P_{bi} [%]	$\bar{\text{CV}}$ in P_{mono} [%]	$\Delta\bar{\text{CV}}$ in P [%, bi. vs. mono.]
HSAT E	0.15	0.14	0.01
HSAT W	0.15	0.14	0.01
Fixed S	0.13	0.12	0.01
Fixed N	0.14	0.13	0.01

Table 6: *Calculated* absolute difference in bifacial vs. monofacial average coefficients of variation in power ($\Delta\bar{\text{CV}}$ in P), across three temperature models. $\bar{\text{CV}}$ in P_{bi}: average CV in bifacial power; $\bar{\text{CV}}$ in P_{mono}: average CV in monofacial power.

	CV in EY_{bi} [%]	CV in EY_{mono} [%]	ΔCV in EY [%, bi. vs. mono.]
HSAT E	0.27	0.26	0.016
HSAT W	0.27	0.26	0.016
Fixed S	0.27	0.25	0.020
Fixed N	0.27	0.25	0.014

Table 7: Calculated absolute difference in coefficients of variation (ΔCV) in bifacial vs. monofacial *annual energy yield* (EY_{bi}, EY_{mono}) across three temperature models.